DISSERTATION

TUNING ANTIMONY ANODES THROUGH ELECTRODEPOSITION TO INFORM ON THE REACTION AND DEGRADATION MECHANISMS IN SODIUM-ION BATTERIES

Submitted by

Kelly Nieto

Department of Chemistry

In partial fulfillment of the requirements

For the Degree of Doctor of Philosophy

Colorado State University

Fort Collins, Colorado

Summer 2023

Doctoral Committee:

Advisor: Amy L. Prieto

Justin Sambur
Amber Krummel
Todd Bandhauer

ABSTRACT

TUNING ANTIMONY ANODES THROUGH ELECTRODEPOSITION TO INFORM ON THE REACTION AND DEGRADATION MECHANISMS IN SODIUM-ION BATTERIES

Electrification of portable devices, transportation, and large grid-level storage necessitate a portfolio of energy storage devices tailored to specific applications. Sodium-ion batteries are a naturally abundant alternative to lithium, but high performing anodes must be developed in order to reach widespread commercialization. Alloy-based anodes such as antimony (Sb) are attractive targets for their high theoretical capacities. However, the electrochemical performance of Sb is poor, and the reaction mechanism is poorly understood. Herein, antimony-based anodes for sodium-ion batteries are explored to elucidate sodiation pathways and investigate the role of electrode fabrication, electrolyte composition, and architecture on the reaction and degradation mechanism. Chapter I describes our research methodology and consists of our synthetic method of electrodeposition, materials characterization, battery assembly, and electrochemical characterization. Through this process, we can develop a better understanding of the electrochemical performance of alloy-based anode materials.

The tunability of electrodeposition as a synthetic technique for the fabrication of Sb-based anodes is exploited in Chapter II. The effects of solution additives in the electrodeposition of Sb anodes are investigated and provide insight into how the morphology and crystallinity of the deposited anodes can be tuned. It was revealed that CTAB and SPS could significantly tune the electrodeposition of Sb films by altering the deposition by causing structural changes that either improved cycle life or rate capabilities. In Chapter III, electrodeposited and slurry cast Sb anodes

were compared through differential capacity analysis, and it was demonstrated that electrode fabrication can significantly impact the sodiation/desodiation reaction pathway. Additionally, electrodeposited Sb anodes provided valuable insight into the mechanism without having to deconvolute the influences of binders and additives necessary in slurry casting.

Chapter IV describes preliminary studies on how electrolyte composition can influence sodiation/desodiation reactions during Sb anode cycling. Traditional battery electrolytes are composed of carbonate species and salts, which are reduced onto the anode surface to form the solid electrolyte interphase (SEI). Due to the inherent volume expansion of Sb anodes when sodiated/desodiated, the SEI is hypothesized to continuously form and affect the cyclability of these anodes. In this investigation, we have found that electrolyte composition can influence the cycle life and sodiation/desodiation pathway, and we describe additional studies to probe how the SEI could hinder sodium ion transport.

Chapter V builds upon Chapter II and explores how electrodeposition can be employed to develop three-dimensional (3D) electrodes to enhance the energy and power density of Sb-based anodes. Although we show that experimental parameters can be tuned to obtain uniform coverage, significant challenges in achieving conformal coverage of the current collector while maintaining high active material loading remain.

The final chapter, Chapter VI, concludes the dissertation by describing further directions required to deepen the understanding of the degradation mechanism for Sb. We have begun to develop a 3D-printed optical, electrochemical cell that can couple operando optical studies with electrochemical studies to understand how electrode composition, structure, and electrolyte composition affect mechanical stability and ionic/electronic diffusivity in these electrodes. Understanding these fundamental processes and developing tools and characterization techniques

to study alloy-based anode materials will lay the foundation for creating earth-abundant energy storage systems with high energy densities and long cycle life.

ACKNOWLEGMENTS

This dissertation would not be possible without the support I have received from numerous people. First, I would like to acknowledge my lab mates, both current and former members of the Prieto Research Group. Thank you for the insightful conversations, research discussions, constant encouragement, and for pushing me to be better while also picking me up when I needed it most (or when all my experiments were failing). Thank you to Jeff for helping me grow and learn in the beginning of my time in graduate school; your mentorship, late night talks, and friendship helped me grow as a scientist and as a person. Your encouragement and guidance when applying for fellowships was also the reason I was able to receive several of these awards. Amanda, thank you for being a wonderful friend and supporter. You were a big help in many of my projects, and I will always be grateful that you were always there to help guide me through my messy thoughts on the white board. Thanks for being my writing buddy and spending countless hours with me at coffee shops and breweries to get this dissertation finished. Nate, thanks for always supporting me and celebrating my big life events. You have always been there for me as a sounding board for any problem and I'll always cherish our long office talks. Rhys, it has been a pleasure being your mentor and watching you grow into the scientist you are now. I've been able to learn and grow alongside you during this time, and without you, I'm not sure the optical project would have ever been able to come to life. I truly appreciate the different perspective you bring, and I can't wait to see what you accomplish next.

To Amy Prieto, thank you for being my advisor these past five years. You are my role model, mentor, and you constantly inspire me, and I am thankful for the time I've had to watch and learn from you. You have helped make Colorado a second home for me, and I appreciate all

that you have done to show your care for me and our group. Your mentorship has helped me become a better leader, your guidance has helped me become more confident and independent, and your example has shown me what I can accomplish. Thank you for your unwavering support, you have taught me to never shy away from a challenge and I will continue to carry these traits onto the next chapter of my career. Without you, my dissertation, my fellowship, and my other accomplishments would not have been possible.

Thank you to my past mentors, including graduate students during my time at Texas A&M, my undergraduate advisor Sarbajit Banerjee, and Todd Alam from Sandia National Lab. Todd, you taught me how to reframe my way of thinking, and how to have an end-goal in mind when starting a new project, which has made a huge difference in my approach to science. Sarbajit, it has been almost 10 years since I met you, and you are still just as supportive now as you were then. Stepping into your research lab my freshman year of college changed the direction of my life, and now I would like to thank you for every bit of support you have given me since then. You have always encouraged me, including your encouragement to pursue graduate school, and helping me find a place that I would be successful. I would not be who I am today if I had not stepped foot into that lab.

To my family and friends, thank you for shaping me into the person I am today outside of the lab. I am grateful to everyone who has listened to me, checked in on me, and supported me to pursue this dream. Each moment I was able to escape the stress of graduate school helped keep me sane. Thank you to my parents, and especially my mom, who encouraged me to step out of my comfort zone and for reminding me that the hardest things in life, are the things most worth doing.

These past five years of my life have been exceptionally challenging but without them I wouldn’t have met the person that I can’t imagine doing life without. To my fiancée, Sarah

Bingham, you have always been a breath of fresh air since the moment we first met. You always know how to make me feel better when times are hard and have always been the best at celebrating me and my accomplishments, no matter how small they are. Thank you for always pushing me to be my best and for reminding me that my best is good enough. I'm so grateful for our little family (Ellie, Rio, Oliver, and Oakley), all our adventures, and the life we have built together. I can't wait for this next chapter of our lives.

TABLE OF CONTENTS

I. ELECTRODEPOSITION AS A FABRICATION TECHNIQUE FOR THE DEVELOPMENT OF Sb-BASED ANODES FOR SODIUM-ION BATTERIES[1]

1.1 Sodium-Ion Batteries for Energy Storage Applications

As the quantity and size of markets for rechargeable batteries continues to grow, it is becoming more clear that there is no one perfect battery to suit every application. In the best case, we would have batteries that store a very large amount of energy per unit mass or volume (energy density), can charge and discharge very quickly (power density), and can cycle many times with a very low loss of efficiency (cycle life). Ideally such a battery would be made from earth abundant, recyclable, sustainably mined or made materials that could be scaled using inexpensive, safe manufacturing. There is, as of now, no such battery. Because we don't have a battery that is one size fits all, the wide range of potential applications for energy storage is a significant driving force for discovering and implementing a diversity of new battery chemistries to meet a wide range of requirements.

Elemental sodium is an attractive alternative to lithium for battery applications because it has a significantly higher earth abundance relative to lithium, good global distribution, lower cost, and a standard reduction potential near that of lithium (-3.04 V for Li/Li^+ and -2.71 V for Na/Na^+).[1] Currently, the chemistries developed for cathodes, anodes, and electrolytes for Na-ion batteries are not nearly as well developed or understood as those of Li.[2–4] A common approach to Na-ion research involves screening the top candidates from Li-ion battery technologies for use in Na-ion

[1] This chapter is intended to motivate the work in this dissertation. Portions of this chapter are adapted from a NSF SSMC grant (#2211067) cowritten with Kelly Nieto, Nathan J. Gimble, Leslie A. Kraynak, and Amy L. Prieto. Other portions of this chapter are from a published manuscript in the *Electrochemical Society: Interface* with Kelly Nieto, Nathan J. Gimble and Amy Prieto (*Electrochem. Soc. Interface*, **2021***,* 30.). Kelly Nieto and Nathan J. Gimble equally wrote and edited the manuscript with supervision and additional help from Amy L. Prieto.

systems. This strategy is not effective because Li and Na exhibit surprisingly different chemistries, despite both being Group I elements. For example, the most common anodes for Li-ion batteries, graphite, and silicon, have negligible capacities for Na.[5] Although pure Na metal is amenable to electroplating and stripping (a requirement for using the pure metal as an anode), it is highly reactive and unstable in common Li-ion electrolytes.

Developing guidelines to accelerate discovery and understanding of next generation anode materials for Na-ion batteries is crucial for the field to progress. In order to understand each novel electrode, one must identify the intermediate structures and their corresponding properties as the anode is cycled. Through this process, a more thorough understanding of the degradation mechanisms can be gained to optimize the anode's performance. However, as batteries are complex, intricately connected systems, understanding how a candidate electrode material reacts with sodium by itself is not sufficient; the complex interactions with all components of the battery are important. Herein, we describe how electrodeposition as a synthetic technique allows for the fundamental investigation of the intrinsic properties of anode materials that can enable precise structure-property measurements, degradation mechanisms, and access to energy dense three-dimensional electrodes for the application of sodium-ion batteries in energy storage systems.

1.2 Developing Alloy-based Anodes for Na-ion Batteries

Viable sodium-ion batteries require materials that can reversibly store large amounts of Na-ions. Materials that alloy with alkali-ions (specifically Na), such as Sn, Sb, Ge and Pb, are attractive anode materials because they can store up to ten times more energy than intercalation materials due to their higher gravimetric and volumetric energy densities.[6,7] However, one of the ongoing challenges has been the large volume changes that occur during insertion and removal of alkali-ions that lead to poor mechanical stability with successive cycling.[8] In recent years,

additional issues of alloys have emerged related to their poor surface stability, grain aggregation, and low alkali-ion diffusivity due to limited knowledge of structural changes and electrode surface interactions during operation.[9,10]

Elemental Sb has received significant attention as a potential Li- and Na-ion anode material since ca. 2000 and has been shown as a useful anode material due to its highly reversible alloying with both Li and Na where for every Sb atom, three Li^+/Na^+ ions are stored resulting in the Li_3Sb/Na_3Sb structure.[11] In its pure form, Sb has a high specific capacity of 660 mAh/g, thermal stability, and electronic conductivity.[7,12] Although Na and Li have the same charge and are relatively close in reduction potentials, isostructural forms of the same structure may experience very different storage mechanisms when cycled. The sodiation/desodiation of Sb is much more complex than the lithiation pathway and amorphous phases such as Na_xSb are present while all phases of the lithiation pathway are crystalline.[11,13–15] The sodiation pathway has been investigated in previous studies, both experimentally and theoretically, but is still not completely understood as different phase transformations are observed in comparable systems.[11,13,14,16,17]

Our work on the sodiation of Sb electrodes cycled over long periods of time demonstrates the wealth of information that can be gained from differential capacity analysis (**Figure 1.1)** to understand the sodiation/desodiation mechanism of Sb anodes. Changes in the peak position of a feature to higher overpotentials in a differential capacity plot can be indicative of kinetic limitations, such as excessive solid electrolyte interface (SEI) formation.[18] The appearance or disappearance of peaks can provide information about phase changes in the electrode material during cycling.[19] Additionally, changes in the peak shape or width can provide information about

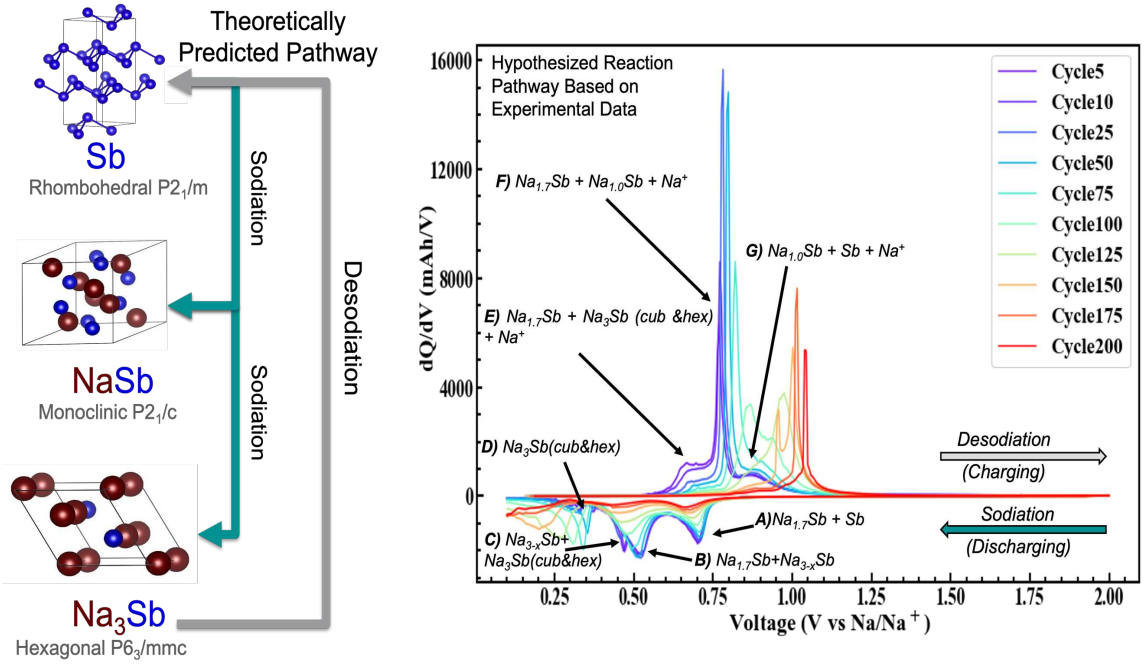

Figure 1.1. (Left) Theorized sodiation/desodiation pathway of elemental Sb. It was predicted that Sb would only have two major sodiation events and one desodiation event.[21,22] (Right) Experimentally obtained differential capacity plot of an electrodeposited Sb thin film with carbon nanotubes on a textured copper foil. The electrode was cycled in a Na-ion battery using 1M $NaPF_6$ with 5% fluoroethylene carbonate (FEC) additive as the electrolyte. The battery was cycled at a rate of ~C/5 from 2V-0.10V vs Na metal for 200 cycles. Cycle progression is demonstrated by the rainbow color gradient starting with cycle 5 in purple and cycle 200 in red. Reactions were assigned based on experimentally obtained data and literature precedent. This figure was adapted from Nieto et al.[23]

phase segregation or aggregation,[20] while decreases in peak intensity suggest active material loss through delamination or poor electronic conductivity.[18] In **Figure 1.1** three significant desodiation (charging) and four sodiation (discharging) events are seen, although it was previously predicted that Sb would only go through two main sodiation events, the formation of NaSb and subsequent formation of Na_3Sb.[7,21,22] This experimentally obtained data was adapted from Nieto et al.[23] and reactions were assigned based on experimentally obtained data as well as reported studies in the literature.[11,14,15] The general consensus in the reported literature is that the formation of an amorphous Na_xSb phase may act as a buffer to relieve anisotropic strain which improves the mechanical stability and rate performance of the cell.[11,14] Additionally, there may be a possible

competition between the formation of the metastable cubic versus the thermodynamically stable hexagonal Na_3Sb in the final sodiation steps (steps c & d).[14,17,24,25] Whether this happens, and how the specific structure of the fully sodiated phase affects the cyclability of the Sb electrode, is not known. Despite some general agreements in the literature over the identity of the phases present while cycling, there are still many discrepancies in the number of reported reactions and redox potentials that could be due to differences in fabrication techniques as demonstrated in Chapter 3. Insight into the phase transformations and the structures and properties of these phases is crucial to understanding the electrochemical properties and to better optimize the overall performance of the system.

Additionally, there are drawbacks to the performance of dense Sb-based electrodes. These anodes suffer limited cycle lifetimes due to large volume changes during battery cycling that pulverize the material and cause irreversible capacity loss as Sb loses electrical connectivity to the rest of the battery. This capacity loss mechanism suggests that it might be possible to mitigate this failure by using Sb in composite materials, as nanostructured morphologies, or as components in M_xSb_y alloys to improve cycle lifetimes.[16,26–29] Optimizing these approaches necessitates first a better understanding of the underlying mechanisms leading to the failure itself. These presented challenges highlight the complexity of Sb-based anodes for sodium-ion batteries and necessitates the development of systematic studies to understand the phase transformations and their structure-property relationships as well the degradation mechanism of the whole electrode to develop and optimize their performance for sodium-ion batteries.

1.3 Fabrication and Experimental Methodology for the Development of Battery Anodes

The fabrication of electrodes for battery applications plays a crucial role in optimizing battery performance and, more importantly, impacts how one can study the intrinsic properties of the

electrode material. Many different fabrication methods are employed to study the performance and structure-property relationships of electrode materials such as slurry casting, sputtering, and electrodeposition.[17,27,30,31] The method of making electrode materials directly affects the structure-property relationships observed while cycling as the same target electrode can be made using different additives and binders. In slurry casting, polymeric binders and amorphous carbon additives are required to cast thin film electrodes. Although these binders and additives can enable improved cycling performance, they add inactive mass and can hinder the ability to study the intrinsic properties of the active material as they convolute the electrochemical and structural data. Sputtering can produce crystalline thin films directly, which can help remove issues related to deconvoluting observed data, but it can be expensive and slow, which is a challenge to employ at commercial levels.[27,32,33]

Electrodeposition is the process of depositing metal ions or complexes on the surface of a conductive substrate in solution by applying an electric current and eliminates the need for binders and additives. In **Figures 1.2** and **1.3** we describe a typical process flow in our lab for the synthesis and characterization of anode electrodes. In **Figure 1.2-part 1**, a common set up for electrodeposition is pictured, in which the copper foil acts as the working electrode, or cathode, where the metal ions from solution are reduced. All three electrodes are immersed in a solution containing the metal ion/complexes, and/or solution additives. By connecting the electrodeposition setup to a potentiostat, chronoamperometry or chronocoulometry can be used (i.e. a constant reduction potential can be applied) and the amount of current, charge passed, or time can be varied, or a constant current can be applied, and the potential can be measured. By controlling these variables, the thickness and mass loading of the reduced metal can be tuned as shown in **Figure 1.2-part 2a**. Although conductive carbon additives are not required, they can still be incorporated

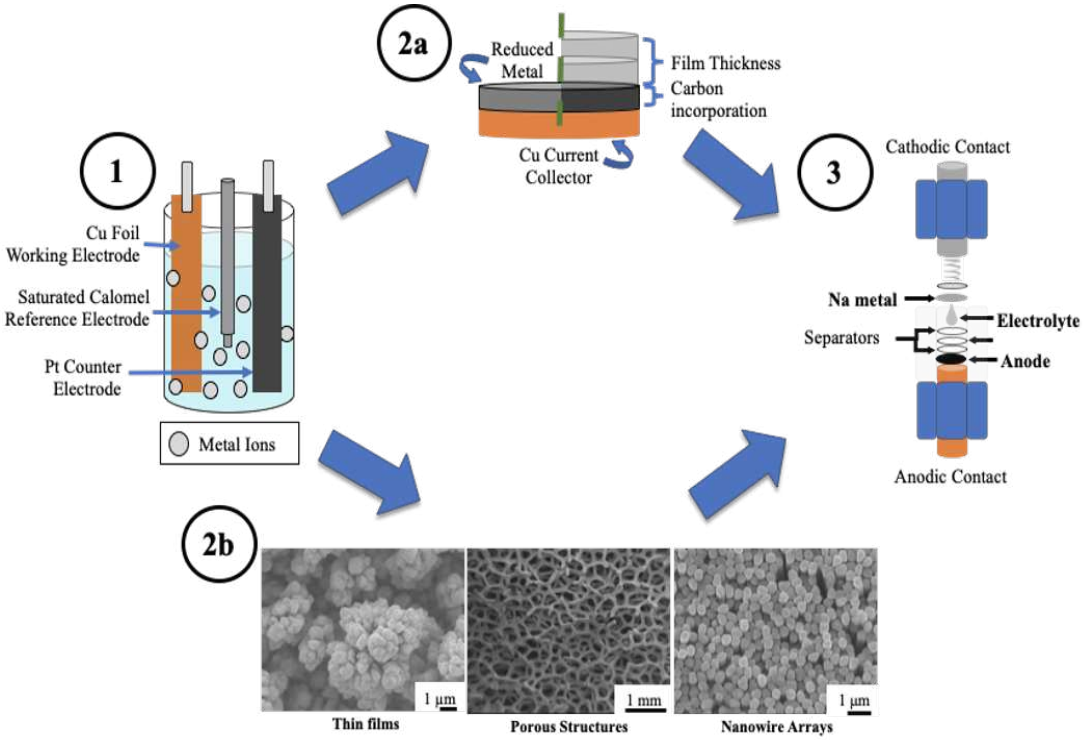

Figure 1.2. Schematic of our general process flow, beginning with (1) the electrodeposition of thin films of materials of interest from solution, which can either be (2a) deposited with controlled thickness to control the amount of active material on the electrode or codeposited with materials such as carbon nanotubes, or (2b) directly deposited onto or into various 3D structures and templates. Then we can (3) directly incorporate those active electrodes into Swagelock cells to test their electrochemical performance.

via well-established co-deposition methods. Through either co-deposition or stepwise deposition, additives such as carbon nanotubes, trace amounts of other metals, or other inorganic components can be incorporated into the electrode to enhance electronic conductivity or maintain mechanical stability as the electrode is cycled.[19,31,32,34–37]

We hypothesize that by directly electrodepositing active electrode material, without binders or additives, all processes, whether interactions in the bulk electrode, at the electrode/current-collector interface, or at electrode/electrolyte interface, can be correlated directly to the material in question. The samples made by direct electrodeposition onto a current collector can help probe and understand reactions previously masked by slurry cast composites.[23] Additionally,

electrodeposited thin films are amenable to being characterized by a host of methods, including structural characterization using X-ray and electron diffraction, but also spectroscopies including IR and Raman spectroscopy, X-ray photoelectron spectroscopy, and optical imaging methods. Complimentary characterization methods are particularly useful when the products deposited are amorphous or contain multiple phases.

To study the intrinsic electrochemical properties of the electrodeposited active material, the film can be cycled in different cell configurations such as a Swagelok cell as shown in **Figure 1.2-part 3**. Thus, the process from electrodeposition to cycling can easily be done to not only quickly synthesize electrodes with different parameters for testing (thickness, mass loading, morphology etc.), but can also be scaled to make multiple electrodes with the same parameters to test other battery components such as electrolyte composition. The cell can then be tested in a battery cycler shown in **Figure 1.3-part 4**, where the cell can be charged and discharged either using constant current conditions, to set voltage limits, or by applying a voltage and measuring current. If the mass of sample is known, and the number of electrons is known per process (e.g. sodiation), the specific capacity can be determined for that electrode. From these experiments a wide range of data can be collected to inform an understanding of cycle life, rate capabilities, cell

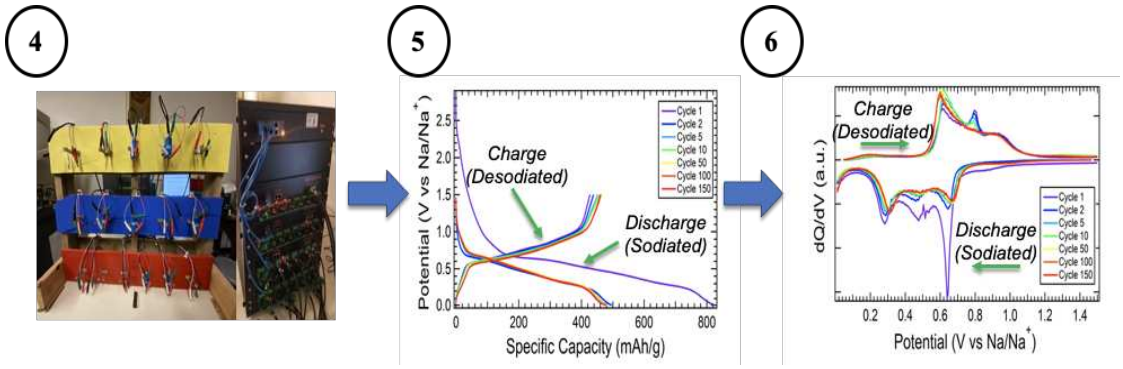

Figure 1.3. Once a swagelock cell is put onto the (4) cycler, experiments such as (5) applied current, measured voltage can be used to identify at what voltages particular transformations occur, and that data can be converted to (6) the differential capacity as a function of voltage in order to identify subtle changes in the phases that are formed.

capacity, and degradation mechanisms. One of the most common forms of data analysis is to evaluate a voltage profile plot, as shown in **Figure 1.3-part 5**. Voltage profiles allow the capacity to be measured, and a plateau on the curve signifies an electrochemical reaction is occurring, meaning specific electrochemical reactions can be directly correlated to changes in cell capacity. The capacity of the cell can then be plotted for each cycle, allowing degradation or a drop in capacity of the cell to be observed. A follow-up technique that can be used to study and understand changes in electrode materials with cycling is differential capacity analysis seen in **Figure 1.3-part 6**. In a differential capacity plot more information can be obtained about the sodiation/desodiation events occurring over a potential range than in the voltage profile of the cell, as features that appear as plateaus in a voltage profile are visualized as peaks in a differential capacity plot, making subtle changes in slope (corresponding to changes in chemical processes) more easily observed. As previously described, differential capacity analysis plots represent a fingerprint that highlights conversion reactions, cell degradation, kinetic bottlenecks, and changes in chemistry that otherwise might not be seen in a voltage profile or the cycle lifetime analysis.

While electrodeposition is a useful method to fabricate electrodes, the composition of the electrode should still be carefully probed not only to understand the properties of the active material but also to ensure, and prevent, the inclusion of impurities. In deposition solutions often there are metal oxides, complexing agents, and other surfactants that may be incorporated into the film during or after electrodeposition.[38–40] Typically, the inclusion of these species is minimal, but it is still important to consider whether these species are affecting the performance and electrochemical reactions seen when the electrode is cycled. Multiple studies have shown that the incorporation of metal oxides can alter the electrochemical performance of electrodes and can cause alternative degradation methods.[41–43] Therefore, it is crucial to understand the solution

chemistry involved in the electrodeposition of active material before claiming to study the true intrinsic properties of the target material. In this dissertation we've monitored how electrodeposition can tune the composition and morphology by implementing solution additives, detailed results from these studies are in Chapter 2 and Chapter 5.

1.4 Accessing Three-dimensional Architectures through Electrodeposition

The synthetic technique of electrodeposition not only enables the observation of the intrinsic properties of electrode materials without binder and additives, but it also allows for the synthesis of various architectures such as thin films, nanowire arrays, and porous three-dimensional (3D) structures, as seen in **Figure 1.2-part 2b**. These 3D structured electrodes achieve higher rate performance, which can translate to high power density for an electrode. The use of 3D architectures can be particularly effective at helping to minimize the evolution of mechanical stresses in electrodes that change volume significantly upon sodiation and desodiation. Most studies have focused on incorporating porous carbon-based composites to access the benefits of 3D electrodes, but it has been reported that these carbon structures can have unwanted reactions with the electrolyte in the cell.[44] Other techniques that incorporate scaffolds as the base template require intricate procedures and acid etching to create the final electrode structure, which can be prohibitively complex to move to commercial scales.[45–47] Electrodeposition bypasses these issues, as additives and binder are not required. Specific examples produced by various groups include the electrodeposition of antimony-based alloys on 3D copper substrates, porous nickel scaffolds, and as self-supported prisms.[48–51] All of these examples use electrodeposition to grow antimony or tin antimonide onto conductive substrates with minimal work up and without binders and additives, demonstrating how electrodeposition allows for the simple fabrication of 3D electrodes with significantly improved rate and performance and capacity.

The ability to electrodeposit active material onto 3D architectures has shown significant promise towards the synthesis of high power electrodes, but fundamental studies on how these novel geometries affect the electrochemical reactions of anode materials are still required. Some inherent issues present in these advanced structures are non-uniform current and voltage distribution, which can lead to inhomogeneous sodiation and desodiation reactions across the electrode.[52,53] Thus, the implementation of varying 3D architectures will greatly influence phase formation pathways during cycling arising from differences in mechanical integrity, diffusion pathways and lengths, and surface areas. Therefore, it is crucial to employ the steps in the process shown in **Figures 1.2 and 1.3** to screen how different architectures impact the sodiation/desodiation reaction mechanism of anode materials.

1.5 Dissertation Overview

Herein, investigations on antimony-based anodes for sodium-ion batteries to elucidate sodiation pathways and exploration into the role of electrode fabrication, architecture, and electrolyte composition on those reaction pathways are described. Our research methodology consists of our synthetic method of electrodeposition, materials characterization, battery assembly, and electrochemical characterization.[54] Through this process we can develop an understanding of the electrochemical performance of our anode materials (e.g., cycle life, degradation mechanisms). Understanding these processes and developing tools and characterization techniques to study alloy-based anode materials will lay the foundation for next-generation energy storage systems.

Chapter II explores the effects of solution additives in the electrodeposition of Sb anodes and investigates how structural changes in the deposits affect the electrochemical performance of Sb in a sodium-ion battery. This chapter was submitted to the Journal of Physical Chemistry C and is currently under revision (Nieto, K.; Windsor, D. S.; Kale, A. R.; Gallawa J. R.; Prieto, A. L.

Structural Control of Electrodeposited Sb Anodes through Solution Additives and Their Influence on Electrochemical Performance in Na-ion Batteries. *J. Phys. Chem. C*., **2023**, under revision.) In this study, Sb films were electrodeposited with various concentrations of cetyltrimethylammonium bromide (CTAB) and bis-(3-sulfopropyl) disulfide (SPS), and the structure, morphology, composition, and electrochemical performance in Na-ion batteries were compared. It was found that CTAB and SPS can significantly alter the electrodeposition of Sb films by inhibiting or accelerating the deposition. These changes in the electrodeposition lead to significant changes in the morphology and crystallinity of the Sb films. The tunablitiy of these characteristics through solution additives in turn lead to influences on cycle life and rate capabilities. More specifically, Sb films deposited with the highest concentrations of CTAB (30 mM) and SPS (30 mM) exhibited markedly different behavior; the inclusion of CTAB promoted stable cycling, and SPS enhanced rate capabilities. These studies provide valuable insight into the tunability of alloy-based films through electrodeposition and solution additives.

Chapter III demonstrates how fabrication methods can influence the reported sodiation/desodiation reactions by comparing the electrochemical performance of Sb films that were electrodeposited to films that were slurry casted. This chapter was published in the Journal of the Electrochemical Society (Nieto, K.; Gimble, N. J.; Rudolph, L. J., Kale, A. R.; Prieto, A. L. Electrodeposition vs Slurry Casting: How Fabrication Affects Electrochemical Reactions of Sb Electrodes in Sodium-Ion Batteries, *J. Electrochem. Soc.* **2022**, *169,* 0500537. https://doi.org/10.1149/1945-7111/ac6b5e.). When comparing the electrochemical performance of electrodeposited to slurry cast Sb films, it was demonstrated through differential capacity analysis that electrode fabrication can have a significant impact on the kinetics and number of electrochemical reactions occurring in Sb-based electrodes. Electrodeposition was shown to be a

powerful fabrication technique to process anode materials and investigate the sodiation/desodiation reactions of Sb anodes without having to deconvolute the influences of binders and additives that are necessary in slurry casting.

Chapter IV describes preliminary studies in understanding how electrolyte composition can influence the sodiation/desodiation reactions that occur when cycling Sb anodes. This work is intended to be submitted to Energy Storage Materials in 2023. Na-ion batteries typically employ electrolytes that are composed of organic carbonates (e.g., ethylene carbonate), salts (e.g., $NaPF_6$) and additives (e.g., fluoroethylene carbonate) and are constantly exchanged to enhance performance (ionic diffusion and lifetime). The electrolyte of a battery decomposes reductively on the anode and forms what is known as the solid electrolyte interphase (SEI). The SEI has also been shown to continuously form as the battery is cycled when new free surfaces are created due to mechanical fracture of the anode.[55,56] Due to the inherent volume expansion experienced in Sb anodes when sodiated/desodiated, the SEI is hypothesized to continuously form and affect the cyclability of these anodes. Therefore, it is crucial to understand what solvents are compatible with Sb-based anodes in sodium-ion batteries. Additionally, we have found that electrolyte composition can influence the redox potentials at which sodiation/desodiation reactions occur and the number of electrochemical reactions. In this chapter we describe hypothesis that could be attributing to changes in cycle life and redox potentials and describe future studies to further investigate the impact electrolyte composition has on the performance and kinetics.

Chapter V focuses on combining all previous work in electrodeposition to develop experimental considerations when advancing from two-dimensional (2D) to three-dimensional (3D) electrodes to enhance energy and power density of Sb-based anodes for sodium-ion batteries. The development of 3D batteries is the clearest solution to maximizing both energy density and

power density towards a better battery, but there have been significant challenges in integrating all components of a battery into a truly interdigitated 3D architecture. Electrodeposition is a viable technique to directly deposit active material onto geometrically complex structures to control active material loading and the electrochemically active surface area to improve battery performance metrics. However, significant challenges remain in achieving conformal coverage of the current collector while maintaining high active material loading. These challenges lead to underutilization of active material and in turn diminish the power and energy density of the 3D battery. We have demonstrated through tunable experimental parameters in electrodeposition we can begin to develop better performing 3D Sb-based anodes for the development of full 3D sodium-ion batteries.

The final chapter, Chapter VI, concludes the dissertation by describing further directions required to continue understanding the degradation mechanism for Sb. We have begun developing a 3D-printed optical electrochemical cell that can couple operando optical studies with electrochemical studies to build understanding of the degradation mechanism of alloy-based anode materials. To further understand how electrode composition, structure, and electrolyte composition affect mechanical stability and ionic/electronic diffusivity in these electrodes, this electrochemical-optical cell well be used to understand how morphology, crystallinity, and protective coatings can improve or diminish mechanical and electrochemical stability. Through future studies, we hope to further understand the sodiation/desodiation phases that Sb exhibits and how to overcome possible bottlenecks related to sluggish ionic conductivity or mechanical degradation. Not only will these studies benefit Sb-based anodes for NIBs, but they will also lead to better fundamental studies and processing of anode materials. Understanding these fundamental processes and developing tools and characterization techniques to study alloy-based anode materials, will lay the foundation for

the creation of energy storage systems that contain earth-abundant materials with high energy densities, and long cycle life.

1.6 References

(1) Larcher, D.; Tarascon, J. M. Towards Greener and More Sustainable Batteries for Electrical Energy Storage. *Nature Chemistry*. Nature Publishing Group January 1, 2015, pp 19–29. https://doi.org/10.1038/nchem.2085.

(2) Iermakova, D. I.; Dugas, R.; Palacín, M. R.; Ponrouch, A. On the Comparative Stability of Li and Na Metal Anode Interfaces in Conventional Alkyl Carbonate Electrolytes. *J. Electrochem. Soc.* **2015**, *162* (13), A7060–A7066. https://doi.org/10.1149/2.0091513jes.

(3) Dugas, R.; Ponrouch, A.; Gachot, G.; David, R.; Palacin, M. R.; Tarascon, J. M. Na Reactivity toward Carbonate-Based Electrolytes: The Effect of FEC as Additive. *J. Electrochem. Soc.* **2016**, *163* (10), A2333–A2339. https://doi.org/10.1149/2.0981610jes.

(4) Pfeifer, K.; Arnold, S.; Becherer, J.; Das, C.; Maibach, J.; Ehrenberg, H.; Dsoke, S. Can Metallic Sodium Electrodes Affect the Electrochemistry of Sodium-Ion Batteries? Reactivity Issues and Perspectives. *ChemSusChem* **2019**, *12* (14), cssc.201901056. https://doi.org/10.1002/cssc.201901056.

(5) Kubota, K.; Komaba, S. Review—Practical Issues and Future Perspective for Na-Ion Batteries. *J. Electrochem. Soc.* **2015**, *162* (14), A2538–A2550. https://doi.org/10.1149/2.0151514jes.

(6) Yabuuchi, N.; Kubota, K.; Dahbi, M.; Komaba, S. Research Development on Sodium-Ion Batteries. **2014**.

(7) He, J.; Wei, Y.; Zhai, T.; Li, H. Antimony-Based Materials as Promising Anodes for Rechargeable Lithium-Ion and Sodium-Ion Batteries. *Mater Chem Front* **2018**, *2*, 437. https://doi.org/10.1039/c7qm00480j.

(8) Ong, S. P.; Chevrier, V. L.; Hautier, G.; Jain, A.; Moore, C.; Kim, S.; Ma, X.; Ceder, G. Voltage, Stability and Diffusion Barrier Differences between Sodium-Ion and Lithium-Ion Intercalation Materials. *Energy Environ. Sci.* **2011**, *4* (9), 3680. https://doi.org/10.1039/c1ee01782a.

(9) Zhang, W.-J. A Review of the Electrochemical Performance of Alloy Anodes for Lithium-Ion Batteries. *J. Power Sources* **2011**, *196* (1), 13–24. https://doi.org/10.1016/j.jpowsour.2010.07.020.

(10) Zhang, W.-J. Lithium Insertion/Extraction Mechanism in Alloy Anodes for Lithium-Ion Batteries. *J. Power Sources* **2011**, *196* (3), 877–885. https://doi.org/10.1016/j.jpowsour.2010.08.114.

(11) Darwiche, A.; Marino, C.; Sougrati, M. T.; Fraisse, B.; Stievano, L.; Monconduit, L. Better Cycling Performances of Bulk Sb in Na-Ion Batteries Compared to Li-Ion Systems: An

Unexpected Electrochemical Mechanism. *J. Am. Chem. Soc.* **2012**, *134*, 20805–20811. https://doi.org/10.1021/ja310347x.

(12) Hwang, J.-Y.; Myung, S.-T.; Sun, Y.-K. Sodium-Ion Batteries: Present and Future. *Chem. Soc. Rev.* **2017**, *46* (12), 3529–3614. https://doi.org/10.1039/C6CS00776G.

(13) Yang, Y.; Yang, X.; Zhang, Y.; Hou, H.; Jing, M.; Zhu, Y.; Fang, L.; Chen, Q.; Ji, X. Cathodically Induced Antimony for Rechargeable Li-Ion and Na-Ion Batteries: The Influences of Hexagonal and Amorphous Phase. *J. Power Sources* **2015**, *282*, 358–367. https://doi.org/10.1016/j.jpowsour.2015.02.071.

(14) Allan, P. K.; Griffin, J. M.; Darwiche, A.; Borkiewicz, O. J.; Wiaderek, K. M.; Chapman, K. W.; Morris, A. J.; Chupas, P. J.; Monconduit, L.; Grey, C. P. Tracking Sodium-Antimonide Phase Transformations in Sodium-Ion Anodes: Insights from Operando Pair Distribution Function Analysis and Solid-State NMR Spectroscopy. *J. Am. Chem. Soc.* **2016**, *138* (7), 2352–2365. https://doi.org/10.1021/jacs.5b13273.

(15) Choi, Y.-S.; Lee, J.-C. Characterizing Multiple Continuous Phase Transitions at an Alloying Anode with Voltammetric Measurements and First-Principles Calculations. *J. Mater. Chem. A* **2019**, *7*, 23121–23129. https://doi.org/10.1039/c9ta07199g.

(16) Schulze, M. C.; Belson, R. M.; Kraynak, L. A.; Prieto, A. L. Electrodeposition of Sb/CNT Composite Films as Anodes for Li- and Na-Ion Batteries. *Energy Storage Mater.* **2020**, *25* (June 2019), 572–584. https://doi.org/10.1016/j.ensm.2019.09.025.

(17) Li, Z.; Tan, X.; Li, P.; Kalisvaart, P.; Janish, M. T.; Mook, W. M.; Luber, E. J.; Jungjohann, K. L.; Carter, C. B.; Mitlin, D. Coupling In Situ TEM and Ex Situ Analysis to Understand Heterogeneous Sodiation of Antimony. *Nano Lett.* **2015**, *15* (10), 6339–6348. https://doi.org/10.1021/acs.nanolett.5b03373.

(18) Smith, A. J.; Dahn, J. R. Delta Differential Capacity Analysis. *J. Electrochem. Soc.* **2012**, *159* (3), A290. https://doi.org/10.1149/2.076203jes.

(19) Schulze, M. C.; Schulze, R. K.; Prieto, A. L. Electrodeposited Thin-Film Cu_xSb Anodes for Li-Ion Batteries: Enhancement of Cycle Life via Tuning of Film Composition and Engineering of the Film-Substrate Interface. *J. Mater. Chem. A* **2018**, *6*, 12708. https://doi.org/10.1039/c8ta01798k.

(20) Courtney, I. A.; McKinnon, W. R.; Dahn, J. R. On the Aggregation of Tin in SnO Composite Glasses Caused by the Reversible Reaction with Lithium. *J. Electrochem. Soc.* **1999**, *146* (1), 59. https://doi.org/10.1149/1.1391565.

(21) Lo¨ıc Baggetto, L.; Ganesh, P.; Sun, C.-N.; Meisner, R. A.; Zawodzinski, T. A.; Veith, G. M.; Baggetto, L.; Ganesh, P.; Sun, C.-N.; Meisner, R. A.; Zawodzinski, T. A.; Veith, G. M. Intrinsic Thermodynamic and Kinetic Properties of Sb Electrodes for Li-Ion and Na-Ion

Batteries: Experiment and Theory. *J. Mater. Chem. A* **2013**, *1*, 7985–7994. https://doi.org/10.1039/c3ta11568b.

(22) Caputo, R. An Insight into Sodiation of Antimony from First-Principles Crystal Structure Prediction. *Electron. Mater.* **2016**, *45* (2), 999–1010. https://doi.org/10.1007/s11664-015-4260-0.

(23) Nieto, K.; Gimble, N. J.; Rudolph, L. J.; Kale, A. R.; Prieto, A. L. Electrodeposition vs Slurry Casting: How Fabrication Affects Electrochemical Reactions of Sb Electrodes in Sodium-Ion Batteries. *J. Electrochem. Soc.* **2022**, *169* (5), 050537. https://doi.org/10.1149/1945-7111/ac6b5e.

(24) Leonova, M. E.; Bdikin, I. K.; Kulinich, S. A.; Gulish, O. K.; Sevast'yanova, L. G.; Burdina, K. P. High-Pressure Phase Transition of Hexagonal Alkali Pnictides. *Inorg. Mater.* **2003**, *39* (3), 332–336. https://doi.org/10.1023/A.

(25) Sauban Ere, M.; Yahia, B.; Ed Eric Lemoigno, F.; Doublet, M.-L. Influence of Polymorphism on the Electrochemical Behavior of M x Sb Negative Electrodes in Li/Na Batteries. *J. Power Sources* **2015**, *280*, 695–702. https://doi.org/10.1016/j.jpowsour.2015.01.093.

(26) Pfeifer, K.; Arnold, S.; Budak, Ö.; Luo, X.; Presser, V.; Ehrenberg, H.; Dsoke, S. Choosing the Right Carbon Additive Is of Vital Importance for High-Performance Sb-Based Na-Ion Batteries. *J. Mater. Chem. A* **2020**, *8* (12), 6092–6104. https://doi.org/10.1039/d0ta00254b.

(27) Liang, S.; Cheng, Y. J.; Zhu, J.; Xia, Y.; Müller-Buschbaum, P. A Chronicle Review of Nonsilicon (Sn, Sb, Ge)-Based Lithium/Sodium-Ion Battery Alloying Anodes. *Small Methods*. John Wiley and Sons Inc. August 1, 2020. https://doi.org/10.1002/smtd.202000218.

(28) Voigt, K.; Heubner, C.; Liebmann, T.; Matthey, B.; Weiser, M.; Schneider, M.; Michaelis, A. Electrodeposition of Versatile Nanostructured Sb/Sb_2O_3 Microcomposites: A Parameter Study. *Adv. Mater. Interfaces* **2020**, *7* (13), 1–10. https://doi.org/10.1002/admi.202000004.

(29) Lv, H.; Qiu, S.; Lu, G.; Fu, Y.; Li, X.; Hu, C.; Liu, J. Nanostructured Antimony/Carbon Composite Fibers as Anode Material for Lithium-Ion Battery. **2014**. https://doi.org/10.1016/j.electacta.2014.11.013.

(30) Jackson, E. D.; Mosby, J. M.; Prieto, A. L. Evaluation of the Electrochemical Properties of Crystalline Copper Antimonide Thin Film Anodes for Lithium Ion Batteries Produced by Single Step Electrodeposition. *Electrochimica Acta* **2016**, *214*, 253–264. https://doi.org/10.1016/j.electacta.2016.07.126.

(31) Schulze, M. C.; Belson, R. M.; Kraynak, L. A.; Prieto, A. L. Electrodeposition of Sb/CNT Composite Films as Anodes for Li- and Na-Ion Batteries. *Energy Storage Mater.* **2019**, *In Press*. https://doi.org/10.1016/j.ensm.2019.09.025.

(32) Gutiérrez-Kolar, J. S.; Baggetto, L.; Sang, X.; Shin, D.; Yurkiv, V.; Mashayek, F.; Veith, G. M.; Shahbazian-Yassar, R.; Unocic, R. R. Interpreting Electrochemical and Chemical Sodiation Mechanisms and Kinetics in Tin Antimony Battery Anodes Using in Situ Transmission Electron Microscopy and Computational Methods. *ACS Appl. Energy Mater.* **2019**, *2* (5), 3578–3586. https://doi.org/10.1021/acsaem.9b00310.

(33) Zhang, Y.; Marschilok, A. C.; Takeuchi, K. J.; Kercher, A. K.; Takeuchi, E. S.; Dudney, N. J. Understanding How Structure and Crystallinity Affect Performance in Solid-State Batteries Using a Glass Ceramic LiV3O8 Cathode. *Chem. Mater.* **2019**, *31* (16), 6135–6144. https://doi.org/10.1021/acs.chemmater.9b01571.

(34) Ma, J.; Prieto, A. L. Electrodeposition of Pure Phase SnSb Exhibiting High Stability as a Sodium-Ion Battery Anode. *Chem. Commun.* **2019**, *55* (48), 6938–6941. https://doi.org/10.1039/c9cc00001a.

(35) De Las Casas, C.; Li, W. A Review of Application of Carbon Nanotubes for Lithium Ion Battery Anode Material. *J. Power Sources* **2012**, *208*, 74–85. https://doi.org/10.1016/j.jpowsour.2012.02.013.

(36) Subramanyan, K.; Aravindan, V. Stibium: A Promising Electrode toward Building High-Performance Na-Ion Full-Cells. *Chem* **2019**, *5*, 3096–3126. https://doi.org/10.1016/j.chempr.2019.08.007.

(37) Chirambatte Peter, S.; sarkar, shreya. An Overview on Sb-Based Intermetallics and Alloys for Sodium-Ion Batteries: Trends, Challenges and Future Prospects from Material Synthesis to Battery Performance. *J. Mater. Chem. A* **2021**. https://doi.org/10.1039/d0ta12063d.

(38) Aroyo, M. S. Leveling in Pulse Plating with Brighteners: Synergistic Effect of Frequency and Hydrodynamically Active Additives. *Plat. Surf. Finish.* **1995**, *82* (11), 53–57.

(39) Aroyo, M. Theoretical and Practical Aspects of Electrodeposition of Metal Coatings with Improved Properties (Part 1). *Plat. Surf. Finish.* **1998**, *85* (8), 69–76.

(40) Gamburg, Y. D.; Zangari, G. *Theory and Practice of Metal Electrodeposition*; 2011; Vol. 1.

(41) Hong, K. S.; Nam, D. H.; Lim, S. J.; Sohn, D.; Kim, T. H.; Kwon, H. Electrochemically Synthesized Sb/Sb2O3 Composites as High-Capacity Anode Materials Utilizing a Reversible Conversion Reaction for Na-Ion Batteries. *ACS Appl. Mater. Interfaces* **2015**, *7* (31), 17264–17271. https://doi.org/10.1021/acsami.5b04225.

(42) Li, D.; Yan, D.; Ma, J.; Qin, W.; Zhang, X.; Lu, T.; Pan, L. One-Step Microwave-Assisted Synthesis of Sb2O3/Reduced Graphene Oxide Composites as Advanced Anode Materials for Sodium-Ion Batteries. *Ceram. Int.* **2016**, *42* (14), 15634–15642. https://doi.org/10.1016/j.ceramint.2016.07.017.

(43) Bryngelsson, H.; Eskhult, J.; Nyholm, L.; Herranen, M.; Alm, O.; Edström, K. Electrodeposited Sb and Sb/Sb2O3 Nanoparticle Coatings as Anode Materials for Li-Ion Batteries. *Chem. Mater.* **2007**, *19* (5), 1170–1180. https://doi.org/10.1021/cm0624769.

(44) Zhang, T.; Ran, F. Design Strategies of 3D Carbon-Based Electrodes for Charge / Ion Transport in Lithium Ion Battery and Sodium Ion Battery. **2021**, *2010041*, 1–29. https://doi.org/10.1002/adfm.202010041.

(45) Ashby, D. S.; Choi, C. S.; Edwards, M. A.; Talin, A. A.; White, H. S.; Dunn, B. S. High-Performance Solid-State Lithium-Ion Battery with Mixed 2D and 3D Electrodes. *ACS Appl. Energy Mater.* **2020**, *3* (9), 8402–8409. https://doi.org/10.1021/acsaem.0c01029.

(46) Chamran, F.; Yeh, Y.; Min, H.-S.; Dunn, B.; Kim, C.-J. Fabrication of High-Aspect-Ratio Electrode Arrays for Three-Dimensional Microbatteries. *J. Microelectromechanical Syst.* **2007**, *16* (4), 844–852. https://doi.org/10.1109/JMEMS.2007.901638.

(47) Yu, M.; Qiu, W.; Wang, F.; Zhai, T.; Fang, P.; Lu, X.; Tong, Y. Three Dimensional Architectures: Design, Assembly and Application in Electrochemical Capacitors. *J. Mater. Chem. A* **2015**, *3* (31), 15792–15823. https://doi.org/10.1039/C5TA02743H.

(48) Fan, X. Y.; Jiang, Z.; Huang, L.; Wang, X.; Han, J.; Sun, R.; Gou, L.; Li, D. L.; Ding, Y. L. 3D Porous Self-Standing Sb Foam Anode with a Conformal Indium Layer for Enhanced Sodium Storage. *ACS Appl. Mater. Interfaces* **2020**, *12* (18), 20344–20353. https://doi.org/10.1021/acsami.9b23501.

(49) Li, X.; Sun, M.; Ni, J.; Li, L. Template-Free Construction of Self-Supported Sb Prisms with Stable Sodium Storage. *Adv. Energy Mater.* **2019**, *9* (24), 1901096. https://doi.org/10.1002/aenm.201901096.

(50) Li, J.; Pu, J.; Liu, Z.; Wang, J.; Wu, W.; Zhang, H.; Ma, H. Porous-Nickel-Scaffolded Tin-Antimony Anodes with Enhanced Electrochemical Properties for Li/Na-Ion Batteries. *ACS Appl. Mater. Interfaces* **2017**, *9* (30), 25250–25256. https://doi.org/10.1021/acsami.7b04635.

(51) Fan, X. Y.; Han, J.; Jiang, Y.; Ni, J.; Gou, L.; Li, D. L.; Li, L. Hierarchical Porous Sb Films on 3D Cu Substrate Have Promise for Stable Sodium Storage. *ACS Appl. Energy Mater.* **2018**, *1* (8), 3598–3602. https://doi.org/10.1021/acsaem.8b00872.

(52) Long, J. W.; Dunn, B.; Rolison, D. R.; White, H. S. 3D Architectures for Batteries and Electrodes. *Adv. Energy Mater.* **2020**, *10* (46), 2002457. https://doi.org/10.1002/aenm.202002457.

(53) Arthur, T. S.; Bates, D. J.; Cirigliano, N.; Johnson, D. C.; Malati, P.; Mosby, J. M.; Perre, E.; Rawls, M. T.; Prieto, A. L.; Dunn, B. Three-Dimensional Electrodes and Battery Architectures. *MRS Bull.* **2011**, *36* (7), 523–531. https://doi.org/10.1557/mrs.2011.156.

(54) Gimble, N. J.; Nieto, K.; Prieto, A. L. Electrodeposition as a Powerful Tool for the Fabrication and Characterization of Next-Generation Anodes for Sodium Ion Rechargeable Batteries. *Electrochem. Soc. Interface* **2021**, *30* (1), 59–63. https://doi.org/10.1149/2.F09211IF.

(55) Peled, E.; Menkin, S. Review—SEI: Past, Present and Future. *J. Electrochem. Soc.* **2017**, *164* (7), A1703. https://doi.org/10.1149/2.1441707jes.

(56) Wang, A.; Kadam, S.; Li, H.; Shi, S.; Qi, Y. Review on Modeling of the Anode Solid Electrolyte Interphase (SEI) for Lithium-Ion Batteries. *Npj Comput. Mater.* **2018**, *4* (1), 15. https://doi.org/10.1038/s41524-018-0064-0.

II. STRUCTURAL CONTROL OF ELECTRODEPOSITED Sb ANODES THROUGH SOLUTION ADDITIVES AND THEIR INFLUENCE ON ELECTROCHEMICAL PERFORMANCE IN Na-ION BATTERIES[2]

2.1 Overview

Alloy-based materials such as antimony (Sb) are of interest for both Li/Na-ion batteries due to their high theoretical capacity and electronic conductivity. Of the various ways to fabricate Sb films (slurry casting, sputtering, etc.) one promising route is through electrodeposition. Electrodeposition is an industrially relevant synthetic technique that allows for the use of solution additives to control different characteristics such as film uniformity, morphology, and electrical conductivity. Solution additives such as cetyltrimethylammonium bromide (CTAB) and bis-(3-sulfopropyl) disulfide (SPS) have been used to control different characteristics such as particle morphology and electrical conductivity in various electrodeposits but have not been applied to the electrodeposition of Sb for battery applications. In this study, Sb films were electrodeposited with varied concentrations of CTAB and SPS and the structure, morphology, composition, and electrochemical performance in Na-ion batteries were compared. We report that CTAB and SPS additives can significantly influence electrodeposited Sb films by altering the morphology and

[2] This manuscript has been published in the *Journal of Physical Chemistry C* with Kelly Nieto, Daniel S. Windsor, Amanda R. Kale, Jessica R. Gallawa, Dylan A. Medina, and Amy L. Prieto (*J. Phys. Chem. C.*, **2023**, just accepted). Kelly Nieto developed initial hypotheses, designed experiments, analyzed data, and led the writing of the manuscript. Daniel S. Windsor developed the ECSA experiments, fit impedance data, analyzed data, and assisted in writing the manuscript. Amanda R. Kale performed and interpreted Rietveld refinements, assisted with hypothesis development and writing the manuscript. Jessica R. Gallawa performed, fit, and analyzed the XPS data and assisted with writing the manuscript. Dylan A. Medina, assisted with the synthesis of anode material and assembly of cells. Amy L. Prieto assisted with the conceptualization of the project, data interpretation, and manuscript editing.

reduce the crystallinity, affecting the electrochemical performance. These studies provide valuable insight into the tunability of alloy-based films through electrodeposition and solution additives for battery applications.

2.2 Introduction

Antimony (Sb) anodes for both sodium-ion and lithium-ion batteries have been extensively studied due to its high theoretical capacity (660 mAh/g) and electronic conductivity.[1–3] Studies have reported high reversible capacities and have implemented the use of conductive additives[4–6] and nanostructuring[7,8] to overcome issues related to mechanical stability, induced by volume expansion that occurs when Sb alloys with either sodium or lithium. To test and optimize the properties and performance of Sb, a variety of synthetic and fabrication techniques have been utilized. Traditionally, Sb thin films have been fabricated through slurry casting that consists of ball milling Sb powder, a conductive carbon additive, and a polymeric binder. Through this technique, various factors can be controlled, such as the strength of the polymeric binder, that helps maintain the mechanical integrity of the film, and the conductive additive that can improve electronic conductivity.[9–11] Other fabrication techniques used to study the properties and performance of Sb involve sputtering of Sb,[12,13] and solvothermal methods,[14,15] but these techniques fall short due to cost and poor scalability.

A less prevalent technique previously reported by our group utilizes electrodeposition to synthesize Sb based anodes.[4,16–19] Through electrodeposition, Sb ions are plated electrochemically from solution onto a charged substrate.[20,21] This technique doesn't require binders and additives, that are necessary in slurry casted films, and vastly simplifies the understanding of the inherent properties of Sb anodes by removing the need to deconvolute the role of binders and additives.[22] In addition, electrodeposition has been found to be a valuable technique to control composition,

film thickness, crystallinity, and morphology of the deposited metal.[7,23–26] This control can be accomplished by a multitude of experimental parameters (temperature, bath composition, current density, etc.) as well as the use of different solution additives.[27]

The electrodeposition of Sb has been reported in several publications using a variety of electrolyte compositions.[22,25,28–30] Commonly used electrodeposition baths consist of acidic aqueous solutions with an Sb precursor ($SbCl_3$, Sb_2O_3, etc.) and various organic additives (tartaric acid, citric acid, etc.) to aid with the complexation of Sb (III).[28,29,31,32] To successfully plate Sb, additives are needed to help improve the stability and solubility of Sb(III), otherwise the deposition proceeds at higher voltages and with slow kinetics due to formation of oxides in solution.[29,33] By tuning the bath composition, studies have shown successful control over the deposition and growth of Sb to form films with desirable properties.[26,30,34]

In combination with the complexing agent, alternative organic compounds have been implemented to control grain refinement and leveling of the deposition.[35] These additives can be known as levelers or brighteners.[27] A leveler is defined as an additive that fills pits in the electrode surface and promotes the deposition of a smooth surface.[36] A brightener can inhibit the rate of the electrodeposition by interacting with the electrode surface and preventing the deposition of the active ion in that area.[37] As a result, brighteners can also help level the micro profile of the electrode surface without the need for polishing after the deposition.[27,37] Additives such as bis-(3-sulfopropyl) disulfide (SPS) that acts a brightner,[38–40] and sodium gluconate,[41,42] are typically used in copper and nickel plating baths, respectively, and an extensive library of additives have been investigated for other metal depositions.[36,43,44] Surfactants such as cetyltrimethylammonium bromide (CTAB), have also been used in deposition baths due to their potential to affect the surface tension between the electrolyte and the electrode that can have effects on coating adhesiveness and

morphology at varying concentrations.[45,46] Depending on the interactions of CTAB with the substrate or the active metal being deposited it may act as a leveling or brightening agent.[47–49] CTAB may also interact directly with the deposited metal instead of the substrate and has been used to cap the growth of particles as demonstrated in nanoparticle synthesis[50–52] and has potential to act as a corrosion inhibitor.[53] However, there are few publications reporting the tunability of electrodeposited Sb anodes for battery applications using solution additives.[7,54]

Herein we report the effect of solution additives such as CTAB and SPS on the electrodeposition of Sb anodes in aqueous-based electrolyte baths and subsequent impacts on the electrodes electrochemical performance in a sodium-ion battery (NIB). We report that both CTAB and SPS can dramatically influence the morphology and crystallinity of the deposited films. These effects are magnified with the increase in concentration of the additive and allows for the tunability of crystallinity and morphology, which impacts the electrochemical performance of these Sb films. In particular, the films deposited with CTAB have more stable cycling due to mechanical robustness, whereas the films deposited with SPS have improved rate capabilities for Na-ion battery applications.

2.3 Experimental

2.3.1 Electrodeposition Solution of Sb

The base electrodeposition solution of Sb has been described in previous work and consists of 200 mM sodium gluconate (Sigma, ACS reagent), and 30 mM antimony trichloride ($SbCl_3$, Sigma-Aldrich, anhydrous >99.0%) in 100 mL of Millipore (>15MΩ*cm) water.[22] Solution additives were added in a variety of concentrations (1 mM, 10 mM, 30 mM) for (1-hexadecyl)trimethylammonium bromide (CTAB, 98%, Alfa Aesar) and bis-(sodium sulfoproply)-

disulfide (SPS, 98.9%, CHEM-IMPEX). In addition, a mixed solution containing both CTAB and SPS was made using the base solution and a concentration of 30 mM CTAB and 30 mM SPS.

For the electrodeposition solutions, sodium gluconate was stirred in a beaker containing 100 mL of Millipore (>15MΩ*cm) water for ~5min. Then either CTAB or SPS was added with a concentration of 1 mM, 10 mM, or 30 mM and was stirred until the additive was dissolved. To finish the solution, 30 mM $SbCl_3$ was added to the solution and sonicated (Cole-Parmer, 08895-01) until a colorless homogeneous mixture was formed.

2.3.2 Electrochemical Characterization of Deposition Solutions

Cyclic voltammetry (CV) was used to characterize the deposition solutions with a Gamry Reference 3000 potentiostat and determine the reduction potential at which to deposit Sb. The CVs were taken in a three-electrode set up consisting of a saturated calomel electrode (SCE) as the reference, a platinum mesh counter electrode, and a platinum disk working electrode at a scan rate of 50 mV/s unless otherwise noted.

2.3.3 Electrodeposition of Sb

The Sb thin film electrodes were electrodeposited using a Gamry Interface 1010E potentiostat and an in-house apparatus described in previous studies.[22] A four-inch square of textured Cu foil (tCu, Oak-Mitsui, TLB-DS Cu foil) was washed with a concentrated H_3PO_4 solution for 30 s to remove surface oxides, followed by Millipore water and ethanol wash to remove excess acid and water on the surface of the film. The electrochemical set up consisted of a tCu working electrode, a stainless-steel mesh as the counter electrode and a SCE as the reference. Using chronocoulometry, a constant negative potential of -1.05V vs SCE was applied and the charge limit was set to 3 C/cm^2. The deposited film was then rinsed with Millipore water and absolute ethanol to remove the remaining deposition solution.

2.3.4 Electrolyte Preparation, Cell Assembly, and Galvanostatic Cycling

All cell assembly and electrolyte preparation was done in an argon filled glovebox ($O_2 < 1$ ppm, $H_2O < 0.5$ ppm). The electrolyte used for all experiments consisted of a 1 M solution of sodium perchlorate ($NaClO_4$, Sigma-Aldrich, ≥98% ACS reagent) with an addition of 5% by volume fluoroethylene carbonate (FEC, Sigma-Aldrich, 99%) in a base electrolyte solution containing polyethylene carbonate (PC, Sigma-Aldrich, 99.7%).

To test the electrochemical performance of the deposited Sb films half-cells were assembled in two electrode Swageloks. The electrodeposited film was cut into circular ½" in diameter punches and were massed out to acquire the amount of the active material. The thin films were used as the working electrode and a polypropylene separator (MTI Corp) followed by a Whatman glass filter, and another polypropylene separator were used as the separator stack. An excess amount of electrolyte, ~200 μL, was placed in the cell after the separators. Na metal (Aldrich, cubes in mineral oil, 99.9%) was then rolled out with a Teflon roller with hexanes, cleaned with an extra soft child's toothbrush and was punched into a ½" circular punch. Pressure was then applied through the SS rod, spring, Cu rod to make sure that all parts were in contact in the Swagelok cell.

Once assembled, the Na-ion half-cells were cycled with an Arbin battery tester (LBT-20084). The cells were allowed to rest for 12 hours after assembly and were galvanostatically cycled at a rate of C/2, unless noted otherwise, with calculated current densities based on the mass of active material. The voltage range at which the cells were cycled was 0.01 V - 1.5 V vs. Na/Na^+ unless otherwise noted. Cycling performance was analyzed and graphed with Python code using the NumPy and Pandas packages.

2.3.5 Electrochemical Characterization of Sb Electrodes

Cyclic voltammetry experiments on a polished copper rod, 30 mM CTAB, 30 mM SPS, and no additive Sb films were done using a three-electrode Swagelok cell in the potential window of 2 V - 2.6 V vs Na/Na^+ at scan rates of 50 mV/s, 100 mV/s, 150 mV/s, 200 mV/s, and 250 mV/s. The Sb electrode acted as the working electrode and sodium metal was used as the counter and reference electrode and a 1M $NaClO_4$ in PC with 5% FEC by volume, solution was used as the electrolyte. Electrochemical impedance spectroscopy (EIS) experiments were conducted on sodium half-cells using a Gamry Interface 1010E potentiostat. Experiments were conducted at room temperature at open circuit potential (OCP) once the cells rested for 12 hours to allow for the cells to equilibrate and reach a stable OCP. A constant AC voltage of 10 mV rms and EIS was carried out over a frequency range of 0.1 to 100,000 Hz.

2.3.6 Materials Characterization

The surface morphology of electrodeposited films was analyzed with Scanning Electron Microscopy (SEM) using a JEOL JSM-6500F Microscope at 15 kV. X-Ray Photoelectron Spectroscopy was performed with a Physical Electronics (PHI) 5800 series Multi-Technique ESCA system with a monochromatic Al Kα ($h\nu$=1486.6 eV) X-ray source operating at 350.0 W. Sputtering with an Ar^+ ion gun was performed at 5 keV for time increments of 30 seconds, and data was worked up using CasaXPS software.[55] Briefly, a GL(0) line shape was used with defined spin-splitting energy differences from reference spectra.[56,57] For p-orbital splitting, peak areas were defined to be 1:2 for $p_{1/2}$ and $p_{3/2}$, respectively, and d-orbital peak areas were defined to be 2:3 for $d_{3/2}$ and $d_{5/2}$ peaks, respectively. A Shirley background was used for all high-resolution spectra and binding energies were calibrated with adventitious carbon at 285.0 eV.

Additional structural characterization was done through powder X-ray Diffraction (PXRD) with a Bruker D8 Discover DaVinci powder X-ray diffractometer using Cu Kα radiation and a 0.2 mm slit opening. Rietveld refinements were performed using Topas v6 (Bruker AXS). Peak profiles were fit using a double-Voigt approach. Preferred orientation was modeled using the March-Dollase model for the (1 0 $\bar{2}$) and (2 $\bar{1}$ 0). Further discussion on how the refinements were done can be found in the supplemental information.

2.4 Results and Discussion

2.4.1 Influences of Solution Additives on the Electrodeposition of Sb

To identify events occurring during deposition, cyclic voltammetry (CV) was performed on the various deposition solutions. In our solutions, $SbCl_3$ is readily dissolved into an aqueous solution containing sodium gluconate, where sodium gluconate is believed to behave as a complexing agent.[58] This complexation aids in dissolving $SbCl_3$ and helps prevent the oxidation

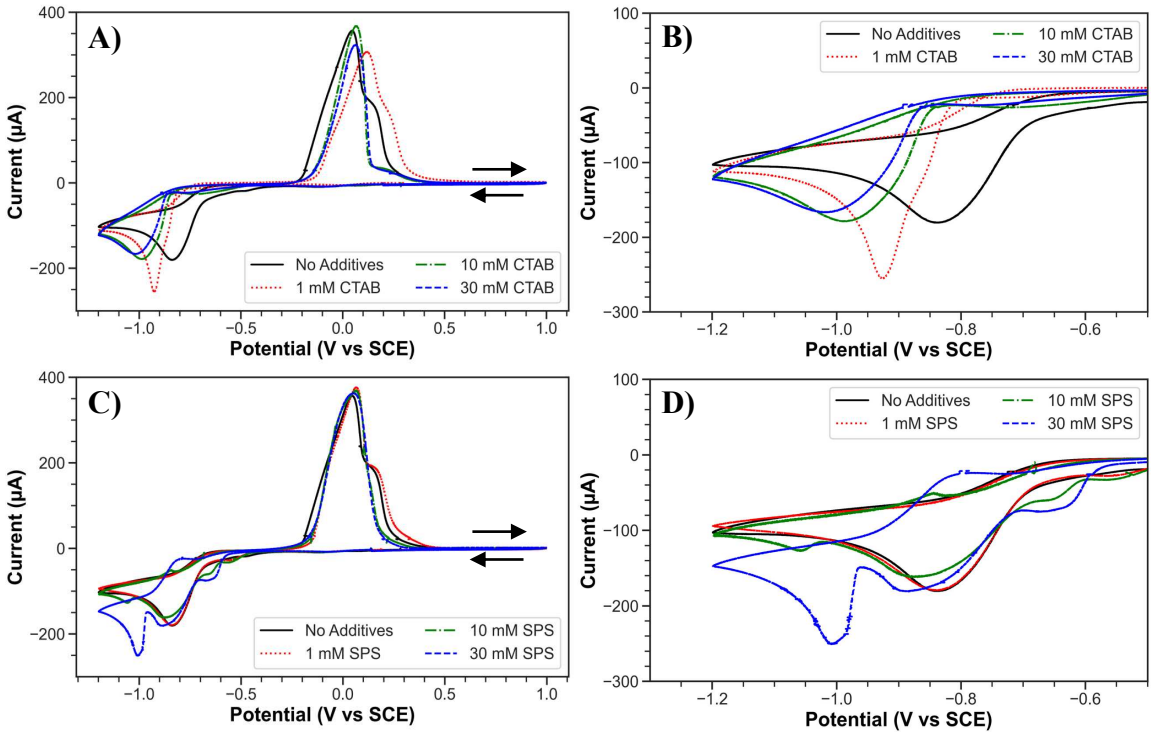

Figure 2.1. Cyclic voltammetry of the Sb deposition solution with varying concentrations of CTAB (A&B) and SPS (C&D). Panels B and D are magnifications of the redox events from -1.2 V – -0.5 V vs SCE.

of Sb. Through cyclic voltammetry, seen in **Figure 2.1A-D**, the solution containing only $SbCl_3$ and sodium gluconate is found to only have one significant reduction event at about -0.85 V vs SCE, associated with the reduction of $Sb^{3+}+3e^- \rightarrow Sb^0$. The large oxidation event at 0 V vs SCE is associated with the oxidation of Sb^0 back to Sb^{3+}. Upon the addition of CTAB, **Figures 2.1A&B,** the Sb reduction peak is shifted to more negative reduction potentials that is indicative of adsorption on to the surface of the electrode, or suppression of the rate of deposition of Sb. When increasing the concentration of CTAB beyond 10mM, the reduction of Sb does not shift further and remains at 1 V vs SCE. Interestingly, when CTAB is used in solution the time it takes to reach the charge limit set for the chronocoulometry deposition increases, **Figure 2.2**. As the concentration is increased to 30 mM, it takes an additional six minutes to reach the charge limit and further leads us to believe that CTAB is suppressing or slowing down the rate of Sb deposition.

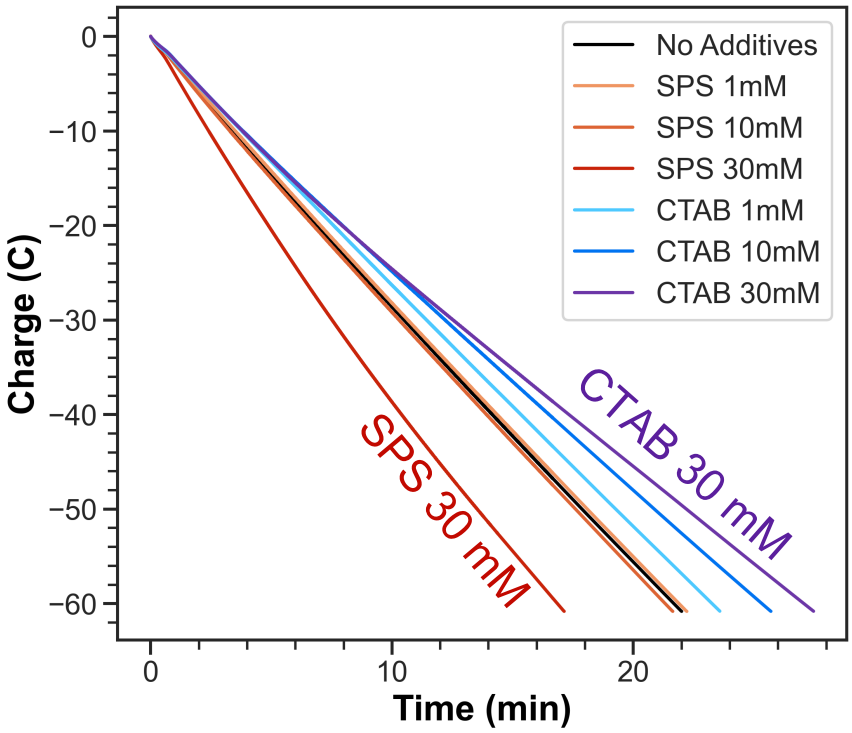

Figure 2.2. Summary of chronocoulometry data of the Sb electrodepositions with different concentrations of CTAB and SPS. Depositions were done using chronocoulometry and the charge limit was set to -60 ˚C.

When using SPS as the additive, **Figure 2.1C&D,** the main reduction peak associated with Sb does not shift to overpotentials, but additional reduction events appear. These reduction events are believed to be related to the complexation of Sb with SPS, as no redox events are seen when SPS is the only species present in solution, **Figure S2.1**. The smaller reduction events could be attributed to fouling of the electrode and disruption of the deposition of Sb as they are not present in the first scan of the CV, **Figure S2.1**. In addition, when SPS is included in the deposition solution it appears to act as an accelerant for the deposition of Sb as seen in **Figure 2.2**. However, this effect only seems to be substantial in the 30 mM SPS solution, and lower concentrations of SPS have minimal effects. This behavior has been observed in the work of Moffat et al., where SPS was found to displace the passivating layer at the copper surface that consisted of Cl^- and poly(ethylene glycol).[59] Displacement occurs because of the preferential adsorption of short chained disulfide or thiol groups in SPS onto the surface of the copper substrate and a high concentration is needed to have a significant effect on displacing the passivating layer.[59]

2.4.2 Structural Characterization of Electrodeposited Sb Films

The morphology and structure of the electrodeposited Sb films with CTAB and SPS appear to be significantly altered as seen through scanning electron microscopy (SEM), **Figure 2.3**. When no additives are used in solution, Sb deposits in small bush like structures with small branches poking out and sharp faceting as seen in the cross-section imaging in **Figure 2.4**. Upon adding 1 mM SPS, Sb begins to deposit in larger agglomerates and as the concentration is increased to 10 mM, the agglomerates continue to increase in size. When the concentration is increased to 30 mM, the morphology changes significantly and crystallites grow in longer branches out from the current collector and due to their weight, bend over horizontally. We hypothesize SPS could be inhibiting the nucleation of Sb ions across the surface of the copper substrate and instead promotes its growth

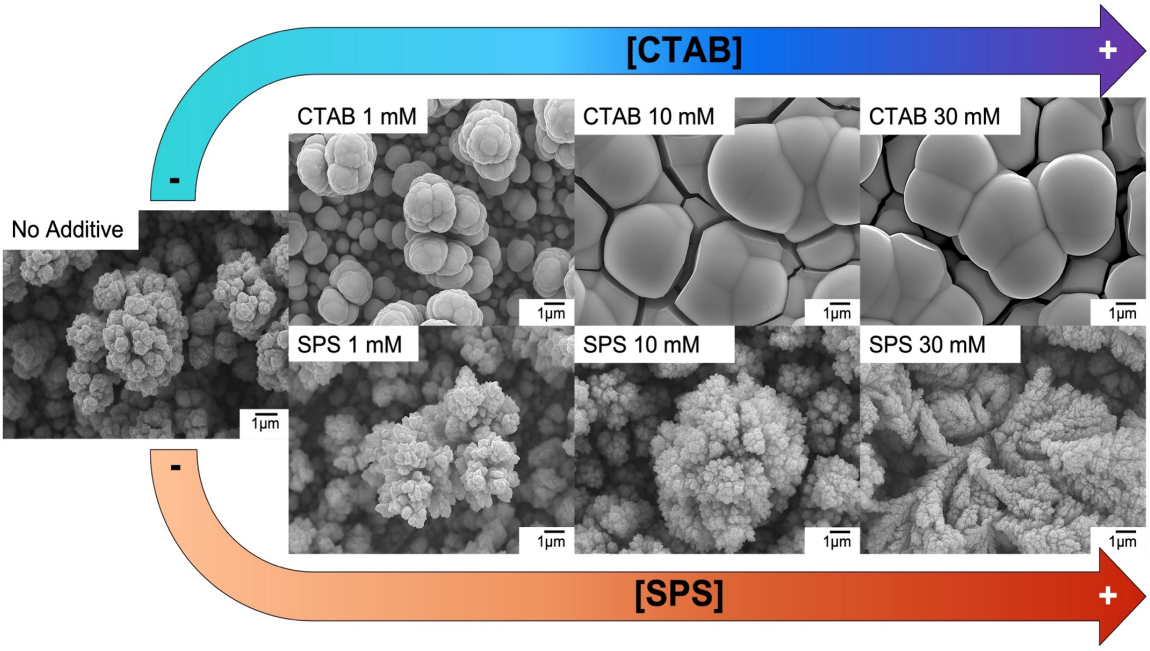

Figure 2.3. SEM images of Sb films deposited with no additive (left) and different concentrations of CTAB (Top) and SPS (Bottom).

along already nucleated areas resulting in columnar growth, as seen in the cross-section imaging, **Figure 2.4**. To determine if SPS is incorporated into the film, X-ray photoelectron spectroscopy (XPS) was conducted on two films of different loadings to identify sulfur components in the electrodeposited antimony films, **Figure 2.5**. Choe *et al.* found that in copper deposition baths, SPS degrades due to a catalytic oxidation reaction with copper ions in solution.[60] Because of this, we hypothesized that sulfur could be trapped at the boundary between copper and the electrodeposited antimony. In the case of both pristine samples, no quantifiable amount of sulfur was identified at the surface of the deposit; however, the low loading/thinner film (deposited for 30 seconds) showed a sulfur peak after 180 seconds of sputtering as well as copper environments related to the surface of the current collector. These results demonstrate that SPS is not significantly incorporated throughout the film, but sulfur is present on the copper substrate, which

is consistent with the hypothesis that SPS adsorption limits the initial surface area on which Sb can deposit.

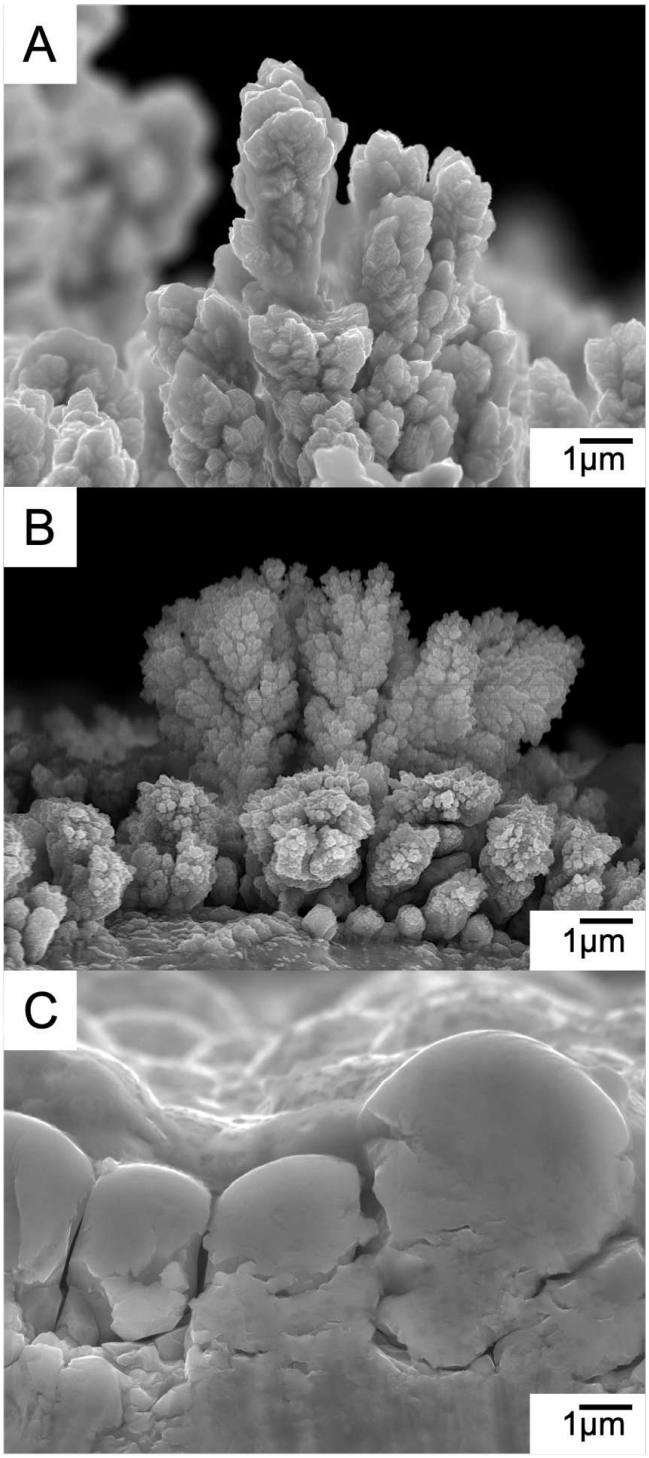

Figure 2.4. Cross section SEM images of the Sb deposited with (A) no additive, (B) SPS 30 mM, and (C) CTAB 30 mM.

When CTAB was implemented into the solution the morphology of the deposited Sb had the most significant change. At a concentration of 1 mM CTAB, the agglomerates began to smooth out and increase in size. We believe the deposition forms smoother particles due to the adsorption of CTAB onto the surface of the deposited Sb which hinders the ability for more Sb to deposit on that surface. In addition, it has been reported that surfactants such as CTAB can help maintain interfacial surface tension over the deposit and can lead to compact deposits.[61] As the concentration is increased to 10 mM, the same smoothing effect is seen and is exacerbated. The film was mainly

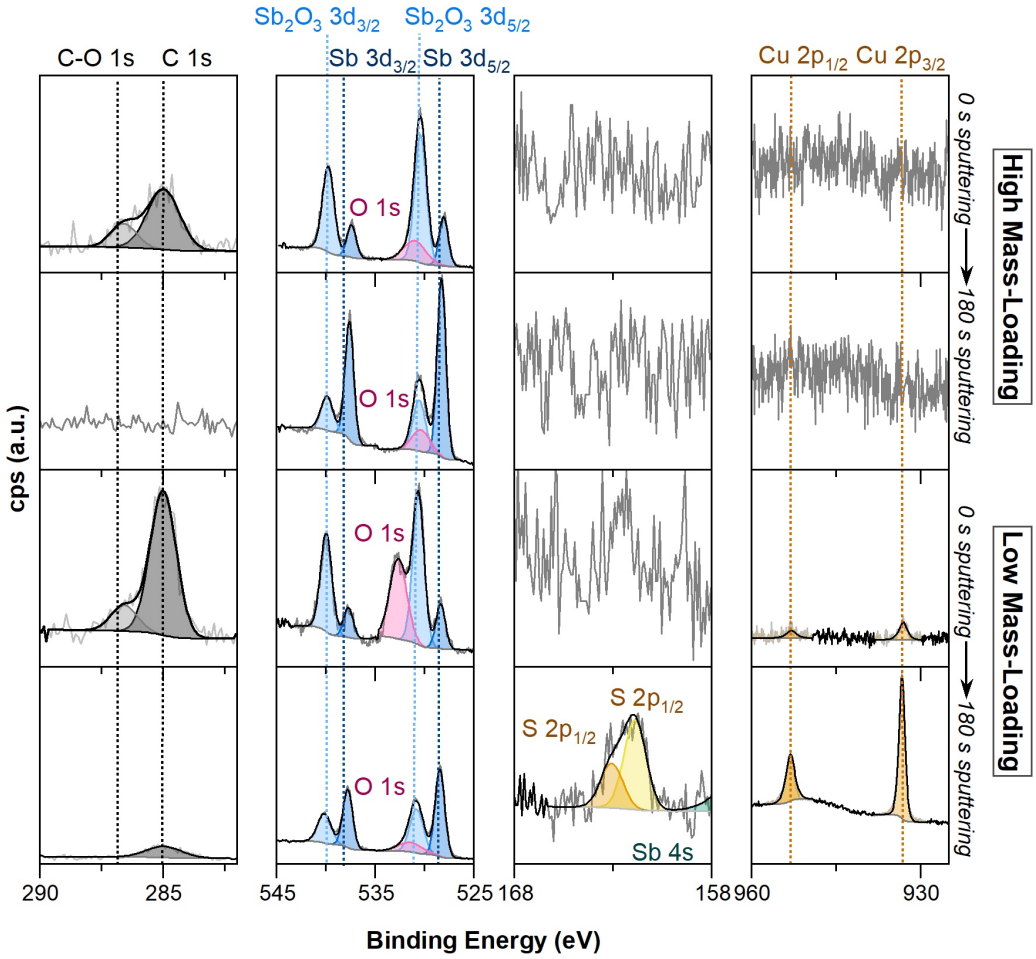

Figure 2.5. High-resolution X-ray photoelectron spectra of Sb electrodeposited on copper with SPS. Carbon, antimony, sulfur, and copper regions are displayed for the full chronocoulometric electrodeposition (high mass-loading) and the 30 second chronoamperometric electrodeposition (low mass-loading), both at pristine conditions and after sputtering for 3 minutes. Equivalent XPS analysis was done on the 30 mM CTAB film and can be found in Figure S2.2 and Figure S2.3.

composed of large densely packed smooth particles as seen in **Figure 2.3** and **Figure 2.4**. However, when increasing the concentration of CTAB to 30 mM the morphology remained the same. When characterizing the composition of the film through XPS, **Figure S2.2 and Figure S2.3**, no components of the additive appear even after sputtering through the film. This leads us to hypothesize that CTAB binding must be reversible and could be influencing the growth of the film, but does not remain incorporated throughout the film.

To investigate if CTAB has a more significant impact on morphology than SPS, we electrodeposited an Sb film with a combination of 30 mM CTAB and SPS. These films had similar morphology to the 30 mM SPS, **Figure S2.4**, as characterized by the long branching but also had some characteristics of the films deposited with CTAB. In pockets of the film, CTAB behaved similarly to how it acts alone, and led to smoothing of the ends of the branches, essentially capping further growth of the deposit. However, throughout most of the film, SPS heavily dominates the deposition by encouraging columnar growth, consistent with blocking of the Cu substrate as previously described. From this deposition, it's clear that CTAB and SPS alter the deposition through separate mechanisms, as both types of modification to the morphology are observed.

Variation in the deposition of Sb with additives results in changes to film morphology, which likely means that a significant change in film structure occurs as well. Components of film structure, such as crystallite size and strain can have a large impact on battery performance.[62–64] To further understand how the solution additives could influence the growth of the Sb deposits, PXRD and subsequent Rietveld refinements were performed, Error! Reference source not found.**A&B** and **Figures S2.5**. PXRD peak breadth increases with an increase in additive concentration, which is indicative of changes in crystal microstructure, and either a decrease in crystallite size or increase in microstrain. The contributions of crystallite size and microstrain can

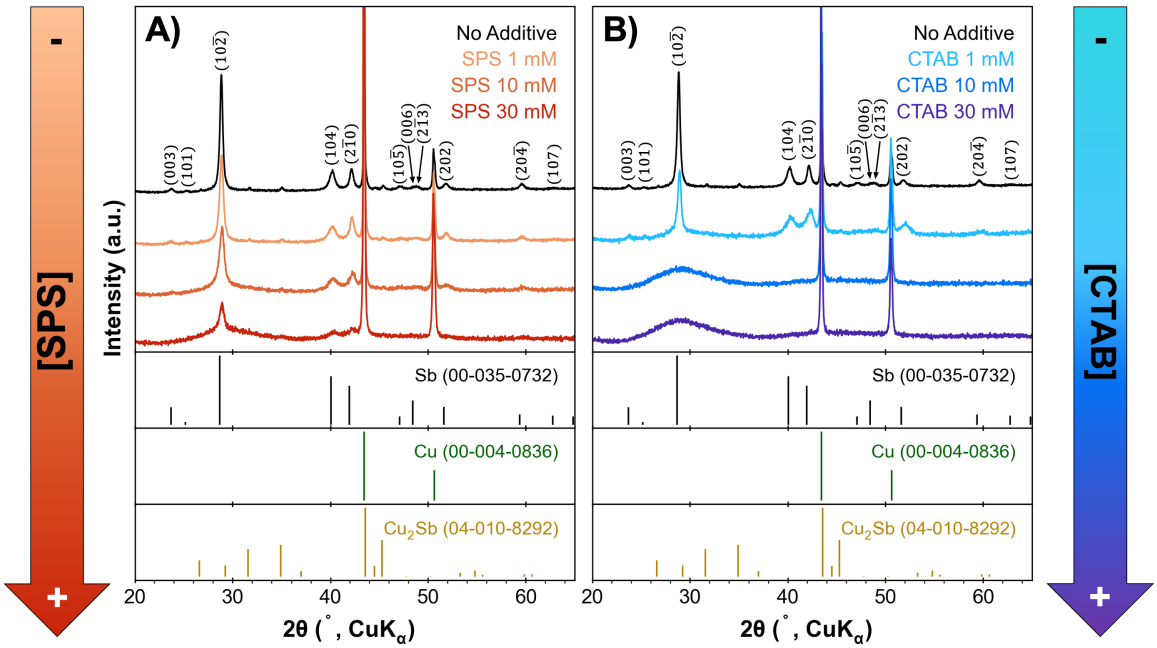

Figure 2.6. PXRD patterns of Sb films deposited with no additive, and varying concentrations of SPS (A) and CTAB (B). Further analysis including Rietveld refinements can be found in Figure S2.5.

be deconvoluted in refinements given sufficient intensity of high 2θ reflections and is discussed further in the supplemental information.[65,66]

The mean crystallite size, microstrain, lattice parameters, (10$\bar{2}$) d-spacing, and preferential orientation were calculated using Rietveld refinements (**Table S2.1**). The no additive film is the most crystalline, and does exhibit microstrain, consistent with the fact that strain is common in electrodeposited films.[22,67,68] Large crystallites of 1 mM SPS and CTAB films are similar in size at ~70 nm, though the CTAB film also has a low crystalline Sb component, < 2 nm, so overall the 1 mM CTAB film is less crystalline. The SPS films are considerably more crystalline for the remaining concentrations of additives than their CTAB counterparts, and crystallite size does not change substantially until a poorly crystalline Sb phase emerges at 30 mM. In the case of CTAB, crystallinity decreases rapidly when the concentration is increased. This is consistent with SEM images, as SPS films appear to have visible grains; at higher CTAB concentrations, films are of

such low crystallinity that grains are difficult to distinguish, and instead only large agglomerates or particles are observed. Preferential orientation is observed in the [$10\bar{2}$] for most films, suggesting that this is the preferred direction of growth. In SPS films, considerable anisotropic broadening is observed, indicating strain in the [104]. Strain in this direction could be caused by the fact that this plane is nearly perpendicular to the ($10\bar{2}$), and rapid growth in the [$10\bar{2}$] could cause strain in the perpendicular direction. [22,67,68]

In both additive systems, film crystallinity decreases, and strain increases with a higher additive concentration. CTAB appears to have a more drastic effect on film microstructure for a given additive concentration, and crystallite size decreases rapidly upon the addition of additive. As CTAB has been shown to be a capping ligand, we propose that it acts so here, capping crystals at small sizes and passivating the film surface so that added Sb must nucleate in a new crystal, rather than incorporating into existing crystals, resulting in nearly amorphous films at high concentrations. In addition, strain is considerable in the 10 and 30 mM CTAB films, observed by decreased ($10\bar{2}$) plane spacing, which likely results from densely packed agglomerates pushing against each other as Sb deposits. In the SPS system, crystallite size decreases more slowly compared to CTAB, but the emergence of the < 2 nm Sb in the 30 mM SPS film once again demonstrates that these two additives influence the nucleation and growth of the film through different mechanisms. We propose that as SPS is an accelerant, it is possible that it causes nucleation to occur more rapidly, resulting in smaller crystallite sizes when the concentration is increased. As previously mentioned, at the high concentrations of 30 mM SPS, it may have reached a sufficient concentration to remove most of the passivating layers of gluconate and/or Cl^-, as seen in other studies, [59] and nucleation could occur much more rapidly, which would explain the drastic decrease to < 2nm crystallite sizes.

2.4.3 Electrochemical Characterization of Electrodeposited Sb Films

Due to the significant morphological and structural changes observed when implementing the use of solution additives, it was necessary to determine how the electrochemical properties of the deposited Sb films were altered. For example, these changes in morphology and particle size can lead to changes in the electrochemical surface area (ECSA) which is defined in this study as the exposed surface of the active electrode in contact with the electrolyte.[69] Due to microstructuring that occurs during the electrodeposition of these films, the geometric surface and ECSA are not equivalent. To determine the ECSA of the electrodeposited films, similar experiments reported in the

field of electrocatalysis were performed.[69,70] To measure the non-faradaic current response and calculate the double layer capacitance, CVs were conducted in the potential range of 2 V- 2.6 V vs Na/Na^+ where no sodiation/desodiation reactions of Sb should occur, **Figure 2.7**. The deposited Sb films were cycled at different scan rates and the current response at 2.3 V vs Na/Na^+ was plotted as a function of the scan rates. The non-faradic current scales linearly with the scan rate and can be used to determine the ECSA. A summary of determined values is reported in **Table S2.2**, and a more in-depth explanation to determine the ECSA as well as all ECSA values determined for Sb films deposited with no additive, 30 mM CTAB, and 30 mM SPS can be found in the supplemental information. However, it is important to note that the ECSA encompasses all electrochemically active sites, which includes Sb_2O_3 that we observe through XPS. When comparing these results to the SEM images in **Figure 2.3** and **Figure 2.4**, the determined ECSA values seem consistent with expected available surface area. The no additive film has the highest ECSA, ($ECSA_{(No\ Additive)}$ = 9.28 ± 0.22 cm^2), due to its growth in small agglomerates across the whole film. In the 30 mM SPS film, ($ECSA_{(SPS\ 30\ mM)}$ = 6.49 ± 0.09 cm^2), the small agglomerates significantly grew in size

into long branches across the film. However, this morphology may lead to the decrease in ECSA due to its denser packing observed in **Figure 2.4**. The Sb film deposited with 30 mM CTAB, ($ECSA_{(CTAB\ 30\ mM)} = 1.60 \pm 0.1\ cm^2$), has the lowest ECSA likely due to the dense packing of the large smooth particles.

Further electrochemical characterization through electrochemical impedance spectroscopy (EIS) has shown that CTAB and SPS also influence the resistivity of the deposited film. From the Nyquist plot shown in **Figure 2.8**, there are three major areas that can be compared visually. These

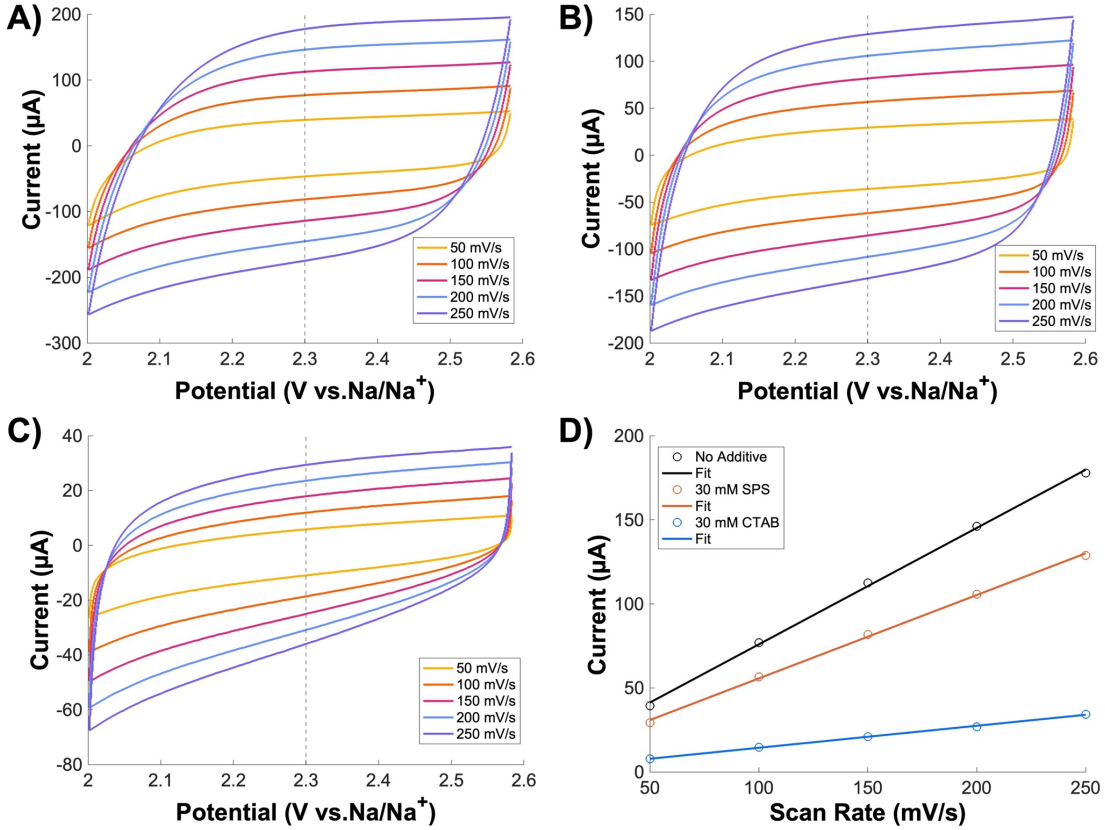

Figure 2.7. CV scans of Sb films deposited with A) No additive, B) 30 mM SPS, and C) 30 mM CTAB. Scans were done in a three-electrode sodium battery with sodium metal as both the reference and counter electrodes in a 1 M $NaClO_4$ in PC and 5% FEC electrolyte. The cells were cycled in the potential range of 2 V- 2.6 V vs Na/Na^+ at scan rates of 50, 100, 150, 200, and 250 mV/s. Scan rates were plotted against the current response at 2.3 V vs Na/Na^+ for the Sb films deposited with no additive (black), 30 mM CTAB (blue), and 30 mM SPS (orange). Values for the determined surface area of all three Sb films can be found in Table 2.1 and Table S2.2.

areas are related to the ionic resistance in solution depicted by the x-axis offset, the charge transfer resistance depicted by width of the semi-circle, and solid-state diffusion throughout the electrode shown by the Warburg tail at lower frequencies. The EIS data was modeled through a modified Randles circuit, **Scheme S2.1**, and values for each component previously described are quantified in **Table S2.3**. From these fits, **Figure 2.8A,** it was determined that Sb films deposited with no additive had the lowest charge transfer resistance (R_{ct}) at 95.95 Ω and the CTAB and SPS films had similar R_{ct} values at 120 Ω and 122.2 Ω. These results demonstrate that the use of SPS and CTAB do not significantly increase charge transfer resistance, either by minuscule inclusions of the additive or changes to grain boundaries. It is difficult to make a strong conclusion about the solid-state diffusion due to challenges in modeling this behavior in porous and alloying electrodes that has been described in the field.[71,72] To attempt to understand the Na^+ diffusion coefficient regardless of the described difficulties, EIS was performed on the no additive, SPS 30 mM, and CTAB 30 mM films after 10 cycles, **Figure 2.8B**. After 10 cycles, the R_{ct} increases for all three films with the no additive film having the highest increase from 95.95 Ω to 225.8 Ω. This increase in R_{ct} is believed to be caused by the poor mechanical stability of the film leading to loss of active material and potentially and excessive buildup of SEI as discussed when analyzing the electrochemical performance of the films. Additionally, we've calculated the Warburg diffusion coefficients for Na (D_{Na}) in the Sb anodes based off of the work by Dashairya et al.[73], **Figure S2.6**. An explanation of how the calculations were done can be found in the supplemental and the determined D_{Na} for each anode can be found in **Table S2.4**. The Warburg diffusion coefficients were calculated for the Sb anodes deposited with no additive, SPS, and CTAB and the values were 1.51E-18 $cm^2\ s^{-1}$, 2.91E-19 $cm^2\ s^{-1}$, and 7.94E-18 $cm^2\ s^{-1}$, respectively. When compared to the work of Dashairya et al., our diffusion coefficients are five orders of magnitude lower. We believe

our diffusion coefficients are smaller because these are densely packed bulk films with no carbon additives, whereas in the study by Dashairya et al. they were investigating the properties of Sb nanoparticles that were embedded in graphite oxide sheets.[73] The smaller particle size and conductive carbon additive can attribute to faster sodium diffusion throughout the electrode.

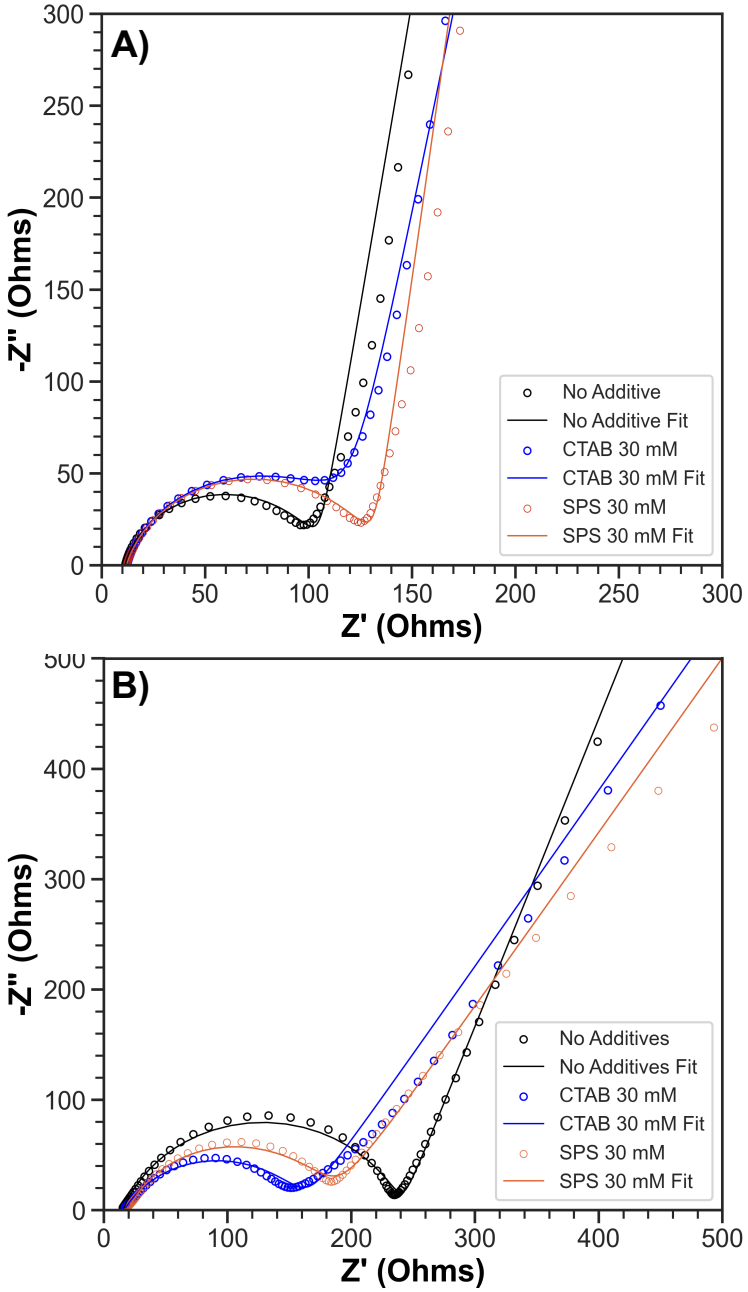

Figure 2.8. Nyquist plots of Sb films deposited with no additives (black), 30 mM CTAB (blue), and SPS (orange). EIS was conducted in a sodium half-cell at room temperature, on the pristine anodes at OCP (A), and after 10 cycles in a sodiated state at 0.01V (B).

Interestingly, in our study the SPS 30 mM film had a higher ECSA than the CTAB films, but it had the lowest diffusion coefficient. These results further demonstrate other factors such as morphology and surface area could affect the electrochemical performance.

2.4.4 Electrochemical Performance of Electrodeposited Sb in Na-ion Half-Cells

Upon comparing the electrochemical performance of the deposited films in a sodium half-cell, **Figure 2.9**, both CTAB and SPS can affect cycling stability. As the concentration of SPS is increased the capacity retention at 60 cycles slightly increases, but there are still significant decreases in capacity present for the 1 mM and 10 mM SPS films at early cycles. When the concentration is increased to 30 mM SPS the capacity decreases and the CE is lower in the first few cycles but remains stable for 50 cycles. We hypothesize that the longer branches produced from the accelerated growth of the films prompted by SPS are more fragile and tend to pulverize upon sodiation/desodiation in early cycles as seen in ex situ post cycling SEM in **Figure S2.7**. This was further shown as active material could be rubbed off the film, characteristic of fragile dendritic growth, and when rinsing the electrode for post cycling ex situ characterization, active material was lost in the rinse, **Figure S2.8**. However, even after cycling the deposited film remained relatively intact with the copper substrate and no copper was seen through the film when compared to the no additive film. After cycling the no additive film has large areas of exposed copper indicating that delamination and pulverization are the main modes of failure for these films. indicating that SPS is improving the adhesion between the deposit and the substrate by preventing delamination and the mechanical integrity of the columnar like growth is the main mode of failure for these films.

Electrodepositing Sb in the presence of 10 mM and 30 mM CTAB significantly improved the capacity retention when compared to the performance of a film deposited with no additive and

with SPS, **Figure 2.9**. The increase in cycling stability and CE is attributed to the improved mechanical stability as seen in post cycling ex situ characterization, **Figure S2.7**. Upon cycling the film does experience mechanical instability inherent to alloying electrodes but remains relatively intact as no exposed copper was seen through ex situ analysis, **Figure S2.7&S2.8**. We believe the improved mechanical stability is due to the densely packed smooth particles that are well adhered to the copper substrate. In addition to the mechanical properties of the film, the 10 and 30 mM CTAB films are nearly amorphous and have smaller crystallite sizes. The amorphous nature of the CTAB films may also lead to improved mechanical stability due to the large volume expansion that crystalline Sb experiences when fully sodiated to Na_3Sb.[74,75] Therefore, the more amorphous films have better capacity retention and higher Coulombic efficiencies (CE) as seen in **Figure 2.9.** Additionally, when comparing the sodiation/desodiation reactions of the Sb anodes deposited with no additives, 30 mM CTAB, and 30 mM SPS, **Figure S2.9**, all three films experience the same sodiation/desodiation reactions further demonstrating that any incorporation of additives in the film are not active in the sodiation/desodiation process.

Rate performance tests, Error! Reference source not found.**A&B**, demonstrate similar trends with cycling stability as the 30 mM CTAB film still has the best capacity retention and CE when cycled at variable rates for 35 cycles. All three films experience substantial kinetic limitations at high rates of 5C, but the SPS film manages to retain capacity at 190 mAh/g. We propose that the higher calculated ECSA for the SPS film allows for better rate capability because more exposed active material is available for sodiation/desodiation. In addition, the smaller crystallite size

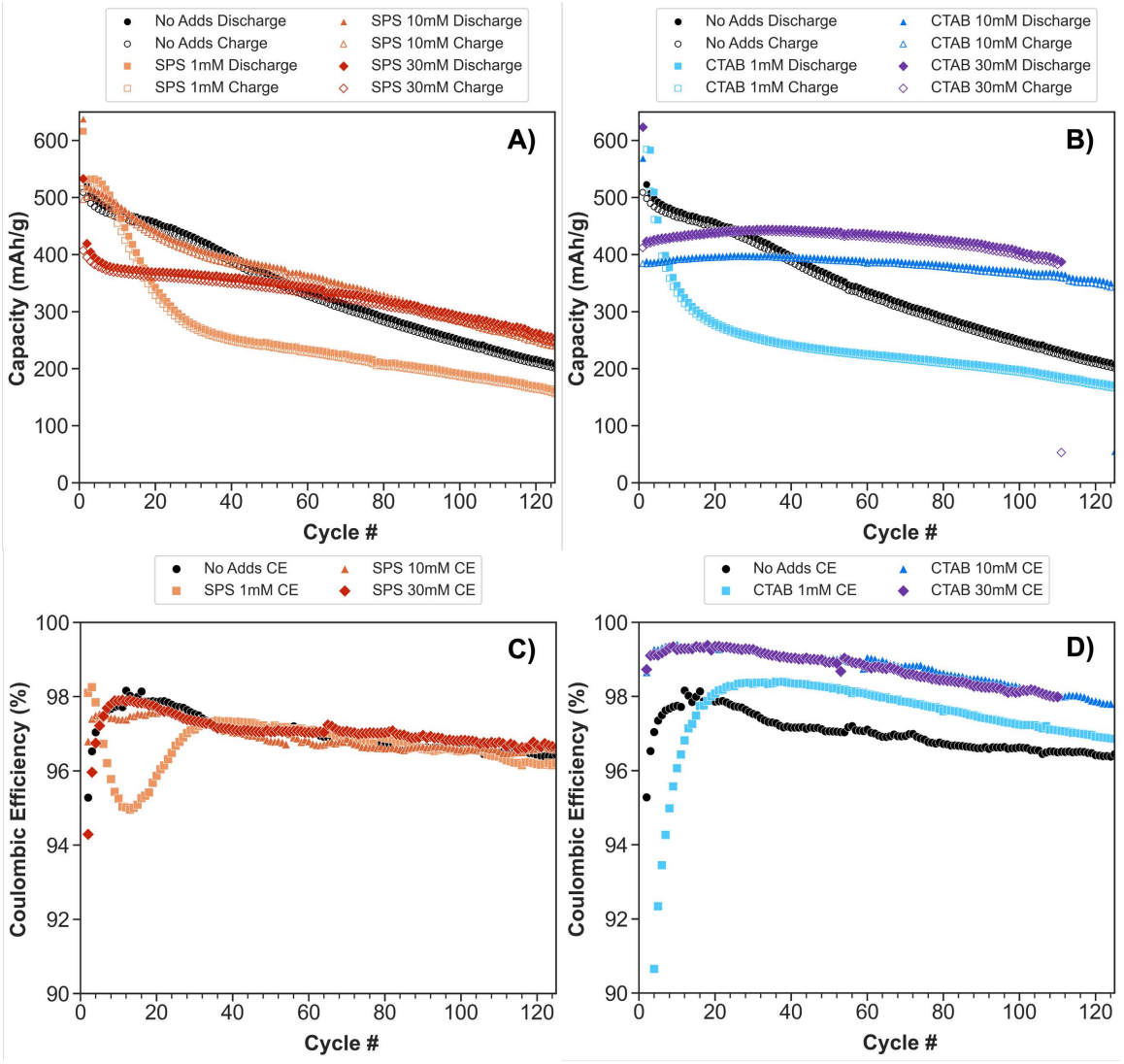

Figure 2.9. Cycling performance and corresponding Coulombic Efficiency (CE) of Sb films deposited with no additives, and at different concentrations of SPS (A&C) and CTAB (B&D). Tests were done in a sodium half-cell at a rate of C/2 in the potential window of 0.01 V-1.5 V vs Na/Na^+.

induced by increasing the concentration of SPS could be leading to better rate capabilities as seen by comparing the performance of all three concentrations in **Figure S2.10**. In contrast, the no additive film was found to have the highest ECSA 9.26 ± 0.2 cm^2 and based on this factor alone would be predicted to have the best rate performance. Instead, it is plagued by detrimental mechanical instability depicted by the lower CE during cycling and the continuous loss of capacity when the cell is returned to a C/10 rate. When considering solely the ECSA, the 30 mM CTAB

film behaves as expected and has poor capacity retention at higher rates. Similar to the SPS films, as the crystallite size decreases with the increase in CTAB, the rate performance also improves,

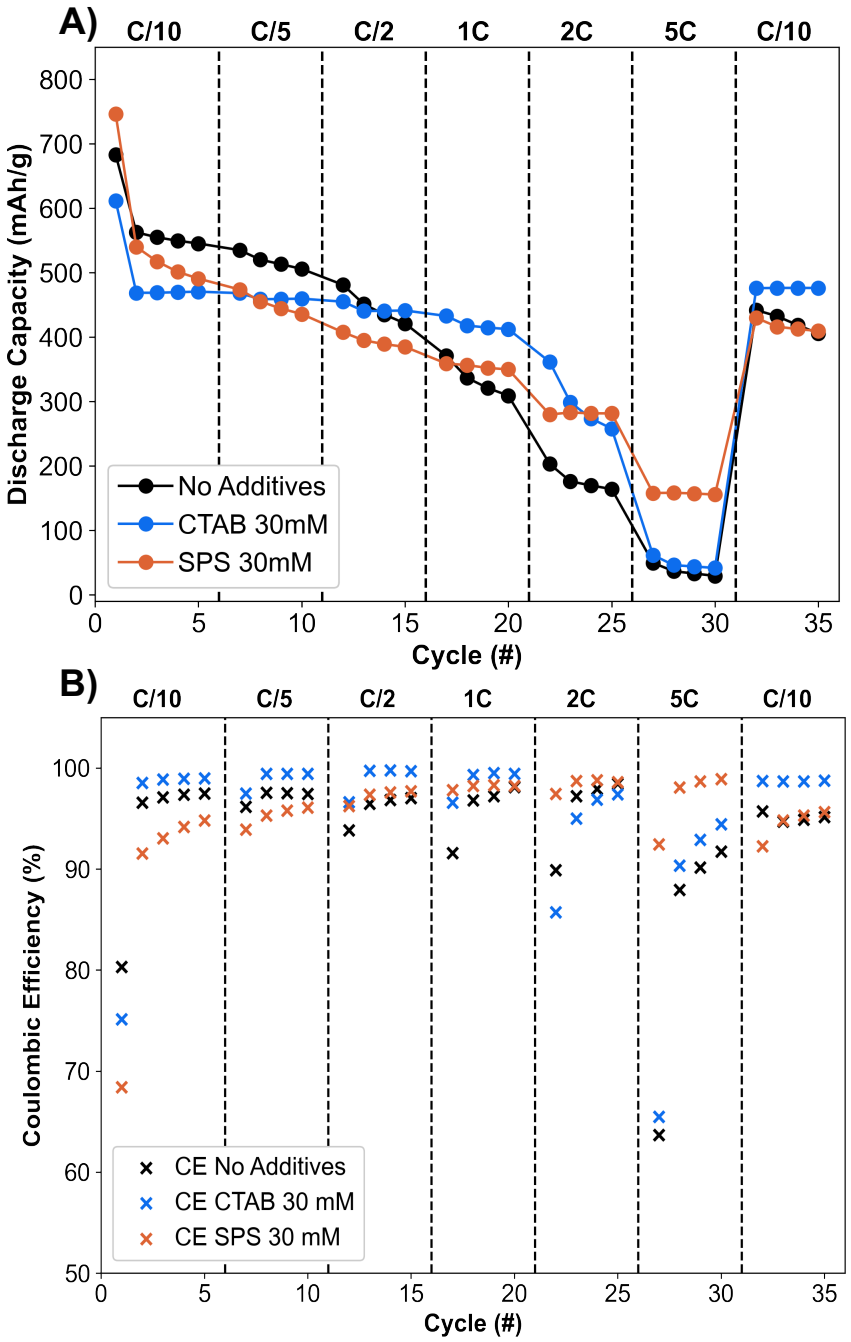

Figure 2.10. The discharge capacity (A) and Coulombic Efficiency (CE) (B) for rate capability tests on the Sb films deposited with no additive (black), with 30 mM CTAB (blue), and 30 mM SPS (orange). These tests were done in a sodium half-cell at 5 cycles for each rate.

Figure S2.10. However, it is challenging to pinpoint one specific property that could explain the improved rate capabilities because the CTAB films also dramatically decreases in overall crystallinity. This decreased crystallinity of the SPS and CTAB films also contributes to slower kinetics in the sodiation/desodiation mechanism as seen in the differential capacity (dQ/dV) data, **Figure S2.9**, and is characterized by the broadening of peaks and shifts in overpotential when compared to the no additive film.

2.5 Conclusion

In this work, we show that the electrodeposition of Sb anodes with solution additives enables significant control and tunability of morphology and crystallinity, which in turn impacts battery performance. The addition of CTAB leads to amorphous, strained films with smooth, densely packed particles. This is likely due to CTAB inhibiting Sb deposition as growth occurs. These films have the lowest ECSA. The SPS films are more crystalline than their CTAB counterparts and exhibit columnar growth; we propose that crystallinity decreases with higher concentrations because of accelerated growth. The combination of morphological and structural changes lead to tradeoffs in the electrochemical performance of these films in NIBs. Due to the mechanical robustness and better adhesion to the copper substrate brought from the influences of CTAB, these films have better capacity retention and remain relatively intact upon continuous sodiation/desodiation. However, the capacity retention diminishes at higher rates potentially due to the amorphous nature of the film. In contrast, the SPS films have worse cycle life due to the increased fragility of the long columnar like morphology. Despite this mechanical instability, SPS films retain higher capacities at rates of 5C when compared to the CTAB and no additive films. We hypothesize that this is a result of the higher ECSA and decreased crystallite size of the deposit and the overall higher crystallinity of the film when compared to the CTAB films.

Controlling specific structural, morphological, and electrochemical properties of the electrodeposited Sb films is of great importance as it significantly impacts the overall performance in a NIB. There are important tradeoffs to consider with lifetime or rate capabilities of the cell, and one could imagine tuning these films according to what application the batteries will be used for. Overall, these studies provide insight into the importance of solution additives and how electrodeposition can be utilized to control material properties of alloy-based anode materials to optimize NIB performance.

2.6 References

(1) Kim, Y.; Ha, K. H.; Oh, S. M.; Lee, K. T. High-Capacity Anode Materials for Sodium-Ion Batteries. *Chemistry - A European Journal* **2014**, *20*, 11980–11992. https://doi.org/10.1002/chem.201402511.

(2) Chirambatte Peter, S.; sarkar, shreya. An Overview on Sb-Based Intermetallics and Alloys for Sodium-Ion Batteries: Trends, Challenges and Future Prospects from Material Synthesis to Battery Performance. *J Mater Chem A Mater* **2021**, *9*, 5164-5196. https://doi.org/10.1039/d0ta12063d.

(3) He, J.; Wei, Y.; Zhai, T.; Li, H. Antimony-Based Materials as Promising Anodes for Rechargeable Lithium-Ion and Sodium-Ion Batteries. *Mater. Chem. Front* **2018**, *2*, 437. https://doi.org/10.1039/c7qm00480j.

(4) Schulze, M. C.; Belson, R. M.; Kraynak, L. A.; Prieto, A. L. Electrodeposition of Sb/CNT Composite Films as Anodes for Li- and Na-Ion Batteries. *Energy Storage Mater* **2020**, *25*, 572–584. https://doi.org/10.1016/j.ensm.2019.09.025.

(5) Pfeifer, K.; Arnold, S.; Budak, Ö.; Luo, X.; Presser, V.; Ehrenberg, H.; Dsoke, S. Choosing the Right Carbon Additive Is of Vital Importance for High-Performance Sb-Based Na-Ion Batteries. *J Mater Chem A Mater* **2020**, *8*, 6092–6104. https://doi.org/10.1039/d0ta00254b.

(6) Liang, S.; Cheng, Y. J.; Zhu, J.; Xia, Y.; Müller-Buschbaum, P. A Chronicle Review of Nonsilicon (Sn, Sb, Ge)-Based Lithium/Sodium-Ion Battery Alloying Anodes. *Small Methods* **2020**, *2000218*. https://doi.org/10.1002/smtd.202000218.

(7) Voigt, K.; Heubner, C.; Liebmann, T.; Matthey, B.; Weiser, M.; Schneider, M.; Michaelis, A. Electrodeposition of Versatile Nanostructured Sb/Sb_2O_3 Microcomposites: A Parameter Study. *Adv Mater Interfaces* **2020**, *7*, 1–10. https://doi.org/10.1002/admi.202000004.

(8) Lv, H.; Qiu, S.; Lu, G.; Fu, Y.; Li, X.; Hu, C.; Liu, J. Nanostructured Antimony/Carbon Composite Fibers as Anode Material for Lithium-Ion Battery. **2014**, *151*, 214-221. https://doi.org/10.1016/j.electacta.2014.11.013.

(9) Nagulapati, V. M.; Yoon, Y. H.; Kim, D. S.; Kim, H.; Lee, W. S.; Lee, J. H.; Kim, K. H.; Hur, J.; Kim, I. T.; Lee, S. G. Effect of Binders and Additives to Tailor the Electrochemical Performance of Sb_2Te_3-TiC Alloy Anodes for High-Performance Sodium-Ion Batteries. *Journal of Industrial and Engineering Chemistry* **2019**, *76*, 419–428. https://doi.org/10.1016/j.jiec.2019.04.008.

(10) Wenzel, V.; Nirschl, H.; Nötzel, D. Challenges in Lithium-Ion-Battery Slurry Preparation and Potential of Modifying Electrode Structures by Different Mixing Processes. *Energy Technology* **2015**, *3*, 692–698. https://doi.org/10.1002/ente.201402218.

(11) Hays, K. A.; Armstrong, B.; Veith, G. M. Ending the Chase for a Perfect Binder: Role of Surface Chemistry Variation and Its Influence on Silicon Anodes. *ChemElectroChem* **2020**, *7*, 3790–3797. https://doi.org/10.1002/celc.202001066.

(12) Baggetto, L.; Ganesh, P.; Sun, C.-N.; Meisner, R. A.; Zawodzinski, T. A.; Veith, G. M. Intrinsic Thermodynamic and Kinetic Properties of Sb Electrodes for Li-Ion and Na-Ion Batteries: Experiment and Theory. *J Mater Chem A Mater* **2013**, *1*, 7985–7994. https://doi.org/10.1039/c3ta11568b.

(13) Li, Z.; Tan, X.; Li, P.; Kalisvaart, P.; Janish, M. T.; Mook, W. M.; Luber, E. J.; Jungjohann, K. L.; Carter, C. B.; Mitlin, D. Coupling In Situ TEM and Ex Situ Analysis to Understand Heterogeneous Sodiation of Antimony. *Nano Lett* **2015**, *15*, 6339–6348. https://doi.org/10.1021/acs.nanolett.5b03373.

(14) Qiu, S.; Wu, X.; Xiao, L.; Ai, X.; Yang, H.; Cao, Y. Antimony Nanocrystals Encapsulated in Carbon Microspheres Synthesized by a Facile Self-Catalyzing Solvothermal Method for High-Performance Sodium-Ion Battery Anodes. *ACS Appl Mater Interfaces* **2016**, *8*, 1337–1343. https://doi.org/10.1021/acsami.5b10182.

(15) Zhang, Y.; Xie, J.; Zhu, T.; Cao, G.; Zhao, X.; Zhang, S. Activation of Electrochemical Lithium and Sodium Storage of Nanocrystalline Antimony by Anchoring on Graphene via a Facile in Situ Solvothermal Route. *J Power Sources* **2014**, *247*, 204–212. https://doi.org/10.1016/j.jpowsour.2013.08.096.

(16) Jackson, E. D.; Prieto, A. L. Copper Antimonide Nanowire Array Lithium Ion Anodes Stabilized by Electrolyte Additives. *ACS Appl. Mater. Interfaces* **2016**, *8*, 30379–30386. https://doi.org/10.1021/acsami.6b08033.

(17) Ma, J.; Prieto, A. L. Electrodeposition of Pure Phase SnSb Exhibiting High Stability as a Sodium-Ion Battery Anode. *Chemical Communications* **2019**, *55*, 6938–6941. https://doi.org/10.1039/c9cc00001a.

(18) Mosby, J. M.; Prieto, A. L. Direct Electrodeposition of Cu_2Sb for Lithium-Ion Battery Anodes. *J Am Chem Soc* **2008**, *130*, 10656–10661. https://doi.org/10.1021/ja801745n.

(19) Jackson, E. D.; Green, S.; Prieto, A. L. Electrochemical Performance of Electrodeposited Zn_4 Sb_3 Films for Sodium-Ion Secondary Battery Anodes. *ACS Appl Mater Interfaces* **2015**, *7*, 7447–7450. https://doi.org/10.1021/am507436u.

(20) Gimble, N. J.; Nieto, K.; Prieto, A. L. Electrodeposition as a Powerful Tool for the Fabrication and Characterization of Next-Generation Anodes for Sodium Ion Rechargeable Batteries. *Electrochemical Society Interface* **2021**, *30*, 59–63. https://doi.org/10.1149/2.F09211IF.

(21) Zangari, G. Electrodeposition of Alloys and Compounds in the Era of Microelectronics and Energy Conversion Technology. *Coatings* **2015**, *5*, 195–218. https://doi.org/10.3390/coatings5020195.

(22) Nieto, K.; Gimble, N. J.; Rudolph, L. J.; Kale, A. R.; Prieto, A. L. Electrodeposition vs Slurry Casting: How Fabrication Affects Electrochemical Reactions of Sb Electrodes in Sodium-Ion Batteries. *J Electrochem Soc* **2022**, *169*, 050537. https://doi.org/10.1149/1945-7111/ac6b5e.

(23) Hong, K.-S.; Nam, D.-H.; Lim, S.-J.; Sohn, D.; Kim, T.-H.; Kwon, H. Electrochemically Synthesized Sb/Sb_2O_3 Composites as High-Capacity Anode Materials Utilizing a Reversible Conversion Reaction for Na-Ion Batteries. *ACS Appl. Mater. Interfaces* **2015**, *7*, 17264–17271. https://doi.org/10.1021/acsami.5b04225.

(24) Ngo, T. T.; Chavhan, S.; Kosta, I.; Miguel, O.; Grande, H. J.; Tena-Zaera, R. Electrodeposition of Antimony Selenide Thin Films and Application in Semiconductor Sensitized Solar Cells. *ACS Appl Mater Interfaces* **2014**, *6*, 2836–2841. https://doi.org/10.1021/am405416a.

(25) Liu, Z.; Cheng, J.; Höfft, O.; Endres, F. In Situ XPS Study of Template-Free Electrodeposition of Antimony Nanowires from an Ionic Liquid. *Journal of Solid State Electrochemistry* **2022**, *27*, 371-378. https://doi.org/10.1007/s10008-022-05321-9.

(26) Leimkühler, G.; Kerkamm, I.; Reineke-Koch, R. Electrodeposition of Antimony Telluride. *J Electrochem Soc* **2002**, *149*, C474. https://doi.org/10.1149/1.1503811.

(27) Gamburg, Y. D.; Zangari, G. *Theory and Practice of Metal Electrodeposition*; Springer New York, NY., 2011. https://doi.org/10.1007/978-1-4419-9669-5

(28) Liu, W.; Yang, T. Z.; Zhou, Q. H.; Zhang, D. C.; Lei, C. M. Electrodeposition of Sb(III) in Alkaline Solutions Containing Xylitol. *Transactions of Nonferrous Metals Society of China (English Edition)* **2012**, *22* (4), 949–957. https://doi.org/10.1016/S1003-6326(11)61269-7.

(29) Majidzade, V. A.; Guliyev, P. H.; Aliyev, A. S.; Elrouby, M.; Tagiyev, D. B. Electrochemical Characterization and Electrode Kinetics for Antimony Electrodeposition from Its Oxychloride Solution in the Presence of Tartaric Acid. *J Mol Struct* **2017**, *1136*, 7–13. https://doi.org/10.1016/j.molstruc.2017.01.082.

(30) Yang, M. H.; Sun, I. W. Electrodeposition of Antimony in a Water-Stable 1-Ethyl-3-Methylimidazolium Chloride Tetrafluoroborate Room Temperature Ionic Liquid. *J Appl Electrochem* **2003**, *33*, 1077–1084. https://doi.org/10.1023/A:1026223314259.

(31) Sadana, Y. N.; Singh, J. P.; Kumar, R. Electrodeposition of Antimony and Antimony Alloys- A Review. *Surface Technology* **1985**, *24*, 319–353. https://doi.org/10.1016/0376-4583(85)90053-6.

(32) Ghosh, J. C.; Kappana, A. N. Electrodeposition of Antimony. *J. Phys. Chem. C.* **1924**, *28*, 149–160.

(33) Li, F.-H.; Wang, W.; Gao, J.-P.; Wang, S.-Y. Electrochemical Reduction Process of Sb(III) on Au Electrode Investigated by CV and EIS. *J Electrochem Soc* **2009**, *156*, D84. https://doi.org/10.1149/1.3049349.

(34) Fan, X.-Y.; Han, J.; Jiang, Y.; Ni, J.; Gou, L.; Li, D.-L.; Li, L. Hierarchical Porous Sb Films on 3D Cu Substrate Have Promise for Stable Sodium Storage. *Applied Energy Material* **2018**, *1*, 3598–3602. https://doi.org/10.1021/acsaem.8b00872.

(35) Aroyo, M. Theoretical and Practical Aspects of Electrodeposition of Metal Coatings with Improved Properties (Part 1). *Plating and Surface Finishing* **1998**, *85*, 69–76.

(36) Schmitz, E. P. S.; Quinaia, S. P.; Garcia, J. R.; de Andrade, C. K.; Lopes, M. C. Influence of Commercial Organic Additives on the Nickel Electroplating. *Int J Electrochem Sci* **2016**, *11*, 983–997.

(37) Aroyo, M. S. Leveling in Pulse Plating with Brighteners: Synergistic Effect of Frequency and Hydrodynamically Active Additives. *Plating and Surface Finishing* **1995**, *82*, 53–57.

(38) Moffat, T. P.; Wheeler, D.; Josell, D. Electrodeposition of Copper in the SPS-PEG-Cl Additive System. *J Electrochem Soc* **2004**, *151*, C262. https://doi.org/10.1149/1.1651530.

(39) Vereecken, P. M.; Deligianni, H.; Binstead, R. A. The Role of SPS in Damascene Copper Electroplating. *IBM J Res Dev* **2005**, *49*, 3–18. https://doi.org/10.1147/rd.491.0003.

(40) Willey, M. J.; West, A. C. SPS Adsorption and Desorption during Copper Electrodeposition and Its Impact on PEG Adsorption. *J Electrochem Soc* **2007**, *154*, D156. https://doi.org/10.1149/1.2431320.

(41) Rudnik, E.; Wojnicki, M.; Włoch, G. Effect of Gluconate Addition on the Electrodeposition of Nickel from Acidic Baths. *Surf Coat Technol* **2012**, *207*, 375–388. https://doi.org/10.1016/j.surfcoat.2012.07.027.

(42) Chat-Wilk, K.; Rudnik, E.; Włoch, G.; Osuch, P. Importance of Anions in Electrodeposition of Nickel from Gluconate Solutions. *Ionics* **2021**, *27*, 4393–4408. https://doi.org/10.1007/s11581-021-04166-y.

(43) Lallemand, F.; Ricq, L.; Berçot, P.; Pagetti, J.; Effects of Organic Additives on Electroplated Iron-Group Metals and Alloys. *Surf. Coat. Technol* **1998**, *44*, 2886.

(44) Sciscenko, I.; Pedre, I.; Hunt, A.; Bogo, H.; González, G. A. Determination of a Typical Additive in Zinc Electroplating Baths. *Microchemical Journal* **2016**, *127*, 226–230. https://doi.org/10.1016/j.microc.2016.03.015.

(45) Maharana, H. S.; Basu, A.; Mondal, K. Effect of CTAB on the Architecture and Hydrophobicity of Electrodeposited Cu–ZrO_2 Nano-Cone Arrays. *Surf Coat Technol* **2019**, *375*, 323–333. https://doi.org/10.1016/j.surfcoat.2019.07.050.

(46) Chen, Y. C.; Kuo, S. L.; Lee, J. L.; Ke, S. T.; Wong, C. H.; Ger, M. der. The Influence of Surfactant CTAB on the Microstructure and Material Properties of Nickel Microelectroforming. *Key Eng Mater* **2008**, *I*, 346–350. https://doi.org/10.4028/www.scientific.net/kem.364-366.346.

(47) Rudnik, E.; Burzyńska, L.; Dolasiński, Ł.; Misiak, M. Electrodeposition of Nickel/SiC Composites in the Presence of Cetyltrimethylammonium Bromide. *Appl Surf Sci* **2010**, *256* (24), 7414–7420. https://doi.org/10.1016/j.apsusc.2010.05.082.

(48) Maharana, H. S.; Basu, A. Evolution and Structure-Property Correlation of CTAB Assisted High Hardness Electrodeposited Cu-ZrO_2 Nano-Cone Arrays. *Surf Coat Technol* **2017**, *310*, 148–156. https://doi.org/10.1016/j.surfcoat.2016.12.064.

(49) Maharana, H. S.; Basu, A.; Mondal, K. Effect of CTAB on the Architecture and Hydrophobicity of Electrodeposited Cu–ZrO2 Nano-Cone Arrays. *Surf Coat Technol* **2019**, *375*, 323–333. https://doi.org/10.1016/j.surfcoat.2019.07.050.

(50) Fenger, R.; Fertitta, E.; Kirmse, H.; Thünemann, A. F.; Rademann, K. Size Dependent Catalysis with CTAB-Stabilized Gold Nanoparticles. *Physical Chemistry Chemical Physics* **2012**, *14*, 9343–9349. https://doi.org/10.1039/c2cp40792b.

(51) Smith, D. K.; Korgel, B. A. The Importance of the CTAB Surfactant on the Colloidal Seed-Mediated Synthesis of Gold Nanorods. *Langmuir* **2008**, *24*, 644–649. https://doi.org/10.1021/la703625a.

(52) Heuer-Jungemann, A.; Feliu, N.; Bakaimi, I.; Hamaly, M.; Alkilany, A.; Chakraborty, I.; Masood, A.; Casula, M. F.; Kostopoulou, A.; Oh, E., et al. The Role of Ligands in the Chemical Synthesis and Applications of Inorganic Nanoparticles. *Chem Rev* **2019**, *119*, 4819–4880. https://doi.org/10.1021/acs.chemrev.8b00733.

(53) Jennane, J.; Ebn Touhami, M.; Zehra, S.; Baymou, Y.; Kim, S. H.; Chung, I. M.; Lgaz, H. Influence of Sodium Gluconate and Cetyltrimethylammonium Bromide on the Corrosion Behavior of Duplex (α-β) Brass in Sulfuric Acid Solution. *Mater Chem Phys* **2019**, *227*, 200–210. https://doi.org/10.1016/j.matchemphys.2019.02.001.

(54) Liang, L.; Xu, Y.; Li, Y.; Dong, H.; Zhou, M.; Zhao, H.; Kaiser, U.; Lei, Y. Facile Synthesis of Hierarchical Fern Leaf-like Sb and Its Application as an Additive-Free Anode for Fast Reversible Na-Ion Storage. *J Mater Chem A Mater* **2017**, *5*, 1749–1755. https://doi.org/10.1039/c6ta10345f.

(55) Fairley, N.; Fernandez, V.; Richard-Plouet, M.; Guillot-Deudon, C.; Walton, J.; Smith, E.; Flahaut, D.; Greiner, M.; Biesinger, M.; Tougaard, S.; Morgan, D.; Baltrusaitis, J.

Systematic and Collaborative Approach to Problem Solving Using X-Ray Photoelectron Spectroscopy. *Applied Surface Science Advances* **2021**, *5*, 100112. https://doi.org/10.1016/J.APSADV.2021.100112.

(56) *Handbook of X-Ray Photoelectron Spectroscopy: A Reference Book of Standard Spectra for Identification and Interpretation of XPS Data*, Moulder, J.F., Stickle, W.F., Sobol, P.E., Bomben, K.D. and Chastain, J.; Perkin-Elmer Corporation, Waltham, 1992.

(57) Kuruvilla, A.; Francis, M.; Sudheer, K. S.; Lakshmi, M. Replacement of Sulphur with Selenium in Antimony Sulphide Thin Films. *Bulletin of Materials Science* **2022**, *45*. https://doi.org/10.1007/s12034-021-02651-8.

(58) Sawyer, D. T. Metal-Gluconate Complexes. *Chem Rev* **1964**, *64*, 633–643. https://doi.org/10.1021/cr60232a003.

(59) Moffat, T. P.; Wheeler, D.; Josell, D. Electrodeposition of Copper in the SPS-PEG-Cl Additive System. *J Electrochem Soc* **2004**, *151*, C262. https://doi.org/10.1149/1.1651530.

(60) Choe, S.; Kim, M. J.; Kim, H. C.; Cho, S. K.; Ahn, S. H.; Kim, S.-K.; Kim, J. J. Degradation of Bis(3-Sulfopropyl) Disulfide and Its Influence on Copper Electrodeposition for Feature Filling. *J Electrochem Soc* **2013**, *160*, D3179–D3185. https://doi.org/10.1149/2.032312jes.

(61) Ghaemi, M.; Khosravi-Fard, L.; Neshati, J. Improved Performance of Rechargeable Alkaline Batteries via Surfactant-Mediated Electrosynthesis of MnO_2. *J Power Sources* **2005**, *141*, 340–350. https://doi.org/10.1016/J.JPOWSOUR.2004.10.004.

(62) Al-Tabbakh, A. A.; Karatepe, N.; Al-Zubaidi, A. B.; Benchaabane, A.; Mahmood, N. B. Crystallite Size and Lattice Strain of Lithiated Spinel Material for Rechargeable Battery by X-Ray Diffraction Peak-Broadening Analysis. *Int J Energy Res* **2019**, *43*, 1903–1911. https://doi.org/10.1002/er.4390.

(63) Domi, Y.; Usui, H.; Sugimoto, K.; Sakaguchi, H. Effect of Silicon Crystallite Size on Its Electrochemical Performance for Lithium-Ion Batteries. *Energy Technology* **2019**, *7*, 1800946. https://doi.org/10.1002/ente.201800946.

(64) Biswal, A.; Panda, P. K.; Acharya, A. N.; Mohapatra, S.; Swain, N.; Tripathy, B. C.; Jiang, Z. T.; Minakshi Sundaram, M. Role of Additives in Electrochemical Deposition of Ternary Metal Oxide Microspheres for Supercapacitor Applications. *ACS Omega* **2020**, *5*, 3405–3417. https://doi.org/10.1021/acsomega.9b03657.

(65) Balzar, D.; Audebrand, N.; Daymond, M. R.; Fitch, A.; Hewat, A.; Langford, J. I.; Le Bail, A.; Louër, D.; Masson, O.; McCowan, C. N., et al. Size-Strain Line-Broadening Analysis of the Ceria Round-Robin Sample. *J Appl Crystallogr* **2004**, *37*, 911–924. https://doi.org/10.1107/S0021889804022551.

(66) Ectors, D.; Goetz-Neunhoeffer, F.; Neubauer, J. Routine (an)Isotropic Crystallite Size Analysis in the Double-Voigt Approximation Done Right? *Powder Diffr* **2017**, *32*, S27–S34. https://doi.org/10.1017/S0885715617000070.

(67) Pereira, R.; Camargo, P. C.; de Oliveira, A. J. A.; Pereira, E. C. Modulation of the Morphology, Microstructural and Magnetic Properties on Electrodeposited NiFeCu Alloys. *Surf Coat Technol* **2017**, *311*, 274–281. https://doi.org/10.1016/j.surfcoat.2016.12.087.

(68) Bouzit, F. Z.; Nemamcha, A.; Moumeni, H.; Rehspringer, J. L. Morphology and Rietveld Analysis of Nanostructured Co-Ni Electrodeposited Thin Films Obtained at Different Current Densities. *Surf Coat Technol* **2017**, *315*, 172–180. https://doi.org/10.1016/j.surfcoat.2017.02.028.

(69) Voiry, D.; Chhowalla, M.; Gogotsi, Y.; Kotov, N. A.; Li, Y.; Penner, R. M.; Schaak, R. E.; Weiss, P. S. Best Practices for Reporting Electrocatalytic Performance of Nanomaterials. *ACS Nano* **2018**, *12*, 9635–9638. https://doi.org/10.1021/acsnano.8b07700.

(70) Wolfe, K. D.; Dervishogullari, D.; Stachurski, C. D.; Passantino, J. M.; Kane Jennings, G.; Cliffel, D. E. Photosystem I Multilayers within Porous Indium Tin Oxide Cathodes Enhance Mediated Electron Transfer. *ChemElectroChem* **2019**. https://doi.org/10.1002/celc.201901628.

(71) Williamson, G. A.; Hu, V. W.; Yoo, T. B.; Affandy, M.; Opie, C.; Paradis, E. K.; Holmberg, V. C. Temperature-Dependent Electrochemical Characteristics of Antimony Nanocrystal Alloying Electrodes for Na-Ion Batteries. **2019**. https://doi.org/10.1021/acsaem.9b01216.

(72) Cooper, S. J.; Bertei, A.; Finegan, D. P.; Brandon, N. P. Simulated Impedance of Diffusion in Porous Media. *Electrochim Acta* **2017**, *251*, 681–689. https://doi.org/10.1016/j.electacta.2017.07.152.

(73) Dashairya, L.; Das, D.; Saha, P. Binder-Free Electrophoretic Deposition of Sb/RGO on Cu Foil for Superior Electrochemical Performance in Li-Ion and Na-Ion Batteries. *Electrochim Acta* **2020**, *358*, 136948. https://doi.org/10.1016/j.electacta.2020.136948.

(74) Darwiche, A.; Marino, C.; Sougrati, M. T.; Fraisse, B.; Stievano, L.; Monconduit, L. Better Cycling Performances of Bulk Sb in Na-Ion Batteries Compared to Li-Ion Systems: An Unexpected Electrochemical Mechanism. *J Am Chem Soc* **2012**, *134*, 20805–20811. https://doi.org/10.1021/ja310347x.

(75) Allan, P. K.; Griffin, J. M.; Darwiche, A.; Borkiewicz, O. J.; Wiaderek, K. M.; Chapman, K. W.; Morris, A. J.; Chupas, P. J.; Monconduit, L.; Grey, C. P. Tracking Sodium-Antimonide Phase Transformations in Sodium-Ion Anodes: Insights from Operando Pair

Distribution Function Analysis and Solid-State NMR Spectroscopy. *J Am Chem Soc* **2016**, *138*, 2352–2365. https://doi.org/10.1021/jacs.5b13273.

III: ELECTRODEPOSITION VS SLURRY CASTING: HOW FABRICATION AFFECTS ELECTROCHEMICAL REACTIONS OF Sb ELECTRODES IN SODIUM-ION BATTERIES[3]

3.1 Overview

Antimony (Sb) electrodes are an ideal anode material for sodium-ion batteries, which are an attractive energy storage system to support grid-level energy storage. These anodes have high thermal stability, good rate performance, and good electronic conductivity, but there are limitations on the fundamental understanding of phases present as the material is sodiated and desodiated. Therefore, detailed investigations of the impact of the structure-property relationships on the performance of Sb electrodes are crucial for understanding how the degradation mechanisms of these electrodes can be controlled. Although significant work has gone into understanding the sodiation/desodiation mechanism of Sb-based anodes, the fabrication method, electrode composition and experimental parameters vary tremendously and there are discrepancies in the reported sodiation/desodiation reactions. Here we report the use of electrodeposition and slurry casting to fabricate Sb composite films to investigate how different fabrication techniques result in different observed sodiation/desodiation mechanisms. We report that electrode fabrication techniques can dramatically impact the sodiation/desodiation reaction mechanism due to

[3] This invited manuscript is published in the Journal of the Electrochemical Society and is featured in the JES focus issue on Women in Electrochemistry. The manuscript was published with Kelly Nieto, Nathan J. Gimble, Layton J. Rudolph, Amanda R. Kale, and Amy L. Prieto (*J. Electrochem. Soc.* **2022**, *169*, 050537.). Kelly Nieto developed the project, hypothesis, carried out carried out all experimental procedures, characterization, and manuscript preparation. Nathan J. Gimble assisted with X-ray photoelectron spectroscopy experiments, analysis, and editing the manuscript. Layton J. Rudolph assisted with battery assembly, anode preparation, and editing the manuscript. Amanda R. Kale assisted with interpretation of X-ray diffraction data, and manuscript editing. Amy L. Prieto assisted with project administration, funding acquisition, and manuscript editing.

mechanical stability, morphology, and composition of the film. Electrodeposition has been shown to be a viable fabrication technique to process anode materials and to study reaction mechanisms at longer lengths scales without the convolution of binders and additives.

3.2 Introduction

Meeting the energy needs for emerging applications such as the electrification of transportation and the growing population necessitates research in alternative renewable energy and energy storage devices. Sodium-ion batteries (NIBs) are an excellent candidate for applications where weight is not a driver, such as large grid energy storage, as sodium (Na) is more naturally abundant, lower in cost, and environmentally benign when compared to popular lithium-ion batteries (LIBs)[1–4]. Many researchers have adapted the chemistry developed from LIBs to formulate Na analogs, but it has been discovered that not all chemistries can be transferred directly between the two systems.[5] Commonly used anode materials such as graphite and silicon in LIBs perform poorly in NIBs as demonstrated by their very low measured capacities in NIBs.[6] Hence, the investigation of alternative anode materials is crucial to obtain higher capacities and cycling stability in NIBs.

Antimony (Sb) is an ideal anode material in NIBs with a high theoretical capacity (660 mAh/g) and has previously been used in both LIBs and NIBs due to antimony's high thermal stability and conductivity. A major shortcoming of this alloy-type anode is the volume expansion experienced through the conversion process from Sb to Na_3Sb, resulting in issues with mechanical stability caused by the pulverization of the electrode. Also, the degradation of liquid electrolytes at the surface of Sb is not well understood. Studies have aimed to combat issues related to volume expansion and electrolyte decomposition on Sb electrodes by using the inclusion of carbon additives,[7–10] and different electrolyte additives,[11–15] Although the lifetime of Sb anodes can be

extended, unanswered questions related to the understanding of structural changes during cycling of the material remain. This insight into structural changes is critical to better understand the stability, cyclability, and rate capability of Sb electrodes. While many researchers are focused on optimizing and engineering a better battery, fundamental studies on identifying structural transitions in alloy electrodes for NIBs are lacking and are crucial to the commercialization of alloy materials. There are a few reports investigating phase transitions in antimony electrodes in NIBs. Previously it was believed that the sodiation of Sb occurred by first sodiating Sb to NaSb and then the final sodiated Na_3Sb phase, similar to the lithiation of Sb, but many reports in the literature have found that the sodiation process is much more complex.[5,14,16–25] Several studies have investigated these phase transitions and have identified various intermediate and metastable phases.[18,19,24,26,27] For example, Darwiche et al. alluded to the possible formation of cubic and hexagonal Na_3Sb as the final sodiated phase using *in situ* X-ray diffraction and Allan et al. was able to identify two sodiated amorphous phases, $Na_{3-x}Sb$ and $Na_{1.7}Sb$, using pair distribution function analysis and solid-state NMR spectroscopy.[5,18] In addition Lee et al. has predicted the possibility of a multitude of metastable intermediate phases forming under commonly used battery cycling conditions.[26]

Although these studies have made significant contributions to the fundamental understanding of the reaction pathway of antimony in Na-ion systems it is hard to compare results obtained between the different studies. The Sb electrodes in these studies are fabricated with different techniques and are cycled using different electrolytes and experimental parameters that can influence the reaction pathway.[5,18] Typically the slurry casting method is utilized to fabricate electrodes and uses different polymeric binders and conductive additives that have been shown to influence electrochemical performance for various reasons such as mechanical stability, excessive

SEI formation and the ability for components other than Sb to reversibly sodiate.[28–33] Other studies investigating Sb electrodes use different additives or even different fabrication techniques, such as sputtering and electrodeposition.[7,23] By comparing the data presented in all these studies that are investigating antimony electrodes, it is apparent that electrode fabrication, electrolytes, and different cycling parameters may be causing significant differences in the electrochemical reactions present.[5,7,18,23,34]

Previously our group has used electrodeposition to form anode films that enables the direct deposition of active material onto a metal foil current collector without the use of additives or binders like that of slurry casted films.[7,35–39] This technique allows for the investigation of the intrinsic properties of the active material without the need to deconvolute data from the active material and inactive binders. Electrodeposition also allows for the co-deposition of antimony with conductive material such as amine functionalized carbon nanotubes (ACNTs) to extend cycle life. Schulze et al., created a co-deposition procedure for the deposition of antimony thin films on textured copper foil with an amine functionalized carbon nanotube (ACNT) network for Li-ion cells.[7] It was found that ACNTs extend cycle lifetime by maintaining electronic conductivity within the Sb film even when cracking due to volume expansion occurs.[7] This mechanical stability allows for Sb/ACNT to act as the model anode and would allow for the study of the sodiation/desodiation pathway at longer cycle lifetimes.

Here we report the use of two fabrication techniques, slurry casting and electrodeposition, to investigate how differences introduced from electrode fabrication, such as composition and morphology, impact the electrochemical reactions occurring as Sb anodes are cycled in NIBs. We used differential capacity analysis (DCA) to compare the electrochemical performance and reaction mechanism of electrodeposited and slurry casted composite films. The inclusion of

electrochemically active binders and conductive additives that sodiate inhibit understanding of the reaction mechanism. In contrast, electrodeposited Sb films allow for a better understanding of the mechanism as this method was found to allow significant control of composition, morphology, and mechanical integrity of Sb anodes. Through electrodeposition, we demonstrate a feasible technique to study the intrinsic properties of Sb and its sodiation/desodiation reactions. By understanding these fundamental processes and developing the tools and characterization techniques to study alloy-based anode materials, these studies will accelerate the understanding and processibility of anodes for energy storage applications.

3.3 Experimental

3.3.1 Electrodeposition Solution of Sb and Sb/ACNT

The electrodeposition solution of Sb and Sb/ACNT were both composed of 200 mM sodium gluconate (Sigma, ACS reagent), and 30 mM of antimony trichloride ($SbCl_3$, Sigma-Aldrich, anhydrous >99.0%). The Sb/ACNT solution additionally had 30 mM of cetyl trimethyl ammonium bromide (CTAB, Alfa Aesar 98%), and 200 mg of ACNTs (Cheap Tubes, outer diameter 20 nm, inside diameter 4 nm, and length from 1-12 μm, >99 wt% purity).

In both electrodeposition solutions, sodium gluconate was stirred in a beaker containing 100 mL of Millipore (>15MΩ*cm) water for ~5min. Then $SbCl_3$ was added to the solution and sonicated (VWR Model 50HT) until a homogeneous mixture was formed. The pure Sb solution was then complete and CTAB was added to the beaker containing the Sb and gluconate solution intended for the Sb/ACNT deposition. The solution was sonicated until clear and mostly colorless. The Sb/ACNT solution was returned to a stir plate in a hood and 200 mg of ACNTs were added. The solution was pulse sonicated for two hours with a 10 min pulse and 2 min rest sequence and then sonicated overnight. The excess ACNTs were then crashed out through centrifugation. The

solution was split evenly into two 50 mL centrifuge tubes and was centrifuged for 5 min at 5000 rpm. The supernatant was decanted and the excess ACNTs were saved for later use.

3.3.2 Electrodeposition Solution of ACNTs

The procedure for the ACNT deposition solution was similar to that of the Sb/ACNT without the use of antimony. The solution was composed of 100 mL of Millipore water, 200 mM sodium gluconate, 30 mM of CTAB, and an excess of ACNT consisting of 1 heaping scoopula of ACNT for every 20 mL of solution. All sonication and centrifugation procedures used for the Sb/ACNT solution were followed.

3.3.3 Electrochemical Characterization of Deposition Solutions

Cyclic voltammetry (CV) was used to characterize the deposition solutions and determine the reduction potential at which to deposit Sb. A Gamry Reference 3000 potentiostat was used to perform these experiments. The CVs were taken in a three-electrode set up consisting of a saturated calomel electrode as the reference, a platinum counter electrode, and a platinum disk working electrode at a scan rate of 50 mV/s unless otherwise noted.

3.3.4 Electrodeposition of Sb@tCu and Sb/ACNT@tCu

The thin film electrodes were electrodeposited using a Gamry Interface 1010E potentiostat and the apparatus pictured in **Figure 3.1**. A four-inch square of textured Cu foil (tCu, Oak-Mitsui,

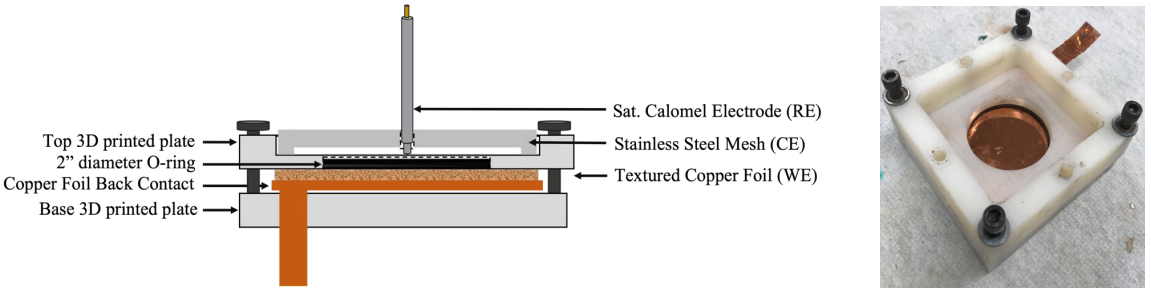

Figure 3.1. Apparatus designed and used for the electrodeposition of Sb/ACNT where the copper foil back contact acts as the working electrode, a stainless-steel mesh acts as the counter electrode, and a saturated calomel electrode is used as the reference electrode.

TLB-DS Cu foil) was washed with a concentrated H_3PO_4 solution for 30 s to remove oxides on the surface, followed by Millipore water and ethanol wash to remove excess acid and water on the surface of the film. The clean film was placed in the apparatus pictured in **Figure 3.1**. Approximately 100 mL of the Sb or Sb/ACNT deposition solution were used to cover the tCu and the stainless-steel (SS) mesh. The saturated calomel electrode (SCE) was placed through an opening in the SS mesh to lessen the distance between the textured copper foil and the SCE to reduce the measured resistance in the system. Using chronocoulometry a constant negative potential of -1.05V vs SCE was applied to the system and the charge limit was set to 3 C/cm^2. When the deposition was complete, the deposited area was washed with Millipore water and absolute ethanol and was dried with nitrogen gas.

3.3.5 Electrophoretic Deposition of ACNTs

A constant negative potential of -1.05 V vs SCE was applied to the system and the charge limit was set to 3 C/cm^2. The deposition was run for ~1hr, similar to the time it took to complete the Sb/ACNT deposition.

3.3.6 Preparation of Slurry Casted Films

The slurry composites consisted of active material, a conductive additive, and a binder at a ratio of 70:15:15 wt%. The composites were doctor bladed onto textured copper foil at a thickness of 150 μm. After casting the films were dried with specific drying procedures depending on the wetting solvent used.

Sodium carboxymethyl cellulose (CMC, Aldrich, DS = 0.7, M_w = 250,000) was first dissolved in 2.5 mL of Millipore water in a vial at 80 ˚C while stirred. The CMC suspension was allowed to stir for one hour or until the powder was completely dissolved and the solution was viscous. Sb powder (~200 mesh, Alfa Aesar, 99.5%), and carbon black (Super P conductive, Alfa

Aesar >99%) were ball milled for one hour in a Fritsch planetary ball mill at 650 rpm. The ball milled powder was then added in batches to the CMC solution and was stirred for 30 mins for each batch. Textured copper foil (tCu, Oak-Mitsui, TLB-DS Cu foil) was then smoothed out on a glass panel with ethanol to prevent the doctor blade from catching on creases in the foil. The doctor blade was then used to cast a 150 μm thick film. The film was dried for 12 hrs at room temperature and then dried in a vacuum oven at 80 ˚C overnight.

The binder poly(acrylic acid) (PAA, Sigma-Aldrich, M_v = 450,000,) was dissolved in 2.5 mL of 1-methyl-2-pyrrolidinone (NMP, Sigma-Aldrich, ACS reagent, ≥99.0%,) in a vial at room temperature while stirred. The PAA suspension was allowed to stir for one hour or until the powder was completely dissolved and the solution was viscous. Sb powder and Super P were ball milled for one hour at 30 Hz in a Retsch Cryomill. The ball milled powder was then added in batches to the PAA solution and was stirred for 30 mins for each batch. The films were casted using the same procedure mentioned for the CMC based slurries. These films were dried in a vacuum oven overnight at 80 ˚C.

All slurry controls were casted using the procedures described above. The Super P control was casted at a 50:50 wt% ratio of Super P to PAA. The PAA and CMC controls were casted using only the binder in question using the solution preparation described above to dissolve the binders in their respective wetting solvents.

3.3.7 Electrolyte Preparation, Cell Assembly, and Galvanostatic Cycling

All tested electrolyte solutions were made in an argon glovebox. The electrolyte used for all experiments consisted of a 1M solution of sodium perchlorate ($NaClO_4$, Sigma-Aldrich, ≥98% ACS reagent) with an addition of 5% by volume fluoroethylene carbonate (FEC, Sigma-Aldrich,

99%) in a base electrolyte solution containing polyethylene carbonate (PC, Sigma-Aldrich, 99.7%).

All half-cells were assembled in two electrode Swageloks, in an argon filled glove box. The electrodeposited film was cut into circular ½" in diameter punches and were weighed out to acquire the mass of the active material. The thin films were used as the working electrode and a polypropylene separator (MTI Corp) followed by a Whatman glass filter, and another polypropylene separator were used to prevent shorting through anode and cathode contact. An excess amount of electrolyte, ~0.20 µL, was placed in the cell after the separators. Na metal (Aldrich, cubes in mineral oil, 99.9%) was then rolled out with a Teflon roller with hexanes, cleaned with an extra soft child's toothbrush and was punched into a ½" circular punch. Pressure was then applied through the spring to the SS rod and the Cu rod to make sure that all parts were in contact in the Swagelok.

Once assembled, the Na-ion half-cells were cycled with an Arbin battery tester (LBT-20084). The cells were allowed to rest for 12 hours after assembly and were galvanostatically cycled at 0.1 mA/mg with calculated current densities based on the mass of active material in the deposited thin films. The voltage range at which the cells were cycled was 0.01 V to 2.0 V vs. Na^+/Na unless otherwise noted. Cycling performance was analyzed and graphed with Python code using the NumPy and Pandas packages.

3.3.8 Materials Characterization

The surface morphology of electrodeposited and slurry casted films was analyzed with Scanning Electron Microscopy (SEM) using a JEOL JSM-6500F Microscope at 15kV, Energy Dispersive X-ray Spectroscopy (EDS) with an Oxford Instrument X-Max and AZtec software. X-ray Photoelectron Spectroscopy (XPS) was performed using a Physical Electronics (PHI) 5800

series Multi-Technique ESCA system with a monochromatic Al Kα (hν=1486.6 eV) X-ray source operating at 350.0 W. Further structural characterization was done with Powder X-ray Diffraction (PXRD) with a Bruker D8 Discover DaVinci powder X-ray diffractometer using Cu Kα radiation.

3.4 Results and Discussion

3.4.1 Electrodeposition of Sb@tCu and Sb/ACNT@tCu Composite Films

Thin films of Sb@tCu and Sb/ACNT@tCu were synthesized through electrodeposition using a solution containing $SbCl_3$, CTAB, sodium gluconate, and ACNT. To maintain the solubility of Sb^{3+} in solution, sodium gluconate has previously been reported to complex with Sb^{3+} in solution to prevent the precipitation of antimony oxide species.[40] Additionally, CTAB acts as the cationic surfactant that aids in the suspension of ACNT in solution.[7,41] In order to find the potential at which Sb should be deposited, CVs of the electrodeposition solution and its individual components were collected. The cyclic voltammogram of the electrodeposition solution revealed two reduction events and two oxidation events as presented in **Figure 3.2**. The reduction peak seen at -1.05 V vs SCE when sweeping in the cathodic direction is representative of the reduction of Sb^{3+} to Sb^0. In the reverse direction, the oxidative event at 0.0 V represents the oxidation of Sb^0 to Sb^{3+} as this event was not present without the use of $SbCl_3$ in the solution. The second oxidative event at +1.05 V represents an irreversible oxidation reaction occurring when CTAB and sodium gluconate are in solution. From these results, the electrodeposition of Sb and Sb/ACNT was conducted at the negative reduction potential of -1.05 V to ensure that only Sb^{3+} was being reduced onto the negatively biased textured Cu foil.

Characterization using SEM, EDS, and XRD was performed to investigate the composition, uniformity of the film, and to confirm that ACNTs were incorporated in the

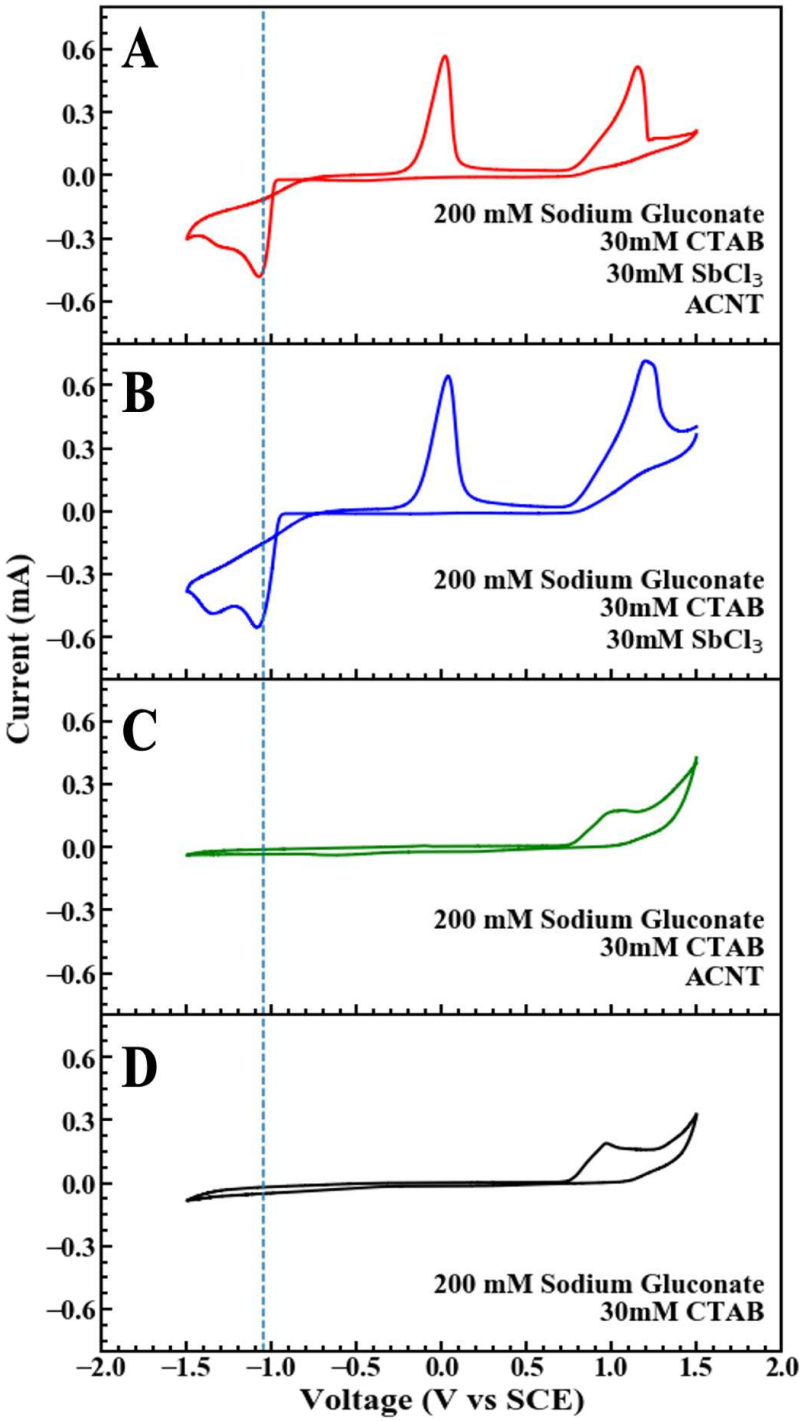

Figure 3.2. Cyclic voltammograms of individual components of the electrodeposition solution for both Sb and Sb/ACNTs. A scan rate of 50 mV/s was used, and the potential was swept to negative potentials then positive potentials. The blue dashed line represents the reduction potential of $Sb^{3+} + 3e^- \rightarrow Sb^0$ vs SCE.

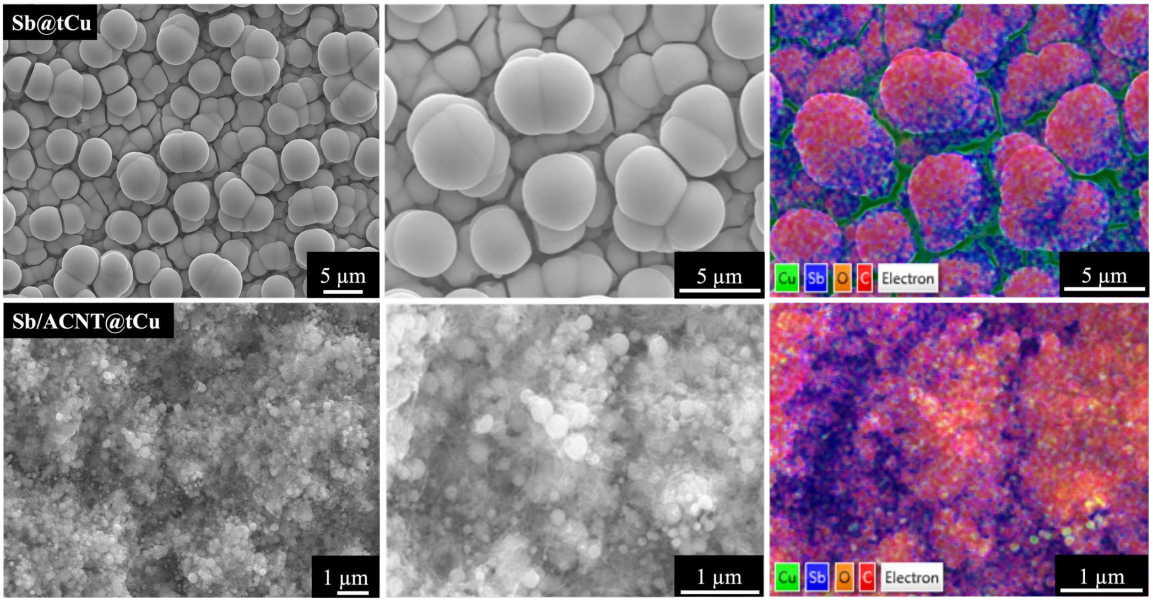

Figure 3.3. SEM and EDS of Sb@tCu (top) and Sb/ACNT@tCu (bottom).

deposition. The Sb was reduced onto the foil in densely packed, spherically shaped particles as seen in **Figure 3.3**. In the Sb/ACNT@tCu film, Sb was reduced onto the ACNTs as seen by the nodular growth of Sb onto the ACNTs through SEM and EDS, **Figure 3.3**, and creates a porous film that in turn increases surface area and increases the number of oxides and SEI build up upon cycling.[7] In addition to the increased porosity of the Sb/ACNT@tCu film, the thickness also increases from approximately 5.34 µm for the Sb@tCu film to 7.55 µm. These thicknesses were calculated from cross-section SEM images seen in **Figure S3.1** and **Figure S3.2**. The Sb particle size between electrodes decreased from approximately 5 µm in the Sb@tCu films to 100 nm in the Sb/ACNT@tCu. During the co-electrodeposition of Sb with ACNTs, ACNTs are directly deposited on the copper foil as well as on Sb particles that have already plated. We believe the inclusion of ACNTs introduces a wider distribution of nucleation sites due to the increase in surface area after the ACNTs have electrophoretically deposited on the copper foil. This change in particle size is expected to affect the rate capabilities of the Sb anode due to Na^+ diffusion and is not investigated in this report.[7] By analyzing the EDS, shown in **Figure 3.3**, we observe that the

majority of the film's surface is made up of Sb and/or Sb with ACNTs. Significant oxygen inclusion can be attributed to the oxidation of the film's surface to form Sb_2O_3. PXRD patterns of both Sb@tCu and Sb/ACNT@tCu films, **Figure 3.4**, show that the films are overwhelmingly Sb of low crystallinity, as indicated by the broad reflection at 29˚ 2θ. We do not observe the presence of any crystalline oxides, and all peaks can be assigned to Sb or the Cu substrate (**Figure S3.3**). The broad peak can be assigned to the Sb $[10\bar{2}]$, and the breadth of this peak is consistent with strain in the film along this direction preferentially. Strain in electrodeposited films made at room temperature is common. The peak position of this peak relative to that of the same peak observed

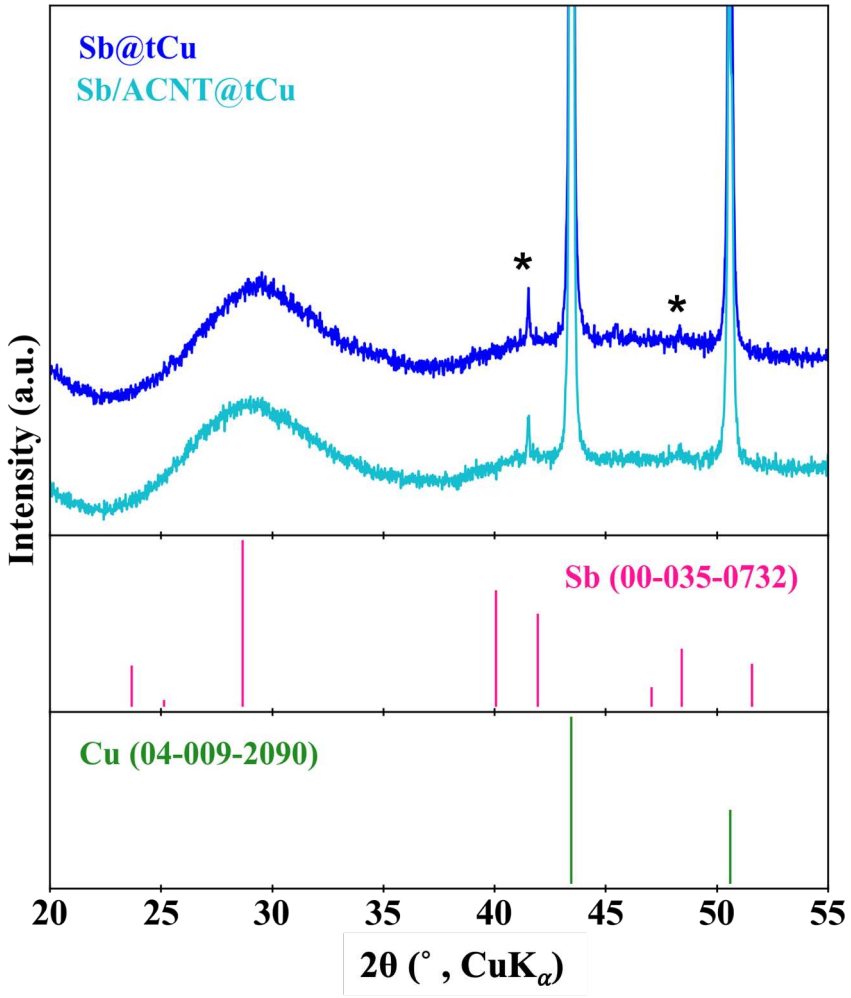

Figure 3.4. PXRD pattern of pre-cycled Sb/ACNT@tCu (blue) and Sb@tCu (cyan). Peaks denoted by asterisks match the XRD pattern for textured copper foil and a pattern can be found in Figure S3.3.

in the slurry casted Sb films (discussed below) suggests that the unit cell is slightly smaller than for the slurry casted Sb, which is consistent with more densely packed Sb and potentially strain.[7] Rietveld refinements for the diffraction patterns seen in **Figure 3.4** can be found in **Figure S3.4**.

The result is potentially significant because the importance of the formation of crystalline or amorphous Sb anodes for NIBs was previously investigated by Yang et al. and it was concluded that after the first cycle Sb remains amorphous.[34] In addition, Allan et al. found that the starting crystalline anode can have implications on the sodiation pathway in the first cycle caused by the shift to overpotentials to break down the crystalline Sb.[18] These discrepancies between amorphous and crystalline anodes were taken into account in the work reported herein, and mechanistic studies were conducted over longer cycle numbers to overcome the large shifts in reaction potentials in the first two cycles.

3.4.2 Electrochemical Performance of Electrodeposited Sb@tCu and Sb/ACNT@tCu in Na-ion Half-Cells

The electrochemical performance of Sb@tCu and Sb/ACNT@tCu in a Na-ion half-cell was first investigated through galvanostatic cycling in a Swagelok with 1M $NaClO_4$ in PC with 5% FEC as the electrolyte. The cycle lifetime and the capacity retention of the electrodeposited films Sb@tCu and Sb/ACNT are shown in **Figure 3.5**. In the first cycle, a significant amount of capacity is lost as it is believed that the first cycle mainly involves the formation of the solid electrolyte interface (SEI).[42] Initially the SEI may serve as a protective layer, but in later cycles leads to capacity fade as the layer is electronically insulating and traps and Na ions, preventing them from entering the anode.[6] Both Sb@tCu and Sb/ACNT@tCu show stable cycling until 50 cycles after which the capacity for the Sb@tCu film quickly diminishes demonstrating how the inclusion of ACNTs has significantly extended the cycle life. This extension in lifetime is crucial

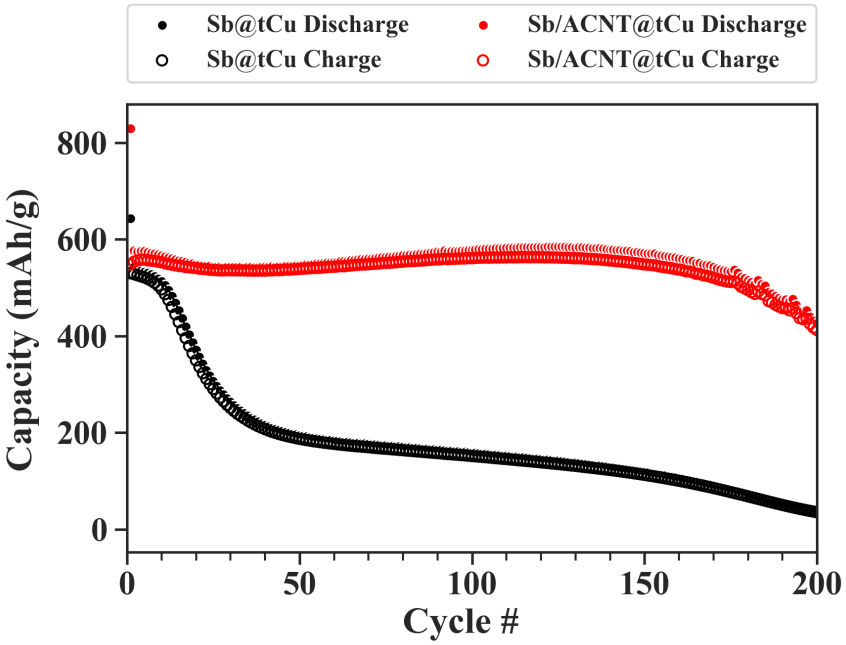

Figure 3.5. Specific Capacity of Sb@tCu and Sb/ACNT@tCu in Na-ion half-cells cycled at 0.1 mA/mg.

for commercialization but also allows for monitoring of significant changes of the electrochemical reactions occurring over time that may provide insight into degradation pathways.

To further compare the performance of Sb@tCu to Sb/ACNT@tCu, differential capacity analysis (DCA) was used to gather information about the sodiation and desodiation events occurring over a potential range. DCA plots represent a fingerprint that highlights cell degradation, failure mechanisms, and changes in chemistry that otherwise might not be seen in a voltage profile or cycle lifetime plots.[43] In **Figure 3.6** four significant sodiation and three desodiation events are present. The number of processes demonstrate complex multistep reactions and intermediate formation that agree with previous studies that focused on the reaction mechanism of Sb-based anodes.[18,23,26] Most studies in the literature show discrepancies between the number of sodiation/desodiation reactions, and assignment of side reactions, with little agreement. Despite these discrepancies, we have postulated the identity of the reactions occurring based on studies

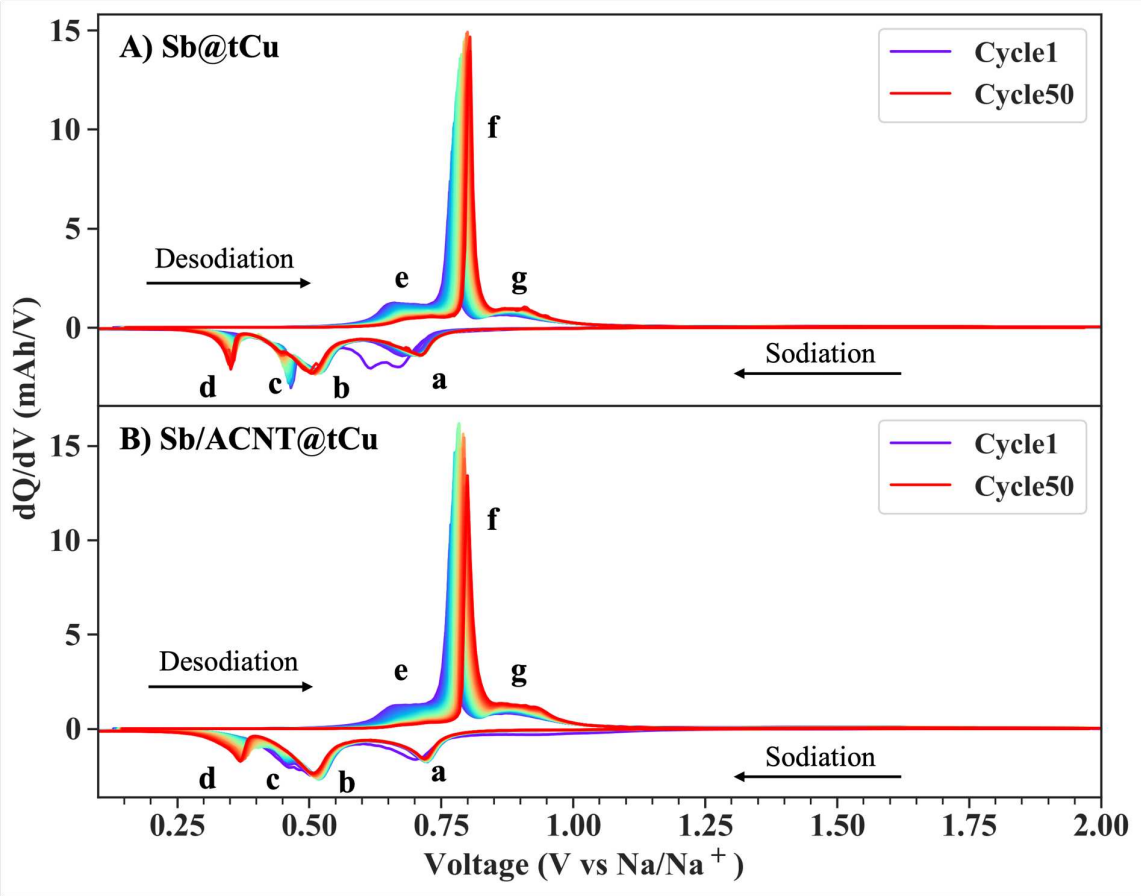

Figure 3.6. Differential capacity plots for both Sb@tCu (A) and Sb/ACNT@tCu (B) cycled at 0.1 mA/mg in a Na-ion half-cell.

closely related to our experimental parameters (**Table 3.1**). Through the DCA plots, it is noted that over time the electrochemical reactions decrease in intensity and begin shifting to overpotentials.

The decrease in intensity of the reactions is due to the loss of active material arising from the volume expansion that Sb-based electrodes experience. In the Sb@tCu film, the diminishing of the peaks occurs much sooner in comparison to the Sb/ACNT@tCu film, and with fewer shifts to overpotentials suggests pulverization and delamination of the film to be the degradation mechanism. Although ACNTs help extend the lifetime by maintaining electronic conductivity and the integrity of the film, more SEI is formed as a result of the increased surface area from the porous nature of the film seen in **Figure 3.3**. This increase in SEI formation leads to overpotentials caused by kinetic limitations induced by the continuous formation of SEI over many cycles and is

Table 3.1. Hypothesized reaction mechanism for the sodiation/desodiation of Sb anodes in Na-ion half-cells ($0<x\leq1\leq y<3$).

Sodiation Reactions (Charging)			**Desodiation Reactions (Discharging)**		
Reaction		V vs Na/Na^+	Reaction		V vs Na/Na^+
a	$Sb + x\ Na^+ \rightarrow Na_xSb$	0.70 V	**e**	$Na_3Sb \rightarrow y\ Na_{3-y}Sb + Na_3Sb$ (hex) + (3-y) Na	0.65 V
b	$Na_xSb + (3-x-y)\ Na^+ \rightarrow Na_xSb + Na_ySb$	0.50 V	**f**	$y\ Na_{3-y}Sb + Na_3Sb$ (hex) $\rightarrow x\ Na_{3-x}Sb$ + (3-x-y) Na	0.77 V
c	$Na_xSb + Na_ySb + (3-x-y)\ Na^+ \rightarrow Na_ySb + Na_3Sb$ (hex)	0.47 V	**g**	$x\ Na_{3-x}Sb \rightarrow Sb + (3-x)\ Na^+$	0.85 V
d	$Na_ySb + (3-y)\ Na^+ \rightarrow Na_3Sb$ (cub &hex)	0.36 V			

suggested to be the main failure mode of Sb/ACNT@tCu films.[7] Electrolyte optimization and its influences on the kinetics of the electrochemical reactions present will be investigated in later studies.

Taking a closer look at the DCA a small broad peak can be seen in the sodiation at 1.0 V vs Na/Na^+ in cycle one and is attributed to the conversion of Sb_2O_3 to Sb. Oxides were shown to be included in the film and its impact on the electrochemical reactions of Sb will be discussed in detail in later sections. The following reaction, Reaction "a", is known to be the initial conversion and sodiation of Sb to Na_xSb ($0<x\leq1$) followed by the continuous sodiation of the intermediate to various Na_ySb ($1<y<3$) phases over the potential ranges of 0.70-0.50 V vs Na/Na^+. In reaction "b", the sodiation of Na_ySb is continued and begins to form the final hexagonal Na_3Sb phase at reaction "c". The final sodiation reaction "d" is not always present in Sb anode reports and at times is ignored because of the low peak intensity. In our electrodeposited films, the final sodiation reaction is readily present and we hypothesize this reaction to be the continued formation of the final sodiated hexagonal Na_3Sb phase, now joined by the formation of the metastable Na_3Sb cubic phase. The metastable Na_3Sb cubic has been seen in very small quantities in previous reports and has been synthesized through solid state methods at high pressures of 10^{-4}-9.0 GPa.[5,24,44,45] We postulate that the formation of the metastable phase may be occurring due to the dense packing of Sb particles (or strain in the film). As mentioned above, the broad peak observed in XRD would

be consistent with a film that was strained prior to cycling. As the majority of the particles begin to sodiate to the final Na_3Sb phase, the internal pressure of the film begins to rise, caused by the particles further pushing against each other which is induced by the volume expansion of the active material. We plan to test this hypothesis in future studies through pressure testing, modeling, and beamline *in situ* XRD experiments. The desodiation process begins with the desodiation of the cubic and hexagonal Na_3Sb phases to the mixture of Na_ySb ($1<y\leq3$) phases and remaining hexagonal Na_3Sb in reaction "e". At 0.77 V vs Na/Na^+, the majority of the film has been desodiated and mainly consists of Na_xSb ($0<x\leq1$) where the desodiation of Sb is believed to be a more spontaneous process than the sodiation and attributes to less distinct processes. The final desodiation step is hypothesized to be the final conversion of Na_xSb ($0<x\leq1$) to amorphous Sb. Although it seems like the predicted sodiation/desodiation mechanism is the same in both Sb@tCu and Sb/ACNT@tCu, there are slight differences in reaction "c", and we have conducted several controls to verify that the electrochemical reactions present were inherent to the innate properties of Sb alone.

3.4.3 Influences of Impurities and Additives on Electrodeposited Sb@tCu and Sb/ACNT@tCu Composite Films

3.4.3.1 Incorporation of ACNTs in Electrodeposited Sb Films

To further understand the sodiation process of Sb/ACNT, a few steps were taken back to solely investigate the sodiation of ACNT. The ACNT thin film was synthesized in a similar fashion as the electrodeposition of Sb/ACNT, except through electrophoretic methods. Using electrophoresis, the positively charged ACNTs were attracted to the negatively biased textured Cu foil and adhered to the surface. To verify that ACNTs were well adhered to the surface of the textured Cu, SEM was conducted. By characterizing the films with SEM, **Figure 3.7**, it was

observed that ACNTs were well dispersed throughout the film and were well adhered even after washing the film. The even dispersion of ACNT was characterized by the web-like features on the textured Cu foil. All cycling parameters were the same as the electrodeposited films to reproduce a similar electrochemical environment. The DCA plot, seen in **Figure 3.7**, verifies that while ACNTs do have some electrochemical activity during the first cycle, all consecutive cycles show a very minimal contribution to the capacity, and it is concluded that ACNTs do not reversibly sodiate in this system.

3.4.3.2 Impact of Sb_2O_3 on Electrodeposited Sb Films

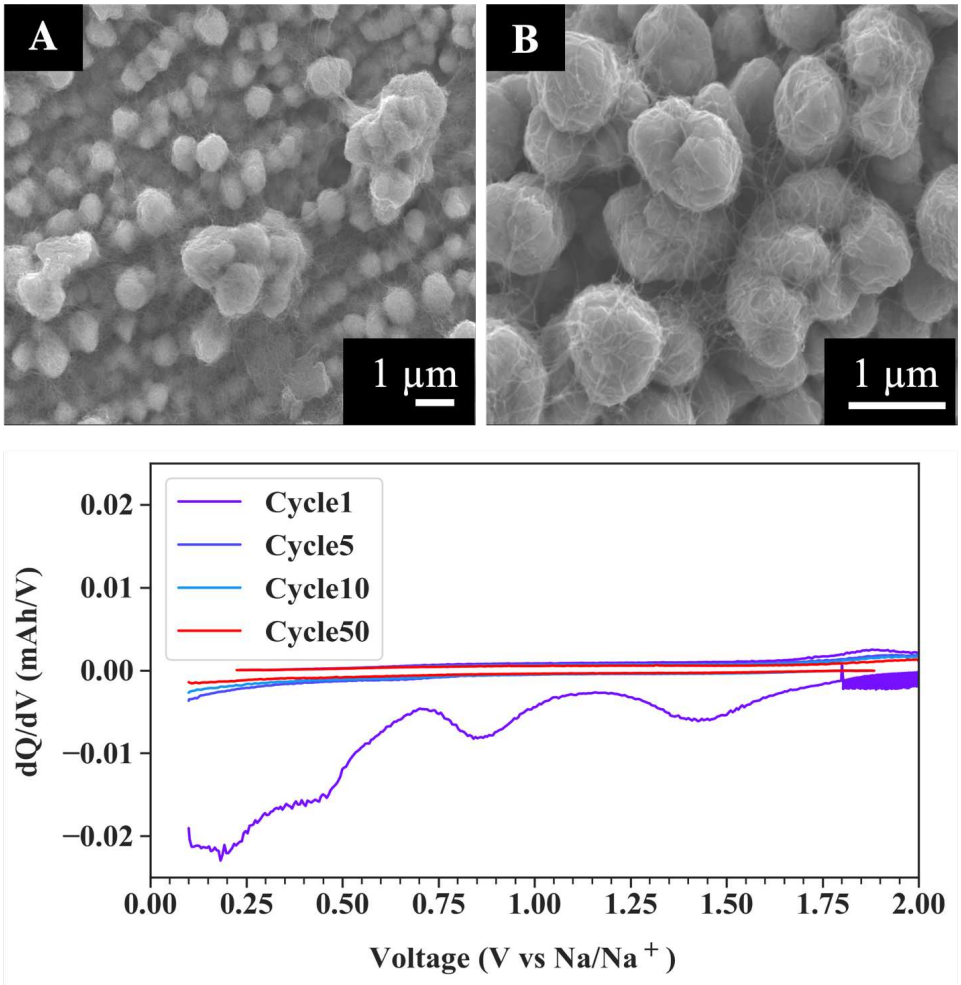

Figure 3.7. SEM images ACNTs electrophoretically deposited on tCu (A-B). Differential capacity plot of ACNT@tCu cycled in a Na-ion half-cell at 0.1 mA/mg in 1M $NaPF_6$ in EC:DEC:DMC with 5% FEC (C).

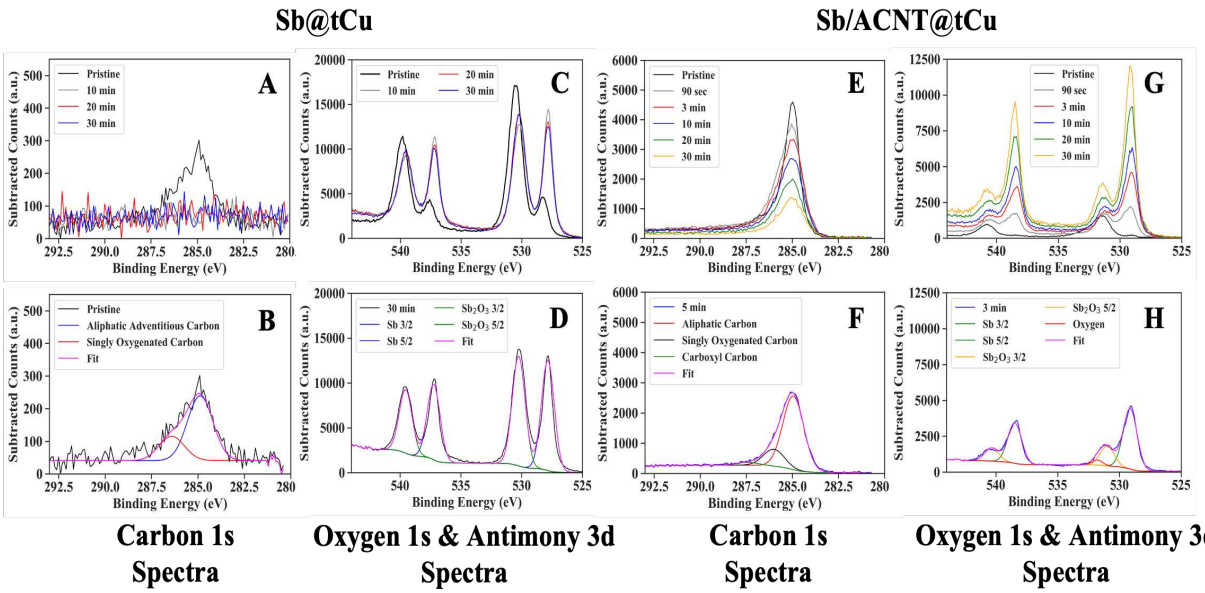

Figure 3.8. XPS of Sb@tCu (left) with the carbon 1s (A,B) and oxygen 1s and antimony 3d spectra (C,D) at different sputtering times. XPS of Sb/ACNT@tCu (right) with the carbon 1s (E,F) and oxygen 1s and antimony 3d spectra (F,H) at different sputtering times. The top row of spectra depict the raw data while the bottom row show the same data with fits.

Carbon 1s XPS spectra shown in **Figure 3.8** indicate that gluconate and CTAB are not significantly included in the electrodeposited films. This is shown by the argon sputtering of the Sb@tCu film not having any carbon signal after the initial adventitious carbon at ~285 eV is removed. The Sb/ACNT@tCu film has carbon present through different times of argon sputtering showing the inclusion of the ACNTs into the film. It is hypothesized that the carbon peak is shrinking over sputter time because the ACNTs sputter away faster than the Sb film. Although electrodeposited Sb films don't include a significant amount of solution additives incorporated in the film, the main impurity present is the incorporation of Sb_2O_3. Through XPS, shown in **Figure 3.8**, Sb_2O_3 3/2 and 5/2 can be seen on the surface of both Sb@tCu and Sb/ACNT@tCu films at 540 and 531 eV respectively. While the Sb^0 concentrations increased as a function of sputter time (Sb 3d 3/2 and 5/2: 537 and 528 eV), oxides are present throughout the bulk of the electrode and the conversion reaction of Sb + Na_2O → Sb_2O_3 can be seen through the DCA shown in **Figure**

3.9B. Although oxides are considered impurities in this study, Sb_2O_3 anodes have been examined for Na-ion battery applications and its inclusion in Sb films has previously been investigated.[46–49] The inclusion of Sb_2O_3 has been seen to be beneficial in terms of capacity and possibly lifetime in other reports, however, our studies focus on understanding the sodiation mechanism of Sb alone.

Table 3.2. Voltage limits for the three conditions tested to control the conversion reactions related to Sb_2O_3.

Condition	Voltage Limits (V vs Na/Na^+)	Cycles
1	0.01 – 2.0 V	1-6
2	0.01 – 2.5 V	7-20
3	0.01 – 1.5 V	21-25

To control and understand the impact of Sb_2O_3 on the reaction mechanism of Sb, we wanted to control or eliminate the presence of Sb_2O_3 in the electrodeposited films. Because these films are deposited in aqueous solutions, in air, it is difficult to control the formation of oxides through this synthetic method and reagents used. Through various studies, researchers have found that the conversion of Sb_2O_3 to Sb and Na_2O occurs at ~1.0 V vs Na/Na^+ and the reformation of Sb_2O_3 from Sb and Na_2O occurs from 1.5-2.5 V vs Na/Na^+.[48] To control the presence of Sb_2O_3 cycling conditions were varied for the same Sb@tCu film in a Na-ion half-cell, **Table 3.2**. The voltage window was varied between three different conditions described in **Table 3.2**. The first condition cycled the cell at a constant current (0.1 mA/mg) from 0.01 – 2.0 V vs Na/Na^+ (regular cycling conditions), then the voltage window was extended to 2.5 V vs Na/Na^+ (Condition 2) to allow for the "complete" conversion of Sb and Na_2O to Sb_2O_3. By extending the upper voltage limit it can be seen in the DCA, shown in **Figure 3.9**, that the conversion reaction from Sb_2O_3 to Sb and Na_2O at 1.0 V vs Na/Na^+ has increased and supports the hypothesis that extending the upper voltage limit does introduce more Sb_2O_3.

The third and final condition decreases the upper voltage limit to 1.5 V vs Na/Na^+ to allow for the complete desodiation of Sb but also prevents the full conversion of Na_2O and Sb to Sb_2O_3. Cycle 22 represents the third cycling condition and the conversion of Sb_2O_3 to Sb at 1.0 V vs Na/Na^+ which decreased significantly. Lowering the upper voltage limit decreases the amount of Sb_2O_3 and provides control on the impact Sb_2O_3 has on the reaction mechanism of electrodeposited Sb films. These voltage control experiments were also conducted on Sb/ACNT@tCu, and similar trends in controlling Sb_2O_3 inclusion can be seen in **Figure S3.5**. Throughout these three cycling conditions the reactions corresponding to the sodiation/desodiation of Sb slightly vary, where the conversion of Sb to Na_xSb in reaction "a" is influenced by the additional conversion of Sb_2O_3 to

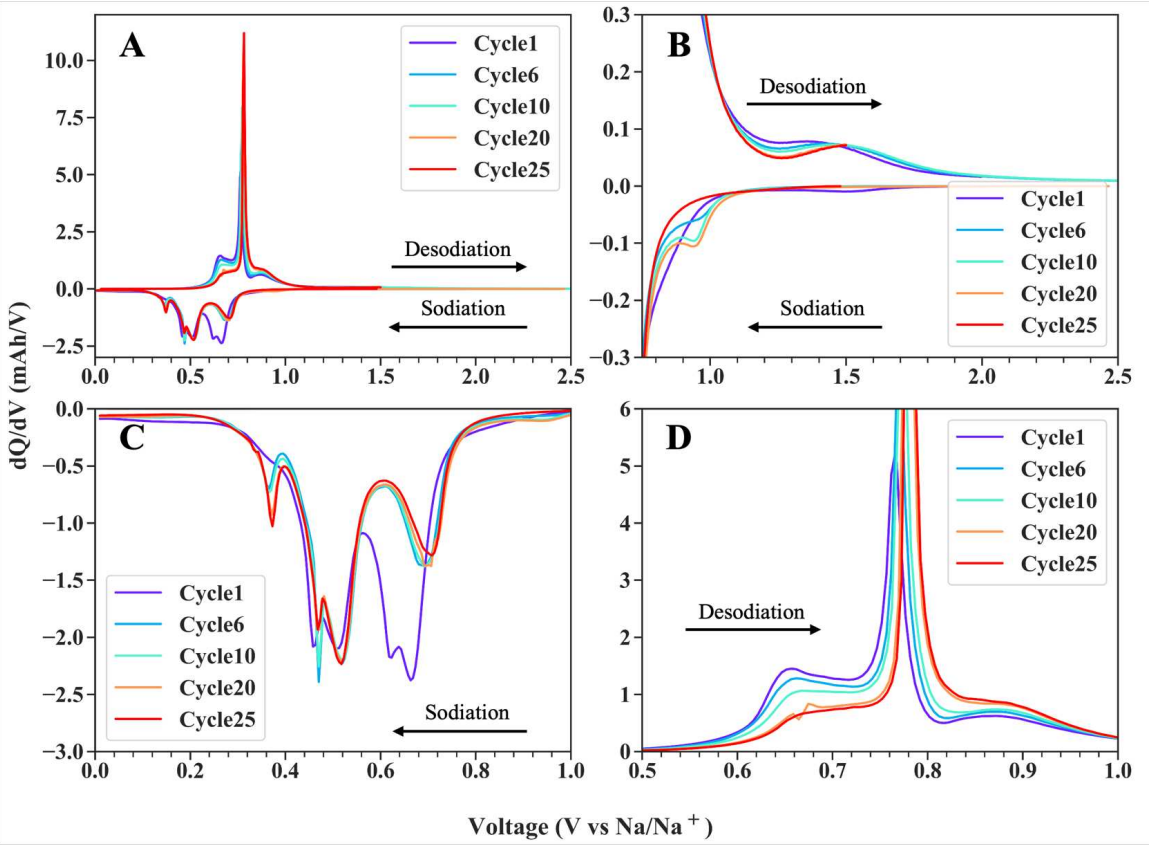

Figure 3.9. Differential capacity plots for Sb@tCu cycled in a Na-ion half-cell cycled at 0.1 mA/mg. (A) demonstrates the complete sodiation/desodiation reactions occurring. While (B) shows a zoomed in look at the conversion of Sb to Sb_2O_3, (C) only shows the sodiation reactions, and (D) shows the desodiation reactions in more detail.

Sb, and the intensity of the peak remains the same from cycles 6-20 and are not brought down by the loss of active material. Reactions "b" and "c" remain unchanged and are thought to be influenced by the previously described degradation mechanism for Sb films. Other significant changes are seen in reaction "d", where the peak increases over cycling. Although this is also a trend when the cell is normally cycled from 0.01-2 V. As previously mentioned, we hypothesized that the fourth reaction could be due to a metastable cubic Na_3Sb phase that has been seen in other studies and has been synthesized through solid state methods under elevated pressures.[44] The increase in intensity of reaction "d" could be due to the additional volume expansion that occurs from the inclusion of unreacted Sb_2O_3 leading to the additional formation of the metastable phase. In addition, increasing the amount of Sb_2O_3 is shown to increase the capacity of both Sb@tCu and Sb/ACNT@tCu in cycles 10 and 20, and the capacity is reduced when the Sb_2O_3 conversion reactions are cut off in cycle 25, seen in the voltage profiles in **Figure S3.6** and **Figure S3.7** for the Sb@tCu and Sb/ACNT@tCu films, respectively. Overall, these cycling conditions demonstrate the ability to "control" the concentration of Sb_2O_3 in the film and its effects on the reaction mechanism of Sb sodiation/desodiation.

3.4.4 Characterization of Slurry Casted Sb Composite Films

To investigate if fabrication methods have a significant influence on the electrochemical reactions of Sb, we fabricated Sb composite films through the commonly used slurry casting method. The slurry casting method typically involves the grinding of active material (Sb), a conductive additive (Super P), and polymeric binder (PVDF, PAA, CMC) at different weight ratios. Then a wetting solvent (NMP, water) is introduced to create a viscous film that can then be cast onto a current collector. Several studies have investigated how different binders and additives can optimize mechanical integrity and rate capabilities, but few have investigated how the

electrochemical reactions of the active material in question are directly influenced by these additives.[50–57]

Two different Sb composites were fabricated through the slurry casting method using two commonly used binders PAA and CMC and Super P as the conductive additive. All slurries were made with a ratio of 70:15:15 wt% of active material, binder, and conductive additive. SEM images, shown in **Figure 3.10**, show a homogenous mixture and dispersion of Sb particles throughout the film that are coated in binder and conductive additive. Some cracks are seen in the CMC based slurry but good adhesion onto the tCu foil was apparent when the films were punched out of the foil and no delamination occurred, shown in **Figure S3.11**. Oxygen is also incorporated in the film and is concentrated on the surface of the Sb particles shown through EDS in **Figure 3.10**. The inclusion of Sb_2O_3 3/2 is minimal at 540 eV in comparison to the electrodeposited films and no Sb^0 is present as seen through XPS in **Figure 3.11**. The limited amount of Sb present means that the components of the slurry cover up the antimony particles. The majority of the XPS signal

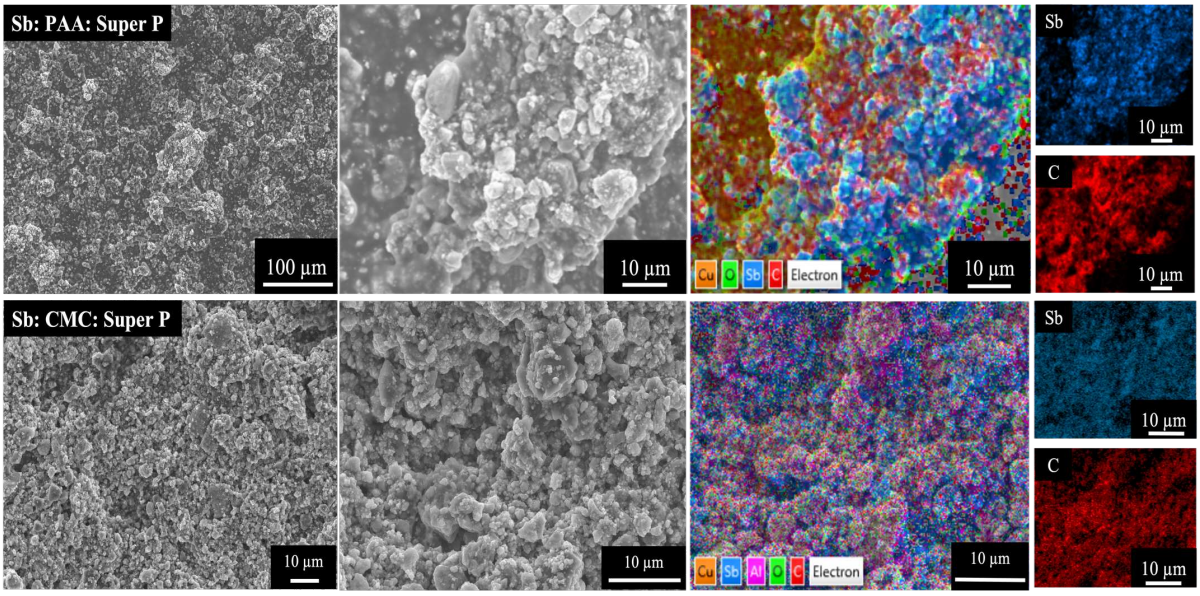

Figure 3.10. SEM images and EDS maps of slurry casted Sb films consisting of Sb:PAA: Super P and Sb:CMC:Super P. Full EDS maps of the Sb:CMC:Super P film are included in Figure S3.9.

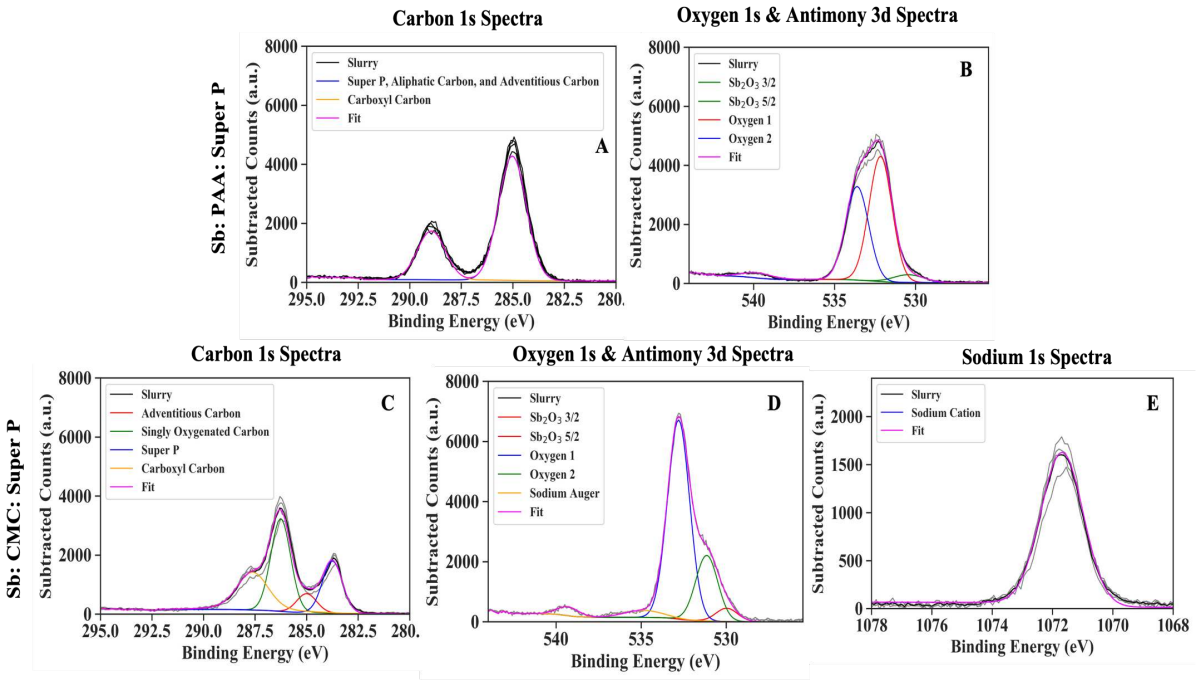

Figure 3.11. Fitted XPS of the Sb:PAA:Super P slurry with carbon 1s (A) and oxygen 1s and antimony 3d environments (B). Fitted XPS of the Sb:CMC:Super P slurry with carbon 1s (C), oxygen 1s and antimony 3d (D) and sodium 1s (E) spectra.

is comprised of the slurry environments. For PAA the carbon and oxygen environments match the O=C and O-C poly carboxyl functional groups of the binder. Na CMC also has appropriate O-C and CO_2 ratios in the carbon and oxygen XPS. XPS also shows the inclusion of sodium cations in the CMC due to the use of the Na CMC salt. To attempt to deconvolute the chemical environments of the slurry by XPS, Na CMC, PAA, and Super P were analyzed individually, these XPS spectra with examples fitting can be found in **Figure S3.10**. Previous work from our group further details how our XPS data is analyzed and fitted.[58,59] Calibration for XPS spectra of slurry casted films is a complicated process as the adventitious aliphatic carbon, which is often used as a self-consistent calibration peak, is difficult to identify in slurry casted films with conductive carbon additives like Super P.[60] This means that clear identification of the starting chemical environments on the surface is muddied and deconvolution of the SEI formed during cycling is nearly impossible.

Using PXRD as a structural characterization method, **Figure 3.12**, Sb in these slurry casted films is crystalline and presents differences in the sodiation potentials of the initial sodiation of Sb in the first cycle due to overpotentials needed to break down the crystalline Sb.[18,34] In addition, the size of the particles in these slurry composites vary in size from 1 to 10 µm and are much larger than the electrodeposited Sb particles but have been significantly reduced from the pristine powder where the largest Sb particles were measured to be approximately 70 µm as seen in the SEM

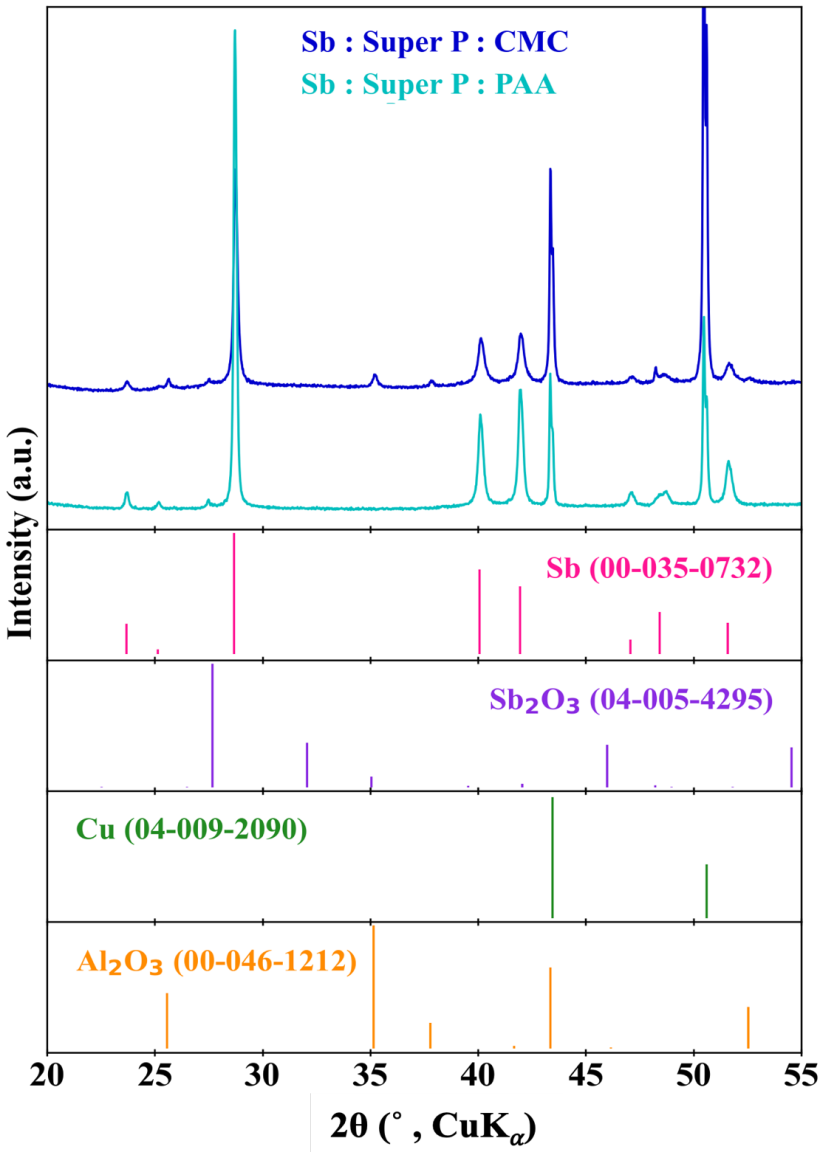

Figure 3.12. PXRD of the slurry casted Sb composites, Sb:PAA:Super P (blue), and Sb:CMC:Super P (cyan).

images of the pristine Sb powder in **Figure S3.8**. The difference in particle size can lead to issues with rate capability due to the longer solid-state diffusion distances the Na ion has to travel. To help reduce kinetic limitations all cells were cycled at 0.1 mA/mg.

3.4.4.1 Electrochemical Performance of Slurry Sb Composite Films in Na-ion Half-Cells

The electrochemical performance of the Sb:PAA:Super P and Sb:CMC:Super P slurries was tested by galvanostatically cycling the films in a Na-ion half-cell with the same electrolyte, and under the same cycling conditions as the Sb@tCu and Sb/ACNT@tCu electrodeposited films. The cycle lifetime and the capacity retention of the slurry casted films are shown in **Figure 3.13**. Both slurry composites had poor cycle life in comparison to the electrodeposited films due to the instability of the slurry casted films. The Sb:PAA:Super P had a very rapid loss in capacity in early cycles and then stabilized at low capacities represented by delamination of the film from the

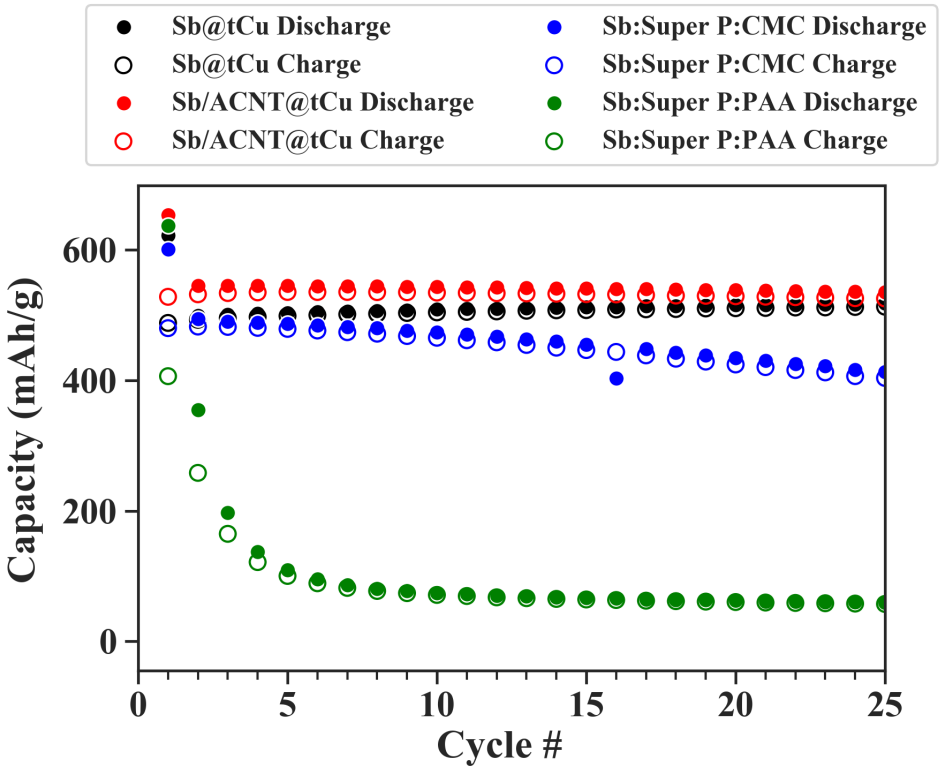

Figure 3.13. Specific capacity electrodeposited Sb@tCu and Sb/ACNT@tCu with the slurry casted Sb composites. All anode films were cycled in a Na-ion half-cell at 0.1 mA/mg..

current collector and/or excessive SEI formation. This delamination was witnessed when the cell was taken apart for *ex situ* studies. Initially, both slurries had good adhesion as evidenced by very little delamination of the film when electrodes were punched out of the foil, **Figure S3.11**. The poor capacity retention is thought to be related to volume expansion of the active material, along with the needed optimization of the electrolyte used. Other reports have reported longer lifetimes with similar composition and fabrication methods but could not be reproduced. Different electrolytes and cycling conditions may also be heavily influencing the performance of specific binders in these anode films.[50–52,56,57]

3.4.5 Influences of Fabrication Method on Sodiation and Desodiation Pathway of Sb Composite Films

Although the slurry casted films have short lifetimes, sufficient cycles were gathered to identify initial electrochemical reactions and how these reactions change over the lifetime of the cell. Initially, when plotting the DCA for the slurry casted films, the DCA showed what is commonly seen in the field, where the sodiation reactions "a-c" were present and reaction "d" was drowned out by the intensity of the peaks around it, seen in **Figure S3.12**. The drowning out of reaction "d" is similar to the Sb_2O_3 conversion reactions discussed previously and demonstrates a need to carefully plot DCA plots at different voltages and intensities. Without careful plotting of DCA many sodiation/desodiation reactions could be ignored and the understanding of these processes would be incomplete.

By taking a closer look at the differential capacity plots in **Figure 3.14**, significant differences in the sodiation and desodiation reactions. In both slurries, the first cycle is dominated by one reaction process at 0.50 V and 0.40 V vs Na/Na^+, for the Sb:CMC:Super P and Sb:PAA:Super P, respectively. This process is representative of the initial breakdown and

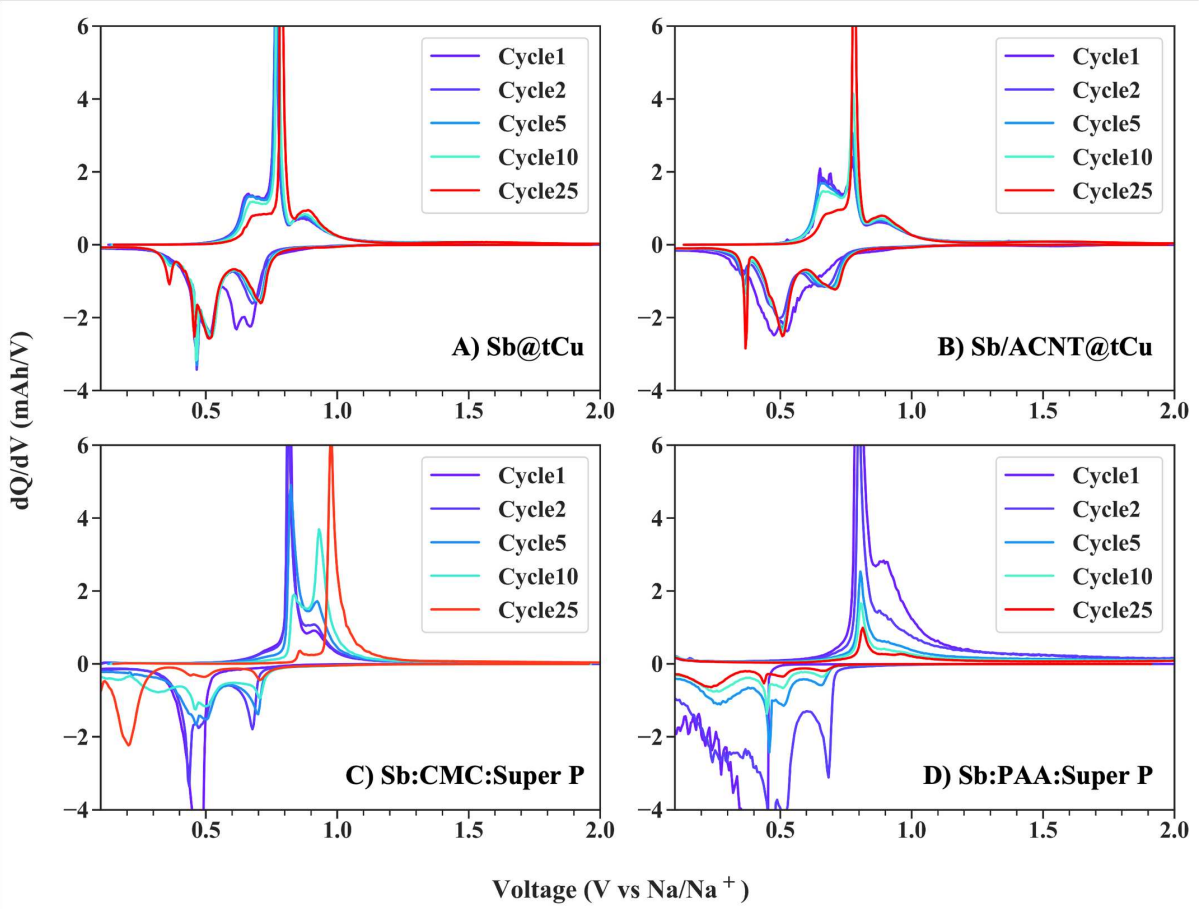

Figure 3.14. Differential capacity plots for electrodeposited Sb@tCu (A), and Sb/ACNT@tCu (B), and slurry casted Sb:CMC:Super P (C), and Sb:PAA: Super P (D). All anodes were cycled in a Na-ion half-cell cycled at 0.1 mA/mg.

sodiation of crystalline Sb.[18] Upon later cycles, this single process separates to form multistep processes that resemble the sodiation processes in the electrodeposited films. For the sodiation reactions in the slurry casted films, reactions "a-c" can be identified clearly after the initial cycle, and the potentials at which they occur closely match the potentials for the electrodeposited films. One significant difference to note is reaction "d", where this reaction occurs soon after reaction "c" and at ~0.36 V vs Na/Na^+ in the electrodeposited films. In the slurry casted films, it is difficult to determine if this reaction is even occurring, or if it has just been shifted to considerable overpotentials when all other reactions are at similar potentials to the electrodeposited films. To

determine if this reaction is related to the final sodiation of Sb or the components of the composite, several controls were conducted on the individual components of the slurry.

To test if the conductive additive had a significant influence on the electrochemical reactions a composite was casted composed of a 50:50 wt% of Super P:PAA. In addition, PAA and CMC were casted onto tCu by suspending the individual binders in their respective solvent and creating a viscous mixture. These controls were galvanostatically cycled under the same cycling parameters previously mentioned and with the same electrolyte. In the DCA plot of Super P in **Figure 3.15A**, it is shown that Super P does sodiate at a range from 0.50-0.10 V vs Na/Na^+. This reaction appears to be slightly reversible and is due to the storage of sodium in graphite interlayers. These results are validated by other studies that also report the sodiation of Super P.[61,62] The sodiation of Super P at these potentials could be the identity of the broad final sodiation peak at ~0.5 V vs Na/Na^+ in both Sb:CMC:Super P and Sb:PAA:Super P composites. The DCA plots of PAA and CMC, shown in **Figure 3.15B** and **Figure 3.15C**, show that the binders do not sodiate but are electrochemically active in the electrolyte used. In cycle 1, both binders exhibit electrochemical reactions that could be from the initial formation of SEI through the reduction of the electrolyte. These findings testify to the complexity that arises from the inclusion of conductive additives and binders in slurry composites. This complexity can lead to the misidentification of

electrochemical processes and can inhibit the understanding of the sodiation/desodiation reactions for electrode materials.

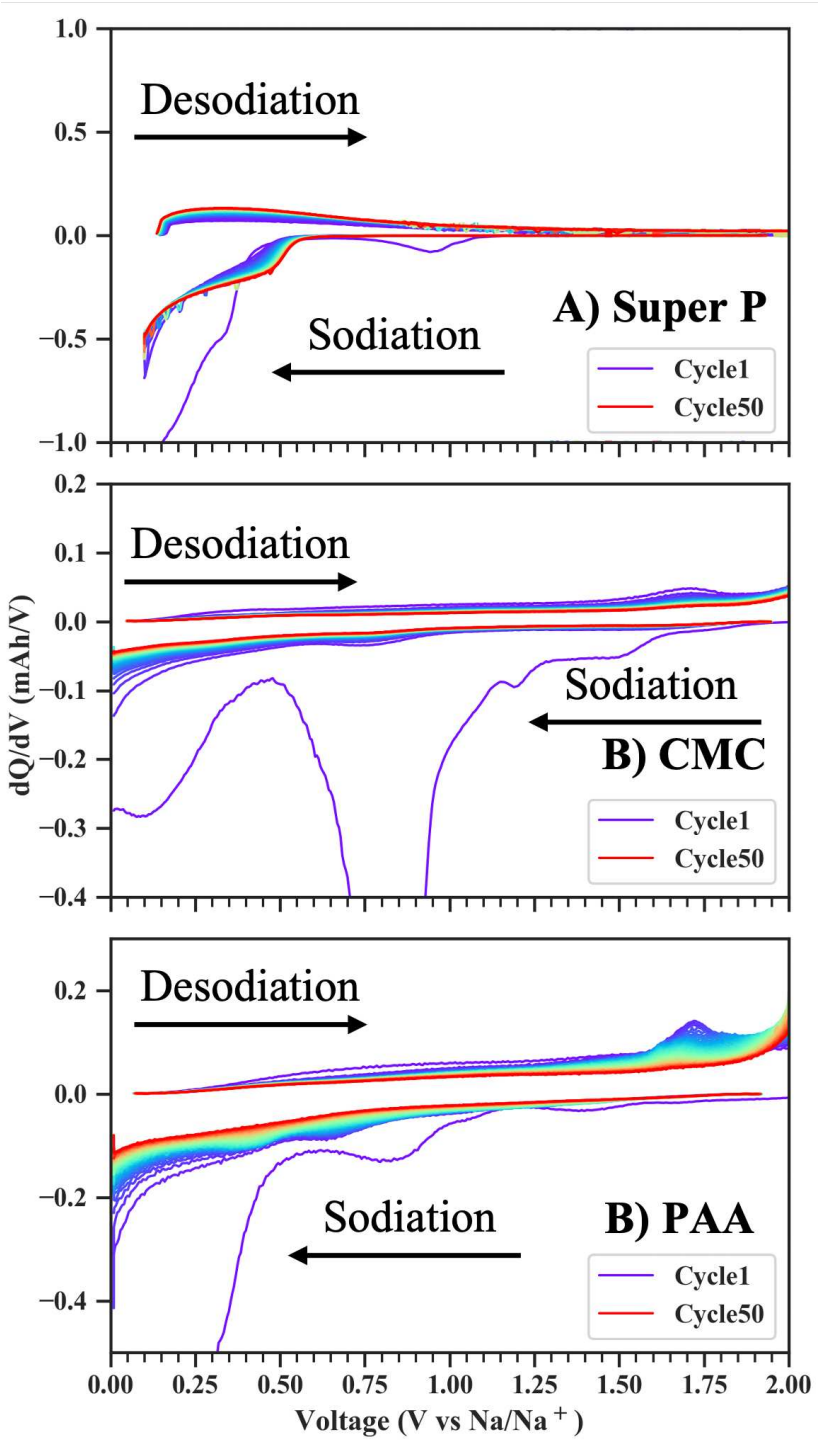

Figure 3.15. DCA plots of slurry casted controls. A 50/50 wt% composite of Super P and PAA (a), a 100 wt% PAA composite (b), and a 100 wt% CMC composite (c). All cells were cycled at 0.1 mA/mg in a Na-ion half-cell.

From the implications introduced by the slurry composite controls, we have predicted that the final sodiation reaction in the electrodeposited Sb@tCu and Sb/ACNT@tCu are related to the continued formation of hexagonal Na_3Sb alongside the formation of the metastable cubic Na_3Sb phase due to internal stress and pressure that occurs with the sodiation of Sb. We hypothesize that the pressures needed to access the metastable phase occur in the electrodeposited films due to the dense packing of Sb particles. These elevated pressures may not be obtainable in the slurry casted films as Sb particles are dispersed in the polymeric binder matrix and are not as densely packed. In addition, the first desodiation reaction is believed to be related to the desodiation of the cubic Na_3Sb phase and initial desodiation of the hexagonal Na_3Sb phase and does not occur in the slurry casted films.

3.5 Conclusion

To aid in the fundamental understanding of the complex sodiation/desodiation mechanism of Sb in Na-ion cells, we have described the impact film composition and fabrication methods have on the electrochemical reactions present while cycling. In this study, the analysis of cycling performance and DCA plots showed that the sodiation of Sb is complex and can easily be influenced by the composition of the film. In slurry casted Sb composites, the lifetime was significantly shorter due to delamination and pulverization of the film and possibly an increase in the SEI. Although the lifetime was short the reaction mechanism was still analyzed for the first 25 cycles through DCA, and significant differences were noted between the slurry casted composites and the electrodeposited films. The slurry composite films consisted of large, dispersed Sb particles, a carbon conductive additive (Super P), and a polymeric binder (CMC or PAA). Through these studies, it was confirmed that Super P does sodiate and complicates the accurate assignment of reactions at specific voltages. In addition, the polymeric binders were seen to be

electrochemically active and decomposed into the SEI during the first cycle, leading to additional polarization of the sodiation and desodiation of Sb.

In contrast, the electrodeposited Sb composites demonstrated how this fabrication technique allows for the control of particle size, morphology, porosity, and composition. Through electrodeposition, Sb is well adhered to the current collector and allows for longer cycle life. In addition, this technique allows for the co-deposition of Sb with conductive additives (ACNTs), while preventing other complexing agents in solution from depositing, allowing for a film mainly composed of Sb and/or Sb/ACNTs. Although Sb_2O_3 is incorporated in these films, it was demonstrated that conversion reactions of Sb_2O_3 can easily be separated from Sb, and the voltage window for cycling these cells can be modified to prevent the conversion of Sb to Sb_2O_3. Through DCA, hypothesized reactions could be assigned without convolution from additives and binders as ACNTs do not sodiate. When comparing the DCA of electrodeposited and slurry casted composites, significant differences were noted in the final sodiation reaction and the first desodiation reaction. These reactions are always present in the electrodeposited films examined in this study and are rarely reported in the literature. Although the slurry casted films show some activity at lower potentials, it is difficult to accurately determine what reactions are occurring due to the composition of the films and the complications due to binders. The final sodiation reaction is hypothesized to be the final conversion to Na_3Sb but may be the metastable cubic phase due to increased strain within in the film caused by volume expansion that could create enough pressure to access the metastable phase. We hypothesize that the formation of the metastable cubic Na_3Sb phase may be present in our electrodeposited films due to the dense packing of Sb particles, where the volume expansion upon sodiation may lead to sufficient pressure within the film to allow access to the metastable phase.

Overall, these studies have demonstrated the viability of electrodeposition as a fabrication method, and how it can provide significant control on the composition, and morphology, of the film. This synthetic control can lead to the detailed, systematic investigation of the sodiation/desodiation reaction mechanisms and other parameters, such as electrolyte composition, and SEI studies, without having to worry about the influences of binders and other conductive additives. These studies and fabrication technique will not only benefit Sb-based anodes but will also lead to better fundamental studies and processing of anode materials and electrolytes for lithium and beyond lithium technologies.

3.6 References

(1) Li, L.; Zheng, Y.; Zhang, S.; Yang, J.; Shao, Z.; Guo, Z. Recent Progress on Sodium Ion Batteries: Potential High-Performance Anodes. *Energy Env. Sci* **2018**, *11*, 2310. https://doi.org/10.1039/c8ee01023d.

(2) Hirsh, H. S.; Li, Y.; Tan, D. H. S.; Zhang, M.; Zhao, E.; Meng, Y. S. Sodium-Ion Batteries Paving the Way for Grid Energy Storage. *Adv. Energy Mater.* **2020**, *10* (32). https://doi.org/10.1002/aenm.202001274.

(3) Sawicki, M.; Shaw, L. L. Advances and Challenges of Sodium Ion Batteries as Post Lithium Ion Batteries. *RSC Adv.* **2015**, *5* (65), 53129–53154. https://doi.org/10.1039/c5ra08321d.

(4) Liang, S.; Cheng, Y. J.; Zhu, J.; Xia, Y.; Müller-Buschbaum, P. A Chronicle Review of Nonsilicon (Sn, Sb, Ge)-Based Lithium/Sodium-Ion Battery Alloying Anodes. *Small Methods* **2020**, *2000218*. https://doi.org/10.1002/smtd.202000218.

(5) Darwiche, A.; Marino, C.; Sougrati, M. T.; Fraisse, B.; Stievano, L.; Monconduit, L. Better Cycling Performances of Bulk Sb in Na-Ion Batteries Compared to Li-Ion Systems: An Unexpected Electrochemical Mechanism. *J. Am. Chem. Soc.* **2012**, *134*, 20805–20811. https://doi.org/10.1021/ja310347x.

(6) He, J.; Wei, Y.; Zhai, T.; Li, H. Antimony-Based Materials as Promising Anodes for Rechargeable Lithium-Ion and Sodium-Ion Batteries. *Mater Chem Front* **2018**, *2*, 437. https://doi.org/10.1039/c7qm00480j.

(7) Schulze, M. C.; Belson, R. M.; Kraynak, L. A.; Prieto, A. L. Electrodeposition of Sb/CNT Composite Films as Anodes for Li- and Na-Ion Batteries. *Energy Storage Mater.* **2020**, *25*, 572–584. https://doi.org/10.1016/j.ensm.2019.09.025.

(8) Liu, H.; Wang, Z.; Wu, Z.; Zhang, S.; Ge, S.; Guo, P.; Hua, M.; Lu, X.; Wang, S.; Zhang, J. Direct Tuning of Meso-/Micro-Porous Structure of Carbon Nanofibers Confining Sb Nanocrystals for Advanced Sodium and Potassium Storage. *J. Alloys Compd.* **2020**, *833*. https://doi.org/10.1016/j.jallcom.2020.155127.

(9) Yuan, Y.; Jan, S.; Wang, Z.; Jin, X. A Simple Synthesis of Nanoporous Sb/C with High Sb Content and Dispersity as an Advanced Anode for Sodium Ion Batteries. *J Mater Chem A* **2018**, *6*, 5555–5559. https://doi.org/10.1039/c8ta00592c.

(10) Zhu, Y.; Han, X.; Xu, Y.; Liu, Y.; Zheng, S.; Xu, K.; Hu, L.; Wang, C. Electrospun Sb/C Fibers for a Stable and Fast Sodium-Ion Battery Anode. *ACS Nano* **2013**, *7* (7), 6378–6386. https://doi.org/10.1021/nn4025674.

(11) Dugas, R.; Ponrouch, A.; Gachot, G.; David, R.; Palacin, M. R.; Tarascon, J. M. Na Reactivity toward Carbonate-Based Electrolytes: The Effect of FEC as Additive. *J. Electrochem. Soc.* **2016**, *163* (10), A2333–A2339. https://doi.org/10.1149/2.0981610jes.

(12) Bian, X.; Dong, Y.; Zhao, D.; Ma, X.; Qiu, M.; Xu, J.; Jiao, L.; Cheng, F.; Zhang, N. Microsized Antimony as a Stable Anode in Fluoroethylene Carbonate Containing Electrolytes for Rechargeable Lithium-/ Sodium-Ion Batteries. *ACS Appl Mater Interfaces* **2020**, *12*, 3562. https://doi.org/10.1021/acsami.9b18006.

(13) Bodenes, L.; Darwiche, A.; Monconduit, L.; Martinez, H. The Solid Electrolyte Interphase a Key Parameter of the High Performance of Sb in Sodium-Ion Batteries: Comparative X-Ray Photoelectron Spectroscopy Study of Sb/Na-Ion and Sb/Li-Ion Batteries. *J. Power Sources* **2015**, *273*, 14–24. https://doi.org/10.1016/j.jpowsour.2014.09.037.

(14) Baggetto, L.; Ganesh, P.; Sun, C.-N.; Meisner, R. A.; Zawodzinski, T. A.; Veith, G. M. Intrinsic Thermodynamic and Kinetic Properties of Sb Electrodes for Li-Ion and Na-Ion Batteries: Experiment and Theory. *J. Mater. Chem. A* **2013**, *1*, 7985–7994. https://doi.org/10.1039/c3ta11568b.

(15) Ji, L.; Gu, M.; Shao, Y.; Li, X.; Engelhard, M. H.; Arey, B. W.; Wang, W.; Nie, Z.; Xiao, J.; Wang, C.; Zhang, J.-G.; Liu, J. Controlling SEI Formation on SnSb-Porous Carbon Nanofibers for Improved Na Ion Storage. *Adv. Mater.* **2014**, *26* (18), 2901–2908. https://doi.org/10.1002/adma.201304962.

(16) Gutierrez-Kolar, J. S.; Baggetto, L.; Sang, X.; Shin, D.; Yurkiv, V.; Mashayek, F.; Veith, G. M.; Shahbazian-Yassar, R.; Unocic, R. R. Interpreting Electrochemical and Chemical Sodiation Mechanisms and Kinetics in Tin Antimony Battery Anodes Using in Situ Transmission Electron Microscopy and Computational Methods. *Appl. Energy Mater.* **2019**, *2*, 3578–3586. https://doi.org/10.1021/acsaem.9b00310.

(17) Baggetto, L.; Hah, H.-Y.; Jumas, J.-C.; Johnson, C. E.; Johnson, J. A.; Keum, J. K.; Bridges, C. A.; Veith, G. M. The Reaction Mechanism of SnSb and Sb Thin Film Anodes for Na-Ion Batteries Studied by X-Ray Diffraction, ^{119}Sn and ^{121}Sb Mössbauer Spectroscopies. *J. Power Sources* **2014**, *267*, 329–336. https://doi.org/10.1016/J.JPOWSOUR.2014.05.083.

(18) Allan, P. K.; Griffin, J. M.; Darwiche, A.; Borkiewicz, O. J.; Wiaderek, K. M.; Chapman, K. W.; Morris, A. J.; Chupas, P. J.; Monconduit, L.; Grey, C. P. Tracking Sodium-Antimonide Phase Transformations in Sodium-Ion Anodes: Insights from Operando Pair Distribution Function Analysis and Solid-State NMR Spectroscopy. *J. Am. Chem. Soc.* **2016**, *138* (7), 2352–2365. https://doi.org/10.1021/jacs.5b13273.

(19) Ma, W.; Wang, J.; Gao, H.; Niu, J.; Luo, F.; Peng, Z.; Zhang, Z. A Mesoporous Antimony-Based Nanocomposite for Advanced Sodium Ion Batteries. *Energy Storage Mater.* **2018**, *13*, 247–256. https://doi.org/10.1016/j.ensm.2018.01.016.

(20) Kong, B.; Zu, L.; Peng, C.; Zhang, Y.; Zhang, W.; Tang, J.; Selomulya, C.; Zhang, L.; Chen, H.; Wang, Y.; Liu, Y.; He, H.; Wei, J.; Lin, X.; Luo, W.; Yang, J.; Zhao, Z.; Liu, Y.; Yang, J.; Zhao, D. Direct Superassemblies of Freestanding Metal−Carbon Frameworks Featuring Reversible Crystalline-Phase Transformation for Electrochemical Sodium Storage. *J Am Chem Soc* **2016**, *12*, 23. https://doi.org/10.1021/jacs.6b10782.

(21) Zhang, H.; An, W.; Song, H.; Xiang, B.; Mei, S.; Hu, Y.; Gao, B. Synthesis of Micro-Sized Porous Antimony via Vapor Dealloying for High-Performance Na-Ion Battery Anode. *Solid State Ion.* **2020**, *352*. https://doi.org/10.1016/j.ssi.2020.115365.

(22) Liang, L.; Xu, Y.; Wang, C.; Wen, L.; Fang, Y.; Mi, Y.; Zhou, M.; Zhao, H.; Lei, Y. Large-Scale Highly Ordered Sb Nanorod Array Anodes with High Capacity and Rate Capability for Sodium-Ion Batteries. *Energy Environ. Sci.* **2015**, *8* (10), 2954–2962. https://doi.org/10.1039/c5ee00878f.

(23) Li, Z.; Tan, X.; Li, P.; Kalisvaart, P.; Janish, M. T.; Mook, W. M.; Luber, E. J.; Jungjohann, K. L.; Carter, C. B.; Mitlin, D. Coupling In Situ TEM and Ex Situ Analysis to Understand Heterogeneous Sodiation of Antimony. *Nano Lett.* **2015**, *15* (10), 6339–6348. https://doi.org/10.1021/acs.nanolett.5b03373.

(24) Sauban Ere, M.; Yahia, B.; Ed Eric Lemoigno, F.; Doublet, M.-L. Influence of Polymorphism on the Electrochemical Behavior of M_xSb Negative Electrodes in Li/Na Batteries. *J. Power Sources* **2015**, *280*, 695–702. https://doi.org/10.1016/j.jpowsour.2015.01.093.

(25) Caputo, R. An Insight into Sodiation of Antimony from First-Principles Crystal Structure Prediction. *Electron. Mater.* **2016**, *45* (2), 999–1010. https://doi.org/10.1007/s11664-015-4260-0.

(26) Choi, Y.-S.; Lee, J.-C. Characterizing Multiple Continuous Phase Transitions at an Alloying Anode with Voltammetric Measurements and First-Principles Calculations. *J. Mater. Chem. A* **2019**, *7*, 23121–23129. https://doi.org/10.1039/c9ta07199g.

(27) Choi, Y.-S.; Lee, J.-C. Continuous/Reversible Phase Transition Behaviors and Their Effect on the Hysteresis Energy Loss of the Anodes in Na-Ion Batteries. *Electrochimica Acta* **2019**, *328*, 135106–135117. https://doi.org/10.1016/J.ELECTACTA.2019.135106.

(28) Liu, C.; Neale, Z. G.; Cao, G. Understanding Electrochemical Potentials of Cathode Materials in Rechargeable Batteries. *Mater. Today* **2016**, *19* (2), 109–123. https://doi.org/10.1016/j.mattod.2015.10.009.

(29) Wu, C. M.; Pan, P. I.; Cheng, Y. W.; Liu, C. P.; Chang, C. C.; Avdeev, M.; Lin, S. kang. The Mechanism of the Sodiation and Desodiation in Super P Carbon Electrode for Sodium-Ion Battery. *J. Power Sources* **2017**, *340*, 14–21. https://doi.org/10.1016/j.jpowsour.2016.11.048.

(30) Nagulapati, V. M.; Yoon, Y. H.; Kim, D. S.; Kim, H.; Lee, W. S.; Lee, J. H.; Kim, K. H.; Hur, J.; Kim, I. T.; Lee, S. G. Effect of Binders and Additives to Tailor the Electrochemical Performance of Sb₂Te₃-TiC Alloy Anodes for High-Performance Sodium-Ion Batteries. *J. Ind. Eng. Chem.* **2019**, *76*, 419–428. https://doi.org/10.1016/j.jiec.2019.04.008.

(31) Nagulapati, V. M.; Kim, D. S.; Oh, J.; Lee, J. H.; Hur, J.; Kim, I. T.; Lee, S. G. Enhancing the Electrochemical Performance of SbTe Bimetallic Anodes for High-Performance Sodium-Ion Batteries: Roles of the Binder and Carbon Support Matrix. *Nanomaterials* **2019**, *9* (8), 1–17. https://doi.org/10.3390/nano9081134.

(32) Piernas-Muñoz, M. J.; Castillo-Martínez, E.; Gómez-Cámer, J. L.; Rojo, T. Optimizing the Electrolyte and Binder Composition for Sodium Prussian Blue, $Na_{1-x}Fe_{x+(1/3)}(CN)_6 \cdot yH_2O$, as Cathode in Sodium Ion Batteries. *Electrochimica Acta* **2016**, *200*, 123–130. https://doi.org/10.1016/j.electacta.2016.02.188.

(33) Vogt, L. O.; El Kazzi, M.; Jämstorp Berg, E.; Pérez Villar, S.; Novák, P.; Villevieille, C. Understanding the Interaction of the Carbonates and Binder in Na-Ion Batteries: A Combined Bulk and Surface Study. *Chem. Mater.* **2015**, *27* (4), 1210–1216. https://doi.org/10.1021/cm5039649.

(34) Yang, Y.; Yang, X.; Zhang, Y.; Hou, H.; Jing, M.; Zhu, Y.; Fang, L.; Chen, Q.; Ji, X. Cathodically Induced Antimony for Rechargeable Li-Ion and Na-Ion Batteries: The Influences of Hexagonal and Amorphous Phase. *J. Power Sources* **2015**, *282*, 358–367. https://doi.org/10.1016/j.jpowsour.2015.02.071.

(35) Gimble, N. J.; Nieto, K.; Prieto, A. L. Electrodeposition as a Powerful Tool for the Fabrication and Characterization of Next-Generation Anodes for Sodium Ion Rechargeable Batteries. *Electrochem. Soc. Interface* **2021**, *30* (1), 59–63. https://doi.org/10.1149/2.F09211IF.

(36) Ma, J.; Prieto, A. L. Electrodeposition of Pure Phase SnSb Exhibiting High Stability as a Sodium-Ion Battery Anode. *Chem. Commun.* **2019**, *55* (48), 6938–6941. https://doi.org/10.1039/c9cc00001a.

(37) Mosby, J. M.; Prieto, A. L. Direct Electrodeposition of Cu_2Sb for Lithium-Ion Battery Anodes. *J. Am. Chem. Soc.* **2008**, *130* (32), 10656–10661. https://doi.org/10.1021/ja801745n.

(38) Jackson, E. D.; Prieto, A. L. Copper Antimonide Nanowire Array Lithium Ion Anodes Stabilized by Electrolyte Additives. *ACS Appl Mater Interfaces* **2016**, *8*, 30379–30386. https://doi.org/10.1021/acsami.6b08033.

(39) Schulze, M. C.; Schulze, R. K.; Prieto, A. L. Electrodeposited Thin-Film Cu_xSb Anodes for Li-Ion Batteries: Enhancement of Cycle Life via Tuning of Film Composition and Engineering of the Film-Substrate Interface. *J. Mater. Chem. A* **2018**, *6*, 12708. https://doi.org/10.1039/c8ta01798k.

(40) Sawyer, D. T. METAL-GLUCONATE COMPLEXES. *Chem. Rev.* **1964**, *64* (6), 633–643.

(41) Hwang, J.-Y.; Myung, S.-T.; Sun, Y.-K. Sodium-Ion Batteries: Present and Future. *Chem. Soc. Rev.* **2017**, *46* (12), 3529–3614. https://doi.org/10.1039/C6CS00776G.

(42) Ma, J.; Prieto, A. L. Electrodeposition of Pure Phase SnSb Exhibiting High Stability as a Sodium-Ion Battery Anode. *Chem. Commun.* **2019**, *55* (48), 6938–6941. https://doi.org/10.1039/C9CC00001A.

(43) Guena, T.; Leblanc, P. How Depth of Discharge Affects the Cycle Life of Lithium-Metal-Polymer Batteries. *INTELEC Int. Telecommun. Energy Conf. Proc.* **2006**. https://doi.org/10.1109/INTLEC.2006.251641.

(44) Leonova, M. E.; Bdikin, I. K.; Kulinich, S. A.; Gulish, O. K.; Sevast'yanova, L. G.; Burdina, K. P. High-Pressure Phase Transition of Hexagonal Alkali Pnictides. *Inorg. Mater.* **2003**, *39* (3), 332–336. https://doi.org/10.1023/A.

(45) Beutl, A.; Cupid, D.; Flandorfer, H. The Li-Sb Phase Diagram Part I: New Experimental Results. *J. Alloys Compd.* **2017**, *695*, 1052–1060. https://doi.org/10.1016/j.jallcom.2016.10.230.

(46) Pan, J.; Wang, N.; Zhou, Y.; Yang, X.; Zhou, W.; Qian, Y.; Yang, J. Simple Synthesis of a Porous Sb/Sb_2O_3 Nanocomposite for a High-Capacity Anode Material in Na-Ion Batteries. *Nano Res.* **2017**, *10* (5), 1794–1803. https://doi.org/10.1007/s12274-017-1501-y.

(47) Ma, W.; Wang, J.; Gao, H.; Niu, J.; Luo, F.; Peng, Z.; Zhang, Z. A Mesoporous Antimony-Based Nanocomposite for Advanced Sodium Ion Batteries. *Energy Storage Mater.* **2018**, *13* (January), 247–256. https://doi.org/10.1016/j.ensm.2018.01.016.

(48) Li, X.; Qu, J.; Xie, H.; Song, Q.; Fu, G.; Yin, H. An Electro-Deoxidation Approach to Co-Converting Antimony Oxide/ Graphene Oxide to Antimony/Graphene Composite for Sodium-Ion Battery Anode. *Electrochimica Acta* **2020**, No. 332, 135501. https://doi.org/10.1016/j.electacta.2019.135501.

(49) Li, D.; Yan, D.; Ma, J.; Qin, W.; Zhang, X.; Lu, T.; Pan, L. One-Step Microwave-Assisted Synthesis of Sb₂O₃/Reduced Graphene Oxide Composites as Advanced Anode Materials for Sodium-Ion Batteries. *Ceram. Int.* **2016**, *42* (14), 15634–15642. https://doi.org/10.1016/j.ceramint.2016.07.017.

(50) Chou, S. L.; Pan, Y.; Wang, J. Z.; Liu, H. K.; Dou, S. X. Small Things Make a Big Difference: Binder Effects on the Performance of Li and Na Batteries. *Phys. Chem. Chem. Phys.* **2014**, *16* (38), 20347–20359. https://doi.org/10.1039/c4cp02475c.

(51) Bommier, C.; Ji, X. Electrolytes, SEI Formation, and Binders: A Review of Nonelectrode Factors for Sodium-Ion Battery Anodes. *Small* **2018**, *14* (16), 1–20. https://doi.org/10.1002/smll.201703576.

(52) Dahbi, M.; Nakano, T.; Yabuuchi, N.; Ishikawa, T.; Kubota, K.; Fukunishi, M.; Shibahara, S.; Son, J. Y.; Cui, Y. T.; Oji, H.; Komaba, S. Sodium Carboxymethyl Cellulose as a Potential Binder for Hard-Carbon Negative Electrodes in Sodium-Ion Batteries. *Electrochem. Commun.* **2014**, *44*, 66–69. https://doi.org/10.1016/j.elecom.2014.04.014.

(53) Komaba, S.; Matsuura, Y.; Ishikawa, T.; Yabuuchi, N.; Murata, W.; Kuze, S. Redox Reaction of Sn-Polyacrylate Electrodes in Aprotic Na Cell. *Electrochem. Commun.* **2012**, *21* (1), 65–68. https://doi.org/10.1016/j.elecom.2012.05.017.

(54) Fan, Q.; Zhang, W.; Duan, J.; Hong, K.; Xue, L.; Huang, Y. Effects of Binders on Electrochemical Performance of Nitrogen-Doped Carbon Nanotube Anode in Sodium-Ion Battery. *Electrochimica Acta* **2015**, *174*, 970–977. https://doi.org/10.1016/j.electacta.2015.06.039.

(55) Dai, K.; Zhao, H.; Wang, Z.; Song, X.; Battaglia, V.; Liu, G. Toward High Specific Capacity and High Cycling Stability of Pure Tin Nanoparticles with Conductive Polymer Binder for Sodium Ion Batteries. *J. Power Sources* **2014**, *263*, 276–279. https://doi.org/10.1016/j.jpowsour.2014.04.012.

(56) Li, R. R.; Yang, Z.; He, X. X.; Liu, X. H.; Zhang, H.; Gao, Y.; Qiao, Y.; Li, L.; Chou, S. L. Binders for Sodium-Ion Batteries: Progress, Challenges and Strategies. *Chem. Commun.* **2021**, *57* (93), 12406–12416. https://doi.org/10.1039/d1cc04563f.

(57) Vogt, L. O.; El Kazzi, M.; Jämstorp Berg, E.; Pérez Villar, S.; Novák, P.; Villevieille, C. Understanding the Interaction of the Carbonates and Binder in Na-Ion Batteries: A Combined Bulk and Surface Study. *Chem. Mater.* **2015**, *27* (4), 1210–1216. https://doi.org/10.1021/cm5039649.

(58) Gimble, N. J.; Kraynak, L. A.; Schneider, J. D.; Schulze, M. C.; Prieto, A. L. X-Ray Photoelectron Spectroscopy as a Probe for Understanding the Potential-Dependent Impact of Fluoroethylene Carbonate on the Solid Electrolyte Interface Formation in Na/Cu_2Sb Batteries. *J. Power Sources* **2021**, *489* (January), 229171. https://doi.org/10.1016/j.jpowsour.2020.229171.

(59) Kraynak, L. A.; Schneider, J. D.; Prieto, A. L. Exploring the Role of Vinylene Carbonate in the Passivation and Capacity Retention of Cu_2Sb Thin Film Anodes. *J. Phys. Chem. C* **2020**, *124* (48), 26083–26093. https://doi.org/10.1021/acs.jpcc.0c04064.

(60) Greczynski, G.; Hultman, L. X-Ray Photoelectron Spectroscopy: Towards Reliable Binding Energy Referencing. *Prog. Mater. Sci.* **2020**, *107* (April 2019), 100591. https://doi.org/10.1016/j.pmatsci.2019.100591.

(61) Peng, B.; Xu, Y.; Wang, X.; Shi, X.; Mulder, F. M. The Electrochemical Performance of Super P Carbon Black in Reversible Li/Na Ion Uptake. *Sci. China Phys. Mech. Astron.* **2017**, *60* (6). https://doi.org/10.1007/s11433-017-9022-y.

(62) Wu, C. M.; Pan, P. I.; Cheng, Y. W.; Liu, C. P.; Chang, C. C.; Avdeev, M.; Lin, S. kang. The Mechanism of the Sodiation and Desodiation in Super P Carbon Electrode for Sodium-Ion Battery. *J. Power Sources* **2017**, *340*, 14–21. https://doi.org/10.1016/j.jpowsour.2016.11.048.

IV. INFLUENCES OF ELECTROLYTE COMPOSITION ON THE ELECTROCHEMICAL PERFORMANCE OF Sb-BASED ANODES

4.1 Introduction

To further the understanding of Sb-based anodes in sodium-ion batteries (NIBs), electrolyte studies were performed as they are crucial to the fundamental understanding of chemical and thermal processes of the electrode. While much emphasis is placed on the anode and cathode, much less is known about the electrolyte. This creates a challenge in studying battery systems as all the components (cathode, anode, and electrolyte) are related to one another and should be considered when one component is changed. While cycling, a battery's electrolyte decomposes reductively on the anode and forms what is known as the solid electrolyte interphase (SEI). It is believed that the SEI is formed in the first cycle and behaves as a protective layer for the anode and can continue to form as fresh active material is exposed upon mechanical pulverization.[1–3] Studies have shown that the SEI formed on Li- and Na-based electrodes are significantly different, even using the same electrolyte solvents.[3–5] Therefore, it is crucial to understand what solvents are compatible with NIBs and, more specifically, with our Sb-based anodes if we wish to thoroughly understand the chemical and electrochemical processes of the electrode.

Developing and optimizing electrolytes for alloy-based electrodes, such as Sb, is critical due to the unstable electrode-electrolyte interface. This instability is caused by mechanical fracturing and pulverization of the electrode as it is cycled, and fresh active material is continuously exposed to the electrolyte. Continuous exposure of active material promotes electrolyte reduction and can generate a thick SEI that impedes electron and ion transport. Although nanostructuring can help reduce the mechanical instability of the anode, electrochemical

performance (cycle life, rate capabilities, etc.) can still be hindered by the composition of the SEI due to detrimental effects on the sodiation kinetics.[6,7] These challenges demonstrate how electrolyte composition is critical and potentially limiting factor in improving electrochemical performance in alloy-based anodes.

Here we report early investigations on a survey of sodium electrolyte solutions to determine how electrolyte composition can affect electrochemical performance and the sodiation/desodiation reaction pathway of Sb electrodes. The two salts investigated in these experiments consist of $NaPF_6$, as it was previously reported to improve cycle life in Na-ion cells due to the formation of NaF, and $NaClO_4$, as it has historically been used in Na-ion cells for its cost and thermal stability.[4] The base electrolyte was also varied and consisted of either polyethylene carbonate (PC) or a 1:1:1 ratio by volume mixture of ethylene carbonate: diethyl carbonate: dimethyl carbonate (EC:DEC:DMC) that is commonly used in the field. Additionally, the function of fluoroethylene carbonate (FEC) and vinylene carbonate (VC) were tested to understand how these species could influence the structure and flexibility of the SEI.[6,8–10] These additives are thought to sacrificially reduce and passivate the surface of the anode from further reduction of the electrolyte, thus forming a stable SEI.[3,11] Electrolyte additives, such as FEC, are traditionally used in Li-ion cells as it has been seen in previous studies that it has a large impact on the overall performance of the cell.[12] These fluorinated compounds also lead to the formation of a thinner and smoother SEI.[1,13] Although some studies report that the addition of VC in an electrolyte solution hinders cycling performance, these studies have mainly been done on LIBs and not NIBs.[1,4,12] Furthermore, VC was also used in this study as an alternate electrolyte additive with $NaClO_4$ to investigate whether or not the involvement of fluorine is genuinely beneficial to the performance. We end this chapter with future directions in characterizing the composition and morphology of the SEI and taking a

deeper look into the impact on sodiation kinetics of Sb anodes through the resulting interfacial resistivities of the SEI.

4.2 Experimental

4.2.1 Electrode Preparation

The electrodeposition of Sb and Sb/ACNT were done with the same procedures as reported in Chapters 2 and 3. Electrodeposition solutions were both composed of 200 mM sodium gluconate (Sigma, ACS reagent), and 30 mM of antimony trichloride ($SbCl_3$, Sigma-Aldrich, anhydrous >99.0%) and 30 mM of cetyl trimethyl ammonium bromide (CTAB, Alfa Aesar 98%). The Sb/ACNT solution had 100 mg of ACNTs (Cheap Tubes, outer diameter 20 nm, inside diameter 4 nm, and length from 1-12 μm, >99 wt% purity). The solution was pulse sonicated for two hours with a 10 min pulse and 2 min rest sequence and then sonicated overnight. The excess ACNTs were then crashed out through centrifugation. The solution was split evenly into two 50 mL centrifuge tubes and was centrifuged for 5 min at 5000 rpm.

The thin film electrodes were electrodeposited on a four-inch square of textured Cu foil (tCu, Oak-Mitsui, TLB-DS Cu foil) that was washed with a concentrated H_3PO_4 solution for 30 s and was rinsed with Millipore water and ethanol. A saturated calomel electrode (SCE) was used as the reference and stainless-steel mesh was used as the counter electrode. Using chronocoulometry a constant negative potential of -1.05V vs SCE was applied to the system and the charge limit was set to 3 C/cm^2. When the deposition was complete, the deposited area was washed with Millipore water and absolute ethanol and was dried with nitrogen gas.

4.2.2 Electrolyte Preparation

All electrolyte preparation was done in an argon filled glovebox ($O_2 < 1$ ppm, $H_2O < 0.5$ ppm). The formulated electrolytes had three major components, the base solution, the sodium salt,

and the additive. All the electrolytes had a 1 M concentration of either sodium perchlorate ($NaClO_4$, Sigma-Aldrich, ≥98% ACS reagent) or sodium hexafluorophosphate ($NaPF_6$, STREM Chemicals). The first base electrolyte solution was composed of ethylene carbonate (EC, anhydrous, Aldrich, 99%), diethyl carbonate (DEC, Sigma-Aldrich, ≥99%), and dimethyl carbonate (DMC, Sigma-Aldrich, anhydrous ≥99%) in a 1:1:1 ratio by volume. The second base electrolyte solely consisted of polyethylene carbonate (PC, Sigma-Aldrich, 99.7%). The two additives, fluoroethylene carbonate (FEC, Sigma-Aldrich, 99%) and vinylene carbonate (VC) were incorporated into the electrolyte solutions at 5% of the total volume of the solution.

4.2.3 Electrochemical Characterization

All half-cells were assembled into Swageloks, in an argon filled glove box as described in previous chapters. Electrodeposited films were punched into ½" in diameter punches and were weighed out to acquire the mass of the active material. The thin films were used as the working electrode and a polypropylene separator (MTI Corp) followed by a Whatman glass filter, and another polypropylene separator were placed into the cell. An excess amount of electrolyte, ~0.20 µL, was placed in the cell after the separators. A ½" circular punch of was Na metal (Aldrich, cubes in mineral oil, 99.9%) was cleaned with an extra soft child's toothbrush and placed over the separators. Once assembled, the Na-ion half-cells were cycled with an Arbin battery tester (LBT-20084). The cells were allowed to rest for 12 hours after assembly and were galvanostatically cycled at C/2 rate with calculated current densities based on the mass of active material with a voltage range of 0.01 V to 2.0 V vs. Na/Na^+. Cycling performance was analyzed and graphed with Python code using the NumPy and Pandas packages.

Electrochemical impedance spectroscopy (EIS) experiments were conducted on sodium half-cells using a Gamry Interface 1010E potentiostat. Experiments were conducted at room

temperature at open circuit potential (OCP) once the cells rested for 12 hours to allow for the cells to equilibrate and reach a stable OCP. A constant AC voltage of 10 mV rms and EIS was carried out over a frequency range of 0.1 to 100,000 Hz.

4.3 Results and Discussion

4.3.1 Impact of Electrolyte Composition on Sb/ACNT

An electrodeposited anode of Sb with amine-functionalized carbon nanotubes (ACNT) was used to evaluate the influences of electrolyte composition due to the improved capacity retention provided by ACNTs in mitigating issues related to mechanical degradation. Additionally, including ACNTs in the deposit can cause the electrode to have a higher porosity and, therefore, a higher surface area. This increase in surface area will promote the reduction of the electrolyte and exaggerate the effects of SEI on the electrochemical performance of the anode. In the analysis of the cycle performance of Sb/ACNT in the six electrolytes, seen in **Figure 4.1**, it can be identified that additives are a crucial component in electrolyte composition for the base electrolyte of EC:DEC:DMC. Electrolytes with either $NaPF_6$ (navy trace) and $NaClO_4$ (brown trace) with no additives performed poorly and had very short cycle lifetimes depicted by the steep drop off in capacity at about cycle 25. In addition, the capacity retention for electrolytes with the same additive but different sodium salts seems to perform with similar capacity retention. The cells cycled with $NaClO_4$ electrolytes begin to drop in capacity earlier than the $NaPF_6$ electrolytes but maintain higher coulombic efficiencies. Interestingly both electrolytes with VC outperformed the electrolytes with FEC. **Figure 4.1** shows the cumulative difference between the discharge and charge capacity summed over cycle number, referred to as excess capacity. The calculated excess capacity can be attributed to sodium consuming reactions such as the formation of the SEI or alternative side reactions. The excess capacities of the electrolytes with FEC are overall much

greater than that of the VC electrolytes, with a rapid increase at about 80 cycles. This increase in excess capacity mirrors the decline in specific capacity and represents the loss of active material.

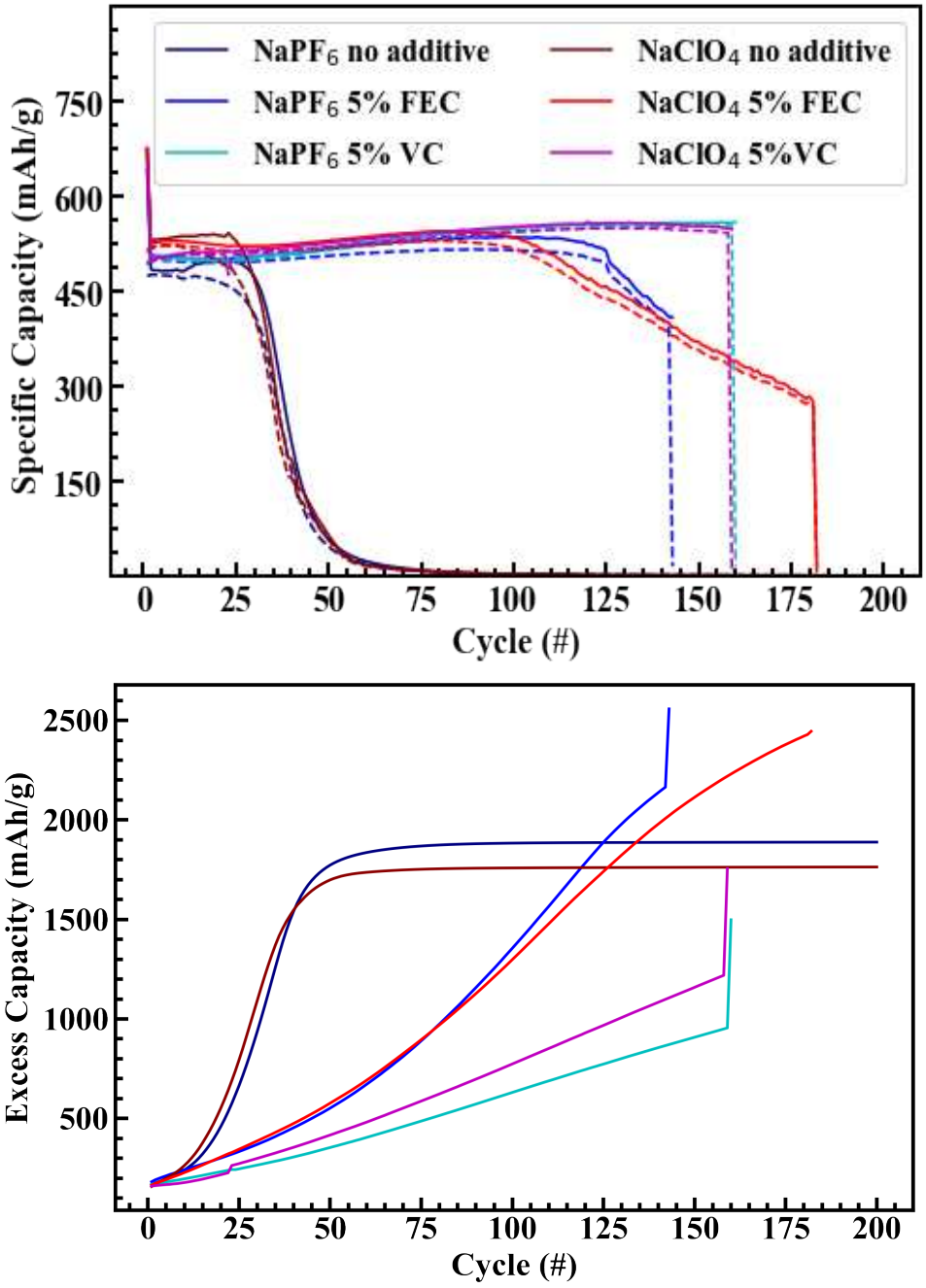

Figure 4.1. Cycle performance, including discharge capacity (solid trace) and charge capacity (dashed trace), of Sb/ACNT in different electrolyte solutions (top). The solid line in the excess capacity plot represents how much excess capacity has gone towards non-reversible electrochemistry such as SEI formation or other side reactions.

From these results, we speculate that the SEI formed with the VC electrolytes is more stable and does not continue growing at the same rate as the FEC electrolytes. The stability of the SEI is related to the composition and mechanical properties, and it has been demonstrated that VC modified SEIs can have a more flexible and robust structure to passivate the anode efficiently.[10,14,15] Various complementary characterization techniques need to be utilized to further understand how VC electrolytes can form a more stable SEI. To begin identifying the composition of the SEI, X-ray Photoelectron Spectroscopy (XPS) can inform on binding environments at the surface of the SEI and potentially through its depth. The morphology and thickness of the SEI can be monitored through Scanning Electron Microscopy (SEM), where a non-stable SEI that experiences continuous growth would be expected to be much thicker in comparison to a stable SEI. Techniques such as Atomic Force Microscopy (AFM) could also inform on the Young's modulus and hardness of the SEI to elucidate how prone the SEI is to cracking.[10]

When comparing the differential capacity of the FEC and VC cells, **Figure 4.2** shows differences in the sodiation and desodiation reactions. All four electrolytes have the same number of reactions reported in Chapter 3, but there are differences in peak broadness when comparing the different additives. These two events are much more distinct in the VC cells, and it is hypothesized that sodiation kinetics are slightly hindered in the FEC electrolytes. Peak broadness and shifts in redox potentials are representatives of sluggish sodiation/desodiation kinetics, and the previously described instability of the FEC modified SEI can be the cause. The morphology of the SEI can lead to high interphase impedance through poor passivation of the anode. Additionally, excessive SEI formation can lead to the isolation of active material leading to the lower intensity of peaks in the dq/dv and the lower cycle life witnessed in **Figure 4.1**. These results are somewhat surprising as SEI enriched with fluorinated species such as LiF and NaF have significantly improved the

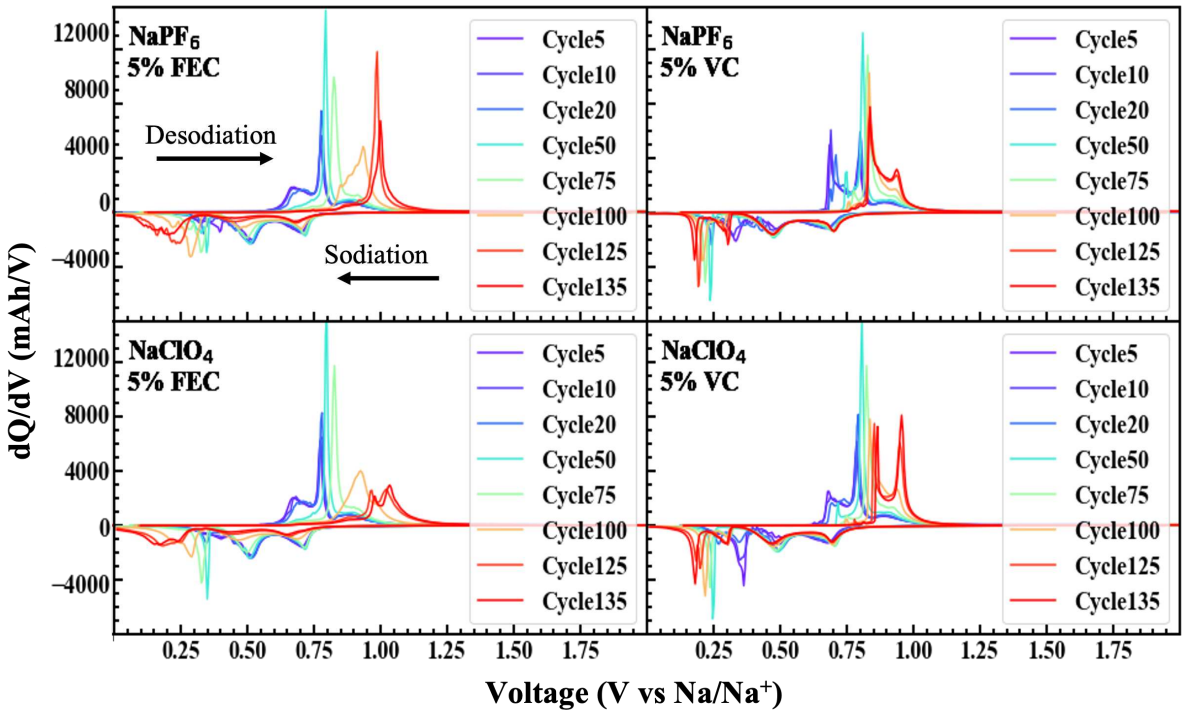

Figure 4.2. Differential capacity plots of Sb/ACNT@tCu in $NaPF_6$ (Top) and $NaClO_4$ (Bottom) electrolyte salts with 5% FEC (left) and 5% VC (right).

cyclability of anodes in various studies.[6,7,16–18] However, a study by He et al. identified that LiF SEI breaks down readily in early cycles and must be repaired in situ by electrolytes that can continuously form LiF.[16] The concentration of fluorinated species in the solution will limit the continuous reparation of the SEI. The reparation will no longer occur after a certain point, leading to an excessive reduction of carbonate species. To investigate the applicability of these results to NIBs, rigorous characterization of a NaF SEI must be done to understand if its breakdown and in situ reparation of the SEI also occurs.

To further analyze if different experimental parameters in the literature could lead to significant changes in the electrochemical performance of Sb anodes, the electrolyte survey was expanded to include electrolytes with a base solution of PC. Currently, in the literature, Sb electrodes are commonly tested with electrolytes composed of 1M $NaClO_4$ in PC and 5% FEC due to good cyclability and capacity retention.[19–22] Despite the improvements in electrochemical

performance, the mechanism for why these electrolytes improve capacity retention in Sb anodes compared to other electrolytes is still not well understood and warrants further investigation. The salt, $NaClO_4$, was kept the same while different carbonate mixtures and additives were changed to reduce the number of tested variables. Once again, the capacity retention for electrolytes with VC was higher than the FEC electrolytes, even with different carbonate mixtures, **Figure 4.3**. The overall lower capacities for the PC-based electrolytes could be caused by excessive oxidation of the electrodes, as the test films in these cells were left out in air. Therefore, this data is insufficient to draw solid conclusions about the lower capacities and needs to be reproduced. Despite these discrepancies, it can still be concluded that VC electrolytes form more stable SEIs in both PC and EC:DEC:DMC. Future studies will more intricately study the role of the carbonate species in the

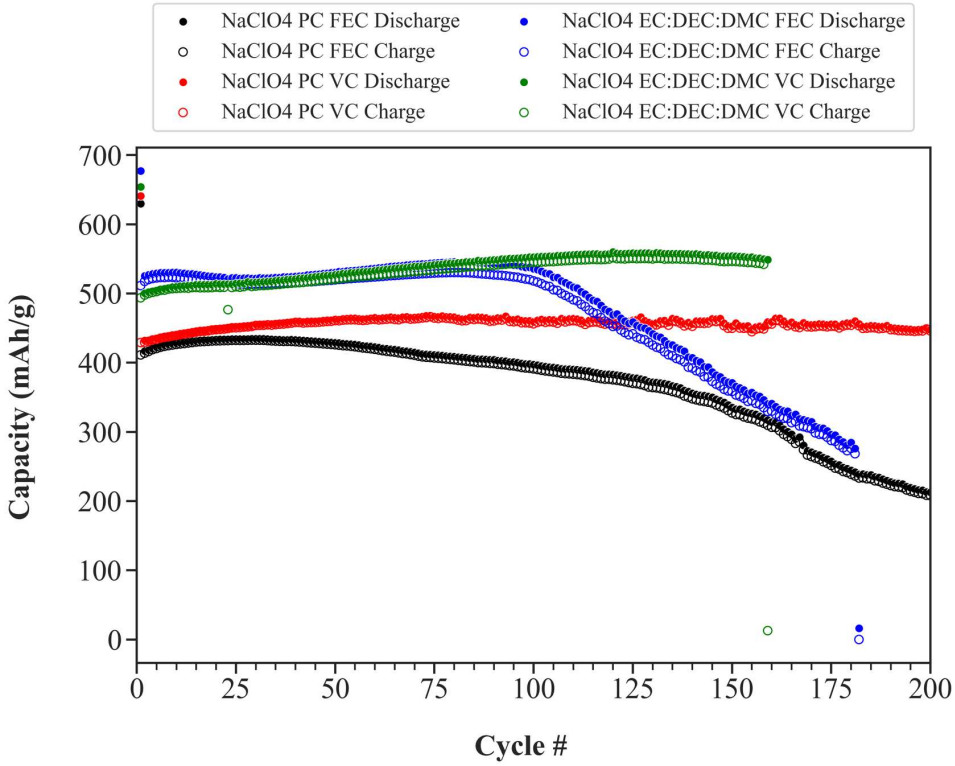

Figure 4.3 Cycle performance, including discharge capacity (solid trace) and charge capacity (open circle), of Sb/ACNT in cycled with electrolytes composed of 1 M $NaClO_4$, a base solution of either EC:DEC:DMC or PC, and 5% FEC or VC. All cells were cycled at a C/5 rate in sodium half cells.

electrolyte and how they decompose in the presence of different additives to better control the composition and morphology of the formed SEI.

4.3.2 Differences in Electrolyte Optimization for Sb and Sb/ACNT

To verify if the surface area of the electrode could exaggerate the influences of electrolyte composition, Sb and Sb/ACNT anodes were cycled with the same electrolyte, 1M $NaClO_4$ in PC with 5% FEC, **Figure 4.4**. Morphological features in the electrodeposited Sb and Sb/ACNT are believed to influence the decomposition of the electrolyte, and the more porous nature of the Sb/ACNT film, seen in **Figure 4.4**, leads to higher charge transfer resistance between the electrolyte and the surface of the electrode even before cycling. The cycling profiles for both Sb and Sb/ACNT are similar, but the capacity of the Sb/ACNT anode begins to fade at earlier cycles. We believe that ACNTs can improve capacity retention, as seen in Chapter 3, but the exposed ACNTs in the deposit, seen in **Figure 4.4**, could be promoting additional decomposition of the electrolyte, as seen in a study by Schulze et. al.[23] The reported results in this chapter highlight how critical electrolyte optimization is to improve the electrochemical performance of Sb anodes, especially when incorporating conductive additives and nanostructuring is utilized to mitigate the effects of mechanical pulverization. Additionally, as higher surface area electrodes such as foams, discussed in Chapter 5, are implemented to achieve higher energy and power density, a

fundamental understanding of the influences of electrolyte composition will be essential to achieve

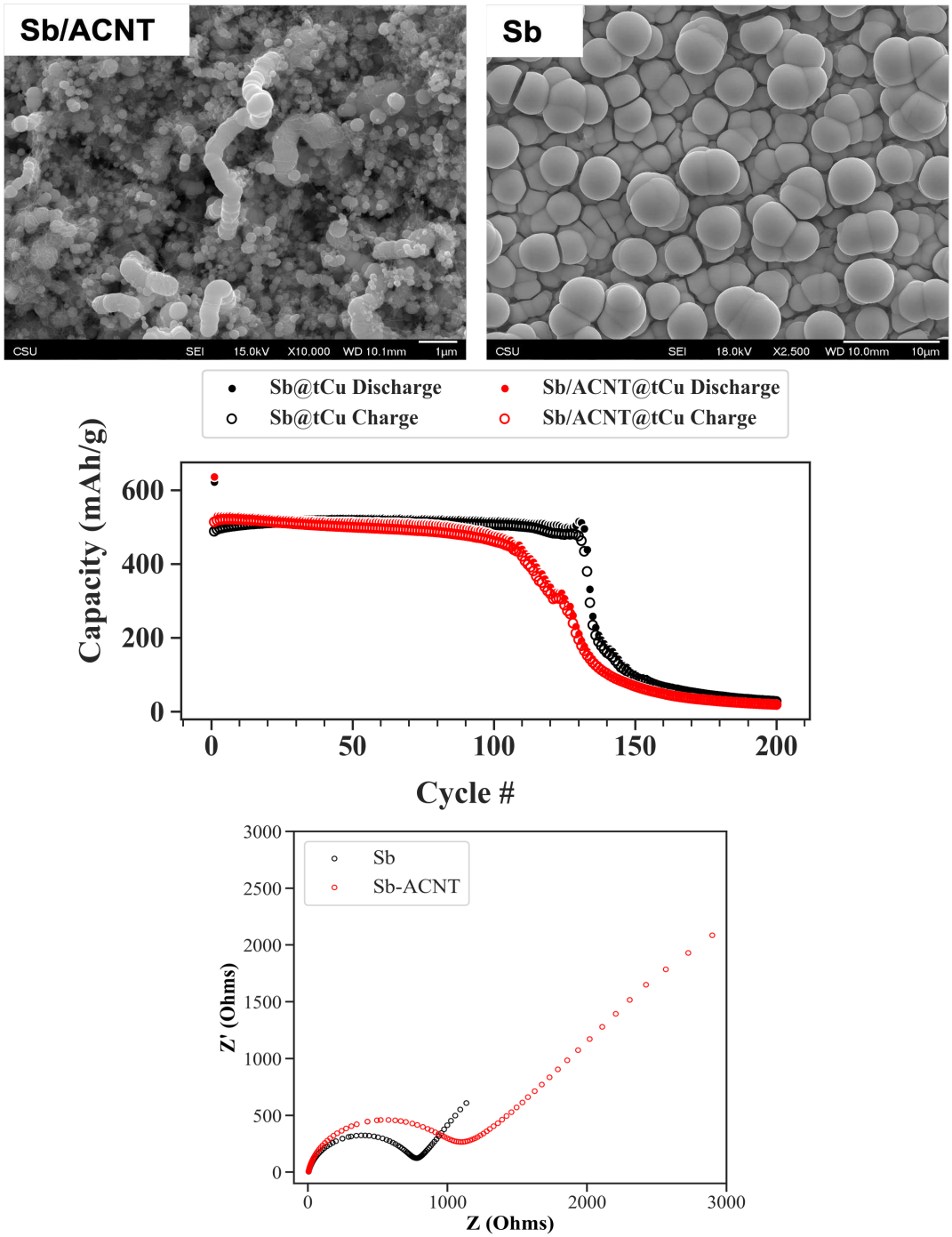

Figure 4.4 SEM images of electrodeposited Sb/ACNT and Sb (Top) Cycle performance, including discharge capacity (solid trace) and charge capacity (open circle), of Sb/ACNT and Sb cycled with 1 M $NaClO_4$, PC, and 5% FEC (Middle). All cells were cycled at a C/5 rate in sodium half cells. Nyquist plots of Sb and Sb/ACNT before cycling. EIS was conducted in a sodium half-cell at room temperature, at OCP, and over a frequency range of 0.1 to 100,000 Hz.

the full benefits of these electrodes.

4.4 Conclusions and Outlook

Multiple conclusions were drawn through the electrolyte survey of $NaPF_6$, $NaClO_4$, FEC, and VC. In the analysis of the cycle performance of these cells, it was determined that using an additive with Sb/ACNT is crucial for sustainable cyclability. The additives, FEC and VC, are predicted to form a protective layer on the anode electrode and prevent the decomposition of the electrolyte. Although these additives aid in the protection of the electrolyte, it is hypothesized that parasitic side reactions with the sodium electrode and consumption of the electrolyte could still occur and could make up a certain amount of the excess capacity reported in **Figure 4.1**.[24,25] o investigate this hypothesis, symmetric cells will be used in the future to remove the possibility of the sodium electrode to cause capacity fade. The removal of the unlimited source of sodium will also allow the actual performance of the Sb/ACNT film to be investigated. In a symmetric cell, a presodiated Sb/ACNT film will be used as the positive electrode and source of sodium (not including the sodium-based electrolyte), and a fresh unsodiated Sb/ACNT film will be used as the negative electrode.[24–26] Through this setup, the actual coulombic efficiency and cycling performance of the cycle can be determined, and the effects of various electrolytes can also be investigated. The role of fluorinated solvents can also be examined using symmetric cells and XPS. The impact of fluorine can be examined by exposing the electrode to a fluorinated electrolyte and then running the symmetric cell with a nonfluorinated electrolyte solvent. The use of a symmetric cell will prevent the consumption of the electrolyte by the counter sodium electrode and will provide a longer cycle life to study the effects of the electrolyte on longer cycles.

4.5 References

(1) Ponrouch, A.; Monti, D.; Boschin, A.; Steen, B.; Johansson, P.; Palacín, M. R. Non-Aqueous Electrolytes for Sodium-Ion Batteries. *J. Mater. Chem. A* **2015**, *3* (1), 22–42. https://doi.org/10.1039/C4TA04428B.

(2) Dahbi, M.; Yabuuchi, N.; Fukunishi, M.; Kubota, K.; Chihara, K.; Tokiwa, K.; Yu, X.; Ushiyama, H.; Yamashita, K.; Son, J.-Y.; Cui, Y.-T.; Oji, H.; Komaba, S. Black Phosphorus as a High-Capacity, High-Capability Negative Electrode for Sodium-Ion Batteries: Investigation of the Electrode/Electrolyte Interface. *Chem. Mater.* **2016**, *28* (6), 1625–1635. https://doi.org/10.1021/acs.chemmater.5b03524.

(3) Kumar, H.; Detsi, E.; Abraham, D. P.; Shenoy, V. B. Fundamental Mechanisms of Solvent Decomposition Involved in Solid-Electrolyte Interphase Formation in Sodium Ion Batteries. *Chem. Mater.* **2016**, *28* (24), 8930–8941. https://doi.org/10.1021/acs.chemmater.6b03403.

(4) Ponrouch, A.; Marchante, E.; Courty, M.; Tarascon, J.-M.; Palacín, M. R. In Search of an Optimized Electrolyte for Na-Ion Batteries. *Energy Environ. Sci.* **2012**, *5* (9), 8572. https://doi.org/10.1039/c2ee22258b.

(5) Komaba, S.; Murata, W.; Ishikawa, T.; Yabuuchi, N.; Ozeki, T.; Nakayama, T.; Ogata, A.; Gotoh, K.; Fujiwara, K. Electrochemical Na Insertion and Solid Electrolyte Interphase for Hard-Carbon Electrodes and Application to Na-Ion Batteries. *Adv. Funct. Mater.* **2011**, *21* (20), 3859–3867. https://doi.org/10.1002/adfm.201100854.

(6) Liu, M.; Yang, Z.; Shen, Y.; Guo, S.; Zhang, J.; Ai, X.; Yang, H.; Qian, J. Chemically Presodiated Sb with a Fluoride-Rich Interphase as a Cycle-Stable Anode for High-Energy Sodium Ion Batteries. *J. Mater. Chem. A* **2021**, *9* (9), 5639–5647. https://doi.org/10.1039/d0ta10880d.

(7) Bian, X.; Dong, Y.; Zhao, D.; Ma, X.; Qiu, M.; Xu, J.; Jiao, L.; Cheng, F.; Zhang, N. Microsized Antimony as a Stable Anode in Fluoroethylene Carbonate Containing Electrolytes for Rechargeable Lithium-/ Sodium-Ion Batteries. *ACS Appl Mater Interfaces* **2020**, *12*, 3562. https://doi.org/10.1021/acsami.9b18006.

(8) Sarkar, S.; Mukherjee, P. P. Synergistic Voltage and Electrolyte Mediation Improves Sodiation Kinetics in M-Sn Alloy-Anodes. *Energy Storage Mater.* **2021**, *43* (September), 305–316. https://doi.org/10.1016/j.ensm.2021.09.014.

(9) Bodenes, L.; Darwiche, A.; Monconduit, L.; Martinez, H. The Solid Electrolyte Interphase a Key Parameter of the High Performance of Sb in Sodium-Ion Batteries: Comparative X-Ray Photoelectron Spectroscopy Study of Sb/Na-Ion and Sb/Li-Ion Batteries. *J. Power Sources* **2015**, *273*, 14–24. https://doi.org/10.1016/j.jpowsour.2014.09.037.

(10) Bai, P.; Han, X.; He, Y.; Xiong, P.; Zhao, Y.; Sun, J.; Xu, Y. Solid Electrolyte Interphase Manipulation towards Highly Stable Hard Carbon Anodes for Sodium Ion Batteries. *Energy Storage Mater.* **2020**, *25*, 324–333. https://doi.org/10.1016/j.ensm.2019.10.006.

(11) Michan, A. L.; Parimalam, Bharathy. S.; Leskes, M.; Kerber, R. N.; Yoon, T.; Grey, C. P.; Lucht, B. L. Fluoroethylene Carbonate and Vinylene Carbonate Reduction: Understanding Lithium-Ion Battery Electrolyte Additives and Solid Electrolyte Interphase Formation. *Chem. Mater.* **2016**, *28* (22), 8149–8159. https://doi.org/10.1021/acs.chemmater.6b02282.

(12) Komaba, S.; Ishikawa, T.; Yabuuchi, N.; Murata, W.; Ito, A.; Ohsawa, Y.; CoO, N. Fluorinated Ethylene Carbonate as Electrolyte Additive for Rechargeable Na Batteries. *ACS Appl Mater Interfaces* **2011**, *3*, 4165–4168. https://doi.org/10.1021/am200973k.

(13) Åvall, G.; Mindemark, J.; Brandell, D.; Johansson, P. Sodium-Ion Battery Electrolytes: Modeling and Simulations. *Adv. Energy Mater.* **2018**, *8* (17), 1703036. https://doi.org/10.1002/aenm.201703036.

(14) Jackson, E. D.; Prieto, A. L. Copper Antimonide Nanowire Array Lithium Ion Anodes Stabilized by Electrolyte Additives. *ACS Appl Mater Interfaces* **2016**, *8*, 30379–30386. https://doi.org/10.1021/acsami.6b08033.

(15) Kraynak, L. A.; Schneider, J. D.; Prieto, A. L. Exploring the Role of Vinylene Carbonate in the Passivation and Capacity Retention of Cu_2Sb Thin Film Anodes. *J. Phys. Chem. C* **2020**, *124* (48), 26083–26093. https://doi.org/10.1021/acs.jpcc.0c04064.

(16) He, M.; Guo, R.; Hobold, G. M.; Gao, H.; Gallant, B. M. The Intrinsic Behavior of Lithium Fluoride in Solid Electrolyte Interphases on Lithium. *Proc. Natl. Acad. Sci.* **2020**, *117* (1), 73–79. https://doi.org/10.1073/pnas.1911017116.

(17) Hirsh, H. S.; Sayahpour, B.; Shen, A.; Li, W.; Lu, B.; Zhao, E.; Zhang, M.; Meng, Y. S. Role of Electrolyte in Stabilizing Hard Carbon as an Anode for Rechargeable Sodium-Ion Batteries with Long Cycle Life. *Energy Storage Mater.* **2021**, *42*, 78–87. https://doi.org/10.1016/j.ensm.2021.07.021.

(18) Tesfamhret, Y.; Carboni, M.; Asfaw, H. D.; Kullgren, J.; Younesi, R. Revealing Capacity Fading in Sb-Based Anodes Using Symmetric Sodium-Ion Cells. *JPhys Mater.* **2021**, *4* (2). https://doi.org/10.1088/2515-7639/abebe9.

(19) Subramanyan, K.; Aravindan, V. Stibium: A Promising Electrode toward Building High-Performance Na-Ion Full-Cells. *Chem* **2019**, *5*, 3096–3126. https://doi.org/10.1016/j.chempr.2019.08.007.

(20) Darwiche, A.; Marino, C.; Sougrati, M. T.; Fraisse, B.; Stievano, L.; Monconduit, L. Better Cycling Performances of Bulk Sb in Na-Ion Batteries Compared to Li-Ion Systems: An

Unexpected Electrochemical Mechanism. *J. Am. Chem. Soc.* **2012**, *134*, 20805–20811. https://doi.org/10.1021/ja310347x.

(21) Chen, B.; Liang, M.; Wu, Q.; Zhu, S.; Zhao, N.; He, C. Recent Developments of Antimony-Based Anodes for Sodium- and Potassium-Ion Batteries. *Trans. Tianjin Univ.* **2022**, *28* (1), 6–32. https://doi.org/10.1007/s12209-021-00304-9.

(22) He, J.; Wei, Y.; Zhai, T.; Li, H. Antimony-Based Materials as Promising Anodes for Rechargeable Lithium-Ion and Sodium-Ion Batteries. *Mater Chem Front* **2018**, *2*, 437. https://doi.org/10.1039/c7qm00480j.

(23) Schulze, M. C.; Belson, R. M.; Kraynak, L. A.; Prieto, A. L. Electrodeposition of Sb/CNT Composite Films as Anodes for Li- and Na-Ion Batteries. *Energy Storage Mater.* **2020**, *25* (June 2019), 572–584. https://doi.org/10.1016/j.ensm.2019.09.025.

(24) Hatchard, T. D.; Obrovac, M. N. Evaluation of Electrolyte Salts and Solvents for Na-Ion Batteries in Symmetric Cells. *J. Electrochem. Soc.* **2014**, *161* (10), A1748–A1752. https://doi.org/10.1149/2.1131410jes.

(25) Pfeifer, K.; Arnold, S.; Becherer, J.; Das, C.; Maibach, J.; Ehrenberg, H.; Dsoke, S. Can Metallic Sodium Electrodes Affect the Electrochemistry of Sodium-Ion Batteries? Reactivity Issues and Perspectives. *ChemSusChem* **2019**, *12*, 3312–3319. https://doi.org/10.1002/cssc.201901056.

(26) Burns, J. C.; Krause, L. J.; Le, D.-B.; Jensen, L. D.; Smith, A. J.; Xiong, D.; Dahn, J. R. Introducing Symmetric Li-Ion Cells as a Tool to Study Cell Degradation Mechanisms. *J. Electrochem. Soc.* **2011**, *158* (12), A1417. https://doi.org/10.1149/2.084112jes.

V. DEVELOPING THREE-DIMENSIONAL BATTERIES THROUGH ELELECTRODEPOSITION[5]

5.1 Introduction

The need for technological improvements for renewable energy applications is an ongoing endeavor that is critically dependent on the rapid advancement of current energy storage devices. Present-day battery systems such as Li-ion batteries (LIBs) have been able to keep up with energy demands for portable electronic devices, but there are many other applications demanding the miniaturization of batteries to power implantable devices, autonomous sensors and additional Internet of things-based (IoT) applications.[1,2] The need for batteries with both high energy and high-power densities in a smaller footprint area, but in very large scale, are also of interest for larger applications such as emerging transportation systems (e.g., electric aviation) and grid-level storage.[3] However, improving energy and power density while reducing the footprint of the battery is a nontrivial problem that requires novel and complex solutions.

There is an inherent tradeoff in conventional planar two-dimensional (2D) batteries, wherein high active material loadings lead to increased capacity but poor power performance, and low loadings lead to high power but low capacities. Three dimensional (3D) batteries avoid this tradeoff and enable a route to vastly improve power *and* energy where commercial 2D batteries fall short, as demonstrated when comparing their performance metrics in **Figure 5.1a**.

[5]Portions of this chapter are from a prepared manuscript for submission to Nature Reviews, Advancements in the Third Dimension: Performance Metrics and Mechanistic Considerations for the Development of 3D Batteries, with Kelly Nieto, Daniel S. Windsor, Bairav S. Vishnugopi, Partha Mukherjee, and Amy L. Prieto. (Nat. Rev., **2023**, in preparation). Kelly Nieto and Daniel S. Windsor are co-first authors and equally wrote and edited the manuscript with supervision and additional help from Amy L. Prieto. Bairav S. Vishnugophi and Partha Mukherjee contributed to writing the computational and mechanistic consideration sections of the manuscript. The experimental results reported on the electrodeposition of antimony on foams in this chapter are intended to be part of a future manuscript for publication.

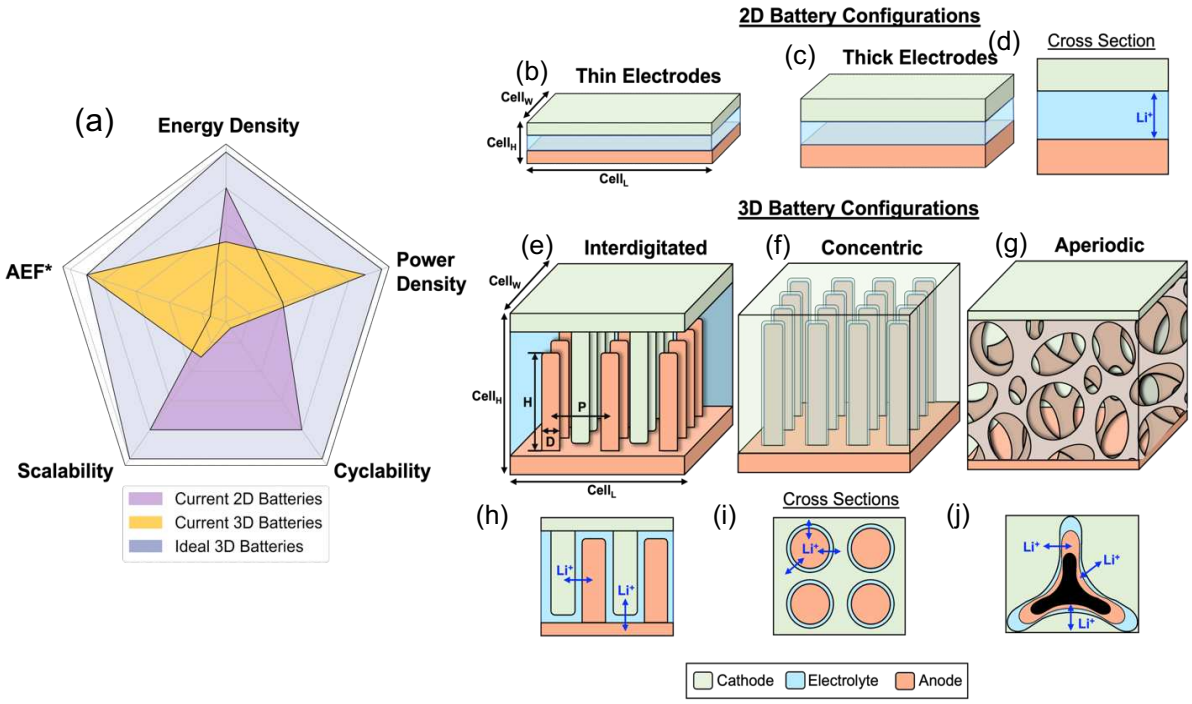

Figure 5.1. Performance metrics and geometric configurations for 2D and 3D Batteries. Performance metrics of current 2D and 3D batteries as well as the ideal performance metrics of a commercialized 3D battery (a). Schematics of 2D batteries demonstrating how energy density is generally improved in this configuration by increasing the thickness of the electrodes (b & c). 2D configurations maybe have complex geometrics but only allow for Li ion diffusion in one plane (d). 3D batteries are produced in many different geometric configurations and generally fall under the categories of interdigitated (e & h), concentric (f & i), and aperiodic (g & j). The cross sections of these geometries demonstrate the multiple pathways Li ions may travel when the cell is cycled (h-j).

Traditionally, 2D batteries consist of layered planar electrodes and may possess complex geometries, but only overlap in one geometric plane, as seen in **Figure 5.1b-d**. This results in a tradeoff between energy density and power density. To improve energy density in these systems, the active material loading must be increased, however this requires thicker electrodes that offer limited performance due to mechanical degradation and restricts the achievable power density due to rate-limiting resistivities and lithium concentration gradients.[4–7] When trying to improve power density, higher surface areas could lead to improved kinetics, but this generally leads to batteries with a larger footprint area or a decrease in active material loading, which actually results in lower energy densities.[4,8] These challenges highlight the limitations in improving performance metrics

for current 2D systems and necessitate advances in multiple geometric planes that 3D batteries can supply.[9–11] The ultimate outcome of an advanced 3D battery would be a single device that possesses the highest energy density possible for the implemented materials system with the power density of a supercapacitor.

While numerous definitions of 3D batteries have been proposed in the literature,[6,11–14] here we define a 3D battery as a battery where all the components (i.e., electrodes and electrolyte) overlap in more than one plane. Examples of 3D battery architectures are shown in **Figure 5.1** and demonstrate the variety of configurations that can be utilized to readily improve the amount of active material and exposed surface area in a smaller footprint. In **Figure 5.1e-j**, three commonly used architectures known as interdigitated, concentric, and aperiodic are shown to demonstrate the various planes where ionic transport can occur.[6,12,15,16] Interdigitated configurations consist of periodically dispersed arrays of cathode and anode plates or rods. The electrodes have a fixed distance from one another and are separated by void space or a solid electrolyte membrane. Concentric based configurations have a similar periodic nature and typically consist of an electrode with a conformally coated electrolyte followed by a conformal coating or void filling of the remaining electrode. Based on this definition, aperiodic structures may be considered "semi-concentric" as they also consist of conformal coverage of the electrolyte onto a 3D network of either the anode or cathode. This is then followed by coverage or filling of the remaining electrode. However, the base structure of the aperiodic configuration originates on a randomly ordered current collector or self-standing electrode, such as a foam, and does not possess the ordered nature of the concentric configuration. The implementation of any of the described configurations is highly dependent on the application as each application has its own cost-effective fabrication technique, such as atomic layer deposition (ALD) for microbatteries or electroplating for

foams.[11,15,17–19] Consequently, the fabrication technique can then limit the choice of active material and thus lends itself to inherent challenges for each configuration in enhancing typical battery performance metrics. The main point of 3D batteries is that they clearly take advantage of the height in the described architectures and, therefore, energy and power density can be decoupled based on interfacial surface area, active material loading, and short ion diffusion paths in a smaller footprint.

It is well known that 3D battery research has progressed significantly since first proposed by Long et al. in 2004, yet the details concerning *exactly* how 3D batteries have advanced over the last 20 years is not immediately apparent.[6] This results from the fact that direct comparisons between two different 3D batteries are very difficult, as the performance of a 3D battery is highly dependent on many inter-related aspects of the battery (i.e. electrode geometry, materials selection, fabrication method, interfacial interactions).[5,11,20] To understand the complexity in comparing reported 3D battery studies, we draw your attention to a recent review by Hung et al. that provides a comprehensive review of experimental data from a range of architectures, with careful attention to rate as a function of architecture and electrode thickness.[9] We have select several metrics we believe to be crucial for evaluating the performance of 3D batteries, and as use them as tools to gauge areas in which 3D batteries require further improvement. We also focus on the roadblocks that remain on the path toward large scale commercialization of 3D batteries. Our generalizations are summarized in **Figure 5.1a**, and are relative comparisons based on our literature review. The comparisons shown in **Figure 5.1a** demonstrates the advantages of 3D batteries, the areas where greatest improvements have been seen, and areas where 3D batteries need to improve to reach commercialization as a function of the performance metrics determined most important by this review. These performance metrics are the area enhancement factor (AEF), power density, energy

density, as well as scalability and cyclability. The AEF is a relative measure of the increase in surface area a 3D battery per footprint area compared to another 3D battery utilizing the same system (i.e., electrode composition, electrolyte) or a planar battery analog. This metric is crucial for understanding how much better (in terms of energy density and power density) a 3D battery *could* be compared to its 2D counterpart. Given the irrefutable potential for decoupling energy and power density, these metrics are crucial for assessing advancements in 3D batteries. Often overlooked, the scalability and cyclability of 3D batteries are critical aspects to consider and are highly important for taking 3D batteries from academic laboratories to industrial applications. Although the performance metrics are significant as standalone parameters, they are also highly dependent on each other, owing to the magnitude and complexity of the interacting components in 3D batteries. As such, it is important that each component of a 3D battery is developed in concert with the other components.

5.1.2 Improving Energy Density in 3D Batteries

One way to improve energy density is by increasing the battery voltage and capacity which are related to the active material composition and packing density for both the cathode and anode. Significant efforts have gone into materials development for 3D batteries by using what has already been discovered in the 2D LIB field. Examples include the use of "champion" materials such as LFP, LCO, LMO, V_2O_5 as cathode materials and graphite, silicon, LTO, and other intercalation oxides as anode materials.[21–26] Solid electrolytes such as LiPON, LiPONB and LiSiPON are also of interest to act as a separator between the cathode and anode.[17,18,27,28] Conversion electrodes can also be adapted for use in 3D batteries because of the void space present in certain configurations that can accommodate volume expansion.[29–31] Simultaneously, the high energy density provided by Li metal anodes can be utilized because of the reduced propensity for

dendrite formation due to a significant reduction in local current densities.[14,20] However, the use of these materials is highly dependent on the size of the battery (micro batteries vs larger applications) and the fabrication technique that could be implemented to allow for conformal coverage (ALD, PVD, EPD, ED, spin coating etc.). Additionally, some of the previously listed materials require the use of binders and additives to achieve good adhesion to the current collector but this reduces the loading of active material and increases the overall weight of the cell. The scaffold used in 3D battery configurations can also heavily influence the calculated energy density depending on whether the scaffold material can be lithiated/delithiated. Therefore "self-standing" electrode materials would be extremely beneficial to improve the overall energy density.[24] One example is the use of 3D carbon scaffolds that can also be utilized in active lithiation/delithiation but problems then arise in the cyclability and lifetime of the cell after continuous utilization of the scaffold.[32]

5.1.3 Electrodeposition of 3D Sb-Based Anodes to Improve Energy Density

Due to the void space present in 3D configurations, conversion anodes, such as antimony, can be implemented to take advantage of their higher theoretical capacities when compared to graphite that is traditionally used as the anode material.[6,14,33] The void space is these configurations allows for accommodation of volume expansion perpendicular to the substrate and can potentially accommodate mechanical degradation. However, to take advantage of the high capacities provided by Sb-based electrodes, they must be well implemented into a 3D configuration as either a robust coating or a self-standing electrode. Our group has demonstrated the viability of electrodeposition to controllably synthesize Sb-based anodes as coatings on metal current collectors or as self-standing nanowires.[34–38] Through electrodeposition the composition, morphology, crystallinity, and mechanical robustness of the deposited electrode can be tuned through various synthetic

parameters and can be implemented at industrial scales.[33,34,39–41] Additionally, conductive additives can be co-deposited with active material to improve electronic conductivity.[35] By electrodepositing Sb-based anodes onto complex geometric scaffolds, such as metal foams, we hypothesize that electrodes with good energy and power density can be fabricated by tuning synthetic parameters to create a robust electrode with uniform thickness for both lithium-ion and sodium-ion batteries. However, electrodeposited active material onto complex geometries can be quite difficult due to the high surface area and the curvature of the current collector. In this chapter we discuss how to begin to overcome the limitations of electrodeposition through synthetic and experimental parameters and show preliminary work in developing Sb-based electrodes for battery applications.

5.1.4 Experimental Considerations

There are many synthetic handles that can be tuned when electrodepositing Sb-based electrodes such as electrolyte composition, solution additives, temperature, applied electrochemical techniques, and the physical set up of the electrodes during the deposition.[42–44] As described in Chapter 1 and 2, in electrodeposition, Sb ions in a solution are electrochemically reduced on to the surface of the working electrode. The electrodeposition bath can be aqueous or organic based and is composed of dissolved antimony salts with solution additives, such as sodium gluconate and citric acid, that complex with the Sb^{3+} ion.[33–36,39,40,45,46] Additionally, levelers and brighteners can also be incorporated in the solution that influence the morphology and uniformity of the deposit as seen in Chapter 2. Due to the curvature of metal foams, levelers are of extreme importance to create deposition with uniform thickness throughout the electrode. If the electrode is thicker in certain areas, then the power density of the battery will diminish due to lithium or sodium concentration gradients across the active material.[47–49] The energy density of the electrode

can also be impacted due to underutilization of the active material in thicker regions of the electrode and can lead to mechanical failure.[47] Temperature is also a crucial parameter than be utilized to help with solubility of the antimony precursors in solution and affects the kinetics of the electrodeposition by improving deposition rates.[39,50]

Electrochemical parameters of the deposition such as the applied electrochemical technique can also influence characteristics of the deposit. Through chronoamperometry, a single constant voltage at the reduction potential of Sb^{3+} to Sb^0 is applied to the working electrode and the deposition is generally limited by the depletion of the metal ion on the surface of the electrode by mass transport.[43,51] By applying repeating chronoamperometry, two alternating voltage steps can be applied. One at the reduction potential of Sb and the other at open circuit potential to replenish the concentration of Sb^{3+} ions at the surface of the electrode. [52–55] To further replenish the concentration of Sb^{3+} ions on the high surface area foam, convectional stirring can be implemented.[43,44] By tunning the described experimental parameters we have been able to gather preliminary results on the electrodeposition of Sb and Sb with amine functionalized carbon nanotubes (ACNTs) on copper foams and have begun testing their electrochemical performance in sodium-ion batteries.

5.2 Electrodeposited Sb and Sb/ACNT on Cu Foam

5.2.1 Experimental

5.2.1.1 Electrodeposition Solutions for Sb and Sb/ACNT

The electrodeposition solution used to deposit Sb has been described in previous work and consists of 200 mM sodium gluconate (Sigma, ACS reagent), 30 mM of (1-hexadecyl)trimethylammonium bromide (CTAB, 98%, Alfa Aesar) and 30 mM antimony trichloride ($SbCl_3$, Sigma-Aldrich, anhydrous >99.0%) in 100 mL of Millipore (>15MΩ*cm)

water.[34] For the solution with amine functionalized carbon nanotubes (ACNTs), 100 mg of ACNTs (Cheap Tubes, outer diameter 20 nm, inside diameter 4 nm, and length from 1-12 μm, >99 wt% purity) were added to the Sb solution. The solution was pulse sonicated for two hours with a 10 min pulse and 2 min rest sequence and then sonicated overnight. The solution for was then split into two 50 mL centrifuge tubes and was centrifuged at 5000 rpm for 5 mins to remove the excess ACNTs that were not suspended in solution.

The deposition solutions were characterized through cyclic voltammetry (CV) using a Gamry Reference 3000 potentiostat to determine the reduction potential of Sb^{3+} to Sb^{0}. The CVs were taken in a three-electrode set up consisting of a saturated calomel electrode (SCE) as the reference, a platinum mesh counter electrode, and a platinum disk working electrode at a scan rate of 50 mV/s at room temperature and 60˚ C with no stirring.

5.2.1.2 Electrodeposition of Sb

The Sb and Sb/ACNT foams were electrodeposited using a Gamry Interface 1010E potentiostat. A 5 cm x 2 cm strip of copper foam (Winfey 110 ppi 1 mm thick) was washed sonicated in a concentrated H_3PO_4 solution for 30 s to remove surface oxides, followed by Millipore water and an ethanol wash to remove excess acid and water on the surface of the film. The electrochemical set up consisted of the copper foam as the working electrode, two stainless-steel meshes as the counter electrodes that sandwiched the working electrode and a SCE as the reference. The three-electrode set up was placed in a jacketed beaker and the deposition either occurred at room temperature or the solution was heated to 60˚C using a heated circulatory system. The Sb and Sb/ACNT deposited were synthesized through repeating chronoamperometry, and two alternating voltage steps were applied. The first voltage step was a constant negative potential of -1.05V vs SCE for 10 s and the second was set to the starting open circuit potential (OCP) for 15

s. The voltage was alternated for 60 steps and amounted to a total deposition time of 600 s. The deposited foam was then rinsed with Millipore water and absolute ethanol to remove the remaining deposition solution.

5.2.1.3. Electrolyte Preparation, Cell Assembly, and Galvanostatic Cycling

All cell assembly and electrolyte preparation was done in an argon filled glovebox ($O_2 < 1$ ppm, $H_2O < 0.5$ ppm). The electrolyte used for all experiments consisted of a 1 M solution of sodium perchlorate ($NaClO_4$, Sigma-Aldrich, ≥98% ACS reagent) with an addition of 5% by volume fluoroethylene carbonate (FEC, Sigma-Aldrich, 99%) in a base electrolyte solution containing polyethylene carbonate (PC, Sigma-Aldrich, 99.7%).

To test the electrochemical performance of the deposited Sb/ACNT foams, half-cells with sodium metal were assembled in pouch cells. The electrodeposited foams were masked with Kapton tape, and a 4 cm^{-2} area was left exposed. An aluminum current collector tab was sonic welded onto the top of the foam strip and a polypropylene separator (MTI Corp) was wrapped around the foam and heat sealed. Another aluminum current collector tab was sonic welded to a 2.5” x 2.5” textured copper foil (tCu, Oak-Mitsui, TLB-DS Cu foil). Sodium metal (Aldrich, cubes in mineral oil, 99.9%) was rolled out into a foil and was wrapped around the polypropylene separator. The textured copper foil was folded over the sodium metal and acted as the current collector. The assembled stack was placed in between the pouch cell encasing and three of the sides were heat sealed shut. An excess amount of electrolyte, ~2.5 mL, was placed in the cell and the last side of the cell was sealed off.

Once assembled, the Na-ion half-cells were cycled with an Arbin battery tester (LBT-20084). The cells were allowed to rest for 12 hours after assembly and were galvanostatically cycled at a rate of C/5 with calculated current densities based on the mass of electrodeposited

active material. The voltage range at which the cells were cycled was 0.01 V - 1.5 V vs. Na/Na^+. Cycling performance was analyzed and graphed with Python code using the NumPy and Pandas packages.

5.2.1.4 Materials Characterization

The surface morphology of electrodeposited films was analyzed with Scanning Electron Microscopy (SEM) using a JEOL JSM-6500F Microscope at 15 kV and Energy Dispersive X-ray Spectroscopy (EDS) with an Oxford Instrument X-Max and AZtec software. Samples for cross-section SEM were prepared by freezing the samples in liquid nitrogen for 20 mins then cutting through them with a frozen razor blade. Because of the nature of this slightly destructive process some mechanical damage is done to the film if the blade was dull, or the sample was not entirely frozen.

5.3 Results and Discussion

To test the applicability of our Sb deposition solutions for foams we electrodeposited Sb and Sb/ACNT onto a copper foam at room temperature. The electrodeposition was conducted using repeating chronoamperometry due to previous studies in our group that demonstrated erratic growth of the deposited material onto a foam while holding a single reduction potential. At room temperature both Sb and Sb/ACNT were successfully deposited onto the foam as seen in the cross-section SEM imaging in **Figure 5.2**. However, for the Sb depositions, **Figure 5.2a** and **Figure 5.2b**, the deposited layer was thin and fragile. This is seen all around the sample as fractured platelets were found at the peaks of the struts where these areas are believed to be high points of stress. A schematic describing terminology to describe foam struts is shown in **Figure 5.3**. The Sb platelets also seemed to have poor adhesion to the copper foam substrate and were delaminating exposing bare copper. Interestingly, in areas with minimal delamination the deposited Sb film was

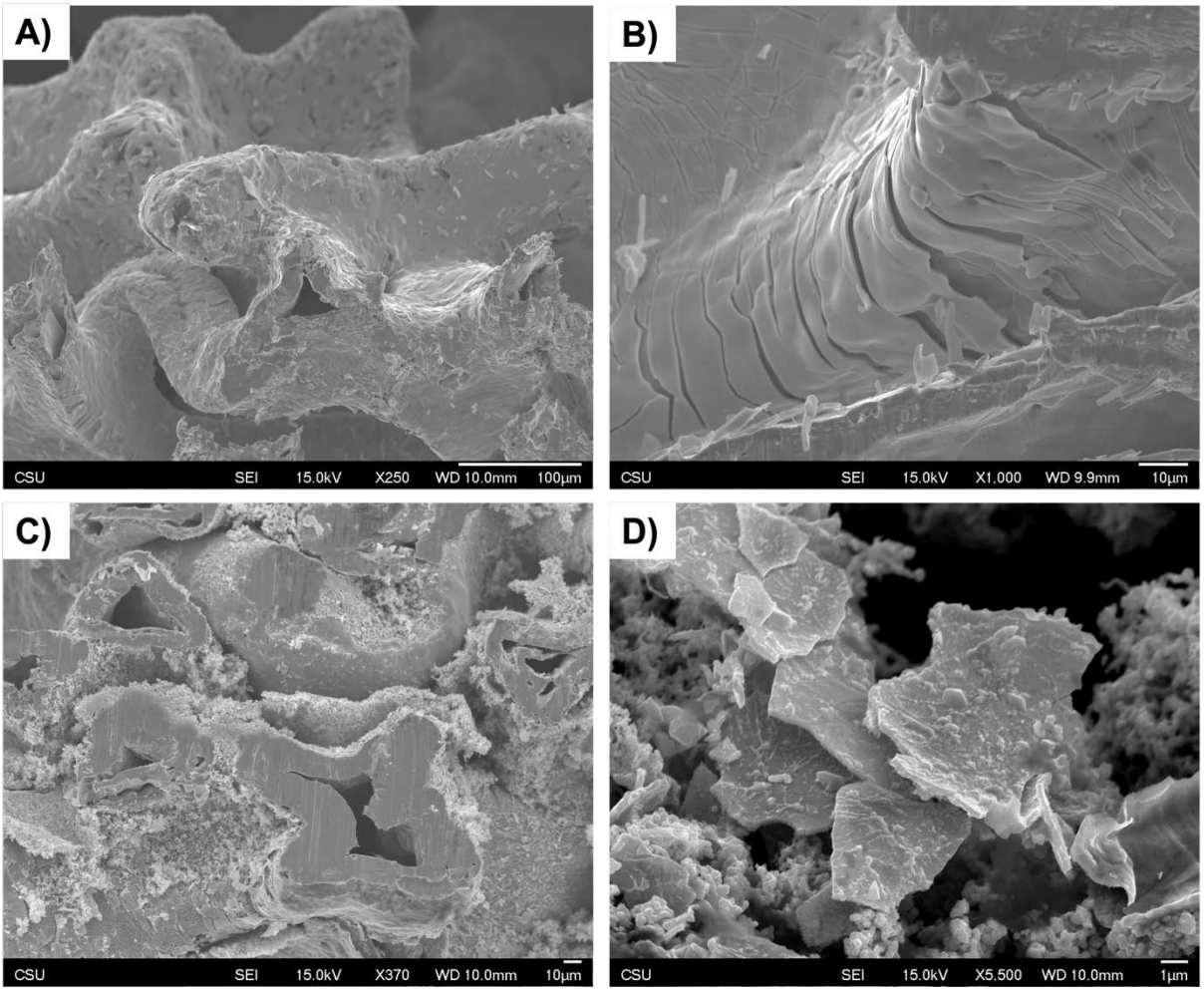

Figure 5.2 Cross-section SEM images of electrodeposited Sb (A & B) and Sb/ACNT (C & D) onto a copper foam substrate at room temperature. Images were taken on the same sample in different areas and various magnifications.

smooth and did not have the same spherical morphology as seen in the 30 mM CTAB deposits in Chapter 2. These results highlight that CTAB, which was seen to act as a leveler and inhibitor in Chapter 2, is no longer behaving in the same manner or is not present in high enough concentrations to have the same effect on the morphology. In Chapter 2, CTAB was proposed to act as a capping ligand and would cap crystals at small sizes and passivate the film surface so that added Sb would continuously nucleate into new crystals, rather than grow onto already nucleated crystals. This nucleation and growth processes likely resulted in the formation of densely packed Sb particles that were well adhered to the copper substrate. These thin film deposits were found to

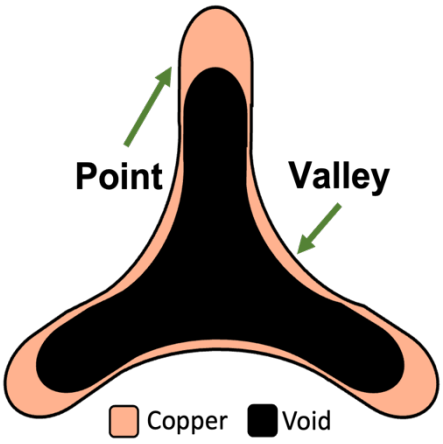

Figure 5.3 Schematic of a cross-section of a copper strut depicting the points and valleys of the structure.

be highly strained through Rietveld refinements and this strain could potentially be enhanced at high points of curvature on the foam. When the highly stressed deposit is sodiated the associated volume expansion could easily lead to fracturing of the deposit. To test this hypothesis stress and strain could be computationally modeled through finite element analysis, as described by Lee et al., and could help understand how high areas of curvature and volume expansion can lead to strain.[56] These results could inform on what solution additives can be utilized to reduce strain in these deposits by tuning the morphology and crystallinity of the deposit and in turn influencing the amount of strain in the deposited electrode.

The Sb/ACNT deposition appeared to be better adhered to the copper foam as seen in **Figure 5.2c** and **Figure 5.2d**. The deposited layer is also thin but appears to grow more uniformly across the substrate. This dendritic morphology is due to the ACNTs as Sb is co-deposited onto the copper foam and the ACNTs and a similar morphology was seen in Chapter 3 for the Sb/ACNT thin film depositions.[34] At the peaks of the struts fractured platelets were also found and demonstrates that both the Sb and Sb/ACNT deposition require optimization in developing more conformal and robust coatings.

To improve mass transport in solution, the temperature of the electrodeposition was increased to 60˚C. In this study only the Sb/ACNT deposition was tested due to the more uniform coating seen at the room temperature studies. Additionally, ACNTs were included in the deposition to help mitigate issues such as mechanical pulverization and loss of electrically conductive as the electrode experiences volume expansion. As such, we wanted to further develop the deposition parameters for Sb/ACNT because we hypothesize that it will have better electrochemical performance. When Sb/ACNT was deposited at 60˚C the uniformity of the deposition substantially increased, **Figure 5.4**. Areas of bare copper were not found, and fragile platelets were no longer seen. In certain regions, **Figure 5.4a** and **Figure 5.4d**, the deposition looks rather uniform across all areas of the strut even through the depth of the foam. We predict that the rise in temperature is aiding mass transport across the foam and allowing for the deposition of a more uniform layer. However, in areas closer to the edge of the foam, Sb/ACNT heavily deposited onto the peaks of the struts. This increase in deposition at the edges of the foam may be due to placement of the foam in regard to the stir bar. Through the whole deposition process, the solution is stirred at a gentle rate to force movement of solution species across the substrate. If areas of the foam, such as the edges or corners, are in closer proximity of the stir bar or in a certain area of the vortex created by stirring then convection is the dominate mode of mass transport. Convection can disrupt the ion concentration gradient and lead to non-uniform deposition. Rotating disk electrodes are more reproducible and this parameter will be tested in future studies.[57] There are also regions with more dendritic growth towards the edges of the foam, **Figure 5.4c**, where the same effects of convection are expected. The composition of the film appears to be fairly Sb rich through EDS analysis, **Figure 5.5**, and further structural characterization is required to determine if higher deposition temperatures are promoting copper diffusion into the deposited substrate. Copper

diffusion into the substrate or at the interface between the substrate and deposit could promote better adhesion to the foam but at a cost to mechanical robustness. Previous studies in our group have identified the formation of Kirkendall voids as copper diffuses into the electrodeposited Sb substrate and leads to mechanical instability of the electrode.[58] Interestingly, nitrogen is also picked up in the elemental mapping and could be associated with the amine functional group on the ACNTs or the CTAB. Our X-ray Photoelectron Spectroscopy (XPS) in Chapter 2 and 3 do not show any nitrogen binding environments related to CTAB in the deposition and therefore we hypothesize that the ACNTs are the major source of nitrogen in the EDS maps.

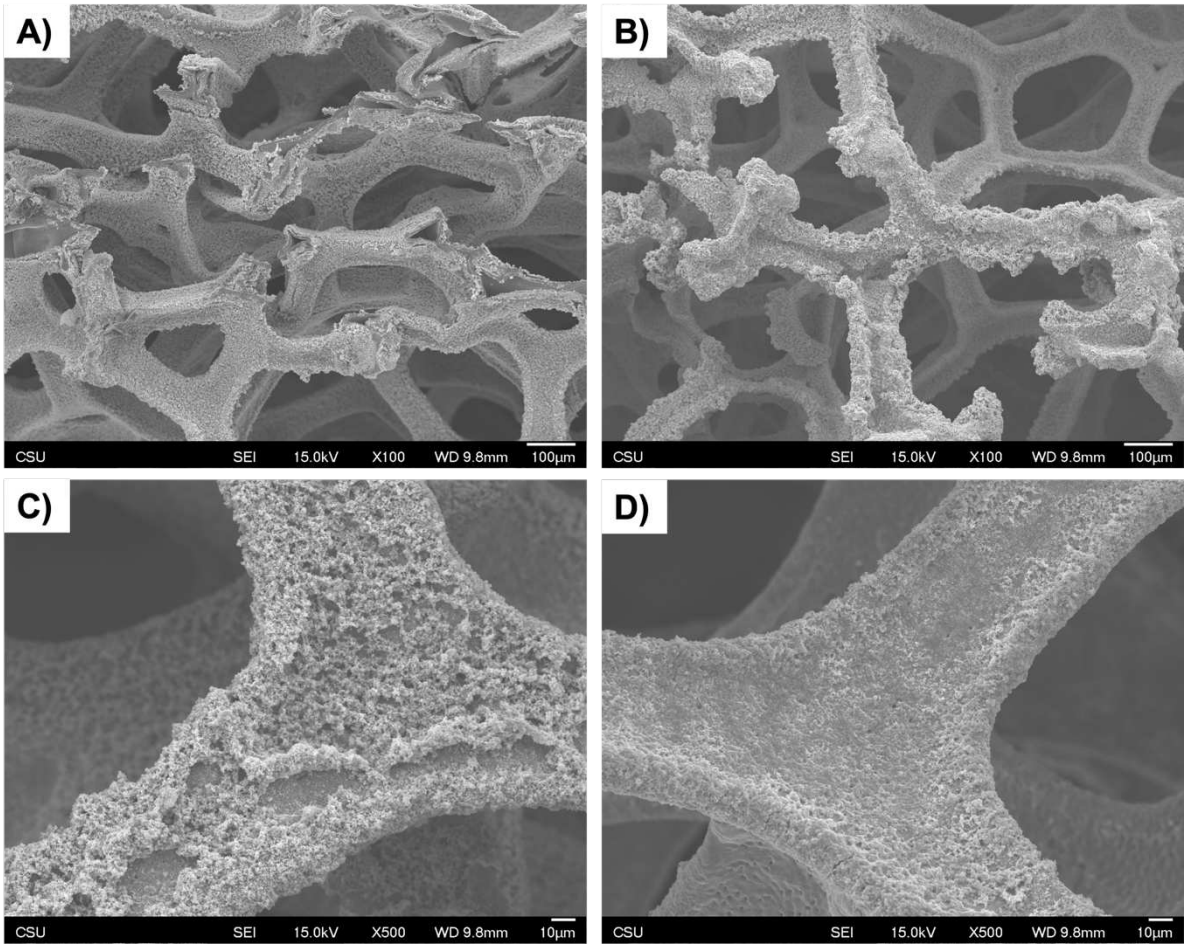

Figure 5.4 Cross-section SEM images of electrodeposited Sb/ACNT onto a copper foam substrate at 60˚C. Images were taken on the same sample in different areas and various magnifications.

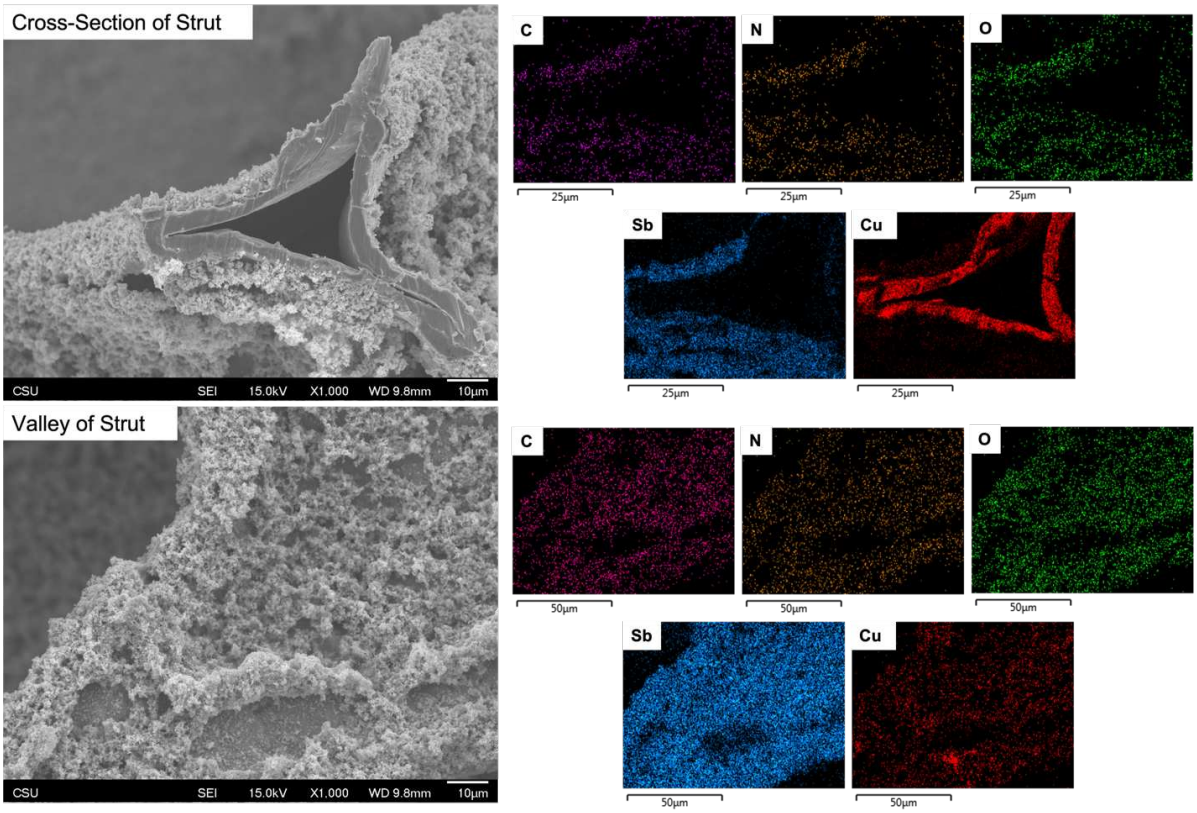

Figure 5.5 Cross-section SEM of strut (top) and the valley of strut (bottom) and elemental mapping.

Although electrodeposition parameters still need to be optimized, we wanted to test the electrochemical performance the Sb/ACNT foam that was deposited at 60˚C to create a baseline to understand how improvements in the deposition are influencing the performance metrics. Because the surface area of the foams is so high (a parameter we hope to test in the future through the determination of the electrochemical surface area experiments show using techniques shown in Chapter 2) a higher amount of electrolyte is required to thoroughly wet the surface of the foam and facilitate ion transport. The excess amount of electrolyte cannot be accommodated in the Swagelok configurations used in the previous chapters and pouch cells were used instead.

The electrochemical performance of two different Sb/ACNT foams were compared to an Sb thin film and the capacity and cycle life were quite poor, **Figure 5.6a** and **Figure 5.6b**. The initial gravimetric capacity for both films was well below the theoretical capacity (660 mAh/g)

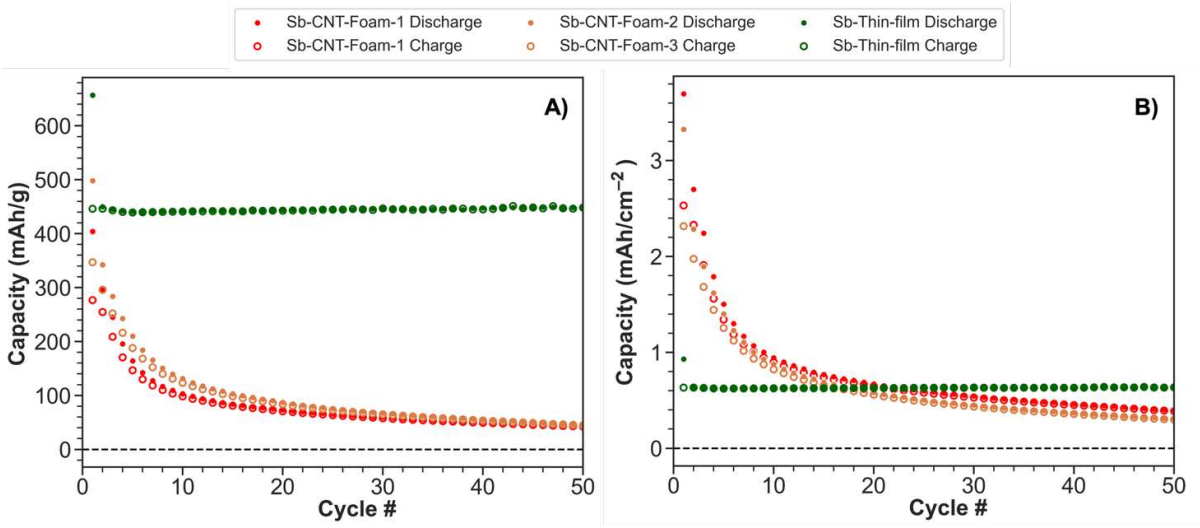

Figure 5.6 A comparison of the cycle life data of two Sb/ACNT copper foams (red and orange) and an electrodeposited thin film of Sb on a textured copper substrate. Capacities were normalized with mass (A) and footprint area of the electrode (B) to demonstrate the potential to achieve higher energy densities with a smaller footprint for the 3D foam electrode. All electrodes were cycled against sodium metal at a rate of C/5 with a 1M $NaClO_4$ PC 5% FEC electrolyte.

and rapidly declined in the first 10 cycles. The lower initial capacity could be due to a variety of reasons, such as loss of active material through battery assembly, inaccurate determination of active mass due to inactive components in the electrode, or excessive underutilization of active material. The capacity continued to steadily decline to about 40 mAh/g. Although the capacity retention was poor, it did not immediately decline to zero and elucidates that not all of the deposited active material was lost in mechanical pulverization. In the literature it is common to report the area capacity of 3D electrodes and batteries, where the capacity is normalized to the footprint area of the electrode or full cell. In **Figure 5.4b**, the initial capacity of the foam electrodes was approximately three times higher than the thin film and demonstrates the potential to improve energy density in a smaller footprint area by utilizing the height of the electrode.

When comparing the sodiation/desodiation reactions of the two architectures, differences are seen in peak broadness, and redox potential at which the reactions occur, **Figure 5.7**. The sodiation reactions of the foam are all slightly shifted to more negative reduction potentials and

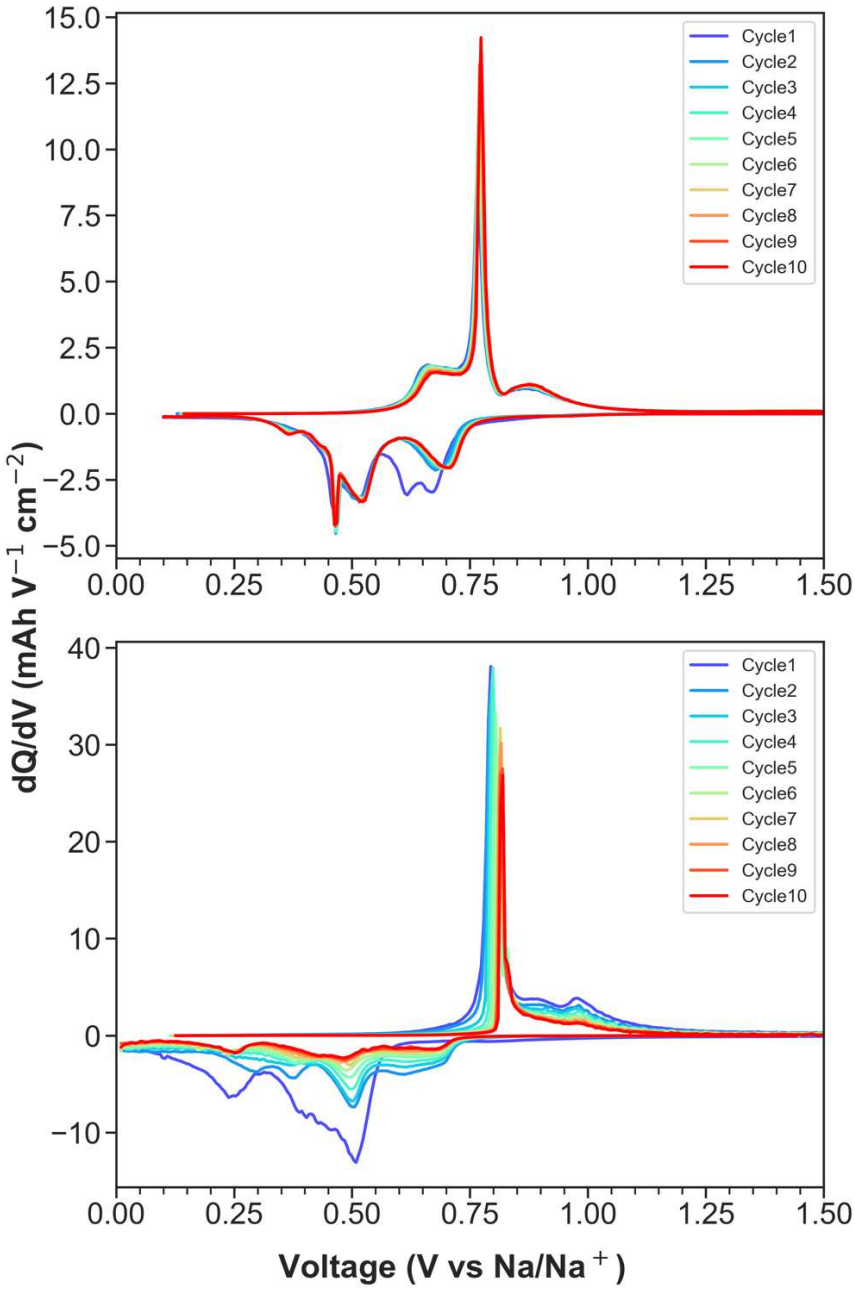

Figure 5.7 Differential capacity analysis of an electrodeposited Sb thin film (A) and an electrodeposited Sb/ACNT foam. Both electrodes were cycled against sodium metal at a rate of C/5 with a 1M NaClO4 PC 5% FEC electrolyte.

continue to shift upon further cycling. This shift in reduction potentials is likely due to kinetic limitations related to impeding ion transport in the foam. We hypothesis that non-uniform thicknesses throughout the film are present, shown in **Figure 5.2**, and create large sodium

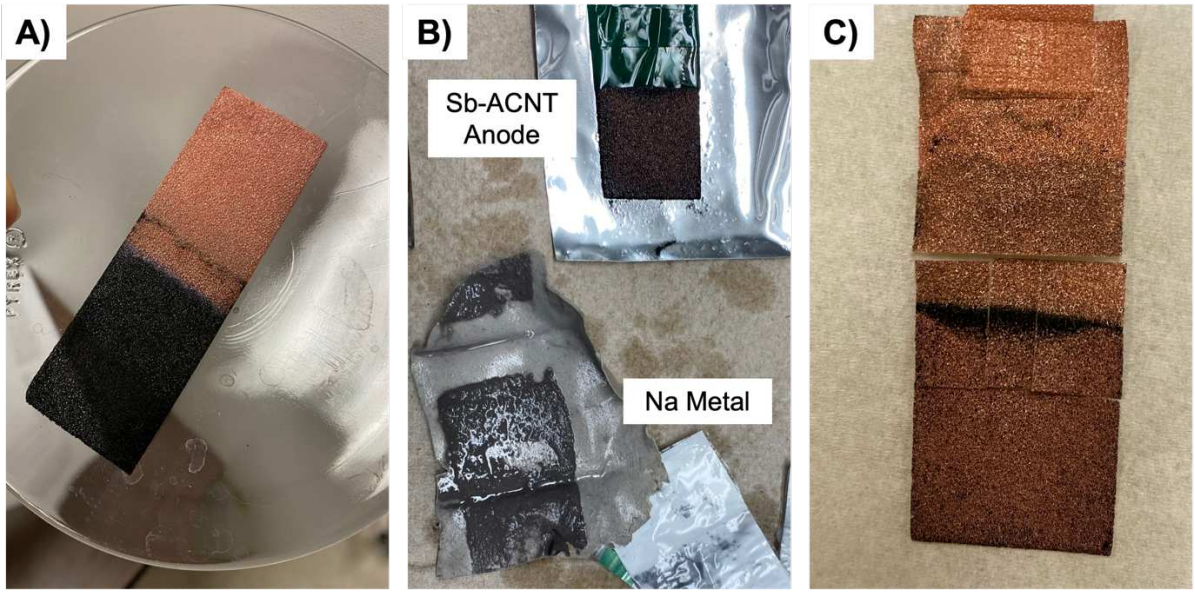

Figure 5.8 Optical images of the freshly deposited Sb/ACNT foam before cycling (A), the Sb/ACNT foam after cycling for 300 cycles (B) and the Sb/ACNT foam after rinsing with isopropanol. From left to right the color of the electrode brightness to reveal the original orange hue of the copper foam before deposition symbolizing that significant amounts of active material are lost when the Sb/ACNT foam is cycled.

concentration gradients throughout areas in the struts. Limitations in sodium ion transport are also leading to peak broadness, where broader peaks signify sluggish electron transfer reactions similar to cyclic voltammetry. Additionally, sodium ion concentration gradients across the substrate signify that different sodiation reactions are occurring simultaneously and could also be leading to poor peak resolution. Alternative hypotheses are related to the excessive SEI formation on the surface the surface of the electrode that could also be introducing higher interfacial impedances and rate limiting sodium ion diffusion from the bulk electrolyte solution into the electrode. Due to the high surface area of the foam electrodes and continues pulverization of active material, SEI formation occurs more rapidly, and electrolyte optimization is crucial to either reduce the formation of SEI or create an SEI with better properties (composition, thickness, elasticity). In future studies we plan to couple electrolyte optimization with electrochemical impedance

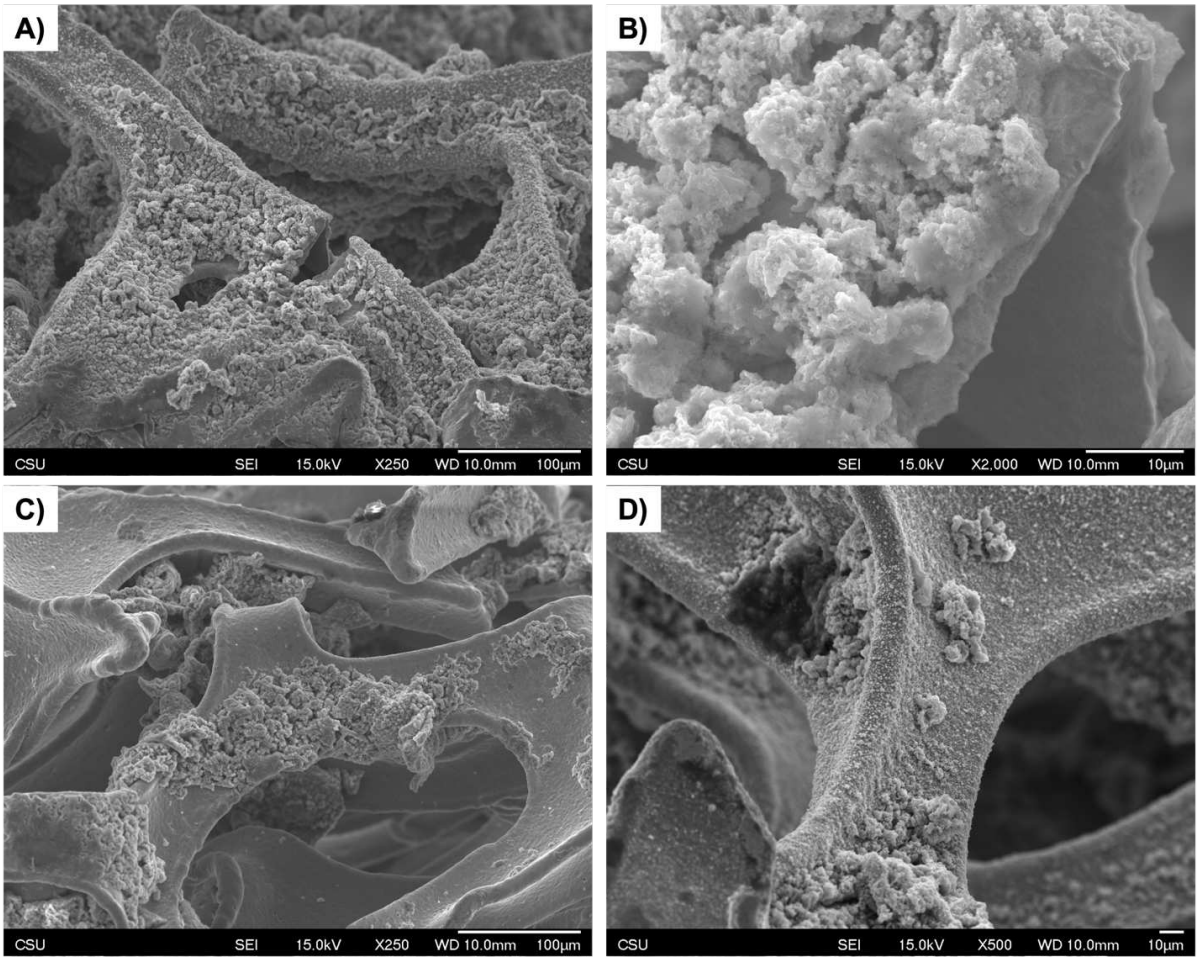

Figure 5.9 Cross-section SEM images of the Sb/ACNT foam after 300 cycles across various areas of the electrode. Due to substantial loss of active material, the bare copper substrate is readily seen and only a few agglomerates of the Sb/ACNT deposition remain.

spectroscopy to decrease interfacial resistance between the bulk electrode and the electrolyte solution and improve rate capabilities.

To understand the rapid decline in capacity of the Sb/ACNT foams ex situ characterization through SEM was conducted. The foam electrodes were disassembled and appeared discolored when compared to the freshly deposited foam **Figure 5.8**. When rinsing the electrode with isopropanol to remove remaining electrolyte and the SEI an excessive amount of active material was also lost in the wash, **Figure 5.8c**. This loss of active material is representative of delamination from the copper substrate or aggressive pulverization upon cycling. As an alternative hypothesis, surface

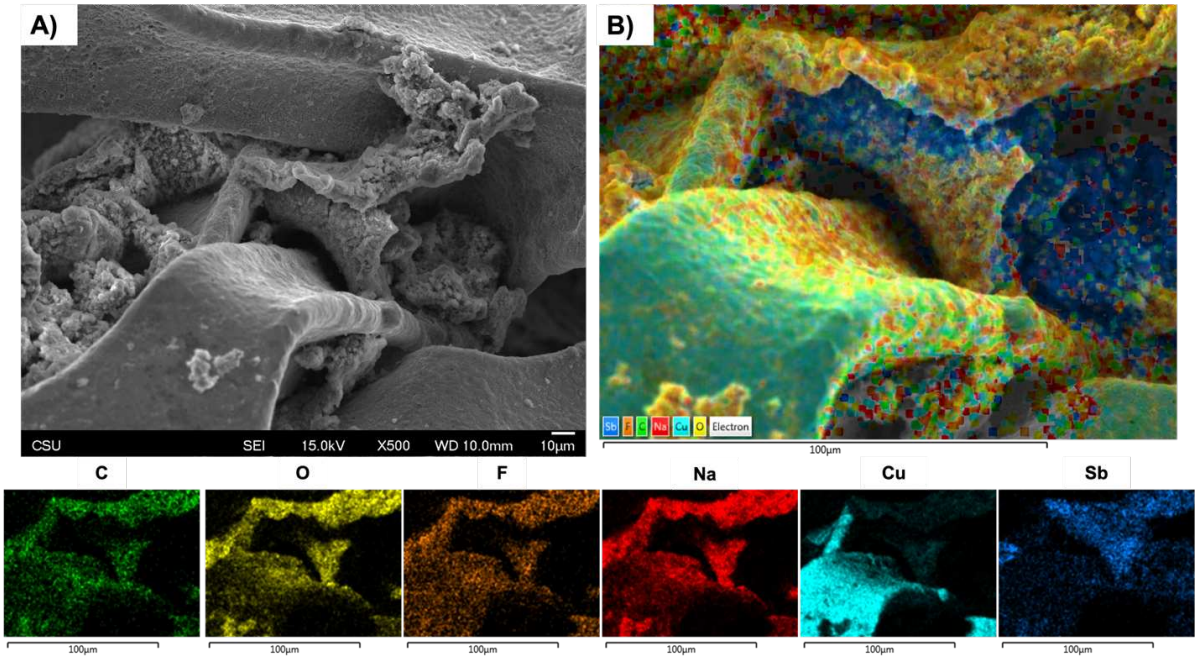

Figure 5.10 Cross-section SEM image of the Sb/ACNT foam after 300 cycles (A) and elemental mapping of C, O, F, Na, Cu, and Sb environments. On this area of the foam delamination of the Sb/ACNT deposit is depicted by the peeling of Sb away from the copper substrate.

oxides may still be present causing poor adhesion between the deposit and the copper foam.[59] In future experiments, the copper foam will be cleaned in a piranha solution and then immediately used for deposition to ensure that the surface is pristine. Through imaging, pockets of Sb/ACNT were found scattered across the electrode and were primarily present in the valleys of the struts, **Figure 5.9**. In areas where large agglomerates of Sb/ACNT remained intact with the copper foam, the previous nodular morphological features had diminished which is representative of excessive pulverization. Interestingly, delamination was also seen, **Figure 5.10**, and elucidates that poor adhesion between the Sb/ACNT deposit and the substrate was the main form of active material loss and poor capacity retention. Additionally, SEI species composed of sodium salts and fluorinated species were seen over the exposed copper strut leading us to believe that the electrolyte is being rapidly consumed to form the SEI on the active material and the freshly exposed copper substrate. Overall, these preliminary results demonstrate that there is a lot of room

for improvement of the deposition of Sb-based anodes on 3D substrates and its electrochemical performance.

5.4 Outlook and Future Directions

In future studies we plan to continue to optimize electrodeposition parameters by tuning the electrodeposition bath composition and the experimental parameter of the deposition. Repeating chronoamperometry has a variety of parameters that can tuned such as the applied constant voltage, the step number and duration of the step.[43,53,60,61] Due to the geometric nature of metal foams the placement of electrodes during the deposition process is also critical. The placement of counter electrodes helps reduce IR drops across the electrochemical cell but due to the density of the foam the center and edges will all experience different current densities. Issues also arise in the depletion of Sb^{3+} concentration at the surface of the foam as the rate of diffusion and migration of ions to the surface and center of the foam will greatly vary. Thus, the composition of the electrodeposition bath and electrochemical parameters of the deposition must be optimized in tandem.

Additionally, the extra surface area that comes from a 3D electrode structure leads to significant buildup of the SEI which leads to shortening of battery lifetimes through impeding ion transfer and contributions to mechanical pulverization.[62,63] Furthermore, in certain 3D architectures, the SEI can obliterate the morphology of the anode over multiple cycles through excessive growth as seen in **Figure 10**.[37] It is important to recognize that although one action can be beneficial to one area of the battery, it can have negative consequences on other components as the whole cell is interconnected. Therefore, improvements on electrochemical performance of 3D electrodes may not only be hindered by uniformity of the deposition but also by electrolyte choice. To improve performance metrics of these electrodes for their implementation into full cells, one

must understand the impact 3D architectures have on the SEI formation and if there are methods to better understand electrolyte degradation on the surfaces of these advanced structures.

As previously mentioned, 3D batteries experience numerous issues with inhomogeneous current densities, lithium concentration gradients, and underutilization of electrode materials that are due to material composition and geometric factors. These issues have also been highlighted through computational studies, that have shown there are hot spots with highly concentrated current densities that are dependent on the architecture in question.[5,64,65] Inhomogeneous current densities may also arise from increasing the height of certain configurations, such as nanorods or pillars and has been found to lead to underutilization of electrode materials that then leads to lower energy densities as demonstrated by Zadin et al., and Talin et al.[47,64] Over utilization of electrode materials can also occur due to current density hotspots and can lead to mechanical degradation related to volume expansion or other physical effects. Therefore, these physical parameters must be taken into account in computational modeling to demonstrate the full effect of inhomogeneous current densities to systematically improve energy density and the overall performance of 3D batteries.

5.5 References

(1) Atzori, L.; Iera, A.; Morabito, G. The Internet of Things: A Survey. *Comput. Netw.* **2010**, *54* (15), 2787–2805. https://doi.org/10.1016/j.comnet.2010.05.010.

(2) Swan, M. Sensor Mania! The Internet of Things, Wearable Computing, Objective Metrics, and the Quantified Self 2.0. *J. Sens. Actuator Netw.* **2012**, *1* (3), 217–253. https://doi.org/10.3390/jsan1030217.

(3) Masias, A.; Marcicki, J.; Paxton, W. A. Opportunities and Challenges of Lithium Ion Batteries in Automotive Applications. *ACS Energy Lett.* **2021**, *6* (2), 621–630. https://doi.org/10.1021/acsenergylett.0c02584.

(4) Miranda, D.; Costa, C. M.; Almeida, A. M.; Lanceros-Méndez, S. Computer Simulations of the Influence of Geometry in the Performance of Conventional and Unconventional Lithium-Ion Batteries. *Appl. Energy* **2016**, *165*, 318–328. https://doi.org/10.1016/j.apenergy.2015.12.068.

(5) McKelvey, K.; Brunet Cabré, M.; Esmeraldo Paiva, A. Continuum Simulations for Microscale 3D Batteries. *Curr. Opin. Electrochem.* **2020**, *21*, 76–83. https://doi.org/10.1016/j.coelec.2020.01.008.

(6) Long, J. W.; Dunn, B.; Rolison, D. R.; White, H. S. Three-Dimensional Battery Architectures. *Chem. Rev.* **2004**, *104* (10), 4463–4492. https://doi.org/10.1021/cr020740l.

(7) Elul, S.; Cohen, Y.; Aurbach, D. The Influence of Geometry in 2D Simulation on the Charge/Discharge Processes in Li-Ion Batteries. *J. Electroanal. Chem.* **2012**, *682*, 53–65. https://doi.org/10.1016/j.jelechem.2012.06.015.

(8) Hung, C. Modeling Current Density Non-Uniformities to Understand High-Rate Limitations in 3D Interdigitated Lithium-Ion Batteries Modeling Current Density Non-Uniformities to Understand High- Rate Limitations in 3D Interdigitated Lithium-Ion Batteries. **2021**. https://doi.org/10.1149/1945-7111/ac2ac5.

(9) Hung, C.-H.; Huynh, P.; Teo, K.; Cobb, C. L. Are Three-Dimensional Batteries Beneficial? Analyzing Historical Data to Elucidate Performance Advantages.

(10) Horowitz, Y.; Strauss, E.; Peled, E.; Golodnitsky, D. How to Pack a Punch – Why 3D Batteries Are Essential. *Isr. J. Chem.* **2021**, *61* (1–2), 38–50. https://doi.org/10.1002/ijch.202100001.

(11) Roberts, M.; Johns, P.; Owen, J.; Brandell, D.; Edstrom, K.; El Enany, G.; Guery, C.; Golodnitsky, D.; Lacey, M.; Lecoeur, C.; Mazor, H.; Peled, E.; Perre, E.; Shaijumon, M. M.; Simon, P.; Taberna, P. L. 3D Lithium Ion Batteries - From Fundamentals to Fabrication. *J. Mater. Chem.* **2011**, *21* (27), 9876–9890. https://doi.org/10.1039/c0jm04396f.

(12) Arthur, T. S.; Bates, D. J.; Cirigliano, N.; Johnson, D. C.; Malati, P.; Mosby, J. M.; Perre, E.; Rawls, M. T.; Prieto, A. L.; Dunn, B. Three-Dimensional Electrodes and Battery Architectures. *MRS Bull.* **2011**, *36* (July), 523–531. https://doi.org/10.1557/mrs.2011.156.

(13) Liu, L.; Zhao, H.; Lei, Y. Advances on Three-Dimensional Electrodes for Micro-Supercapacitors : A Mini-Review. **2019**, No. April, 74–84. https://doi.org/10.1002/inf2.12007.

(14) Long, J. W.; Dunn, B.; Rolison, D. R.; White, H. S. 3D Architectures for Batteries and Electrodes. *Adv. Energy Mater.* **2020**, *10*, 2002457–2002457. https://doi.org/10.1002/aenm.202002457.

(15) Ferrari, S.; Loveridge, M.; Beattie, S. D.; Jahn, M.; Dashwood, R. J.; Bhagat, R. Latest Advances in the Manufacturing of 3D Rechargeable Lithium Microbatteries. *J. Power Sources* **2015**, *286*, 25–46. https://doi.org/10.1016/j.jpowsour.2015.03.133.

(16) Rolison, D. R.; Long, J. W.; Lytle, J. C.; Fischer, A. E.; Rhodes, C. P.; Mc Evoy, T. M.; Bourg, M. E.; Lubers, A. M. Multifunctional 3D Nanoarchitectures for Energy Storage and Conversion. *Chem. Soc. Rev.* **2009**, *38* (1), 226–252. https://doi.org/10.1039/b801151f.

(17) Han, L.; Hsieh, C.-T.; Chandra Mallick, B.; Li, J.; Ashraf Gandomi, Y. Recent Progress and Future Prospects of Atomic Layer Deposition to Prepare/Modify Solid-State Electrolytes and Interfaces between Electrodes for next-Generation Lithium Batteries. *Nanoscale Adv.* **2021**, *3* (10), 2728–2740. https://doi.org/10.1039/D0NA01072C.

(18) Tolganbek, N.; Mentbayeva, A.; Serik, N.; Batyrgali, N.; Naizakarayev, M.; Kanamura, K.; Bakenov, Z. Design and Preparation of Thin Film Gel Polymer Electrolyte for 3D Li-Ion Battery. *J. Power Sources* **2021**, *493*. https://doi.org/10.1016/j.jpowsour.2021.229686.

(19) Lyu, Z.; Lim, G. J. H.; Koh, J. J.; Li, Y.; Ma, Y.; Ding, J.; Wang, J. J.; Hu, Z.; Wang, J. J.; Chen, W.; Chen, Y. Design and Manufacture of 3D-Printed Batteries. **2021**, 89–114. https://doi.org/10.1016/j.joule.2020.11.010.

(20) Jetybayeva, A.; Uzakbaiuly, B.; Mukanova, A.; Myung, S. T.; Bakenov, Z. Recent Advancements in Solid Electrolytes Integrated into All-Solid-State 2D and 3D Lithium-Ion Microbatteries. *J. Mater. Chem. A* **2021**, *9* (27), 15140–15178. https://doi.org/10.1039/d1ta02652f.

(21) Valvo, M.; Roberts, M.; Oltean, G.; Sun, B.; Rehnlund, D.; Brandell, D.; Nyholm, L.; Gustafsson, T.; Edström, K. Electrochemical Elaboration of Electrodes and Electrolytes for 3D Structured Batteries. *J. Mater. Chem. A* **2013**, *1* (32), 9281–9293. https://doi.org/10.1039/c3ta11921a.

(22) Asfaw, H. D.; Roberts, M. R.; Tai, C.-W.; Younesi, R.; Valvo, M.; Nyholm, L.; Edström, K. Nanosized LiFePO $_4$ -Decorated Emulsion-Templated Carbon Foam for 3D Micro

Batteries: A Study of Structure and Electrochemical Performance. *Nanoscale* **2014**, *6* (15), 8804–8813. https://doi.org/10.1039/C4NR01682C.

(23) Lai, J.; Nsabimana, A.; Luque, R.; Xu, G. 3D Porous Carbonaceous Electrodes for Electrocatalytic Applications. *Joule* **2018**, *2* (1), 76–93. https://doi.org/10.1016/j.joule.2017.10.005.

(24) Ellis, B. L.; Knauth, P.; Djenizian, T. Three-Dimensional Self-Supported Metal Oxides for Advanced Energy Storage. *Adv. Mater.* **2014**, *26* (21), 3368–3397. https://doi.org/10.1002/adma.201306126.

(25) Moitzheim, S.; Balder, J. E.; Ritasalo, R.; Ek, S.; Poodt, P.; Unnikrishnan, S.; De Gendt, S.; Vereecken, P. M. Toward 3D Thin-Film Batteries: Optimal Current-Collector Design and Scalable Fabrication of TiO2 Thin-Film Electrodes. *ACS Appl. Energy Mater.* **2019**, *2* (3), 1774–1783. https://doi.org/10.1021/acsaem.8b01905.

(26) Tan, S.; Perre, E.; Gustafsson, T.; Brandell, D. A Solid State 3-D Microbattery Based on Cu 2Sb Nanopillar Anodes. In *Solid State Ionics*; 2012; Vol. 225, pp 510–512. https://doi.org/10.1016/j.ssi.2011.11.005.

(27) Pearse, A. J.; Schmitt, T. E.; Fuller, E. J.; El-Gabaly, F.; Lin, C.-F.; Gerasopoulos, K.; Kozen, A. C.; Talin, A. A.; Rubloff, G.; Gregorczyk, K. E. Nanoscale Solid State Batteries Enabled by Thermal Atomic Layer Deposition of a Lithium Polyphosphazene Solid State Electrolyte. *Chem. Mater.* **2017**, *29* (8), 3740–3753. https://doi.org/10.1021/acs.chemmater.7b00805.

(28) Ashby, D. S.; Choi, C. S.; Edwards, M. A.; Talin, A. A.; White, H. S.; Dunn, B. S. High-Performance Solid-State Lithium-Ion Battery with Mixed 2D and 3D Electrodes. *ACS Appl. Energy Mater.* **2020**, *3* (9), 8402–8409. https://doi.org/10.1021/acsaem.0c01029.

(29) Wang, Z.; Jing, L.; Zheng, X.; Xu, Z.; Yuan, Y.; Liu, X.; Fu, A.; Guo, Y. G.; Li, H. Microspheres of Si@Carbon-CNTs Composites with a Stable 3D Interpenetrating Structure Applied in High-Performance Lithium-Ion Battery. *J. Colloid Interface Sci.* **2023**, *629*, 511–521. https://doi.org/10.1016/j.jcis.2022.09.087.

(30) Nurpeissova, A.; Murat, E.; Adi, A.; Bakenov, Z. 3D Intermetallic Anodes for Lithium-Ion Batteries. *Mater. Today Proc.* **2018**, *5* (11), 22877–22881. https://doi.org/10.1016/j.matpr.2018.07.103.

(31) Baggetto, L.; Niessen, R. A. H.; Roozehoom, F.; Notten, P. H. L. High Energy Density All-Solid-State Batteries: A Challenging Concept towards 3D Integration. *Adv. Funct. Mater.* **2008**, *18* (7), 1057–1066. https://doi.org/10.1002/adfm.200701245.

(32) Zhang, T.; Ran, F. Design Strategies of 3D Carbon-Based Electrodes for Charge/Ion Transport in Lithium Ion Battery and Sodium Ion Battery. *Adv. Funct. Mater.* **2021**, *31* (17), 2010041. https://doi.org/10.1002/adfm.202010041.

(33) Sadana, Y. N.; Singh, J. P.; Kumar, R. Electrodeposition of Antimony and Antimony Alloys- A Review. *Surf. Technol.* **1985**, *24* (4), 319–353. https://doi.org/10.1016/0376-4583(85)90053-6.

(34) Nieto, K.; Gimble, N. J.; Rudolph, L. J.; Kale, A. R.; Prieto, A. L. Electrodeposition vs Slurry Casting: How Fabrication Affects Electrochemical Reactions of Sb Electrodes in Sodium-Ion Batteries. *J. Electrochem. Soc.* **2022**, *169* (5), 050537. https://doi.org/10.1149/1945-7111/ac6b5e.

(35) Schulze, M. C.; Belson, R. M.; Kraynak, L. A.; Prieto, A. L. Electrodeposition of Sb/CNT Composite Films as Anodes for Li- and Na-Ion Batteries. *Energy Storage Mater.* **2020**, *25* (June 2019), 572–584. https://doi.org/10.1016/j.ensm.2019.09.025.

(36) Ma, J.; Prieto, A. L. Electrodeposition of Pure Phase SnSb Exhibiting High Stability as a Sodium-Ion Battery Anode. *Chem. Commun.* **2019**, *55* (48), 6938–6941. https://doi.org/10.1039/c9cc00001a.

(37) Jackson, E. D.; Prieto, A. L. Copper Antimonide Nanowire Array Lithium Ion Anodes Stabilized by Electrolyte Additives. *ACS Appl. Mater. Interfaces* **2016**, *8* (44), 30379–30386. https://doi.org/10.1021/acsami.6b08033.

(38) Jackson, E. D.; Mosby, J. M.; Prieto, A. L. Evaluation of the Electrochemical Properties of Crystalline Copper Antimonide Thin Film Anodes for Lithium Ion Batteries Produced by Single Step Electrodeposition. *Electrochimica Acta* **2016**, *214*, 253–264. https://doi.org/10.1016/j.electacta.2016.07.126.

(39) Majidzade, V. A.; Guliyev, P. H.; Aliyev, A. S.; Elrouby, M.; Tagiyev, D. B. Electrochemical Characterization and Electrode Kinetics for Antimony Electrodeposition from Its Oxychloride Solution in the Presence of Tartaric Acid. *J. Mol. Struct.* **2017**, *1136*, 7–13. https://doi.org/10.1016/j.molstruc.2017.01.082.

(40) Liu, W.; Yang, T. Z.; Zhou, Q. H.; Zhang, D. C.; Lei, C. M. Electrodeposition of Sb(III) in Alkaline Solutions Containing Xylitol. *Trans. Nonferrous Met. Soc. China Engl. Ed.* **2012**, *22* (4), 949–957. https://doi.org/10.1016/S1003-6326(11)61269-7.

(41) Liu, Z.; Cheng, J.; Höfft, O.; Endres, F. In Situ XPS Study of Template-Free Electrodeposition of Antimony Nanowires from an Ionic Liquid. *J. Solid State Electrochem.* **2022**, No. 0123456789. https://doi.org/10.1007/s10008-022-05321-9.

(42) Aroyo, M. Theoretical and Practical Aspects of Electrodeposition of Metal Coatings with Improved Properties (Part 1). *Plat. Surf. Finish.* **1998**, *85* (8), 69–76.

(43) Gamburg, Y. D.; Zangari, G. *Theory and Practice of Metal Electrodeposition*; 2011; Vol. 1.

(44) Elgrishi, N. N.; Rountree, K. J.; Mccarthy, B. D.; Rountree, E. S.; Eisenhart, T. T.; Dempsey, J. L. A Practical Beginner's Guide to Cyclic Voltammetry. *J. Chem. Educ.* **2018**, *95* (2), 197–206. https://doi.org/10.1021/acs.jchemed.7b00361.

(45) Ghosh, J. C.; Kappana, A. N. Electrodeposition of Antimony. *J. Phys. Chem. C* **1924**, *28* (2), 149–160.

(46) AL-Esary, H. F. Influence of Additives on Electrodeposition of Metals from Deep Eutectic Solvents. **2017**, No. November, 1–267.

(47) Zadin, V.; Kasemägi, H.; Aabloo, A.; Brandell, D. Modelling Electrode Material Utilization in the Trench Model 3D-Microbattery by Finite Element Analysis. *J. Power Sources* **2010**, *195* (18), 6218–6224. https://doi.org/10.1016/j.jpowsour.2010.02.056.

(48) Zadin, V.; Brandell, D.; Kasemägi, H.; Aabloo, A.; Thomas, J. O. Finite Element Modelling of Ion Transport in the Electrolyte of a 3D-Microbattery. *Solid State Ion.* **2011**, *192* (1), 279–283. https://doi.org/10.1016/j.ssi.2010.02.007.

(49) Priimägi, P.; Brandell, D.; Srivastav, S.; Aabloo, A.; Kasemägi, H.; Zadin, V. Optimizing the Design of 3D-Pillar Microbatteries Using Finite Element Modelling. *Electrochimica Acta* **2016**, *209*, 138–148. https://doi.org/10.1016/j.electacta.2016.05.047.

(50) Zhang, W.; Guebey, J.; Toben, M. A Novel Electrolyte for the High Speed Electrodeposition of Bright Pure Tin at Elevated Temperatures. *Met. Finish.* **2011**, *109* (1), 13–19. https://doi.org/10.1016/S0026-0576(11)00006-7.

(51) Jung, A.; Natter, H.; Hempelmann, R.; Diebels, S.; Koblischka, M. R.; Hartmann, U.; Lach, E. Electrodeposition of Nanocrystalline Metals on Open Cell Metal Foams: Improved Mechanical Properties. *ECS Trans.* **2010**, *25* (41), 165. https://doi.org/10.1149/1.3422510.

(52) Pu, W.; He, X.; Ren, J.; Wan, C.; Jiang, C. Electrodeposition of Sn–Cu Alloy Anodes for Lithium Batteries. *Electrochimica Acta* **2005**, *50* (20), 4140–4145. https://doi.org/10.1016/j.electacta.2005.01.041.

(53) Beattie, S. D.; Dahn, J. R. Single Bath, Pulsed Electrodeposition of Copper-Tin Alloy Negative Electrodes for Lithium-Ion Batteries. *J. Electrochem. Soc.* **2003**, *150* (7), A894. https://doi.org/10.1149/1.1577336.

(54) Claudel, F.; Stein, N.; Allain, N.; Tidu, A.; Hajczak, N.; Lallement, R.; Close, D. Pulse Electrodeposition and Characterization of Zn–Mn Coatings Deposited from Additive-Free Chloride Electrolytes. *J. Appl. Electrochem.* **2019**, *49* (4), 399–411. https://doi.org/10.1007/s10800-019-01295-1.

(55) Saadi-motaallegh, S.; Javanbakht, M.; Omidvar, H.; Habibzadeh, S. Pulsed Electro-Synthesized Tunable Crystallite Sizes ZnMn2O4/Mn2O3 Nanocomposite as High-

Performance Cathode Material for Aqueous Zinc-Ion Batteries. *J. Alloys Compd.* **2022**, *914*, 165249–165249. https://doi.org/10.1016/j.jallcom.2022.165249.

(56) Lee, S. W.; Ryu, I.; Nix, W. D.; Cui, Y. Fracture of Crystalline Germanium during Electrochemical Lithium Insertion. *Extreme Mech. Lett.* **2015**, *2*, 15–19. https://doi.org/10.1016/j.eml.2015.01.009.

(57) Oldham, K. B.; Zoski, C. G. Chapter 2 Mass Transport to Electrodes. In *Comprehensive Chemical Kinetics*; Bamford, C. H., Compton, R. G., Eds.; Electrode Kinetics: Principles and Methodology; Elsevier, 1986; Vol. 26, pp 79–143. https://doi.org/10.1016/S0069-8040(08)70026-8.

(58) Schulze, M. C.; Schulze, R. K.; Prieto, A. L. Electrodeposited Thin-Film Cu_xSb Anodes for Li-Ion Batteries: Enhancement of Cycle Life via Tuning of Film Composition and Engineering of the Film-Substrate Interface. *J. Mater. Chem. A* **2018**, *6*, 12708. https://doi.org/10.1039/c8ta01798k.

(59) B08 Committee. *Guide for Cleaning Metals Prior to Electroplating*; ASTM International. https://doi.org/10.1520/B0322-99R14.

(60) Monti, P.; Bacciu, A.; Arrigo, P.; Marceddu, S.; Migheli, Q.; Serra, P. A.; Rocchitta, G. Chronoamperometry as Effective Alternative Technique for Electro-Synthesis of Ortho-Phenylendiamine Permselective Films for Biosensor Applications. *J. Appl. Polym. Sci.* **2020**, *137* (39), 49172. https://doi.org/10.1002/app.49172.

(61) Schulz, E. N.; Salinas, D. R.; García, S. G. Electrodeposition of Rhodium onto a Pre-Treated Glassy Carbon Surface. *Electrochem. Commun.* **2010**, *12* (4), 583–586. https://doi.org/10.1016/j.elecom.2010.02.005.

(62) An, S. J.; Li, J.; Daniel, C.; Mohanty, D.; Nagpure, S.; Wood, D. L. The State of Understanding of the Lithium-Ion-Battery Graphite Solid Electrolyte Interphase (SEI) and Its Relationship to Formation Cycling. *Carbon* **2016**, *105*, 52–76. https://doi.org/10.1016/j.carbon.2016.04.008.

(63) Peled, E.; Menkin, S. Review—SEI: Past, Present and Future. *J. Electrochem. Soc.* **2017**, *164* (7), A1703–A1719. https://doi.org/10.1149/2.1441707jes.

(64) Talin, A. A.; Ruzmetov, D.; Kolmakov, A.; McKelvey, K.; Ware, N.; El Gabaly, F.; Dunn, B.; White, H. S. Fabrication, Testing, and Simulation of All-Solid-State Three-Dimensional Li-Ion Batteries. *ACS Appl. Mater. Interfaces* **2016**, *8* (47), 32385–32391. https://doi.org/10.1021/acsami.6b12244.

(65) Cobb, C. L.; Blanco, M. Modeling Mass and Density Distribution Effects on the Performance of Co-Extruded Electrodes for High Energy Density Lithium-Ion Batteries. *J. Power Sources* **2014**, *249*, 357–366. https://doi.org/10.1016/j.jpowsour.2013.10.084.

VI. OUTLOOK AND FUTURE DIRECTIONS: UNDERSTANDING THE DEGRADATION MECHANISM OF ALLOY-BASED BATTERY ELECTRODES[6]

6.1. Introduction

Alloy-based materials are of interest for lithium-ion (LIBs) and sodium-ion batteries (NIBs) because of their ability to store high quantities of lithium or sodium ions per unit of mass or volume, providing higher theoretical capacities. For example, silicon has a theoretical capacity of 4200 mAh/g in LIBs, and antimony has a theoretical capacity of 660 mAh/g in LIBs and NIBs.[1–4] However, their downfall is associated with the significant volume changes that occur during cycling that lead to the failure of the battery.[2–6] Silicon, for example, experiences a volume change of 310 % when fully lithiated, and antimony expands 293% when sodiated versus 135% when lithiated .[1,2,4,7] Additionally, common cathode materials like lithium metal oxides also experience volume changes (sometimes known as breathing) when accommodating for lithium ions, given it is at a much lesser degree. However, these changes still lead to strain and cracking in the electrode.[8,9] Mechanical instability in these electrodes causes fracturing, pulverization, or delamination from the current collector that then leads to loss of active material (decreases in capacity) and excessive solid electrolyte interphase (SEI) formation (decreases in capacity and rate capabilities).[1,7,10,11] These challenges require fundamental studies investigating the degradation mechanisms of alloying anodes and their impact on electrochemical performance to inform mitigation strategies.

[6] Optical and electrochemical data shown in this chapter are part of a submitted manuscript to *ACS Applied Engineering Materials*. (Rhys A. Otten, Kelly Nieto, Maxwell C. Schulze, Amy L. Prieto, *ACS Appl. Eng. Mater.*, **2023**) Rhys A. Otten developed the MATLAB code and methodology and wrote the manuscript. Kelly Nieto helped with data analysis, development of the project, and writing of the manuscript. Maxwell C. Schulze performed the experiment and collected the data. Amy L. Prieto helped with project development and writing of the manuscript.

Mitigation strategies to lessen the effects of mechanical degradation have been investigated and are currently being implemented in commercial batteries. Some standard techniques include nanostructuring the active material, optimizing the polymeric binder in the electrode composite, the inclusion of carbon additives to maintain electrical contact, and protective coatings.[10,12–18] These tactics have improved cycle life by creating void space in the electrode to alleviate mechanical stress or help maintain electrical contact even if cracking occurs. However, there are performance tradeoffs for each of these strategies, and there is still much room for additional studies to understand how exactly these techniques improve battery performance. For example, studies in our group have demonstrated how carbon nanotubes can influence the cycle life of antimony anodes in both LIBs and NIBs; the exact reason why this occurs is not well understood.[16] Carbon nanotubes are hypothesized to help maintain electrical conductivity as antimony begins to pulverize. However, the nanostructuring of antimony also occurs when it is co-deposited with CNTs, and this change in particle size and morphology could also help accommodate stress in the electrode.[10,19] Understanding how these strategies improve battery performance requires complex characterization techniques.

Characterization techniques that facilitate *in situ* and *in operando* experiments have gained popularity to track the sodiation/lithiation of electrode materials at the nanoscale.[9,11,20–23] A study by Gutiérrez-Kolar et al. used *in situ* transmission electron microscopy (TEM) and electron diffraction to track the sodiation mechanism of SnSb thin films.[24] In this work, they were able to watch chemical and electrochemical sodiation fronts and identified that significant grain restructuring and amorphization occurred along these diffusion fronts. Through this restructuring, fracturing can occur, leading to islands within the electrode at various stages of sodiation. This study highlights the power *in situ* characterization techniques provide in characterizing the

degradation mechanism. However, questions remain in extrapolating results at the nanoscale to applications in the bulk regime, including potential mitigation procedures.

A previous study in our group coupled ex situ scanning electron microscopy with electrochemistry to evaluate the electrochemical performance of electrodeposited Cu_2Sb.[25] By electrodepositing the Cu_2Sb electrode, they could control the stochiometric ratio of Cu:Sb and eliminate the need for conductive additives and binders. This synthetic control allowed them to study the intrinsic behavior of the film and begin to understand the failure mechanism of this alloy-based material. In this study, a Cu_2Sb electrode was cycled against lithium metal to specific phase transformations seen in the differential capacity analysis, **Figure 6.1b**. The potential was held at the reaction potential until equilibrium was reached, and its structure and morphology were then analyzed through *ex situ* powder X-ray diffraction (PXRD) and scanning electron microscopy (SEM). They successfully tracked the lithiation/delithiation reactions and monitored how volume expansion caused mechanical instability in these films, **Figure 6.1a-c**. As the film was lithiated, buckling of the film and delamination from the substrate was observed, likely to accommodate the large volume expansion during lithiation. The buckling subsided when the film was delithiated, but artifacts believed to be caused by trapped lithium in the Li_xCuSb phase remained. Additionally, large cracks appeared in the substrate after full delithiation and are likely caused by the evolution of high film stresses which were then imparted onto the substrate. This study was one of the first investigations to demonstrate the severity of fracturing in an alloy-based film at different points of the lithiation/delithiation process and explained the importance of visualizing the evolution of mechanical degradation on a bulk film across a more extended length scale. However, the implemented characterization techniques were done *ex situ,* and the cell was taken apart to remove the Cu_2Sb film, perform analysis, and then reassembled back into the cell to continue cycling. This

method of analysis could consequently influence the results due to the relaxation of the electrode and its air and moisture sensitivity.

Both studies provided vital information on the reaction and degradation mechanisms of the studied electrodes, but these findings are based on a tiny sliver of the whole picture as these

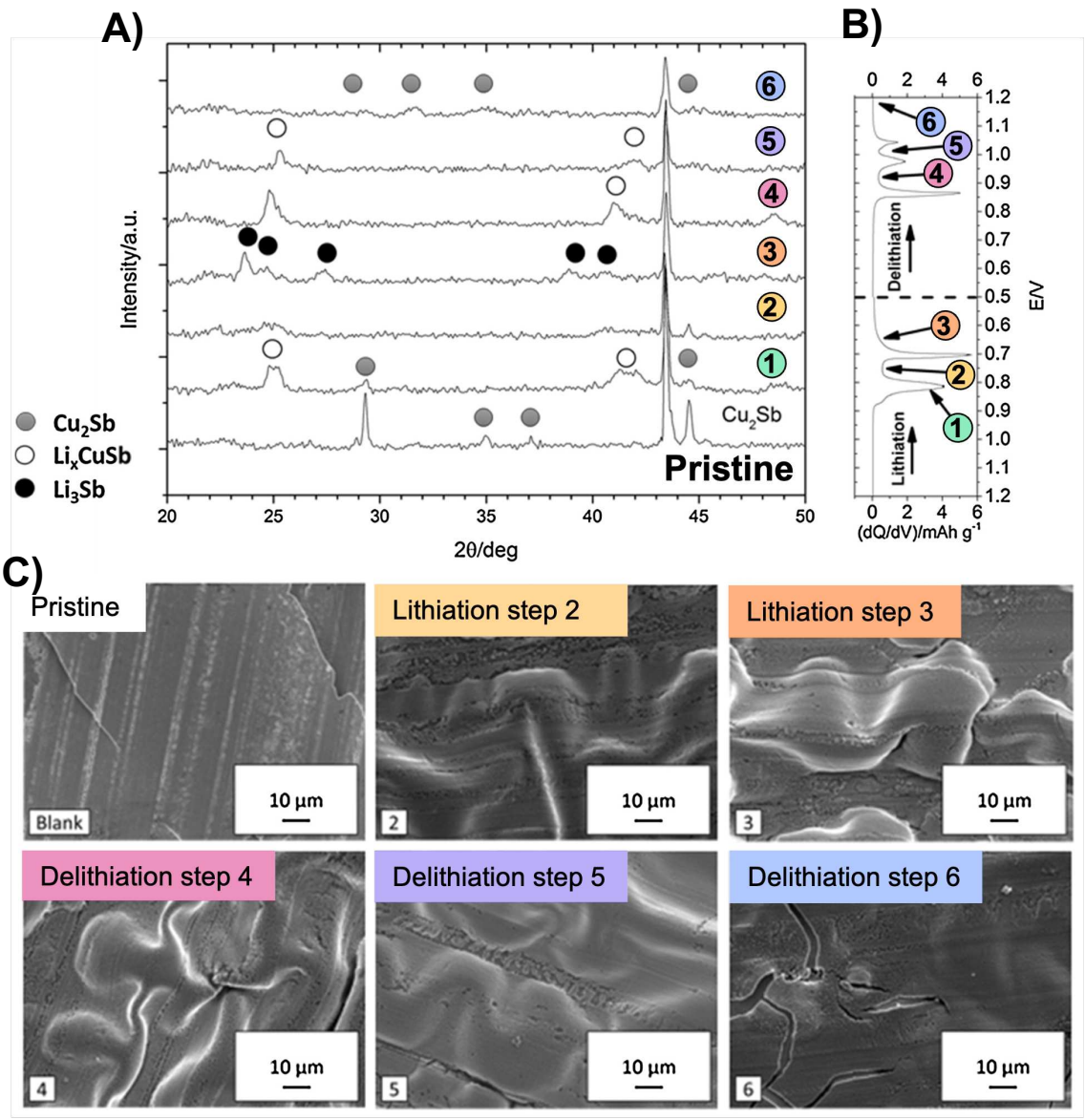

Figure 6.1. Figures A-C were adapted with permission from Jackson et al. 2016. (A) Powder X-ray diffraction data collected on an electrodeposited Cu_2Sb film ex situ at certain voltages pertaining to phase transformations along the differential capacity plot in panel (B). The samples were analyzed at six different states of charge, 1) 0.825 V, 2) 0.750 V, 3) 0.650 V, 4) 0.915 V, 5) 1.025 V, and 6) 1.20 V vs Li/Li^+. Scanning electron microscopy images were taken at the same points shown in (A) and (B) and were performed ex situ on different points across the Cu_2Sb electrode.

investigations were only conducted on the first few cycles of the battery. This is an essential consideration, as changes that occur over multiple cycles can significantly impact the electrochemical performance throughout the lifetime of the battery. In addition, duplicate cells may experience differences in degradation due to subtle interfacial changes and require a more statistical analysis of degradation and electrochemical performance in multiple cells.[20] Studies at the bulk scale combining testing conditions utilizing *in situ* or operando visualization techniques are necessary to continue investigating what structural defects catalyze degradation to more effectively implement mitigation strategies.

6.2 Developing Tools to Optically Track Degradation of Electrodes

We have begun developing a 3D-printed optical-electrochemical cell that would allow for the visualization of a bulk thin film electrode while cycling in a similar experimental setup commonly used in the battery literature, **Figure 6.2**. We hypothesize that by being able to perform operando visual analysis while the battery is cycling, we can gather more information on the degradation mechanism as well as begin to understand how mitigation strategies can alleviate large mechanical stresses in alloy-based electrodes, such as antimony.[26] Optical microscopy will not allow for the exact resolution SEM or TEM provides. However, it can still inform on the macroscopic behavior of the film seen through extreme mechanical fracturing and color changes related to reaction fronts or electrochemical reduction of the electrolyte. By 3D printing this cell, we hope to have a broader impact on the community by developing an optical, electrochemical cell that can be easily manufactured and accessed.

There are many important parameters to consider when developing a new characterization apparatus, which are discussed below.

6.2.1 Sealing & Air Free Conditions

To perform accurate electrochemical tests, the experimental setup must be assembled under inert gas in a glove box or in an air-free vessel. Therefore, being able to seal the 3D-printed cell effectively is of extreme importance. Through several iterations, we have found that implementing

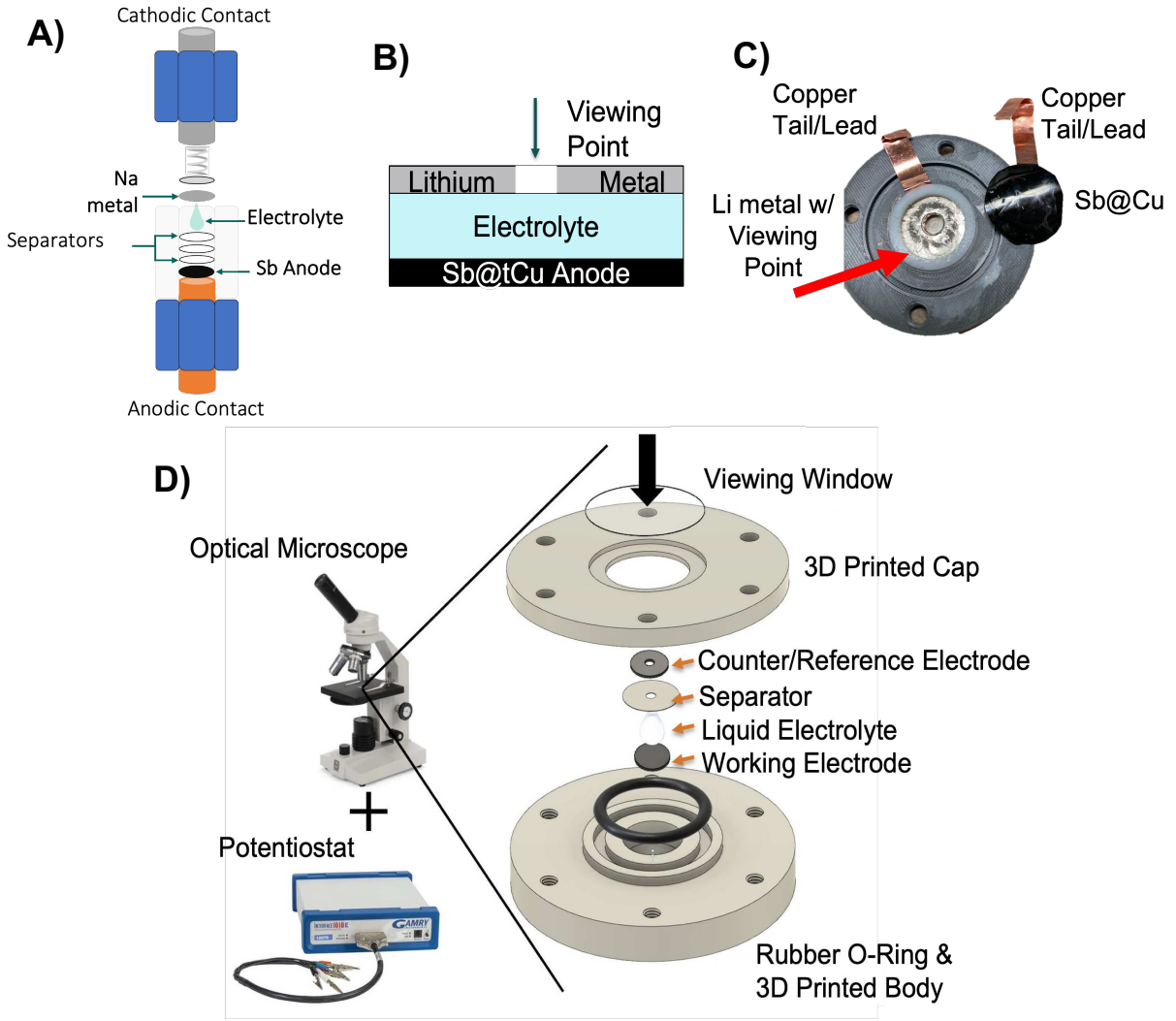

Figure 6.2. A) A Swagelok battery assembly that is commonly used in academia to evaluate battery performance. B) A simplified schematic depicted the electrochemical set up in the optical cell that shows lithium metal as the counter and working electrode with a small hole in the middle allowing for visualization of the working electrode. In this set up the electrodeposited Sb-based anode will act as the working electrode. C) A prototype of the 3D printed optical cell demonstrating the copper tabs that extend outside of the cell that allow for connection to the potentiostat. D) The current optical electrochemical cell in an exploded view to show the experimental set up. Not shown in this schematic are the copper contacts for both the working and counter/reference electrode.

an O-ring and distributing the points of sealing pressure with the screws was necessary. Currently, the developed cell is nearly air-free, but there are still some issues with electrolyte leaking out of the cell. This is due to overfill, and we are currently developing alternative ways to fill the cell with electrolyte.

6.2.2 Ability to Perform Electrochemical Tests

Once the cell has been assembled, there need to be clear access points to the reference, counter, and working electrodes to perform electrochemical tests. We have accounted for this by electrodepositing Sb onto a copper substrate with a tail extending outside the cell when sealed. The lithium metal reference/counter electrode is in contact through a similar method, where the metal is pressed against a copper current collector with a tail.

6.2.3 Geometric Considerations for Optimal Experimental Conditions

This has been the most challenging consideration in the development of this cell. There are several studies in the field demonstrating how the placement of the reference/counter can influence current density distribution and lithium concentration gradients across the substrate based on finite element analysis.[27] We had seen this when the viewing window through the lithium metal was too large, and lithium diffusion to the center of the antimony electrode was kinetically hindered. Even under slow cycling rates, lithiated phases were not found in the center of the electrode through energy dispersive spectroscopy. Additionally, the working distance of the microscope lens must be taken into consideration. By reducing the size of the view window and the height between the lithium metal and Sb electrode, we have improved the electrode's current density distributions and visualization.

6.2.4 Safety & Ease of Assembly

The overall cost, safety, and ease of assembly are of extreme importance to us to have a broader impact on the battery community. We intend to publish the blueprints of this optical cell so it can be used in research and teaching labs to provide visual information on the degradation of electrode materials and to build a fundamental understanding of how batteries operate for undergraduate students. Key things to consider for the safety of this cell are the flammability and corrosive behavior of the utilized electrolyte. The seal and robustness of the cell are essential to prevent electrolyte leakage. Of more significant concern is the exposure of lithium or sodium metal to the environment due to its reactivity. We have considered these factors and developed a prototype sufficient to prevent air exposure and will continue to test the safety of the optical cell.

6.3 Preliminary Studies on the Degradation of Sb Electrodes in a Lithium Half-Cell

We have begun preliminary investigations coupling operando optical studies with electrochemical experiments on Sb-based anodes in lithium-ion systems. Focus has been shifted back to the lithium system instead of sodium due to the ability to track the lithiated phases of Sb more easily. The lithiation of Sb is also less complex when compared to the sodiation, as seen in **Figure 6.3**, as Sb is lithiated to Li_2Sb and the final Li_3Sb phase. In the differential capacity analysis in **Figure 6.3a** and **Figure 6.3b**, it is observed that when Sb is lithiated it only goes through one broad lithiation reaction that can encompass both the Li_2Sb and Li_3Sb phases as opposed to the four sodiation phases.[28,29] The shadowed sodiation reactions in **Figure 6.3a**, represent sodiation phases that are amorphous and require more complex characterization such as pair distribution function analysis (PDF). Therefore, to couple our optical experiments with additional characterization techniques such as XRD, we have done our preliminary experiments with lithium metal.

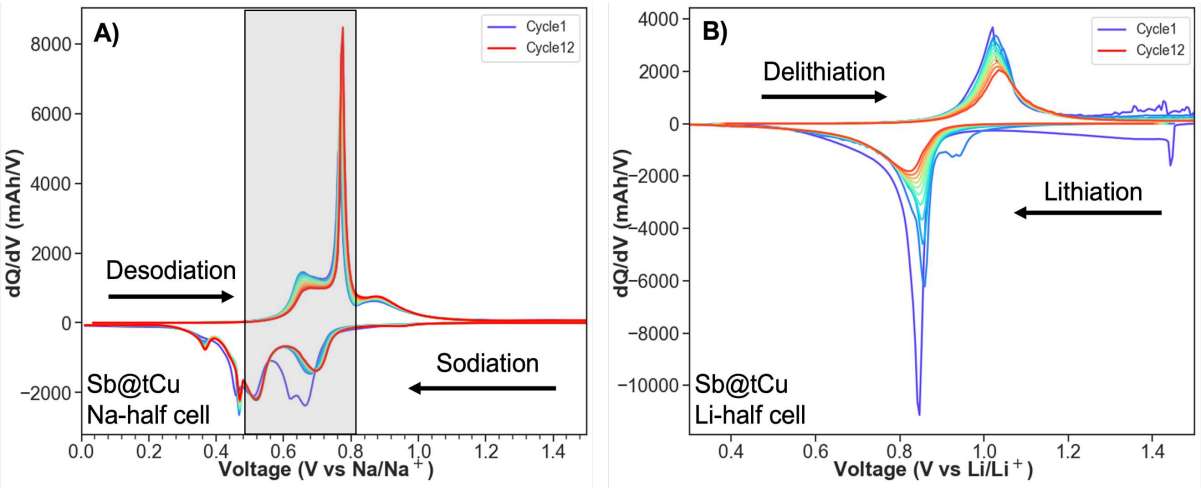

Figure 6.3. Differential capacity analysis of electrodeposited Sb in a sodium (A) and lithium (B) half-cell. In both systems Sb was cycled at a rate of C/2 at voltage ranges of 1.5 – 0.01 V vs Na/Na^+ and 1.5 – 0.01 V vs Li/Li^+. The sodiation/desodiation of Sb is more complex based on the number of reactions and phases transformations that occur when cycled. Additionally, the intermediate phases are highlight in grey and are generally amorphous in nature and are difficult to characterize through XRD. The lithiation of Sb consists of Sb lithiated to Li_2Sb and then to the final Li_3Sb phase shown by the broad lithiation peak at 0.75 V vs Li/Li^+. These phases are crystalline and can be tracked through XRD to help determine if the optical cell is allowing for lithiation/delithiation of the Sb electrode.

Using an elementary optical cell, we have collected optical video while cycling an electrodeposited Sb film in a full cell with lithium cobalt oxide as the cathode in an electrolyte composed of 1 M LiPF6 in 3:7 ethylene carbonate:diethyl carbonate. The Sb anode was electrodeposited with a solution consisting of 200 mM sodium gluconate (Sigma-Aldrich, ACS reagent) with 30 mM antimony trichloride (Sigma-Aldrich, anhydrous ≥ 99.0%) in 100 mL of Millipore water and it was titrated to a pH of 6 with a sodium hydroxide solution. The film was electrodeposited onto a nickel foil at room temperature by applying a steady voltage of -1.05 V vs. a saturated calomel electrode with a charge limit of 3 C cm^{-2}. The assembled cell was galvanostatically cycled in the voltage range of -1.8 to -3.8 V vs. Li/Li+ by setting the current rate to C/5 based on the mass of the deposited Sb.

Operando video microscopy was collected for cycle 10, and the collected data is shown in **Figure 6.4**. The data shown in this chapter is part of a submitted manuscript to Chemistry of Materials (Rhys A. Otten, Kelly Nieto, Maxwell C. Schulze, Amy L. Prieto, *Chem. Mater.*, **2023**). When the cell was discharged, the Sb film was lithiated, and darkening of the electrode occurred along with small cracks, shown by white areas in the film, **Figure 6.4a**. Darkening of the film is believed to be associated with the lithiation of Sb or contrasting effects related to buckling of the film related to mechanical stress induced by the stark volume change from the Sb unit cell to the

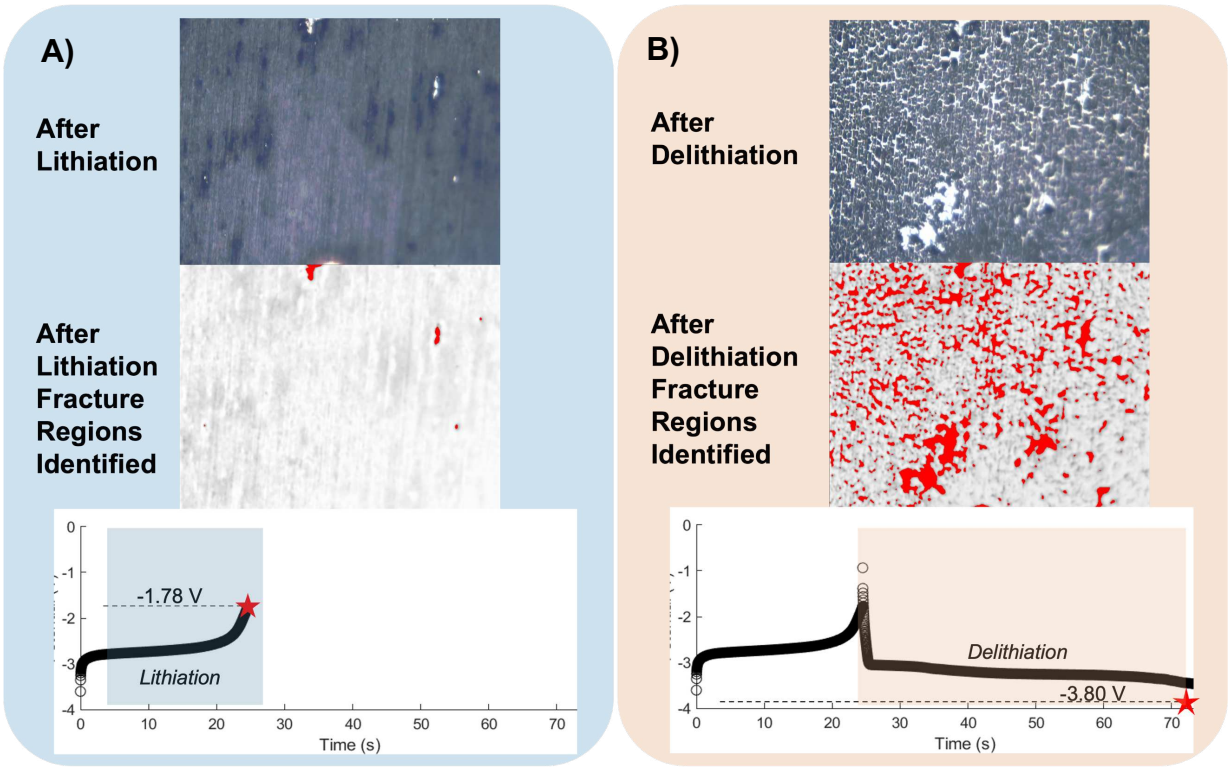

Figure 6.4. Operando optical imaging was collected during the 10th cycle and frames after lithiation and delithiation are shown in panels (A) and (B). The electrodeposited Sb anode was cycled against lithium cobalt oxide at C/5 rate between the voltage range of -1.80 V to -3.8 V vs Li/Li$^+$. In panel (A) the cell was discharge to -1.78 V vs Li/Li$^+$ and Sb was lithiated. In panel (B) the cell was charge to -3.80 V vs Li/Li$^+$ and Sb was delithiated. The corresponding images were used to track the amount of loss active material and regions identified as pulverized material are highlighted in red. This data is part of a submitted manuscript to Chemistry of Materials (Abby J. Otten, Kelly Nieto, Maxwell C. Schulze, Amy L. Prieto, *ACS Appl. Eng. Mater.*, **2023**.).

Li_2Sb and Li_3Sb unit cells. As the Sb film was delithiated, the film continued to darken, followed by the appearance of cracks and vigorous pulverization throughout the discharge process.

We hypothesize that many of the cracks formed occur during lithiation as the expansion of the film creates points of weakness due to stress. As the film is delithiated, the film shrinks back, and the previously formed cracks now expand and leave void space in between islands of active material, **Figure 6.4b**. The increase in contrast as the film is delithiated could potentially be related to the delamination of the film from the glass substrate that would be consistent with findings from the previously discussed Jackson et al. study.[25] To quantify the amount of lost active material we have developed an image processing method through MATLAB and ImageJ that is reported in the submitted manuscript to Chemistry of Materials. In summary, this technique maps out superpixels based on x and y-coordinates and determines whether the pixel contains pulverized material or void space based on the contrast in the image. The identified regions of pulverization are highlighted in red in **Figure 6.4a** and **Figure 6.4b**. The camera and microscope were calibrated to allow for the conversion between pixels and a known distance in microns. This quantification then enables us to start determining the loss of active material based on the area of the pulverized regions. From this preliminary data, we have demonstrated the ability to perform operando optical microscopy with electrochemistry to begin to understand the degradation process of Sb anodes for lithium-ion batteries. With this baseline, we intend to test how additives such as carbon nanotubes, electrolyte composition, and changes in the structure of the film through various synthetic parameters may mitigate the degradation of the film.

6.4 Outlook

The presented optical cell and results demonstrate the ability to couple operando optical studies with electrochemistry to further understand the degradation of alloy-based anode materials.

Due to the configuration of the cell, the system can be used to test a variety of different structural parameters of the synthesized anode material, such as crystallinity, nanostructuring, advanced geometric architectures, and composition.[14,30–35] To test how these parameters can influence degradation, *in situ* characterization such as XRD will need to be used to identify at what voltage crystalline phases are present to couple phase transformations with mechanical fracturing of the film. Additionally, as changes to structure can increase the surface area that then leads to excessive reduction of the electrolyte onto the surface of the anode, optimization of the electrolyte will also be required. Formation of the SEI can also be tracked optically as color changes in the electrolyte, and SEI could be optically monitored at different states of charge.[36–41] Recently, the development of conductive protective coatings for alloy-based materials have been of interest in the field , as they may act as a barrier to prevent complete isolation of pulverized material and maintain electrical contact, even after significant pulverization has occurred.[42–45] Polymer coatings such as cyclized polyacrylonitrile (c-PAN) have shown promise in mitigating mechanical pulverization and through optical microscopy we can continue to monitor how changes in the coating (thickness, composition, etc.) can extend the lifetime of alloy-based materials.[46–49] Overall, we hope this optical cell can act as a complementary technique in the toolbox to further understand the degradation of alloy-based materials and how experimental parameters can help mitigate mechanical degradation to improve electrochemical performance overall.

6.5 References

(1) McDowell, M. T.; Lee, S. W.; Nix, W. D.; Cui, Y. 25th Anniversary Article: Understanding the Lithiation of Silicon and Other Alloying Anodes for Lithium-Ion Batteries. *Adv. Mater.* **2013**, *25* (36), 4966–4985. https://doi.org/10.1002/adma.201301795.

(2) Subramanyan, K.; Aravindan, V. Stibium: A Promising Electrode toward Building High-Performance Na-Ion Full-Cells. *Chem* **2019**, *5*, 3096–3126. https://doi.org/10.1016/j.chempr.2019.08.007.

(3) Liang, S.; Cheng, Y. J.; Zhu, J.; Xia, Y.; Müller-Buschbaum, P. A Chronicle Review of Nonsilicon (Sn, Sb, Ge)-Based Lithium/Sodium-Ion Battery Alloying Anodes. *Small Methods* **2020**, *2000218*. https://doi.org/10.1002/smtd.202000218.

(4) He, J.; Wei, Y.; Zhai, T.; Li, H. Antimony-Based Materials as Promising Anodes for Rechargeable Lithium-Ion and Sodium-Ion Batteries. *Mater Chem Front* **2018**, *2*, 437. https://doi.org/10.1039/c7qm00480j.

(5) Beaulieu, L. Y.; Eberman, K. W.; Turner, R. L.; Krause, L. J.; Dahn, J. R. Colossal Reversible Volume Changes in Lithium Alloys. *Electrochem. Solid-State Lett.* **2001**, *4* (9), A137. https://doi.org/10.1149/1.1388178.

(6) Huggins, R. A.; Nix, W. D. Decrepitation Model for Capacity Loss during Cycling of Alloys in Rechargeable Electrochemical Systems. *Ionics* **2000**, *6* (1), 57–63. https://doi.org/10.1007/BF02375547.

(7) Demko, M. T.; Xun, S.; Kim, S.-H.; Liu, H.; Mai, T.; Nguyen, P.; Featherer, R.; Lin, X.; Subramoney, S.; Warrington, K. An Examination of the Cycling Performance and Failure Mechanisms in Mechanically Alloyed Composites Containing Antimony Metal, Iron Oxide, and Carbon Black. **2016**. https://doi.org/10.1016/j.electacta.2016.09.051.

(8) Zhou, Y.-N.; Ma, J.; Hu, E.; Yu, X.; Gu, L.; Nam, K.-W.; Chen, L.; Wang, Z.; Yang, X.-Q. Tuning Charge–Discharge Induced Unit Cell Breathing in Layer-Structured Cathode Materials for Lithium-Ion Batteries. *Nat. Commun.* **2014**, *5* (1), 5381. https://doi.org/10.1038/ncomms6381.

(9) Bak, S.-M.; Shadike, Z.; Lin, R.; Yu, X.; Yang, X.-Q. In Situ/Operando Synchrotron-Based X-Ray Techniques for Lithium-Ion Battery Research. *NPG Asia Mater.* **2018**, *10*, 563–580. https://doi.org/10.1038/s41427-018-0056-z.

(10) Liu, C.; Zeng, F.; Xu, L.; Liu, S.; Liu, J.; Ai, X.; Yang, H.; Cao, Y. Enhanced Cycling Stability of Antimony Anode by Downsizing Particle and Combining Carbon Nanotube for High-Performance Sodium-Ion Batteries. *J. Mater. Sci. Technol.* **2019**. https://doi.org/10.1016/j.jmst.2019.05.031.

(11) Tripathi, A. M.; Su, W.-N.; Hwang, B. J. *In Situ* Analytical Techniques for Battery Interface Analysis. *Chem. Soc. Rev.* **2018**, *47* (3), 736–851. https://doi.org/10.1039/C7CS00180K.

(12) Dai, K.; Zhao, H.; Wang, Z.; Song, X.; Battaglia, V.; Liu, G. Toward High Specific Capacity and High Cycling Stability of Pure Tin Nanoparticles with Conductive Polymer Binder for Sodium Ion Batteries. *J. Power Sources* **2014**, *263*, 276–279. https://doi.org/10.1016/j.jpowsour.2014.04.012.

(13) Chan, C. K.; Peng, H.; Liu, G.; McIlwrath, K.; Zhang, X. F.; Huggins, R. A.; Cui, Y. High-Performance Lithium Battery Anodes Using Silicon Nanowires. *Nat. Nanotechnol.* **2008**, *3* (1), 31–35. https://doi.org/10.1038/nnano.2007.411.

(14) Liu, X. H.; Zhong, L.; Huang, S.; Mao, S. X.; Zhu, T.; Huang, J. Y. Size-Dependent Fracture of Silicon Nanoparticles During Lithiation. *ACS Nano* **2012**, *6* (2), 1522–1531. https://doi.org/10.1021/nn204476h.

(15) Yu, Y.; Zhu, J.; Zeng, K.; Jiang, M. Mechanically Robust and Superior Conductive N-Type Polymer Binders for High-Performance Micro-Silicon Anodes in Lithium-Ion Batteries. *J. Mater. Chem. A* **2021**, *9* (6), 3472–3481. https://doi.org/10.1039/d0ta10525b.

(16) Schulze, M. C.; Belson, R. M.; Kraynak, L. A.; Prieto, A. L. Electrodeposition of Sb/CNT Composite Films as Anodes for Li- and Na-Ion Batteries. *Energy Storage Mater.* **2020**, *25* (June 2019), 572–584. https://doi.org/10.1016/j.ensm.2019.09.025.

(17) Oszajca, M. F.; Bodnarchuk, M. I.; Kovalenko, M. V. Precisely Engineered Colloidal Nanoparticles and Nanocrystals for Li-Ion and Na-Ion Batteries: Model Systems or Practical Solutions? †. *Chem Mater* **2014**, *26*, 5432. https://doi.org/10.1021/cm5024508.

(18) Li, R. R.; Yang, Z.; He, X. X.; Liu, X. H.; Zhang, H.; Gao, Y.; Qiao, Y.; Li, L.; Chou, S. L. Binders for Sodium-Ion Batteries: Progress, Challenges and Strategies. *Chem. Commun.* **2021**, *57* (93), 12406–12416. https://doi.org/10.1039/d1cc04563f.

(19) Nieto, K.; Gimble, N. J.; Rudolph, L. J.; Kale, A. R.; Prieto, A. L. Electrodeposition vs Slurry Casting: How Fabrication Affects Electrochemical Reactions of Sb Electrodes in Sodium-Ion Batteries. *J. Electrochem. Soc.* **2022**, *169* (5), 050537. https://doi.org/10.1149/1945-7111/ac6b5e.

(20) Boebinger, M. G.; Lewis, J. A.; Sandoval, S. E.; Mcdowell, M. T.; Woodruff, G. W. Understanding Transformations in Battery Materials Using in Situ and Operando Experiments: Progress and Outlook. **2020**, *19*, 44. https://doi.org/10.1021/acsenergylett.9b02514.

(21) Brennhagen, A.; Cavallo, C.; Wragg, D. S.; Sottmann, J.; Koposov, A. Y.; Fjellvåg, H. Understanding the (De)Sodiation Mechanisms in Na-Based Batteries through Operando X-

Ray Methods. *Batter. Supercaps* **2021**, *4* (7), 1039–1063. https://doi.org/10.1002/batt.202000294.

(22) Wolf, M.; May, B. M.; Cabana, J. Visualization of Electrochemical Reactions in Battery Materials with X-Ray Microscopy and Mapping. *Chem. Mater.* **2009**, *29*, 3347–3362. https://doi.org/10.1021/acs.chemmater.6b05114.

(23) Wang, J.; Eng, C.; Chen-Wiegart, Y. C. K.; Wang, J. Probing Three-Dimensional Sodiation-Desodiation Equilibrium in Sodium-Ion Batteries by in Situ Hard X-Ray Nanotomography. *Nat. Commun.* **2015**, *6* (May). https://doi.org/10.1038/ncomms8496.

(24) Gutierrez-Kolar, J. S.; Baggetto, L.; Sang, X.; Shin, D.; Yurkiv, V.; Mashayek, F.; Veith, G. M.; Shahbazian-Yassar, R.; Unocic, R. R. Interpreting Electrochemical and Chemical Sodiation Mechanisms and Kinetics in Tin Antimony Battery Anodes Using in Situ Transmission Electron Microscopy and Computational Methods. *Appl. Energy Mater.* **2019**, *2*, 3578–3586. https://doi.org/10.1021/acsaem.9b00310.

(25) Jackson, E. D.; Mosby, J. M.; Prieto, A. L. Evaluation of the Electrochemical Properties of Crystalline Copper Antimonide Thin Film Anodes for Lithium Ion Batteries Produced by Single Step Electrodeposition. *Electrochimica Acta* **2016**, *214*, 253–264. https://doi.org/10.1016/j.electacta.2016.07.126.

(26) Li, W.; Lutz, D. M.; Wang, L.; Takeuchi, K. J.; Marschilok, A. C. Perspective Peering into Batteries : Electrochemical Insight Through In Situ and Operando Methods over Multiple Length Scales. *Joule* **2021**, *5* (1), 77–88. https://doi.org/10.1016/j.joule.2020.11.003.

(27) Sanchez, A. J.; Kazyak, E.; Chen, Y.; Chen, K.-H.; Pattison, E. R.; Dasgupta, N. P. Plan-View *Operando* Video Microscopy of Li Metal Anodes: Identifying the Coupled Relationships among Nucleation, Morphology, and Reversibility. *ACS Energy Lett.* **2020**, *5* (3), 994–1004. https://doi.org/10.1021/acsenergylett.0c00215.

(28) Mayo, M.; Morris, A. J. Structure Prediction of Li−Sn and Li−Sb Intermetallics for Lithium-Ion Batteries Anodes. **2017**. https://doi.org/10.1021/acs.chemmater.6b04914.

(29) Allan, P. K.; Griffin, J. M.; Darwiche, A.; Borkiewicz, O. J.; Wiaderek, K. M.; Chapman, K. W.; Morris, A. J.; Chupas, P. J.; Monconduit, L.; Grey, C. P. Tracking Sodium-Antimonide Phase Transformations in Sodium-Ion Anodes: Insights from Operando Pair Distribution Function Analysis and Solid-State NMR Spectroscopy. *J. Am. Chem. Soc.* **2016**, *138* (7), 2352–2365. https://doi.org/10.1021/jacs.5b13273.

(30) Jackson, E. D.; Prieto, A. L. Copper Antimonide Nanowire Array Lithium Ion Anodes Stabilized by Electrolyte Additives. *ACS Appl Mater Interfaces* **2016**, *8*, 30379–30386. https://doi.org/10.1021/acsami.6b08033.

(31) Markevich, E.; Fridman, K.; Sharabi, R.; Elazari, R.; Salitra, G.; Gottlieb, H. E.; Gershinsky, G.; Garsuch, A.; Semrau, G.; Schmidt, M. A.; Aurbach, D. Amorphous

Columnar Silicon Anodes for Advanced High Voltage Lithium Ion Full Cells: Dominant Factors Governing Cycling Performance. *J. Electrochem. Soc.* **2013**, *160* (10), A1824–A1833. https://doi.org/10.1149/2.085310jes.

(32) Yang, Y.; Yang, X.; Zhang, Y.; Hou, H.; Jing, M.; Zhu, Y.; Fang, L.; Chen, Q.; Ji, X. Cathodically Induced Antimony for Rechargeable Li-Ion and Na-Ion Batteries: The Influences of Hexagonal and Amorphous Phase. *J. Power Sources* **2015**, *282*, 358–367. https://doi.org/10.1016/j.jpowsour.2015.02.071.

(33) Bian, X.; Dong, Y.; Zhao, D.; Ma, X.; Qiu, M.; Xu, J.; Jiao, L.; Cheng, F.; Zhang, N. Microsized Antimony as a Stable Anode in Fluoroethylene Carbonate Containing Electrolytes for Rechargeable Lithium-/ Sodium-Ion Batteries. *ACS Appl Mater Interfaces* **2020**, *12*, 3562. https://doi.org/10.1021/acsami.9b18006.

(34) Domi, Y.; Usui, H.; Sugimoto, K.; Sakaguchi, H. Effect of Silicon Crystallite Size on Its Electrochemical Performance for Lithium-Ion Batteries. *Energy Technol.* **2019**, *7* (5). https://doi.org/10.1002/ente.201800946.

(35) Long, J. W.; Dunn, B.; Rolison, D. R.; White, H. S. 3D Architectures for Batteries and Electrodes. *Adv. Energy Mater.* **2020**, *10*, 2002457–2002457. https://doi.org/10.1002/aenm.202002457.

(36) Gimble, N. J.; Prieto, A. L. Spontaneous Solid Electrolyte Interface Formation in Uncycled Sodium Half-Cell Batteries: Using X-Ray Photoelectron Spectroscopy to Explore the Pre-Passivation of Sodium Metal by Fluoroethylene Carbonate before Potentials Are Applied. *Sustain. Energy Fuels* **2022**, *6* (20), 4736–4740. https://doi.org/10.1039/d2se00888b.

(37) Gimble, N. J.; Kraynak, L. A.; Schneider, J. D.; Schulze, M. C.; Prieto, A. L. X-Ray Photoelectron Spectroscopy as a Probe for Understanding the Potential-Dependent Impact of Fluoroethylene Carbonate on the Solid Electrolyte Interface Formation in Na/Cu_2Sb Batteries. *J. Power Sources* **2021**, *489* (January), 229171. https://doi.org/10.1016/j.jpowsour.2020.229171.

(38) Kraynak, L. A.; Schneider, J. D.; Prieto, A. L. Exploring the Role of Vinylene Carbonate in the Passivation and Capacity Retention of Cu_2Sb Thin Film Anodes. *J. Phys. Chem. C* **2020**, *124* (48), 26083–26093. https://doi.org/10.1021/acs.jpcc.0c04064.

(39) Pfeifer, K.; Arnold, S.; Becherer, J.; Das, C.; Maibach, J.; Ehrenberg, H.; Dsoke, S. Can Metallic Sodium Electrodes Affect the Electrochemistry of Sodium-Ion Batteries? Reactivity Issues and Perspectives. *ChemSusChem* **2019**, *12*, 3312–3319. https://doi.org/10.1002/cssc.201901056.

(40) Peled, E.; Menkin, S. Review—SEI: Past, Present and Future. *J. Electrochem. Soc.* **2017**, *164* (7), A1703. https://doi.org/10.1149/2.1441707jes.

(41) Peled, E. The Electrochemical Behavior of Alkali and Alkaline Earth Metals in Nonaqueous Battery Systems—The Solid Electrolyte Interphase Model. *J. Electrochem. Soc.* **1979**, *126* (12), 2047. https://doi.org/10.1149/1.2128859.

(42) Hall, D. S.; Gauthier, R.; Eldesoky, A.; Murray, V. S.; Dahn, J. R. New Chemical Insights into the Beneficial Role of Al 2 O 3 Cathode Coatings in Lithium-Ion Cells. *ACS Appl. Mater. Interfaces* **2019**, *11* (15), 14095–14100. https://doi.org/10.1021/acsami.8b22743.

(43) Zhu, Y.; Jiang, J.; Yang, L.; Xu, C.; Zhang, Q.; Zhu, X.; Li, X.; Jin, J.; Zhou, Q.; Song, Z. Study of Ag[Sbnd]Sb Coatings Prepared by Non-Cyanide Electrodeposition. *Surf. Coat. Technol.* **2021**, *421* (June). https://doi.org/10.1016/j.surfcoat.2021.127415.

(44) Piper, D. M.; Yersak, T. A.; Son, S.-B.; Kim, S. C.; Kang, C. S.; Oh, K. H.; Ban, C.; Dillon, A. C.; Lee, S.-H. Conformal Coatings of Cyclized-PAN for Mechanically Resilient Si Nano-Composite Anodes. *Adv. Energy Mater.* **2013**, *3* (6), 697–702. https://doi.org/10.1002/aenm.201200850.

(45) Li, J.; Cai, Y.; Wu, H.; Yu, Z.; Yan, X.; Zhang, Q.; Gao, T. Z.; Liu, K.; Jia, X.; Bao, Z. Polymers in Lithium-Ion and Lithium Metal Batteries. *Adv. Energy Mater.* **2021**, *11* (15), 2003239. https://doi.org/10.1002/aenm.202003239.

(46) Dunlap, N. A.; Kim, J.; Oh, K. H.; Lee, S.-H. Slurry-Coated Sheet-Style Sn-PAN Anodes for All-Solid-State Li-Ion Batteries. *J. Electrochem. Soc.* **2019**, *166* (6), A915. https://doi.org/10.1149/2.0151906jes.

(47) Zhang, W.; Sun, M.; Yin, J.; Abou-Hamad, E.; Schwingenschlögl, U.; Costa, P. M. F. J.; Alshareef, H. N. A Cyclized Polyacrylonitrile Anode for Alkali Metal Ion Batteries. *Angew. Chem. Int. Ed.* **2021**, *60* (3), 1355–1363. https://doi.org/10.1002/anie.202011484.

(48) Schulze, M. C.; Prieto, A. L. Mixed-Conducting Properties of Annealed Polyacrylonitrile Activated by n-Doping of Conjugated Domains. *Chem. Sci.* **2022**, *13* (1), 225–235. https://doi.org/10.1039/d1sc02350k.

(49) Datta, M. K.; Kumta, P. N. Silicon and Carbon Based Composite Anodes for Lithium Ion Batteries. *J. Power Sources* **2006**, *158* (1), 557–563. https://doi.org/10.1016/j.jpowsour.2005.09.016.

APPENDIX I: SUPPORTING INFORMATION FOR CHAPTER II: STRUCTURAL CONTROL OF ELECTRODEPOSITED Sb ANODES THROUGH SOLUTION ADDITIVES AND THEIR INFLUENCE ON ELECTROCHEMICAL PERFORMANCE IN Na-ION BATTERIES

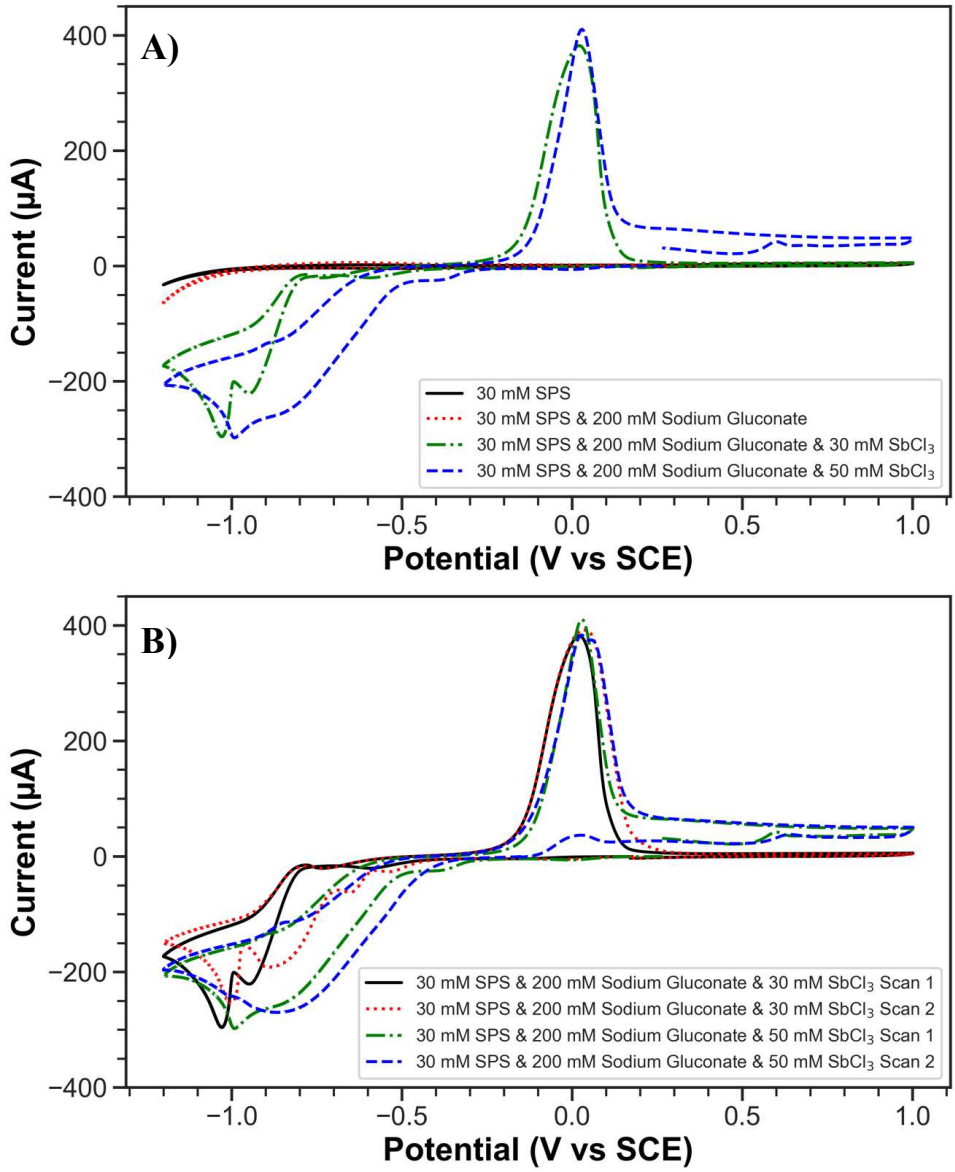

Figure S2.1. CVs of electrolyte solution containing only SPS dissolved in water, SPS with sodium gluconate, and the whole solution composed of SPS, sodium gluconate, and $SbCl_3$ (A). CVs of the electrolyte solution with different concentrations of $SbCl_3$ with multiple scans (B) is shown to demonstrate further hinderance or fouling of the electrode upon SPS adsorption.

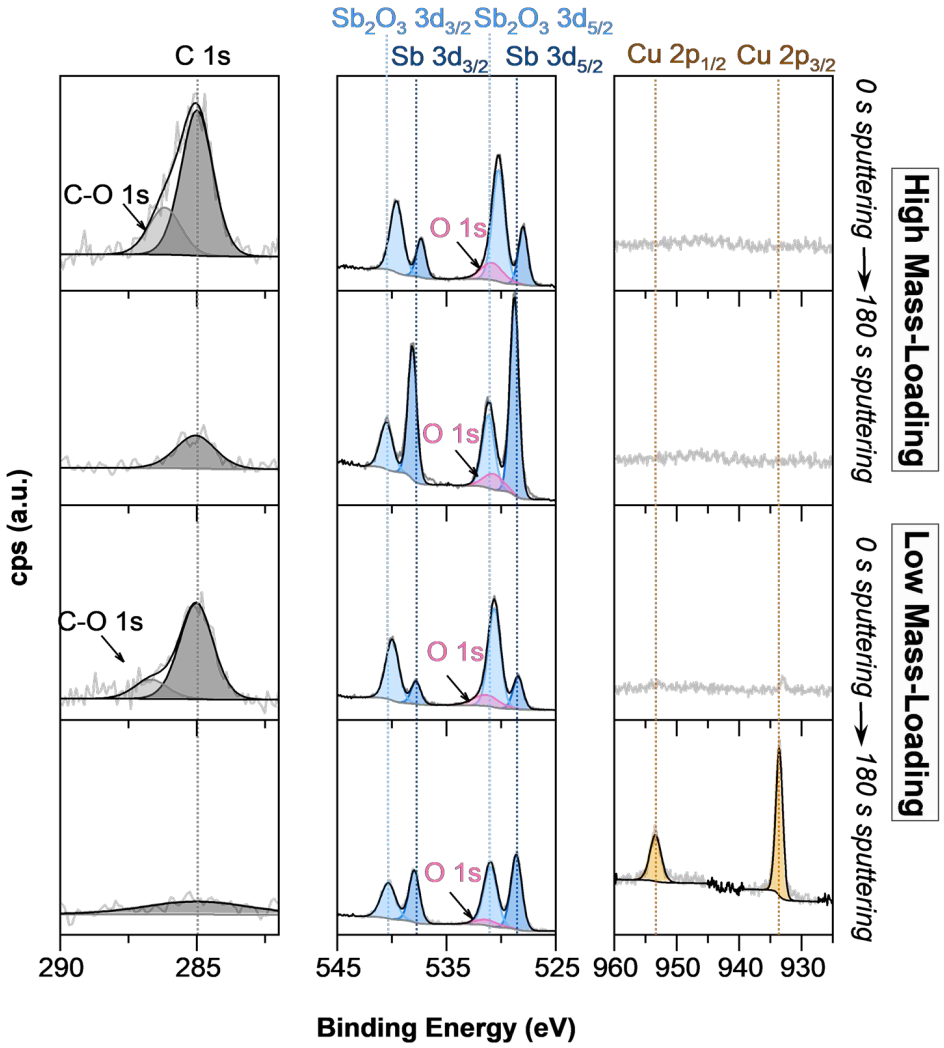

Figure S2.2. High-resolution X-ray photoelectron spectra of Sb electrodeposited on copper from CTAB solution. Carbon, antimony, and copper regions are displayed for the full chronocoulometric electrodeposition (high mass-loading) and the 30 second chronoamperometric electrodeposition (low mass-loading), both of the pristine sample and of the sample after sputtering for 3 minutes.

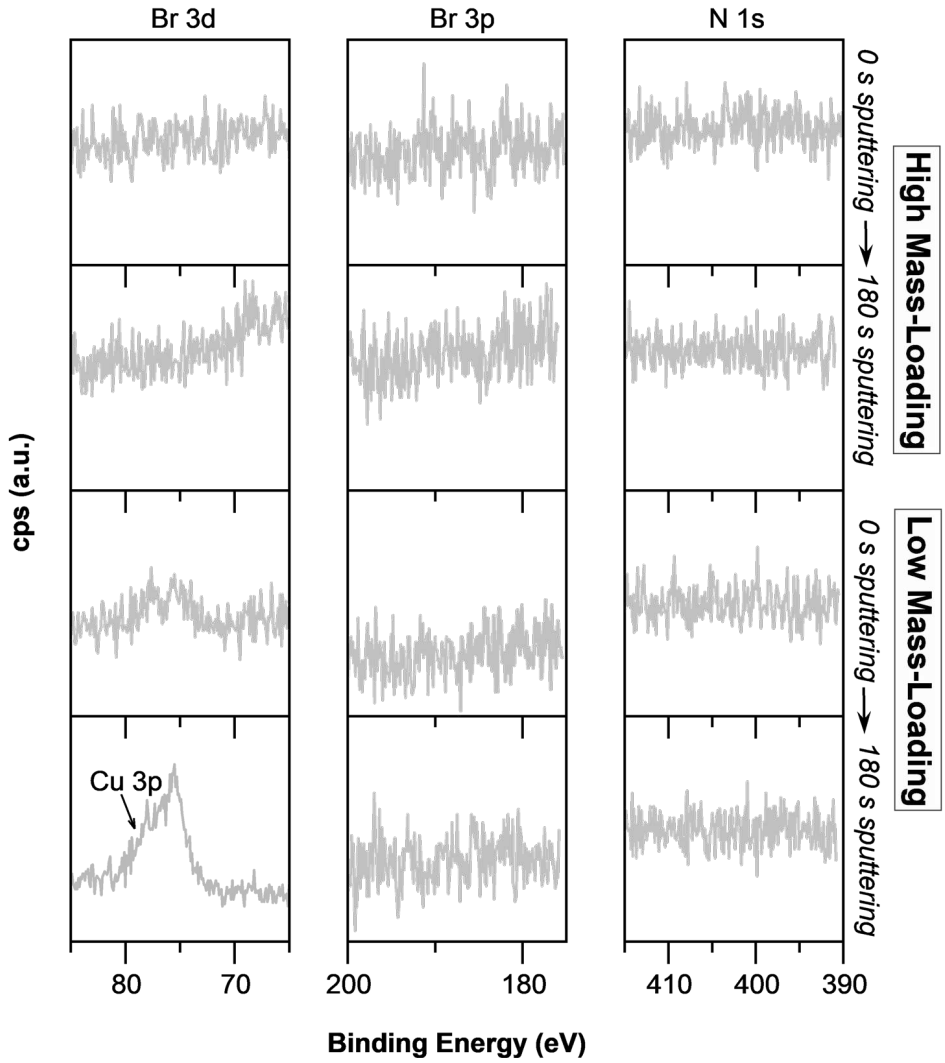

Figure S2.3. High-resolution X-ray photoelectron spectra of Sb electrodeposited on copper from CTAB solution. Bromine 3d, bromine 3p and nitrogen 1s regions are displayed for the full chronocoulometric electrodeposition (high mass-loading) and the 30 second chronoamperometric electrodeposition (low mass-loading), both of the pristine sample and of the sample after sputtering for 3 minutes.

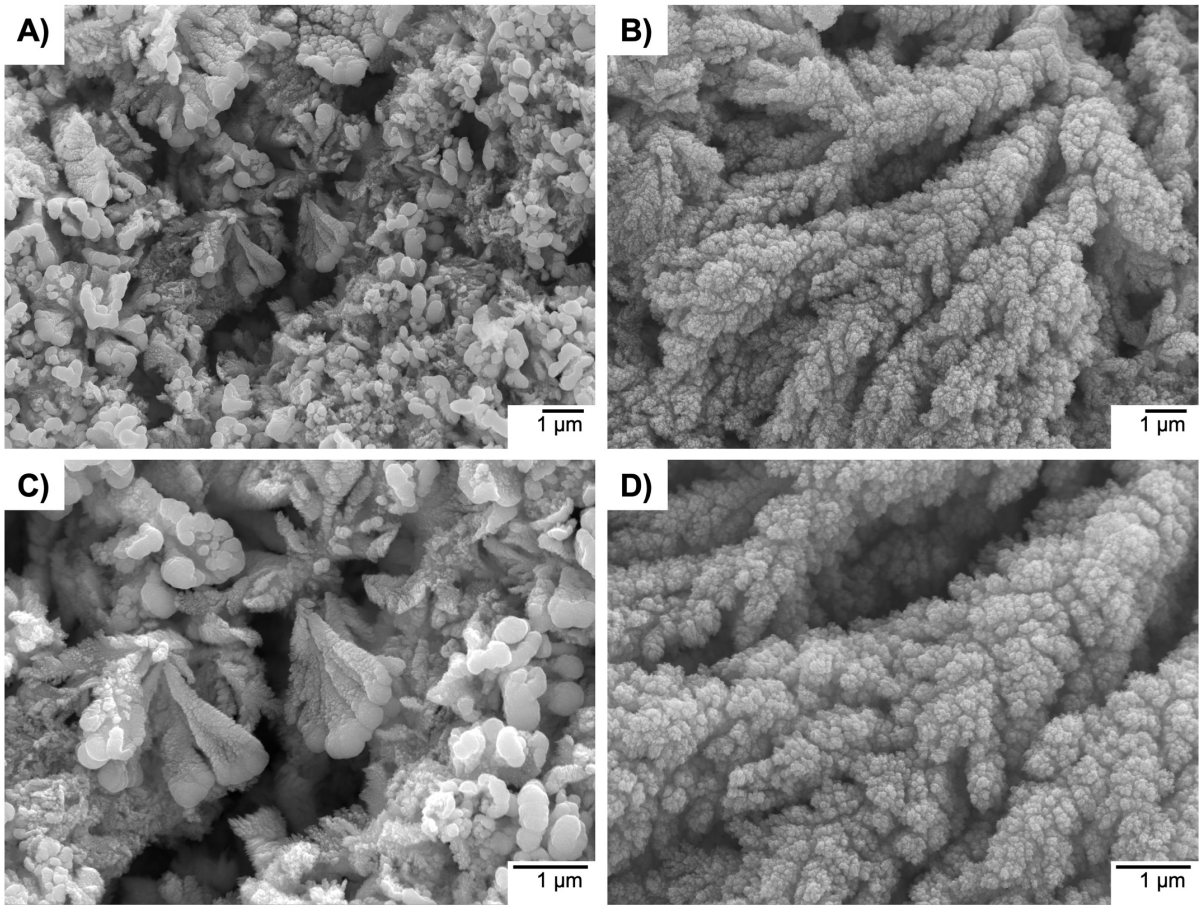

Figure S2.4. SEM images of an Sb film electrodeposited with a mix of 30 mM CTAB and 30 mM SPS at two different spots in the film. Images A) and C) depict the small influence CTAB has on the growth of the film where capping of the branches occurs. Images B) and D) represent what the majority of the film's morphology is composed of and demonstrates that when present at equal concentrations SPS's effects are more dramatic than CTAB.

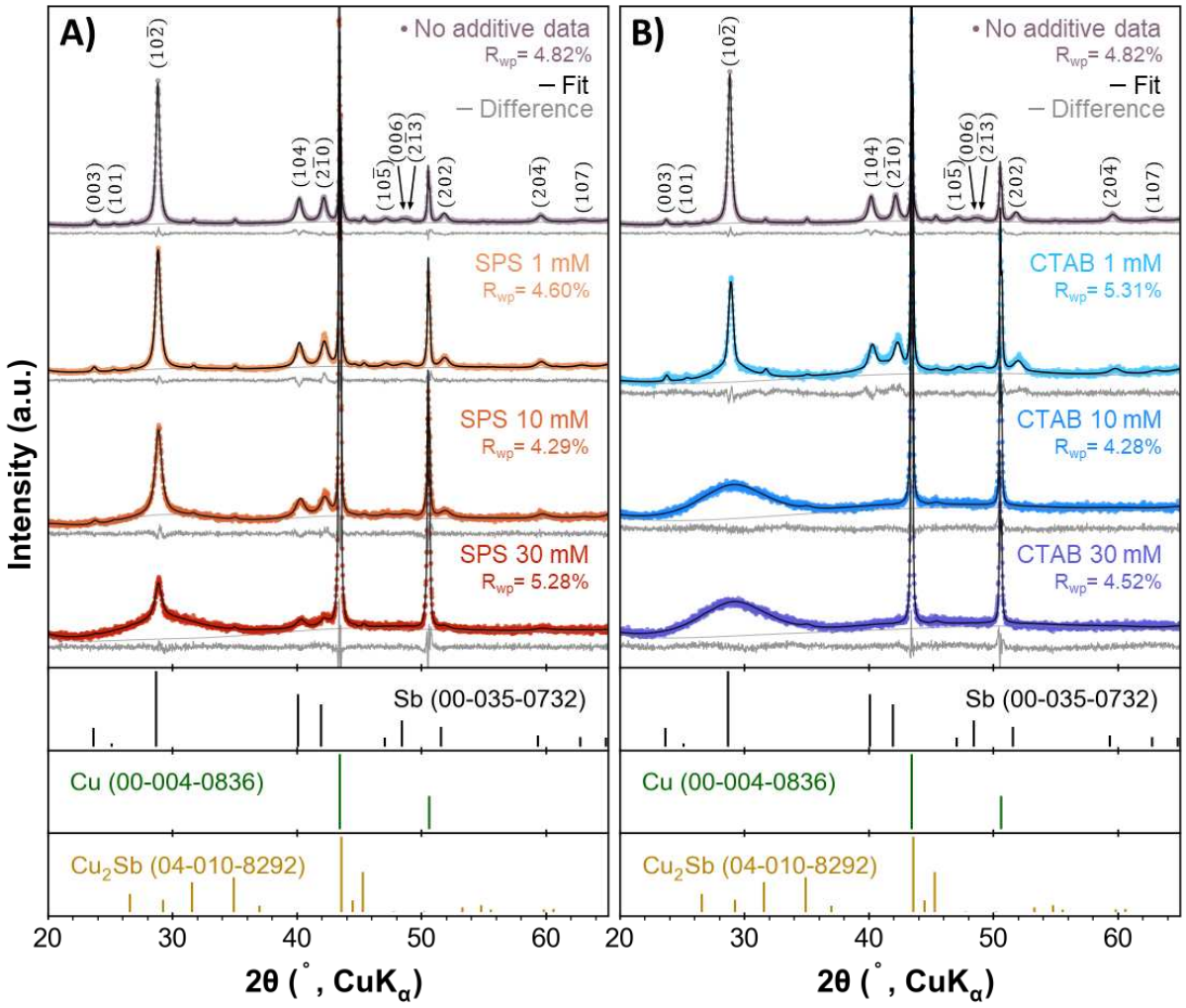

Figure S2.5. PXRD patterns and Rietveld refinements of Sb films deposited with no additive, and varying concentrations of SPS (A) and CTAB (B). Peaks corresponding to Sb are indexed in the no additive trace.

S2.1 Rietveld Refinement Details

As mentioned in the main text, Rietveld refinements were performed using Topas v6 (Bruker AXS). Though both crystallite size and microstrain contribute to peak broadening, the two can be deconvoluted through the use of the double-Voigt approach to peak profile fitting[1]: two-voigt functions were convoluted on top of a predetermined instrument function. From this, a crystallite size, L_{vol}, and microstrain, ε_0, can be extracted. We note that this method requires sufficient intensity of second order reflections (found at higher 2θs)[2], and when such peaks are nearly

indistinguishable from the background, crystallite size and microstrain cannot be deconvoluted. This is the case for films of very low crystallinity, < 2 nm, as the contribution of microstrain cannot be quantified with only one or two broad peaks. However, the presence of only one broad peak at $(10\bar{2})$ means that films are either highly strained and/or have strong preferential orientation. Unit cell parameters also cannot be refined for such films, and as such the d-spacing of the $(10\bar{2})$ peak positions have been reported, and smaller d-spacings indicate an increase in strain in one direction. In some films, two Sb fits were required, one of a higher crystallinity, and one of a very low crystallinity, < 2 nm, meaning that there are two main populations of Sb crystallite sizes in that film.

Table S2.1. Values obtained from Rietveld refinements. **In films with only one or two main peaks, strain cannot be quantified, though the appearance of only one broad peak either means that films are highly strained or preferential orientation is high, as quantified by the March-Dollase model.† A smaller number indicates greater preferential orientation.*

Film	Fit	mean cryst. size (L_{vol})	Micro-strain ε_0 (%)	a (Å)	c (Å)	Cell V (Å^3)	d-spacing (1 0 $\bar{2}$) (Å)	Pref. orient. (1 0 $\bar{2}$)†
Sb bulk reference (00-0735-0732)	--	--	--	4.307	11.273	181.1	3.109	--
No additive	1	> 400 nm	0.25	4.296	11.293	180.5	3.106	0.73
1 mM CTAB	1 (large cryst.)	52 nm	0.29	4.282	11.278	179.1	3.101	none
	2 (small cryst.)	< 2 nm, likely strained*		--	--	--	3.09	none
10 mM CTAB	1	< 2 nm, likely strained*		--	--	--	3.08	yes*
30 mM CTAB	1	< 2 nm, likely strained*		--	--	--	3.08	yes*
1 mM SPS	1	48	0.25	4.292	11.296	180.2	3.105	0.82
10 mM SPS	1	45	0.38	4.289	11.267	179.5	3.101	0.93
30 mM SPS	1 (large cryst.)	< 40	> 0.25	--	--	--	3.10	0.73
	2 (small cryst.)	< 2 nm, likely strained*		--	--	--	3.09	yes*

S2.2 Electrochemical Surface Area Calculations

Table S2.2. Additional surface area values for Sb films deposited with no additive, 30 mM SPS, and 30 mM CTAB based off cyclic voltammetry data presented in Figure 7 and Table 1.

Electrochemical Surface Area Calculations (cm^2)					
Additive Concentration	**Trial 1**	**Trial 2**	**Trial 3**	**Average**	**Standard Deviation**
No Additive	9.03	9.41	9.34	9.28	0.22
SPS 30 mM	6.46	6.59	6.41	6.49	0.09
CTAB 30 mM	1.71	1.53	1.55	1.59	0.10

$$C_{dl} = \frac{j}{v} \qquad \text{Equation (1)}$$

$$ECSA = \frac{C_{dl}}{C_{dl(Reference)}} \qquad \text{Equation (2)}$$

$$A_{Electrode} = A_{Geometric} \times ECSA \qquad \text{Equation (3)}$$

The active electrochemical surface area (ECSA) of the Sb anodes studied in this investigation were calculated using equations 1-3, as detailed in the work of Viory et al.[3] More specifically, the electric-double layer capacitance (C_{dl}) was calculated by plotting the non-faradaic current density over different scan rates, with the slope of the line being the C_{dl}, equation 1. This was achieved by assembling the various Sb electrodes into three-electrode Swagelok cells with sodium metal as the reference and counter electrodes, followed by cyclic voltammetry experiments at 50mV/s, 100mV/s, 150mV/s, 200mV/s, and 250mV/s. The non-faradaic current density at 2.3 V vs Na/Na^+ was plotted as a function of these scans rates, as this was roughly the mid-point of our potential window (2.0V-2.6 V vs. Na/Na^+).[4] After the C_{dl} was calculated for each experimental

condition, the surface roughness factor was deduced by dividing the calculated C_{dl} for each electrode by the $C_{dl(Reference)}$ of a clean Cu-electrode, acting as the reference for the geometric surface, equation 2. The ECSA was then calculated by multiplying the respective surface roughness factor by the geometric surface area of the electrode, equation 3.

S2.3 Electrochemical Impedance and Sodium Diffusion Coefficients

Table S2.3. Fit parameters and goodness of fit (Chi^2) for Sb films deposited with no additive, 30 mM SPS, and 30 mM CTAB, at OCP before cycling.

	Chi^2	**Sum of sq**	**R_{sol} (Ω)**	**R_{ct} (Ω)**	**W_{c-T} (s^{CPE-P}/Ω)**	**W_{c-P} (s^{CPE-P}/Ω)**	**CPE-T (s^{CPE-P}/Ω)**	**CPE-P (n)**
No Additive Pristine	4.48E-4	0.0533	11.20	95.95	6.63E-4	0.906	1.23E-5	0.860
SPS 30 mM Pristine	2.01E-4	0.0239	11.94	122.2	7.28E-4	0.921	1.29E-5	0.834
CTAB 30 mM Pristine	5.51E-4	0.0655	12.09	120.0	1.39E-4	0.889	1.17E-5	0.846
No Additive 10 Cycles	4.62E-4	0.0618	15.46	225.8	1.11E-2	0.781	1.61E-5	0.781
SPS 30 mM 10 Cycles	7.81E-4	0.1046	19.66	167.4	2.83E-3	0.641	1.98E-5	0.758
CTAB 30 mM 10 Cycles	9.51E-4	0.1293	16.41	147.5	7.18E-3	0.644	4.35E-5	0.691

Scheme S2.1. A modified Randles Circuit was used as an equivalent circuit model for the quantitative analysis of the electrochemical impedance spectra collected in this investigation.

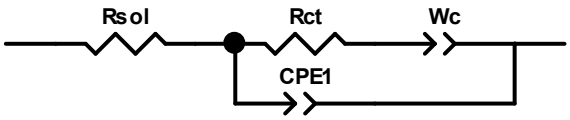

The methodological approach for fitting the EIS spectra collected during this investigation is as follows. A modified Randles circuit, **Scheme S2.1**, was chosen to model the electrochemical phenomena due to the prevalent use of this model in the battery field for quantitative analysis of the impedance behavior found in battery electrodes[5]. A constant phase element replaced the capacitor commonly found in a Randles Circuit due to the inhomogeneous charging of the electric double layer at the electrode-electrolyte interface. A second constant phase element replaced the traditional Finite-length Warburg element in the Randles circuit. This change in the element used to model the diffusion impedance of the electrode occurred because the EIS spectra only demonstrated high frequency impedance data consistent of a Warburg element, although the data did not demonstrate such behavior at low frequencies. During the actual fitting process, terms in the Zview software where only "fixed" when their %errors were less than 2%. This was done to maximize goodness of fit, while at the same time sticking to the modified Randles circuit used owing to its physical relevance.

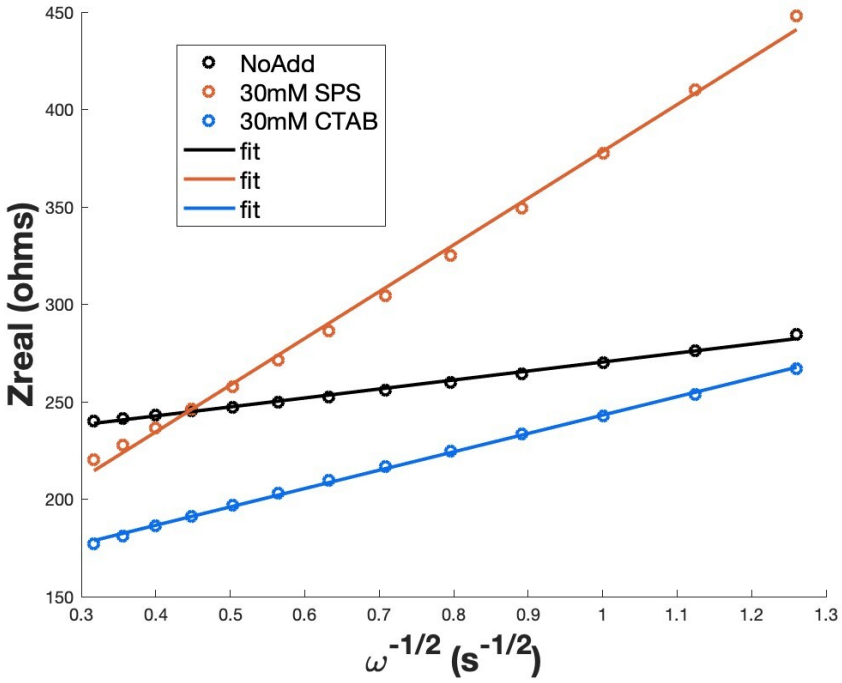

Figure S2.6. Relationship between Zreal and $\omega^{-1/2}$ in the low frequency region for Sb anodes deposited with no additives (black), SPS 30 mM (orange), and CTAB 30 mM (blue). The anodes were cycled for 10 cycles in a sodium half-cell and were full discharged (sodiated) when EIS was performed. The R^2 value for all traces was 0.99.

$$Z_{re} = R_{elec} + R_{ct} + \sigma_w \omega^{-1/2} \qquad \text{Equation (4)}$$

$$D_{Na} = \frac{R^2 T^2}{2A^2 n^4 F^4 C^2 \sigma_w^2} \qquad \text{Equation (5)}$$

Table S2.4. Calculated Warburg diffusion coefficients (D_{Na}) for the Sb anodes deposited with no additives, 30 mM SPS and 30 mM CTAB.

	Diffusion Coefficient (cm^2 s^{-1})
No Additives	1.51E-18
SPS 30 mM	2.91E-19
CTAB 30 mM	7.94E-18

To calculate the Warburg diffusion coefficients (D_{Na}) Equations 4-5 were applied based on the work by Dashairya et al.[6] EIS was performed on sodiated Sb anodes that had been cycled 10 times. The real impedance (Z_{real}) was plotted against the reciprocal of the square root of the lower angular frequency ($\omega^{-1/2}$) to calculate the Warburg Factor (σ_w) from the slope of the line using Equation 4. Using Equation 5, the D_{Na} was calculated based on the capacity for the charged cycle for the Sb anodes deposited with no additives, 30 mM SPS, and 30 mM CTAB and the values are shown in Table S4.

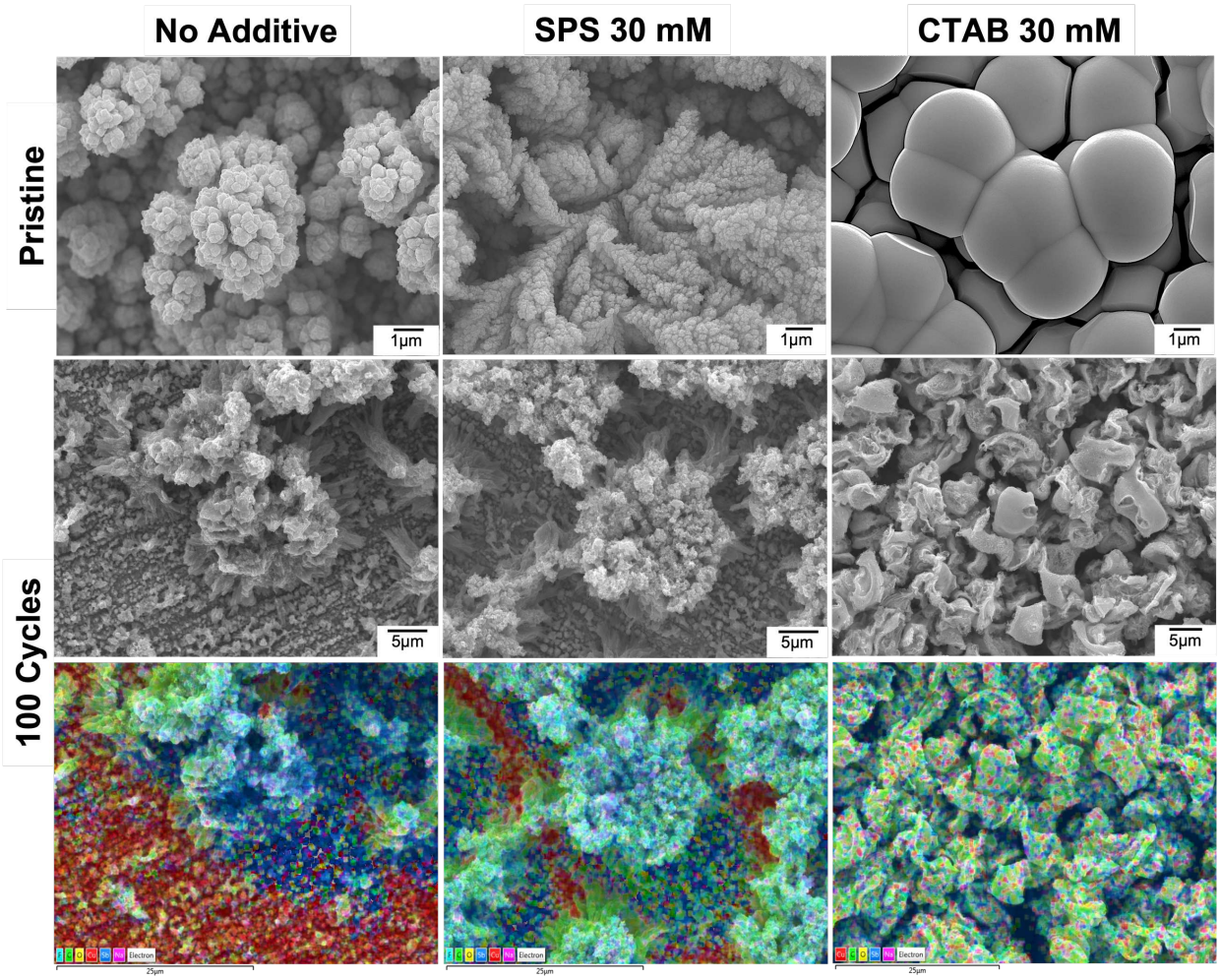

Figure S2.7. Ex situ SEM on pristine and post cycling films for the (left) no additive, (middle) SPS 30 mM, and (right) 30 mM CTAB films. Elemental analysis was done on the post cycling films to demonstrate how the no additive and SPS 30 mM films delaminate, and copper is exposed. Films were cycled at a C/2 rate with the conditions previously discussed in the Methods section.

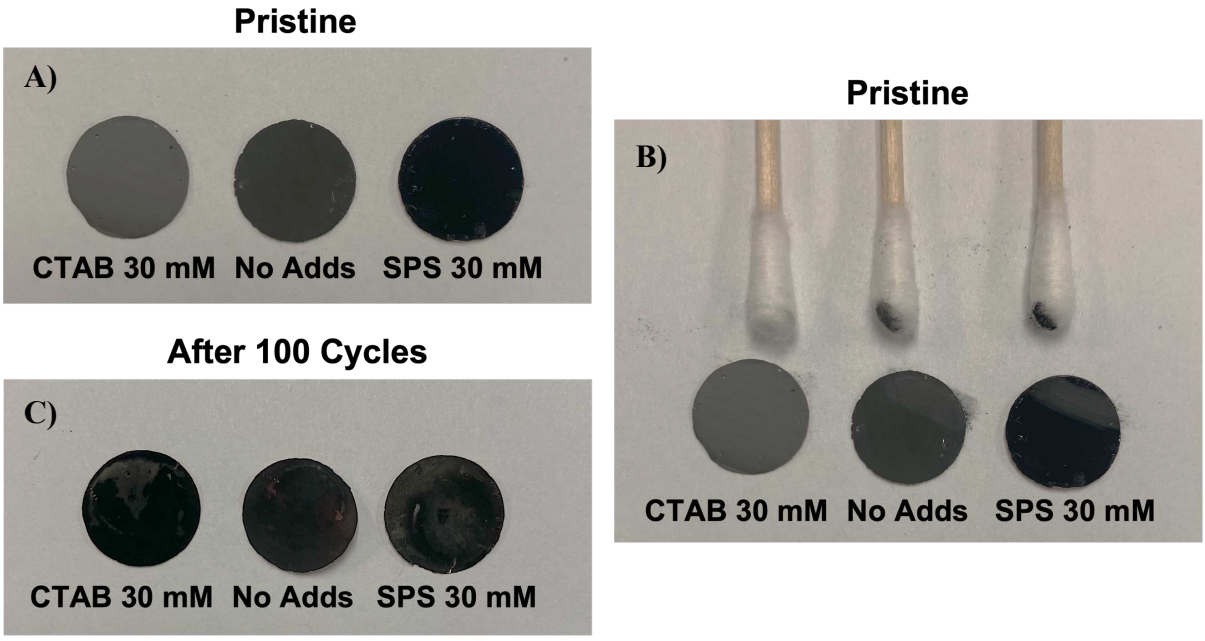

Figure S2.6. Optical image of pristine Sb anodes deposited with no additives, 30 mM CTAB, and 30 mM SPS (A). A dendrite test was conducted by rubbing a Q-tip across the substrate. (B) Both the no additive and SPS 30 mM film are dendritic. Image of the representative anodes after 100 cycles and before ex situ SEM analysis. The no additive film has pulverized and delaminated and is demonstrated by the exposed copper.

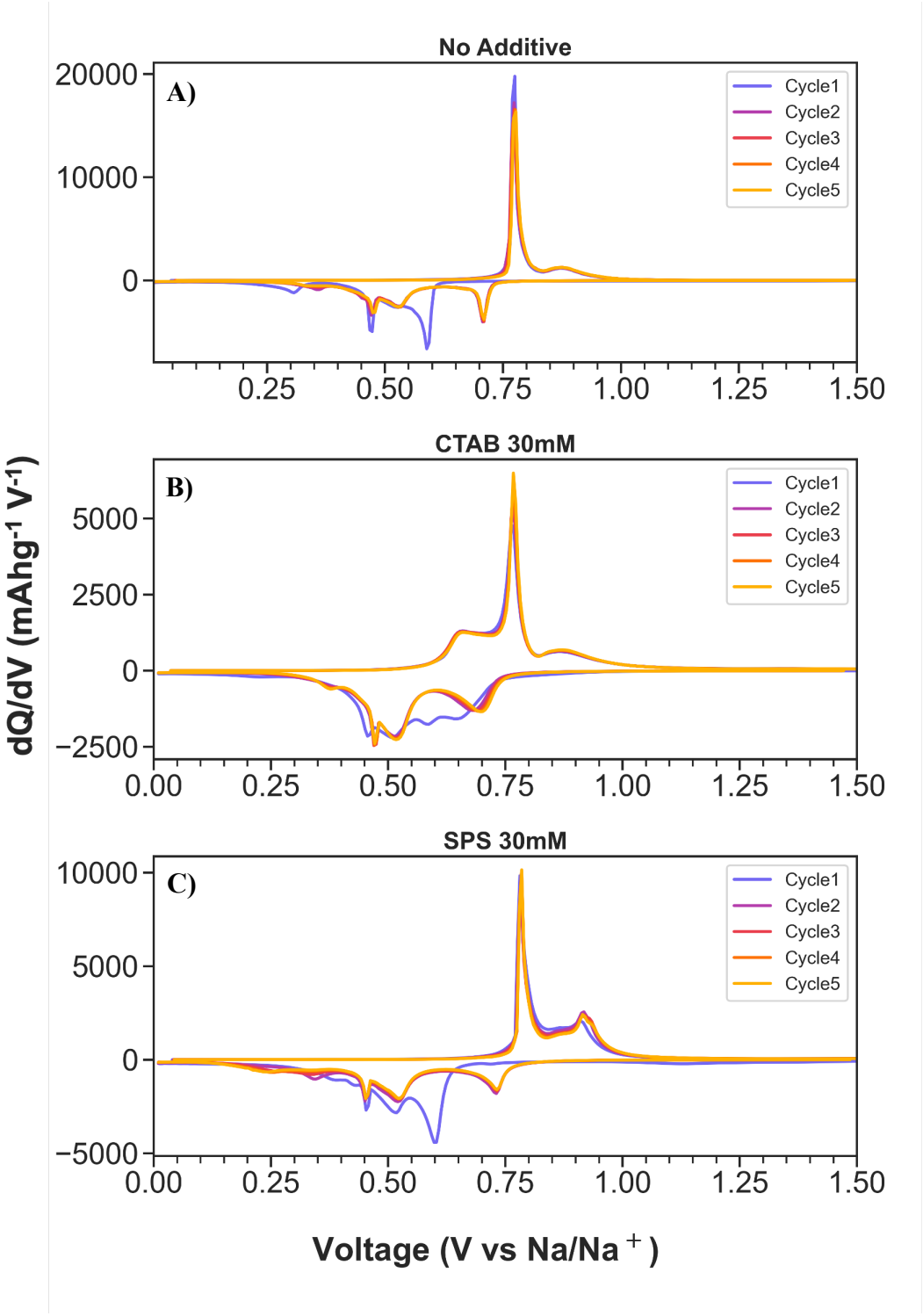

Figure S2.9. Differential capacity analysis of the Sb films deposited with (A) no additive, (B) 30 mM CTAB, and (C) 30 mM SPS at a C/10 rate (66mA/g).

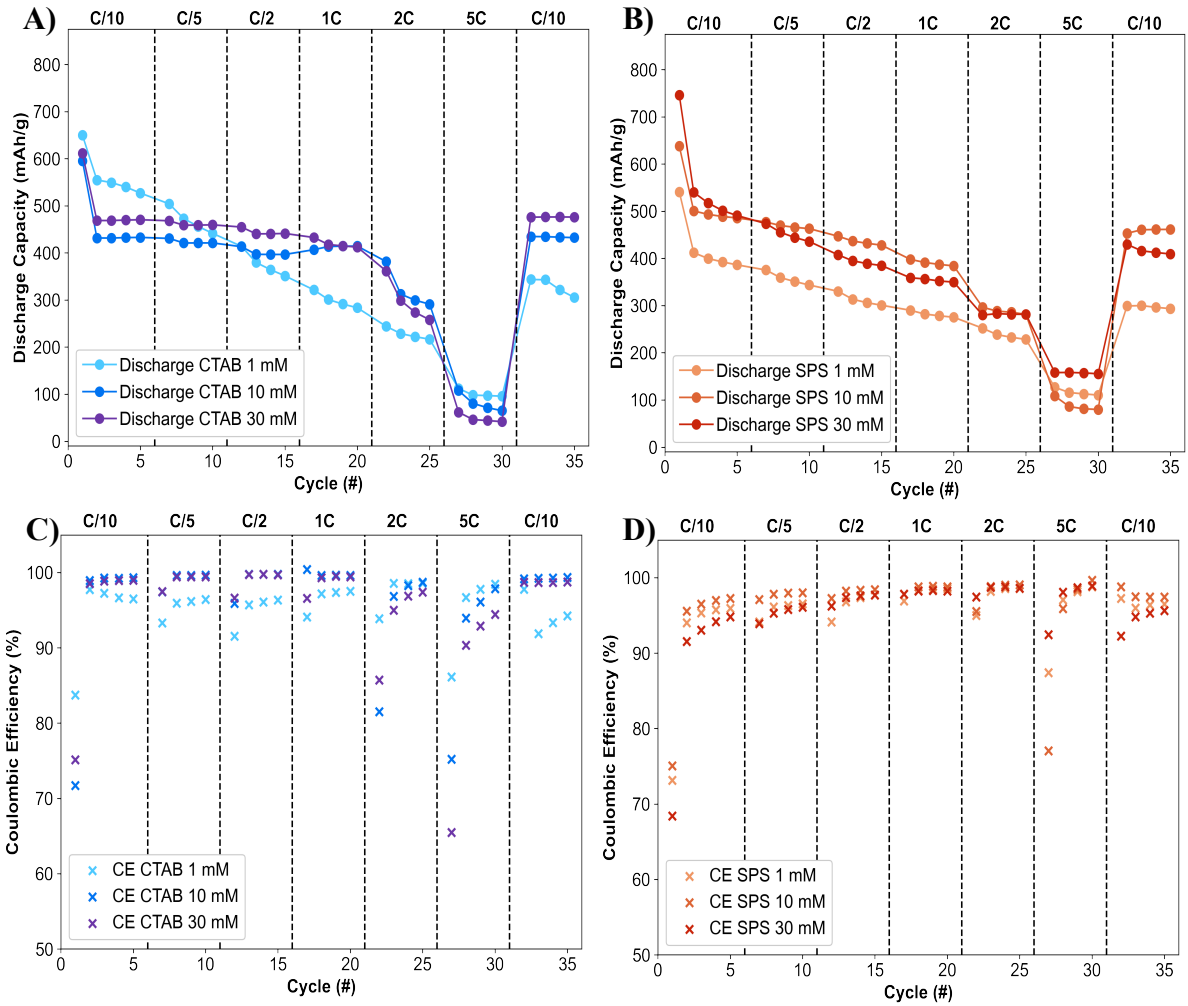

Figure S2.10. The discharge capacity (A&B) and Coulombic Efficiency (CE) (C&D) for rate capability tests on the Sb films deposited with various concentrations of (A&B) CTAB and (B&D) SPS. These tests were done in a sodium half-cell at 5 cycles for each rate. The potential range was set to 0.01 V-1.5 V vs Na/Na^+.

S2.4 References

(1) Balzar, D.; Audebrand, N.; Daymond, M. R.; Fitch, A.; Hewat, A.; Langford, J. I.; Le Bail, A.; Louër, D.; Masson, O.; McCowan, C. N.; Popa, N. C.; Stephens, P. W.; Toby, B. H. Size-Strain Line-Broadening Analysis of the Ceria Round-Robin Sample. *J Appl Crystallogr* **2004**, *37* (6), 911–924. https://doi.org/10.1107/S0021889804022551.

(2) Ectors, D.; Goetz-Neunhoeffer, F.; Neubauer, J. Routine (an)Isotropic Crystallite Size Analysis in the Double-Voigt Approximation Done Right? *Powder Diffr* **2017**, *32* (S1), S27–S34. https://doi.org/10.1017/S0885715617000070.

(3) Voiry, D.; Chhowalla, M.; Gogotsi, Y.; Kotov, N. A.; Li, Y.; Penner, R. M.; Schaak, R. E.; Weiss, P. S. Best Practices for Reporting Electrocatalytic Performance of Nanomaterials. *ACS Nano*. American Chemical Society October 23, 2018, pp 9635–9638. https://doi.org/10.1021/acsnano.8b07700.

(4) Wolfe, K. D.; Dervishogullari, D.; Stachurski, C. D.; Passantino, J. M.; Kane Jennings, G.; Cliffel, D. E. Photosystem I Multilayers within Porous Indium Tin Oxide Cathodes Enhance Mediated Electron Transfer. *ChemElectroChem* **2019**. https://doi.org/10.1002/celc.201901628.

(5) Alavi, S. M. M.; Birkl, C. R.; Howey, D. A. Time-Domain Fitting of Battery Electrochemical Impedance Models. *J Power Sources* **2015**, *288*, 345–352. https://doi.org/10.1016/j.jpowsour.2015.04.099.

(6) Dashairya, L.; Das, D.; Saha, P. Binder-Free Electrophoretic Deposition of Sb/RGO on Cu Foil for Superior Electrochemical Performance in Li-Ion and Na-Ion Batteries. *Electrochim Acta* **2020**, *358*, 136948. https://doi.org/10.1016/j.electacta.2020.136948.

APPENDIX II: SUPPORTING INFORMATION FOR CHAPTER III:

ELECTRODEPOSITION VS SLURRY CASTING: HOW FABRICATION AFFECTS

ELECTROCHEMICAL REACTIONS OF Sb ELECTRODES IN SODIUM-ION BATTERIES

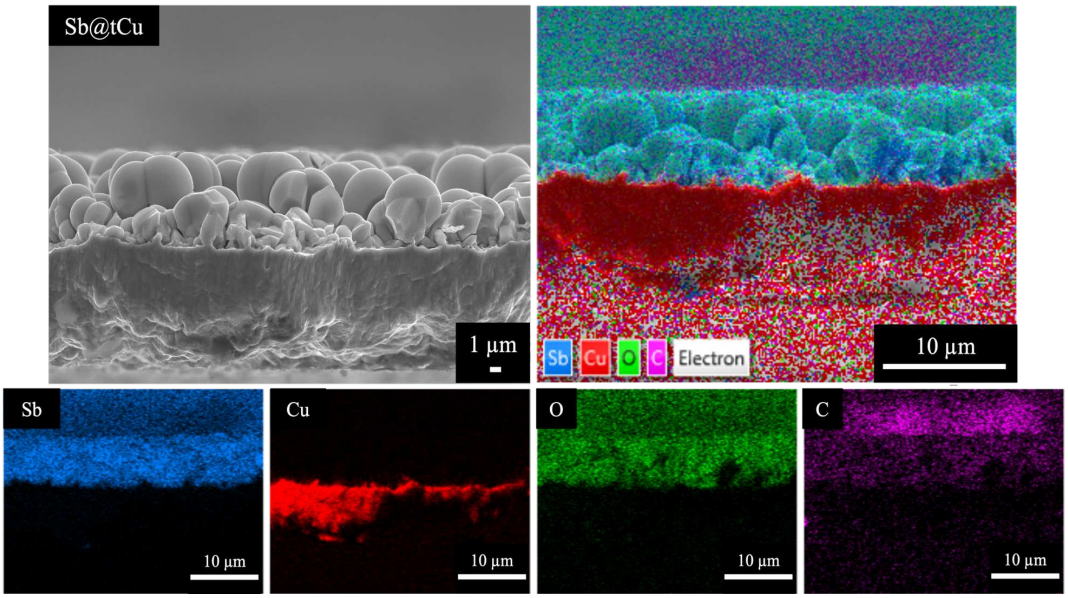

Figure S3.1. SEM images of a cross section for Sb@tCu. EDS maps are shown to help determine the thickness of the electrodeposition. The average thickness for a Sb@tCu film was determined to be 5.34 µm.

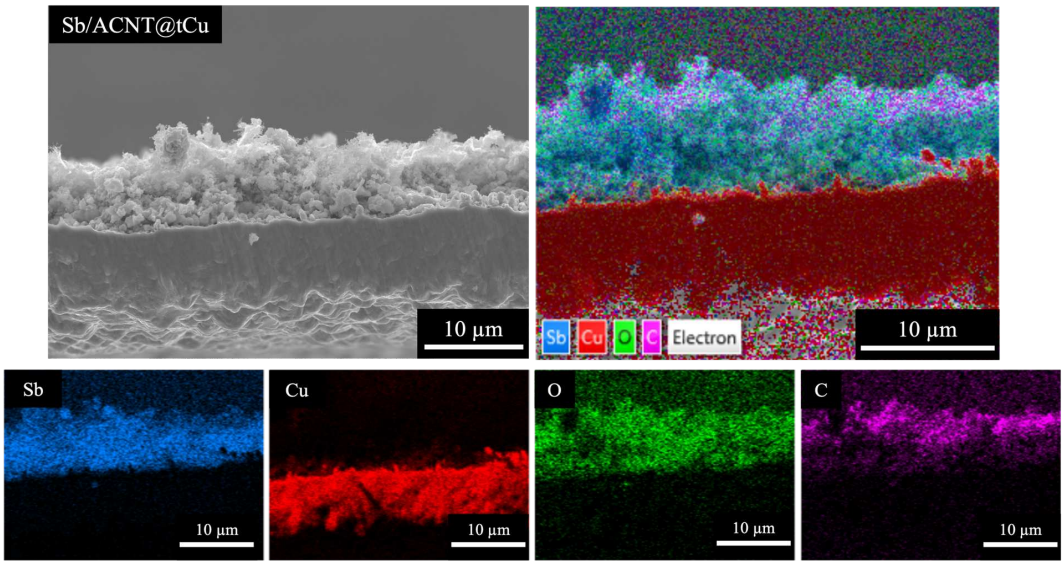

Figure S3.2. SEM images of a cross section for Sb@tCu. EDS maps are shown to help determine the thickness of the electrodeposition. The average thickness for a Sb@tCu film was determined to be 7.55 µm.

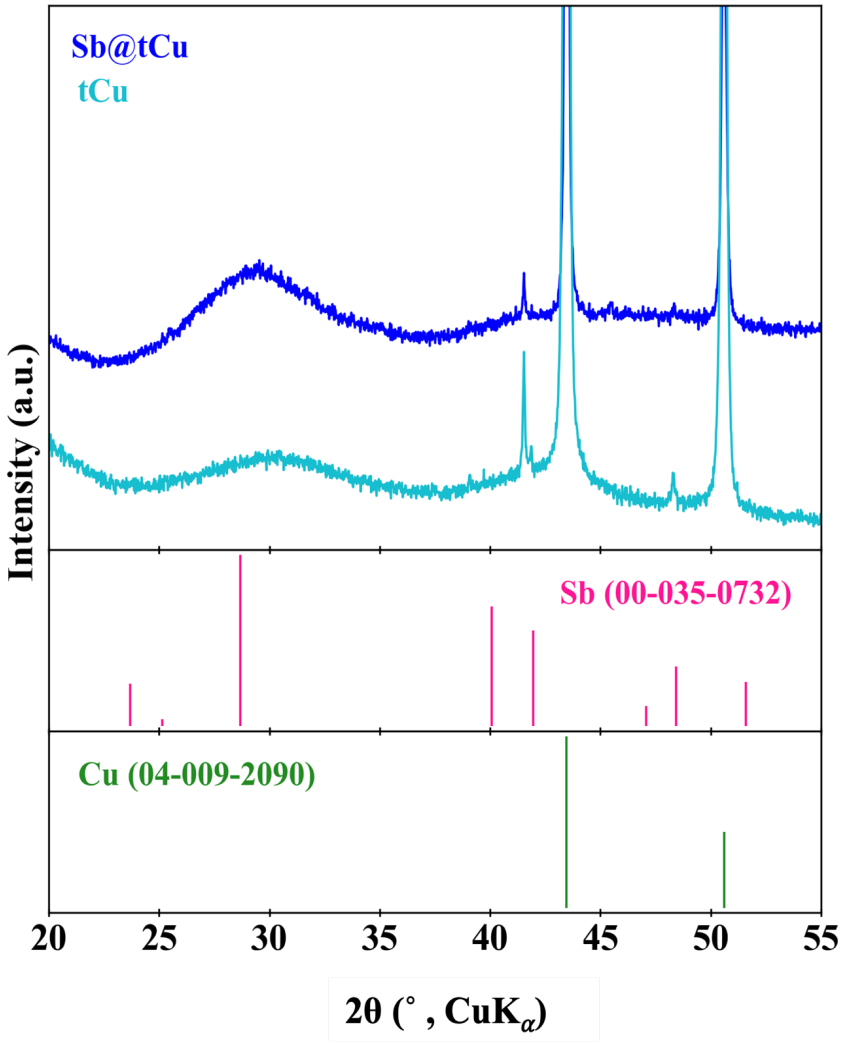

Figure S3.3. PXRD pattern of pre-cycled Sb@tCu (blue) and textured copper foil (cyan).

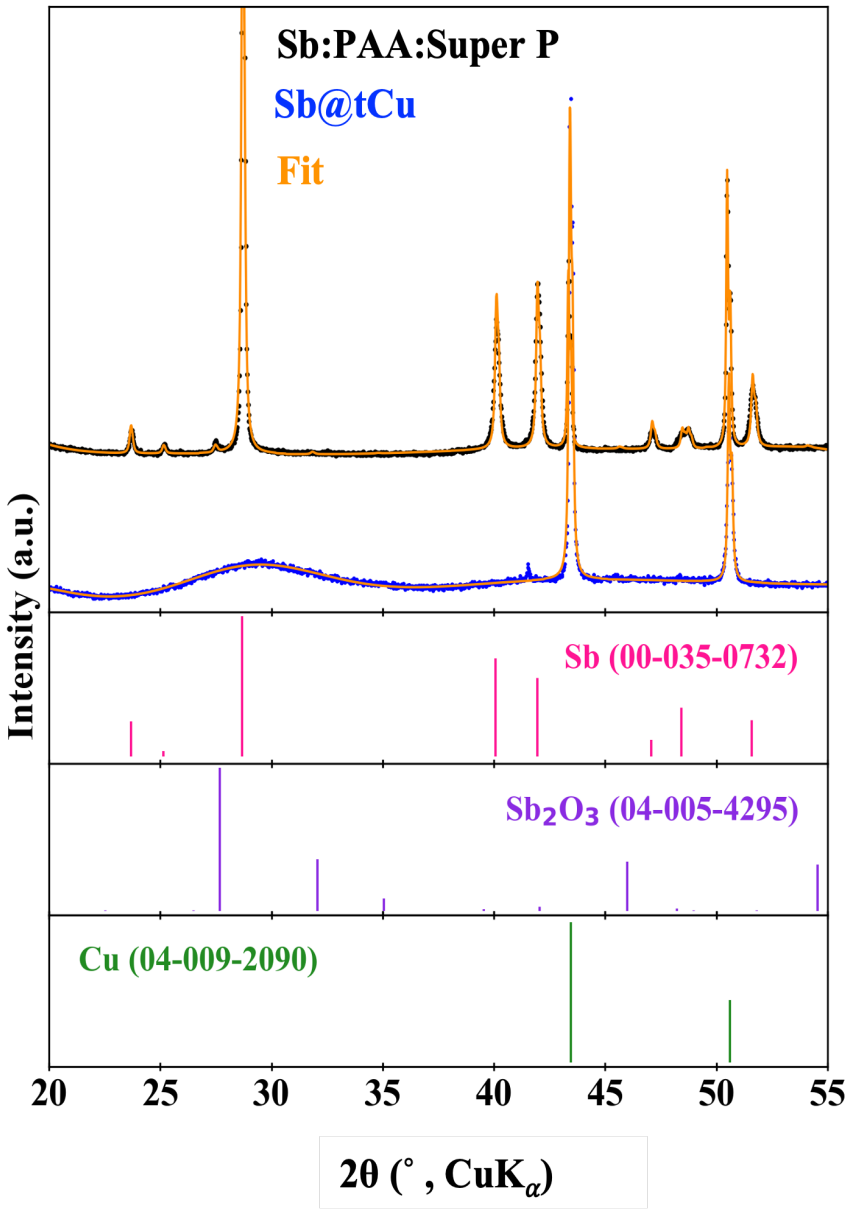

Figure S3.4. PXRD and corresponding Rietveld refinements for Sb:PAA:Super P and Sb@tCu. Rietveld refinements were performed with Topaz software

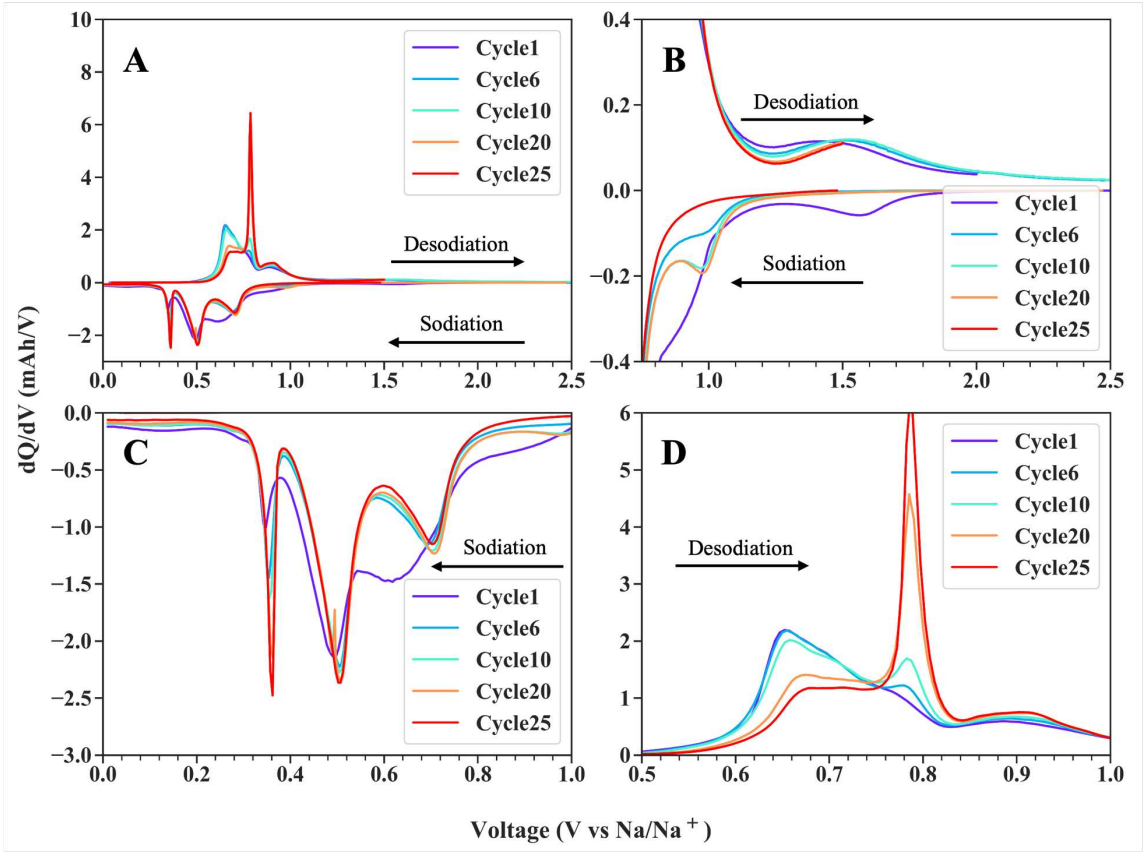

Figure S3.5. Differential capacity plots for Sb/ACNT@tCu cycled in a Na-ion half-cell cycled at 0.1 mA/mg. (A) demonstrates the complete sodiation/desodiation reactions occurring. While (B) shows a zoomed in look at the conversion of Sb to Sb_2O_3, (C) only shows the sodiation reactions, and (D) shows the desodiation reactions in more detail.

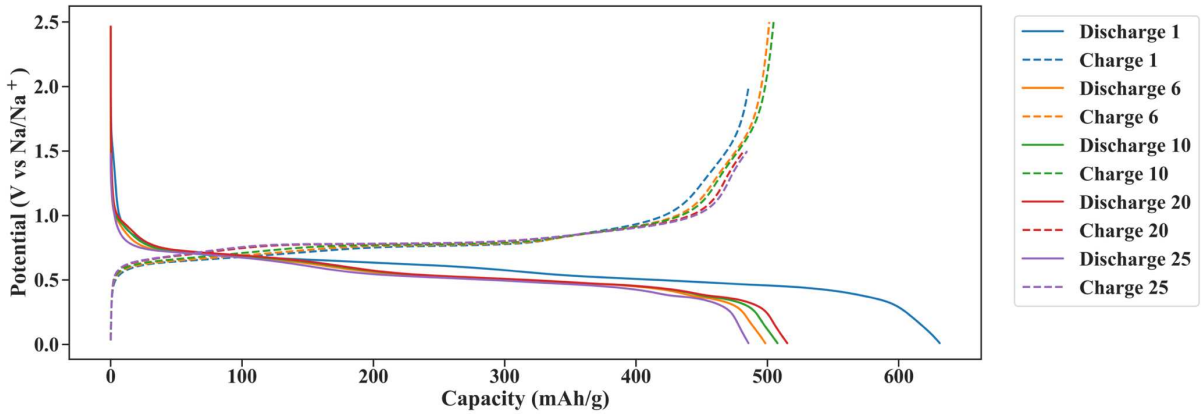

Figure S3.6. Voltage profile of Sb@tCu cycled in a Na-ion half-cell cycled at 0.1 mA/mg. Cycles 1and 6 were cycled using condition 1, cycles 10 and 20 were cycled with condition 2, and cycle 25 was cycled with condition 3 as described in Table 2.

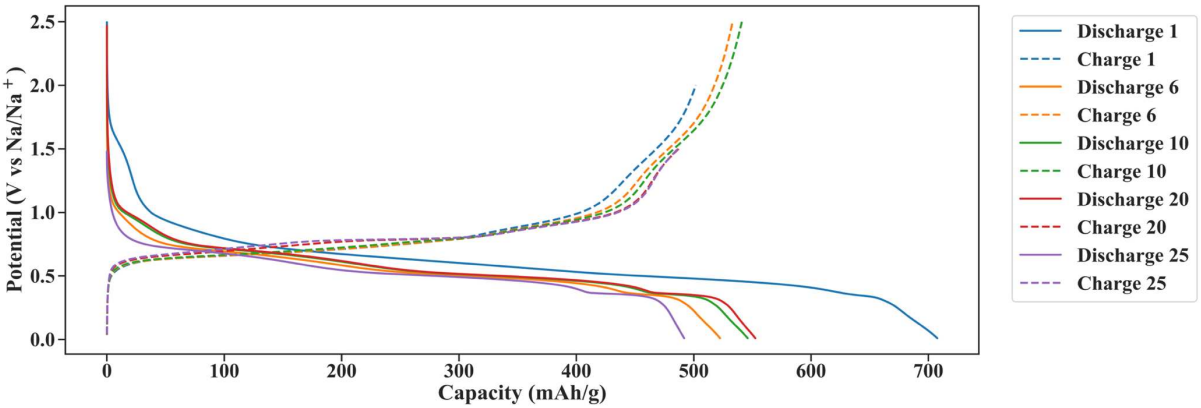

Figure S3.7. Voltage profile of Sb/ACNT@tCu cycled in a Na-ion half-cell cycled at 0.1 mA/mg. Cycles 1and 6 were cycled using condition 1, cycles 10 and 20 were cycled with condition 2, and cycle 25 was cycled with condition 3 as described in Table 2.

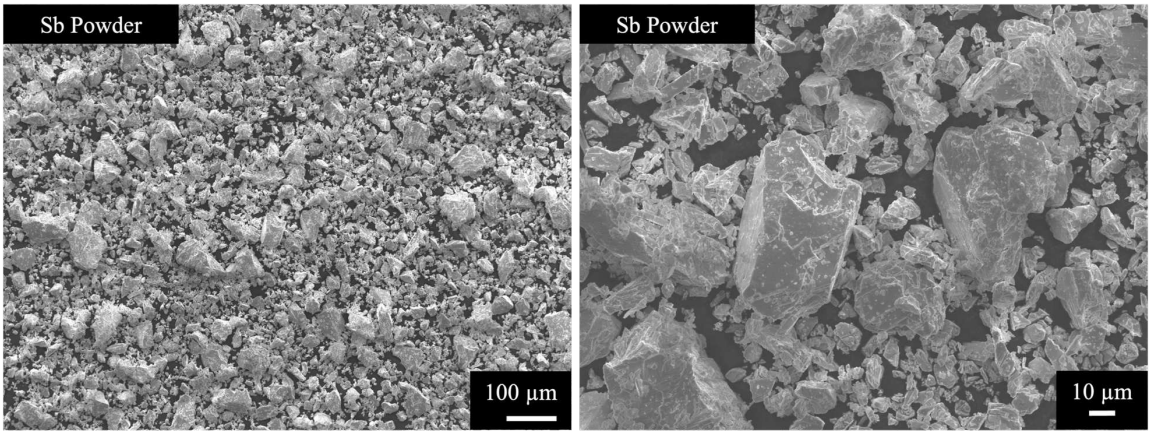

Figure S3.8. SEM images of Sb powder before ball milling with Super P to form the slurry. The largest particles were measured to be 70-78 µm in length.

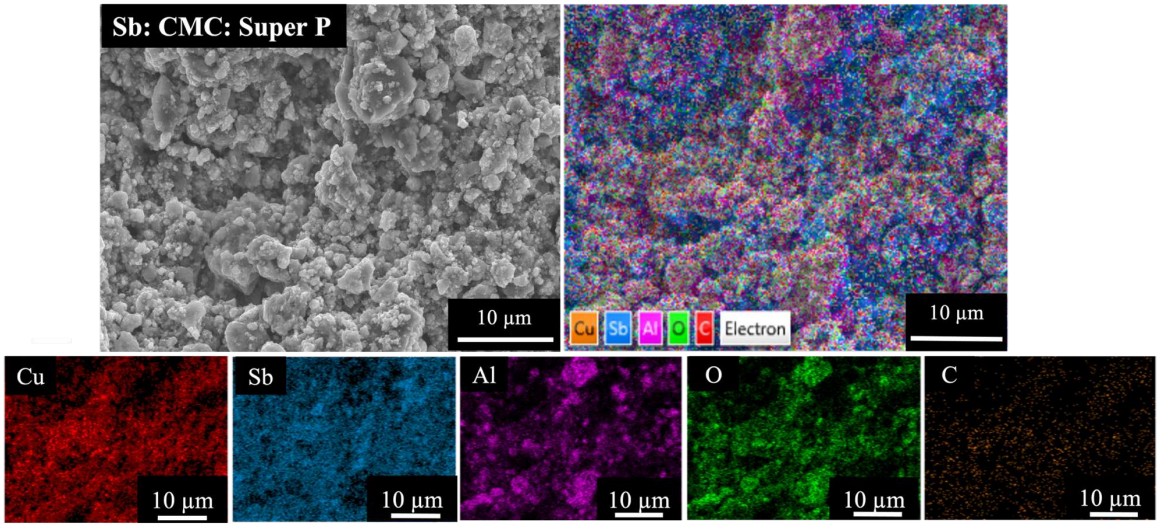

Figure S3.9. SEM images of slurry casted Sb:CMC:Super P with full EDS mapping.

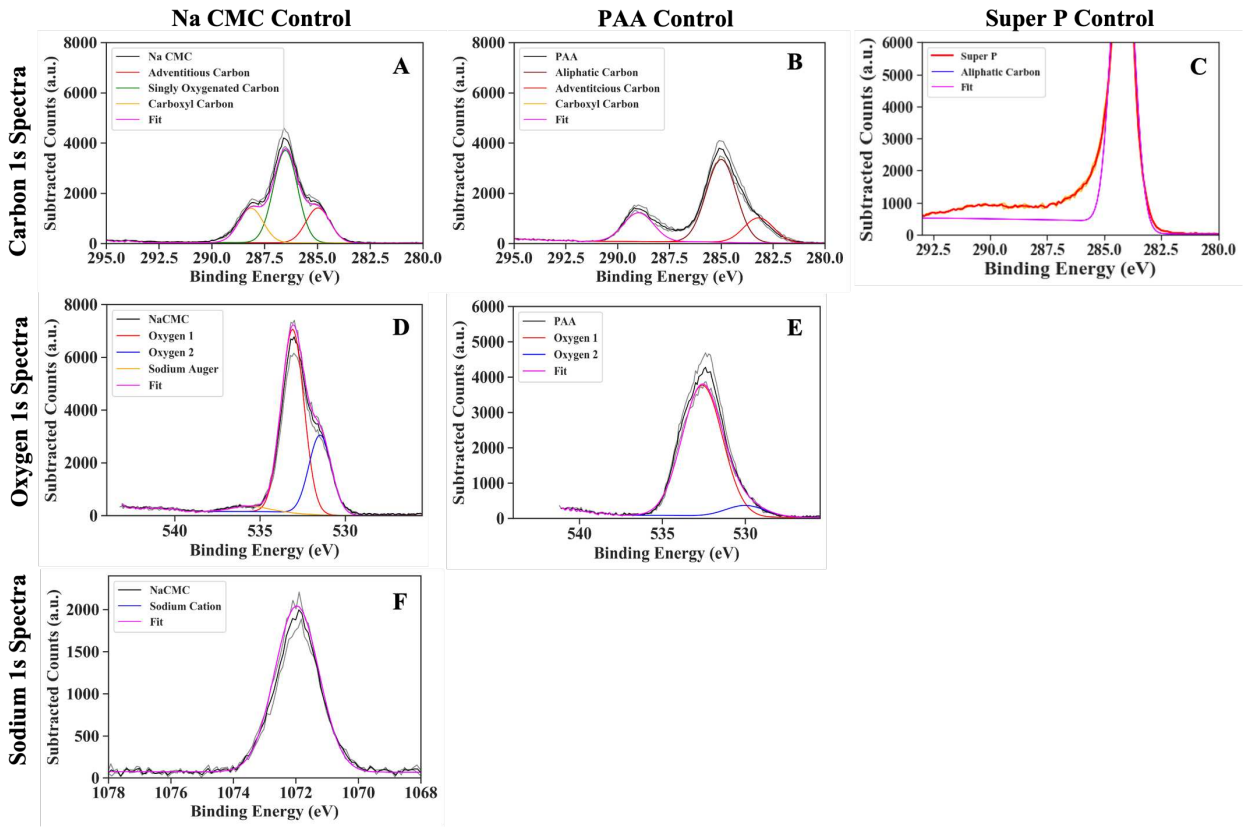

Figure S3.10. XPS of individual slurry components. Each component was ran as a control to understand how the individual additive/binder attributed to the overall slurry composite environments. Spectra (A,D,F) describe the carbon, oxygen and sodium environments of Na CMC. Spectra (B,F) describe the environments in PAA and spectra (C) describes the carbon environments in Super P. Each graph includes the raw data from each scan with an example of how the data was fit.

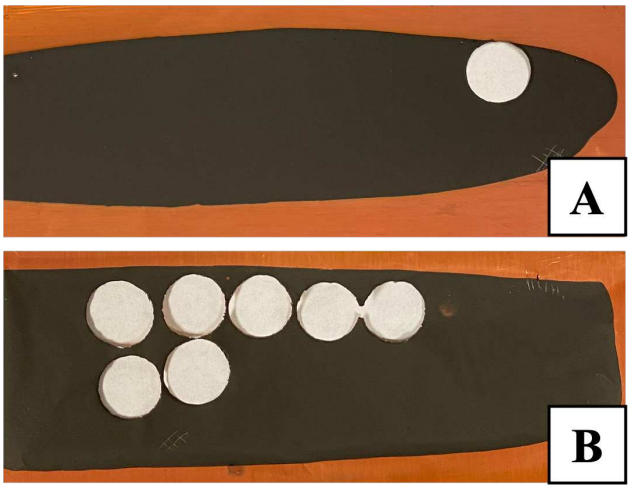

Figure S3.11. Images of slurry casted Sb:PAA:Super P (A) and Sb:CMC:Super P (B).

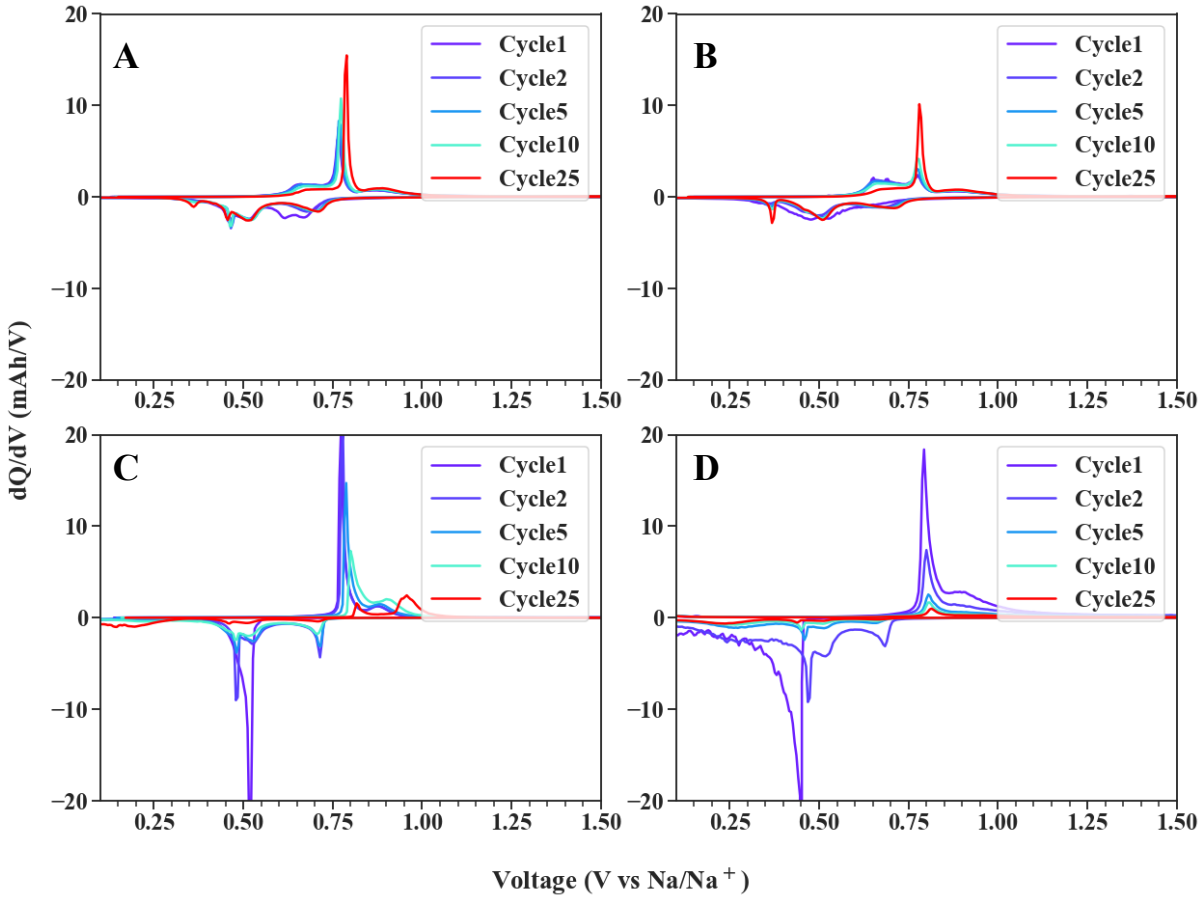

Figure S3.12. Zoomed out differential capacity plots for electrodeposited Sb@tCu (A), and Sb/ACNT@tCu (B), and slurry casted Sb:CMC:Super P (C), and Sb:PAA: Super P (D). All anodes were cycled in a Na-ion half-cell cycled at 0.1 mA/mg.